Optimal conditions and sensitivity of brain MRE : from homogeneous to heterogeneous media

Fatiha Andoh

Thèse de doctorat

NNT : 2021UPAST042

université PARIS-SACLAY

Optimal conditions and sensitivity of brain MRE: from homogeneous to heterogeneous media

Conditions optimales et sensibilité de l'ERM cérébrale : milieux homogènes à hétérogènes

Thèse de doctorat de l'Université Paris-Saclay

École doctorale n°575, Electrical, Optical, Bio: physics and engineering (EOBE)
Spécialité de doctorat : Imagerie et physique médicale
Unité de recherche : Université Paris-Saclay, CEA, CNRS, Inserm, Laboratoire d'Imagerie Biomédicale Multimodale Paris Saclay, 91401, Orsay, France
Référent : Faculté de Sciences d'Orsay

Thèse présentée et soutenue à Orsay, le 29 mars 2021, par

Fatiha ANDOH

Composition du Jury

Najat SALAMEH Professeure, HDR, AMT Center, Basel, Switzerland	Présidente
Jonathan VAPPOU Chargé de Recherche CNRS, HDR, iCUBE, Strasbourg, France	Rapporteur & Examinateur
Jens WÜRFEL Neurologue, HDR, CEO, MIAC AG, Basel, Switzerland	Rapporteur & Examinateur
Viviane BOUILLERET Neurologue, HDR, UPSaclay, CHU Bicêtre (UNCE), Le Kremlin-Bicêtre, France	Examinatrice
Jean-Pierre REMENIERAS Ingénieur de Recherche, HDR, iBrain, Tours, France	Examinateur
Ralph SINKUS Professeur, HDR, King's College, London, United-Kingdom	Examinateur

Direction de la thèse

Xavier MAÎTRE Chargé de Recherche CNRS, BioMaps, Orsay, France	Directeur de thèse
Claire PELLOT-BARAKAT Chargée de Recherche Inserm, BioMaps, Orsay, France	Co-encadrante de thèse

Contents

Acknowledgements

These three years as PhD student was a memorable human and scientific experience which allowed me to enter in the wide world of medical imaging, and in particular in the world of the magnetic resonance elastography, which is an interdisciplinary technique requiring a broad knowledge and therefore a varied staff. Thus, I would like to thank many people who contributed in one way or another during this three-year thesis:

- Claire Pellot-Barakat and Xavier Maître for supervising my doctoral thesis in a complementary way. Thank you for supporting me in every thesis steps and encouraging me to participate in many conferences during these three years' thesis work. Your guidance and advices have been precious and allowed me to work self-directed.
- All the members of the Biomaps laboratory. Particularly, Rose-Marie Dubuisson, Georges Willoquet, Albine Pinseel, Laurène Jourdain, for their help in various tasks and useful advice during my thesis.
- The formers doctoral students, Tanguy Boucneau, Felicia Julea, Jinlong Yue, and Khalil Rachid, with whom it was a pleasure to work and share our experiences.
- Marion Tardieu, Philippe Garteiser, Gwenaël Pagé for helping me carry out the phantom experiments essential for my thesis.
- Luc Darrasse and Vincent Lebon for welcoming me at the SHFJ in this transitory period between IR4M and BioMaps Laboratory.
- Jens Würfel and Jonathan Vappou for accepting to be the reviewers of this work and Najat Salameh, Jean Pierre Reminieras, Ralph Sinkus and Viviane Bouilleret for accepting to be the jury members.
- And last but not the least, my parents and my brothers and sisters who have always pushed me to excellence and to never give up in the face of failure.

Résumé de thèse

L'élastographie par résonance magnétique (ERM) est une technique d'imagerie pour la caractérisation mécanique des tissus biologiques. Cette technique est capable de fournir des informations supplémentaires sur le développement de processus pathologiques pouvant survenir dans des maladies comme la fibrose, le cancer, l'hypertension ou les traumatismes, car ces affections s'accompagnent généralement de modifications des propriétés mécaniques des tissus. Ces altérations sont facilement détectées en routine clinique par palpation même si cette approche est limitée aux organes superficiels et produit des résultats globaux, qualitatifs et dépendants de l'opérateur. L'approche par ERM surmonte ces limitations en cartographiant en trois dimensions les propriétés mécaniques des organes profonds, inaccessibles autrement, comme le cerveau. L'ERM consiste à enregistrer par IRM en contraste de phase les champs de déplacement induits par la propagation d'une onde de cisaillement générée dans le tissu cible. Des paramètres mécaniques tels que la vitesse de l'onde de cisaillement, l'élasticité ou la viscosité de cisaillement peuvent ensuite être déduits en inversant les équations différentielles des champs de déplacement 3D.

Cependant, la promesse d'une quantification absolue des modules viscoélastiques de cisaillement par ERM est minée par la dépendance multiple des résultats aux paramètres d'acquisition et aux méthodes de reconstruction. Des travaux récents ont montré que les facteurs déterminant l'exactitude et la précision de la mesure par ERM peuvent finalement être ramenés à deux paramètres qui caractérisent essentiellement la qualité de l'échantillonnage de l'onde de cisaillement se propageant : le facteur d'échantillonnage spatial (ou nombre de voxels par longueur d'onde), $s = \lambda/a$, et le facteur d'échantillonnage d'amplitude (ou facteur de qualité des données), $Q = q \,/\, \Delta q$, où λ est la longueur d'onde de cisaillement, a, la taille du voxel, q, l'amplitude du rotationnel du champ de déplacement, et Δq , l'incertitude de mesure associée. Il a été montré que, dans des milieux mécaniquement homogènes où la propagation des ondes de cisaillement se fait à une unique longueur d'onde, Les conditions sur s et Q doivent être optimisées pour réaliser une mesure la plus précise et la plus exacte possible et ainsi rendre les résultats de l'ERM valides.

Dans ce travail, les conditions optimales ont été étudiées dans des milieux hétérogènes et structurés afin qu'elles puissent être appliquées au cerveau. Compte tenu des contraintes associées, la précision et l'exactitude de la vitesse et des modules viscoélastiques ont été déterminées pas à pas d'abord dans des fantômes, puis in vivo, à la fois à l'intérieur et en dehors des conditions optimales de l'ERM.

Ce manuscrit commence par une introduction établissant une revue des différents résultats obtenus dans la littérature en ERM cérébrale. Elle établit les limites de la

technique et des pratiques. Elle détermine les orientations des travaux réalisés au cours de cette thèse.

Dans le chapitre 1, les principes physiques de base, de l'acquisition et de la reconstruction en ERM sont posés. Les hypothèses et les équations derrière l'élastographie par résonance magnétique utilisés tout au long de la thèse sont détaillés. Les méthodes et les instruments que nous avons développés pour pouvoir appliquer la technique dans le cerveau y sont décrits.

Dans les chapitres 2, 3 et 4, les conditions optimales sur s et Q sont étudiées tout d'abord dans des milieux homogènes d'élasticité différentes puis dans des milieux hétérogènes. La précision et l'exactitude de la vitesse et des modules viscoélastiques de cisaillement ont été déterminées pas à pas d'abord dans des fantômes, puis in vivo dans le cerveau, à la fois à l'intérieur et en dehors des conditions optimales de l'ERM.

Dans le chapitre 2, la précision et l'exactitude de l'ERM sont étudiées selon différentes stratégies d'échantillonnage optimal en réalisant des expériences multifréquence sur un ensemble de fantômes calibrés mécaniquement qui représentent quatre stades de la fibrose hépatique (Figure 1). Une quantification absolue et une gradation significative de la *fibrose* ne peuvent être obtenues que lorsque les conditions optimales sont remplies soit prospectivement par une excitation multifréquence adéquate, soit rétrospectivement par un multi-rééchantillonnage des données (Figure 1).

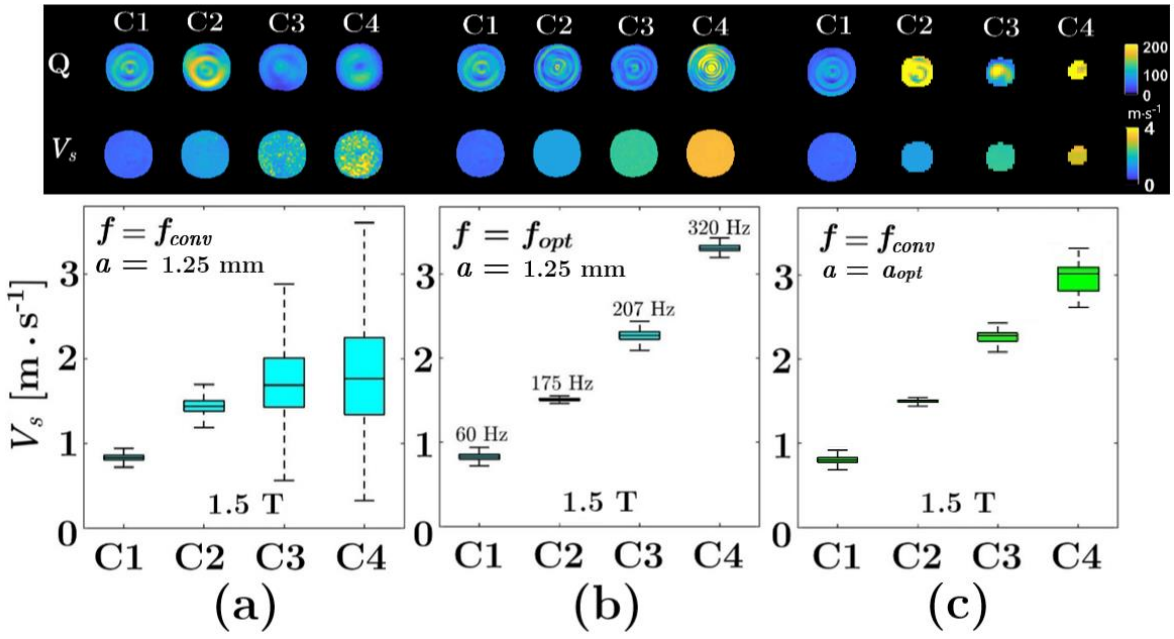

Figure 1 : Acquisitions ERM multifréquence pour la quantification des paramètres mécaniques et une discrimination significative de fantômes représentant quatre grades de fibrose hépatique à 1.5 T. En haut, cartes de facteur de qualité, Q, et de vitesse de cisaillement, V_s. En bas, à la fréquence d'excitation conventionnelle, f = 60 Hz, les vitesses de cisaillement estimées (V_s) sont très dispersées, conduisant à des mesures sur différents fantômes qui se chevauchent (graphique (a)). Aux fréquences d'excitation

optimales, $f = f_{opt}$ (graphique (a)) et pour des données rééchantillonnées avec des tailles de voxels adaptées, $a = a_{opt}$ (graphique (c)), l'échantillonnage spatial des ondes de cisaillement étant optimale, les mesures sont à la fois précises et exactes et les fantômes sont facilement discriminés (graphique (b) et graphique (c)).

Dans le chapitre 3, les conditions optimales de l'ERM sont déterminées sur un fantôme mammaire hétérogène contenant des inclusions modélisant des lésions tumorales plus rigides que le parenchyme homogène environnant. Cette seconde étude a permis de montrer la nécessité de définir différents facteurs d'échantillonnage optimaux par des acquisitions à différentes fréquences d'excitation afin, d'une part, de déterminer les paramètres mécaniques régionaux avec les meilleures précision et exactitude possibles et d'autre part, de discriminer significativement mieux différentes régions mécaniques du fantôme (Figure 2).

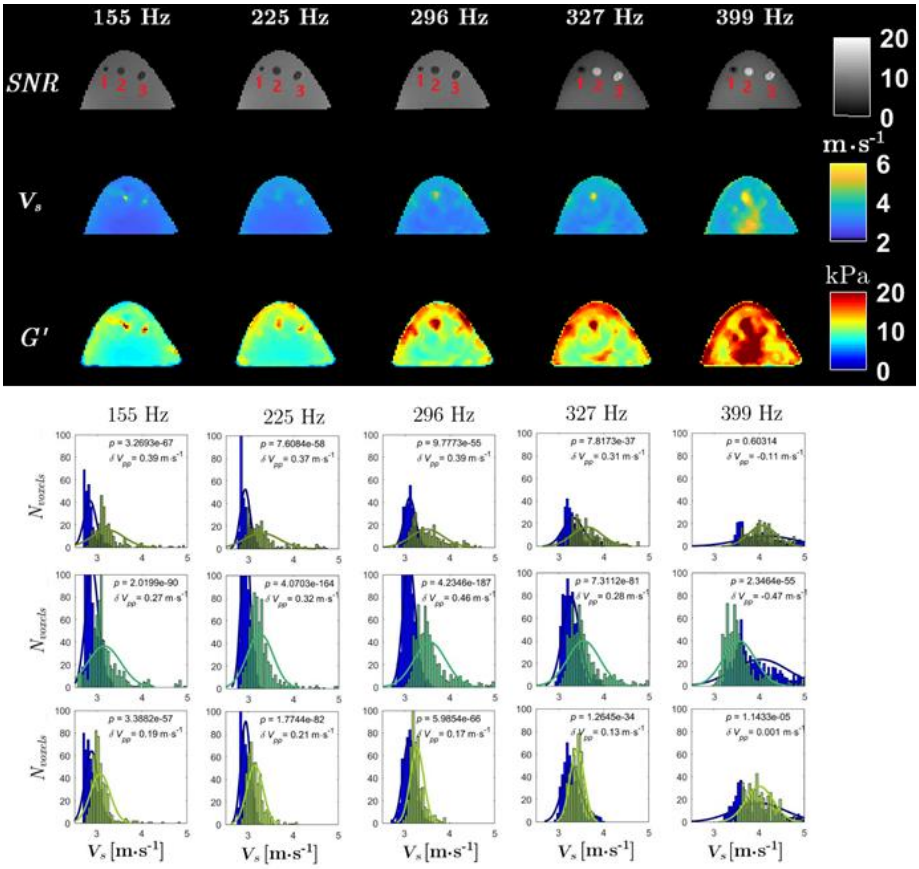

Figure 2 : Acquisitions ERM multifréquence pour la quantification des paramètres mécaniques et la discrimination optimale des quatre régions d'intérêt du fantôme hétérogène (parenchyme en bleu, inclusion 1 en kaki, inclusion 2 en turquoise et inclusion 3 en vert citron). Le meilleur compromis pour discriminer mécaniquement de manière significative (p-values obtenue à partir de tests Wilcoxon inférieur à 10^{-3}) les différentes régions et pour déterminer la vitesse de cisaillement avec un écart-type minimal est à 296 Hz pour les trois inclusions. À cette fréquence, s se trouve dans le domaine optimal.

Dans le chapitre 4, des acquisitions d'ERM cérébrale à différentes fréquences d'excitation permettent d'étudier les meilleures conditions pour discriminer avec précision et exactitude la matière blanche, la matière grise et le cervelet chez un sujet sain (Figure 3 (a),(b) et (c)). Le cervelet s'avère moins élastique et visqueux que les matières blanche et grise du cerveau, qui présentent des modules viscoélastiques de cisaillement similaires en dépit de leurs structures anatomiques différentes. Ces résultats corroborent les résultats récemment trouvés dans la littérature et remettent en question la sensibilité générale de la technique à caractériser mécaniquement les maladies cérébrales.

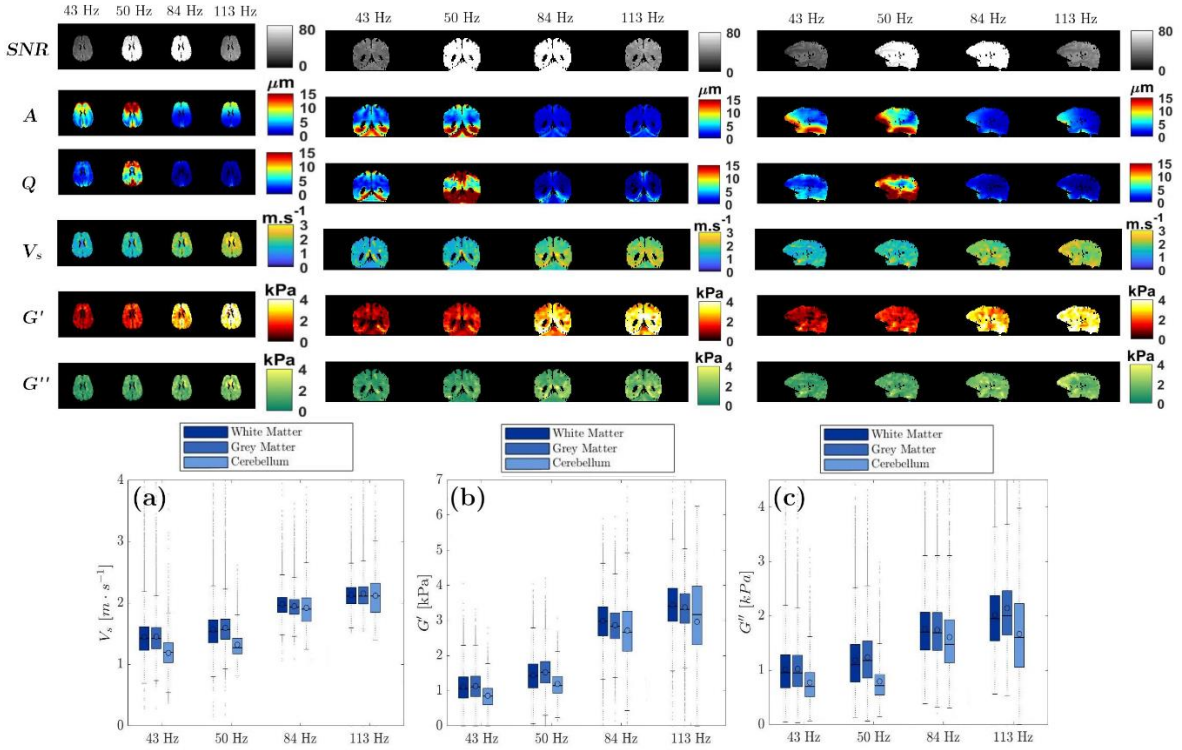

Figure 3 : Cartes de rapport signal-à-bruit, SNR, amplitude du champ de déplacement, A, facteur de qualité, Q, vitesse de cisaillement, V_s, et modules de viscoélasticité de cisaillement, G', et G' pour $f_{exc} = \{43,50,83,113\}$ Hz dans les plans axial, frontal et sagittal. Détermination des conditions optimales pour la discrimination de la matière blanche (bleu foncé), la matière grise (bleu) et le cervelet (bleu clair). Le cervelet présente des paramètres mécaniques (vitesse de cisaillement V_s, élasticité G' et viscosité G'') toujours plus faible que dans la matière blanche et la matière grise qui sont difficilement discriminables même à fréquence optimale.

Enfin, dans le chapitre 5, des conditions physiologiques analogues à la microgravité ont été mises en œuvre dans le tunnel de l'appareil IRM pour modifier les propriétés mécaniques du cerveau et éprouver la sensibilité de l'ERM aux changements induits (Figure 4).

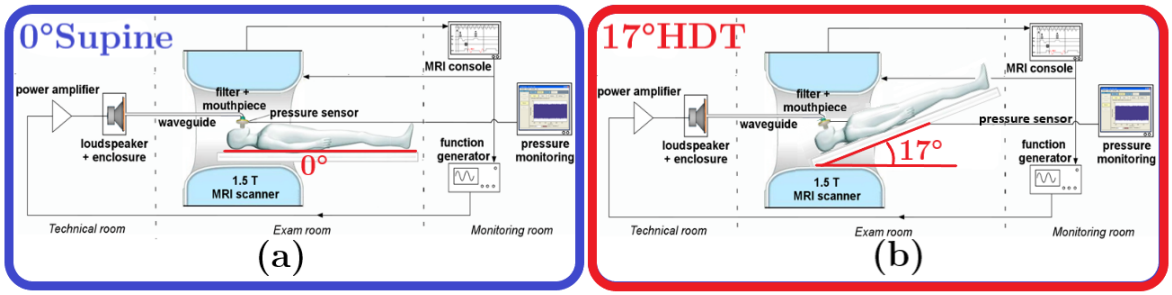

Figure 4 : Schéma de la configuration des acquisitions ERM en décubitus dorsal à 0 ° (a) et à 17° (b). Le sujet est placé dans un IRM 1.5 T avec la tête placée dans une antenne tête standard (Philips Healthcare, Eindhoven, Les Pays-Bas). Les ondes de pression générées et amplifiées à distance sont guidées au centre de l'aimant de l'IRM jusqu'à la cavité buccale du sujet. Le niveau d'onde de pression est surveillé à la bouche via un capteur à fibre optique. Les ondes de pression sont synchronisées à la séquence d'acquisition IRM.

Lorsqu'un sujet est incliné la tête en bas, le déplacement attendu des fluides céphaliques peut augmenter la pression intracrânienne chez des sujets sains comme dans un vol spatial en apesanteur. Les acquisitions d'ERM sont réalisées dans des conditions optimales pour sonder les propriétés mécaniques d'un cerveau subissant des variations de pression contrôlées par la gravité. À travers une augmentation significative de la vitesse et du module dynamique de cisaillement dans tout le cerveau (Figure 5), en particulier dans les régions périphériques supérieures, l'ERM révèle le durcissement associé des tissus. En revanche, aucune différence significative de la durée de vie du signal, T_2, entre 17° et 0° n'est mesurée. Dans de telles conditions de pression, l'ERM fournit une mesure plus sensible de l'état du tissu cérébral que les résultats de relaxométrie par résonance magnétique publié dans la littérature. Par la suite, l'ERM cérébrale, réalisée dans des conditions optimales, pourrait être avantageusement utilisée pour détecter des altérations mécaniques dues à des changements de pression similaires ou inverses dans des processus pathologiques tels que l'hémorragie, l'hydrocéphalie ou le cancer qui sont accompagnés généralement d'une redistribution du flux sanguin et d'une accumulation ou d'une diminution du liquide cérébrospinal.

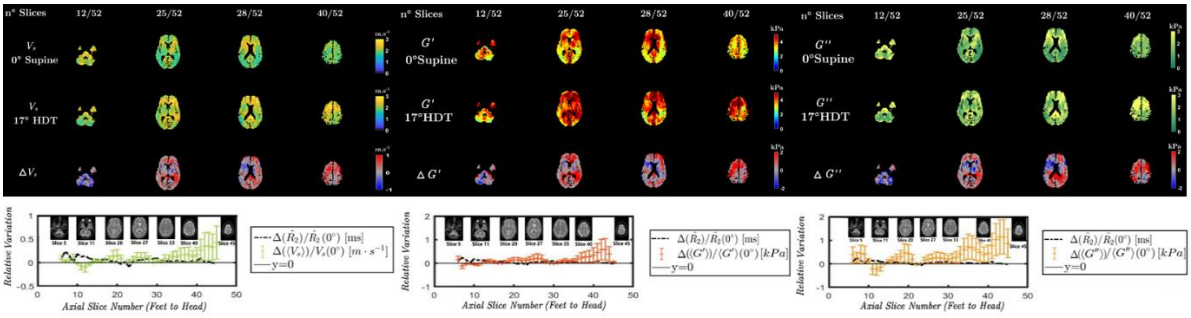

Figure 5: Acquisitions ERM à 104 Hz pour la quantification des paramètres mécaniques (vitesse de cisaillement V_s à gauche, module d'élasticité G' au milieu et

viscosité à droite, G') en décubitus dorsal à 0° (première ligne) et à 17° (deuxième ligne) et différence des paramètres mécaniques entre les deux positions (troisième ligne). Les courbes de variation relative (en bas) montrent une augmentation globale de la vitesse de cisaillement (courbe verte) et des modules de viscoélasticité (courbe orange foncé et orange clair) dans le cerveau en inclinée à 17° avec un gradient positif le long de l'axe inférieur-supérieur. Aucune différence significative mesurable des valeurs de T_2 entre 17° et 0° n'est mesurée (courbe noire).

L'ensemble de ces quatre études sur fantômes et cerveau soutiennent les exigences de remplir les conditions optimales de l'ERM pour améliorer l'incertitude de mesure et produire une réponse mécanique valide dans les tissus ciblés. Elles remettent évidemment en question les approches actuelles mises en œuvre aujourd'hui en routine clinique où les valeurs rapportées des modules de viscoélasticité de cisaillement dans des organes difficile d'accès comme le cerveau peuvent souvent être biaisées et imprécises. Dans de telles situations, les tissus mécaniquement différents ou les tissus sains et pathologiques peuvent être mécaniquement confus et le diagnostic peut être non concluant ou, pire encore, produire des faux positifs et des faux négatifs. Dans les conditions optimales vérifiées ici, l'ERM multifréquence pourrait être avantageusement appliquée au-delà de la médecine spatiale à la pathologie générale du cerveau.

Introduction

Background

Since the end of the 19th century, technological advances have continuously made the field of medical imaging evolve to become the foundation of modern medicine. Through the physically measurable element in the human body, medical imaging is able to reveal anatomical, functional and molecular abnormalities allowing the detection, characterization and diagnosis of disease in a non-invasive manner. Nowadays, there are several imaging modalities allowing the detection and therapeutic monitoring of the disease: those which are said to be non-ionizing such as Magnetic Resonance Imaging (MRI), ultrasound and optical imaging and those which are said to be ionizing, such as X-ray imaging or nuclear imaging. These modalities make it possible to anticipate the advanced stages of a disease because they support the detection of functional or molecular abnormalities that may appear in the disease progression earlier than anatomical abnormalities which often appear in an advanced stage of the disease. Although these modalities are complementary, MRI has the advantage of providing both functional and anatomical information in a non-ionizing manner.

One of the challenge of medical imaging research is to combine imaging methods in order to provide as much information as possible on the characteristic features of the disease to be detected, thus making the clinical follow-up and treatment decision easier and earlier. In the field of oncology for example, detection of a tumor can sometimes be facilitated by the association of MRI with PET. However, these two modalities cannot provide information on the mechanical properties of the tumor. The knowledge of these properties is important for the clinician as mechanical properties are generally altered at an early stage during a pathological process and this change could yield invaluable insights in the clinical diagnosis and therapeutic monitoring of many diseases.

Currently, biopsy is the gold standard for deciding on the classification and staging of a disease like cancer. However, a biopsy is an invasive technique with potential complications, which is too drastic in the case of benign lesions. Alternatively, clinicians may use palpation, which involves looking for an abnormality in soft tissue and assessing the tissue stiffness within an organ. However, this technique is limited to superficial organs with global, qualitative, and operator dependent results. In order to overcome these limitations and to increase the sensitivity of the estimated stiffness for a reliable clinical diagnosis, imaging techniques were developed in the 1990s to objectively and quantitatively access the mechanical properties of tissues in a non-invasive manner: it is elastography. Initially introduced by the Ophir's team [1], the term elastography was subsequently associated with any imaging modality mapping the mechanical properties

such as ultrasound elastography [1] or magnetic resonance elastography (MRE) [2]. These two techniques generally consist in exerting a stress on a target tissue and imaging the deformation as the response of the tissue to the stress.

MRE combines magnetic resonance imaging with elastography. It consists in recording, with MRI, the displacement fields induced by the propagation of a shear wave generated in the target tissue. Mechanical parameters like shear wave velocity or shear elasticity and shear viscosity can then be deduced by inverting the differential equations of the 3D displacement fields [2] a priori without theoretical bias [3], [4].

In recent years, the MRE technique has made it possible to obtain measurements of viscoelastic properties while assuming homogeneity and isotropy in organs such as the liver [5] and the breast [4]. The brain, where so far ultrasound elastography fails, has also been studied with MRE [6]. It represents a challenge because this organ is structured and complex according to its morphological heterogeneity and anisotropy. The primary results obtained on the viscoelastic properties of brain tissues support the use of the MRE technique to anticipate and improve clinical diagnosis in the brain. At the same time, the diversity of the results reported in the literature on the mechanical characterization of brain tissues shows the difficulty, first, to establish nominal mechanical parameters with relevant accuracy and precision for clinical prognosis [7] and, second, to significantly distinguish healthy from pathological tissues [8]. Although MRE has become a clinical routine examination to study, for example, hepatic fibrosis and cirrhosis with radical change of the liver stiffness, the results obtained with brain MRE techniques show a large variety of measurement outcomes depending on the research group [9]. The brain is a mechanically complex organ, with distinct structures presenting a priori different mechanical properties [10], [11]. In addition, it is mechanically rather well protected from external stresses by the successive layers of the cranial bone and the meninges so, despite many original attempts to transgress those natural barriers, the induced stress is often limited and can be too weak to yield meaningful results. Finally, the measurements presented in the literature are limited to mechanical values averaged either to the whole brain [12]–[15] or to different regions in the brain using anatomical segmentations to address, for instance, the white and grey matters in the cerebrum [6], [16]–[22] or the cerebellum [18], [23]–[26], or in the different cerebral lobes but voxel-wise analysis has never been considered. The mechanical properties of brain tissues were compared in healthy and pathological tissues because some cerebral pathologies such as Normal Pressure Hydrocephalus (NPH), Alzheimer disease (AD), Lewis bodies dementia (DLB) or tumors such as glioblastomas, gliomas, meningioma etc. are expected to regionally (Figure f, [27]) or globally modify the mechanical properties therein [23], [26], [28].

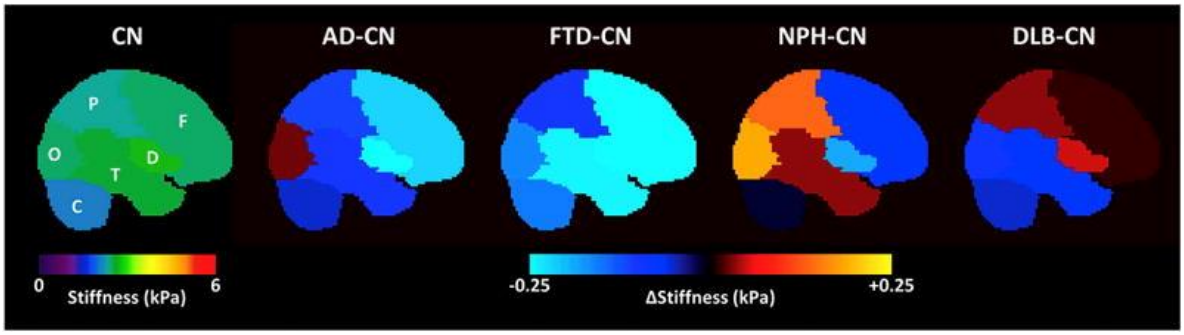

Figure f: Sagittal diagram of regional stiffness changes in patients with Alzheimer's disease (AD), frontotemporal dementia (FTD), normal pressure hydrocephalus (NPH), and dementia with Lewy bodies (DLB) compared with cognitively normal control (CN) subjects published in study of Yin et al. [27]. The left panel is a sagittal view of a lobar brain atlas color-coded with each region's mean stiffness in CN group. The right four panels show the mean stiffness difference between the dementia groups and the CN group in each region.

However, as there is not one shared standard approach, each research group has developed and implemented their own with dedicated elastography hardware, pulse sequences, inversion algorithms. It is thus difficult to compare the results of the viscoelastic moduli obtained by the different research teams.

In the first part of this introductory chapter, we will see that the establishment of a reference atlas of nominal viscoelastic moduli in the healthy brain is undermined by the wide dispersion of results existing in the literature. In the first two parts of this chapter, the shear viscoelasticity and the shear stiffness magnitude, obtained by different research groups, were compared in the whole brain and segmented regions. Then, in the third part of this chapter, the mechanical parameters were compared between research studies for different diseases to gauge the efficiency of MRE in discriminating pathological tissues from healthy ones, different types of diseases, and different stages of a disease. These different introductive parts will highlight the context and the motivations of this thesis work as well as the challenges that MRE faces to become a reliable, precise and accurate technique in the quantitative and regional determination of the mechanical parameters in healthy and diseased brain. This sets the objectives of the MRE experiments presented throughout this manuscript.

Mechanical parameters in the healthy brain

Brain MRE provides the quantitative measurement of the displacement fields induced in the brain that yield to a quantitative measurement of the complex shear modulus G^*. We will see in 0 that this complex shear modulus, G^*, comprises the shear elasticity modulus (also called storage modulus) G' and the shear viscosity modulus (also called loss modulus), G'', such that $G^* = G' + iG''$. Some studies in the literature

preferably report the magnitude of the shear stiffness $|G^*| = \sqrt{(G')^2 + (G'')^2}$ [14], [23], [24], [28], while other studies only report the elasticity modulus G' [6], [16]–[21]. The G' and G'' moduli are two parameters that may vary with the physiopathology such as tumoral or fibrous tissues [12], [23], [26], [28], [29]. They may also be highly relevant for pre-surgical planning as they could predict the fluidic or fibrotic type of a tumor and the ease of the resectability [30].

The complex shear viscoelasticity G^* is computed from phase contrast MRI. The displacement fields induced by the propagation through the targeted tissue of mechanical shear waves generated by a continuously applied mechanical vibration are mapped onto the MRI phase [2]. Motion encoding gradients are adapted to the pulse sequences used in the different studies; a few will be detailed in 0. Any study fulfilled the limits of the mechanical vibrations exerted to the human body as established by the European directive for the exposure of workers to mechanical vibrations (*Directive EU2002/44/EC)*; most of the studies carried so far have used excitation frequencies ranging from 40 Hz and 90 Hz [31].

Global analysis

The first MRE studies on human brains estimated the global values of the elastic modulus G' or the complex shear modulus G^* in the cerebrum. These values therefore do not allow to characterize the different structures in the brain; they rather provide an overall value of the elasticity in the cerebral parenchyma.

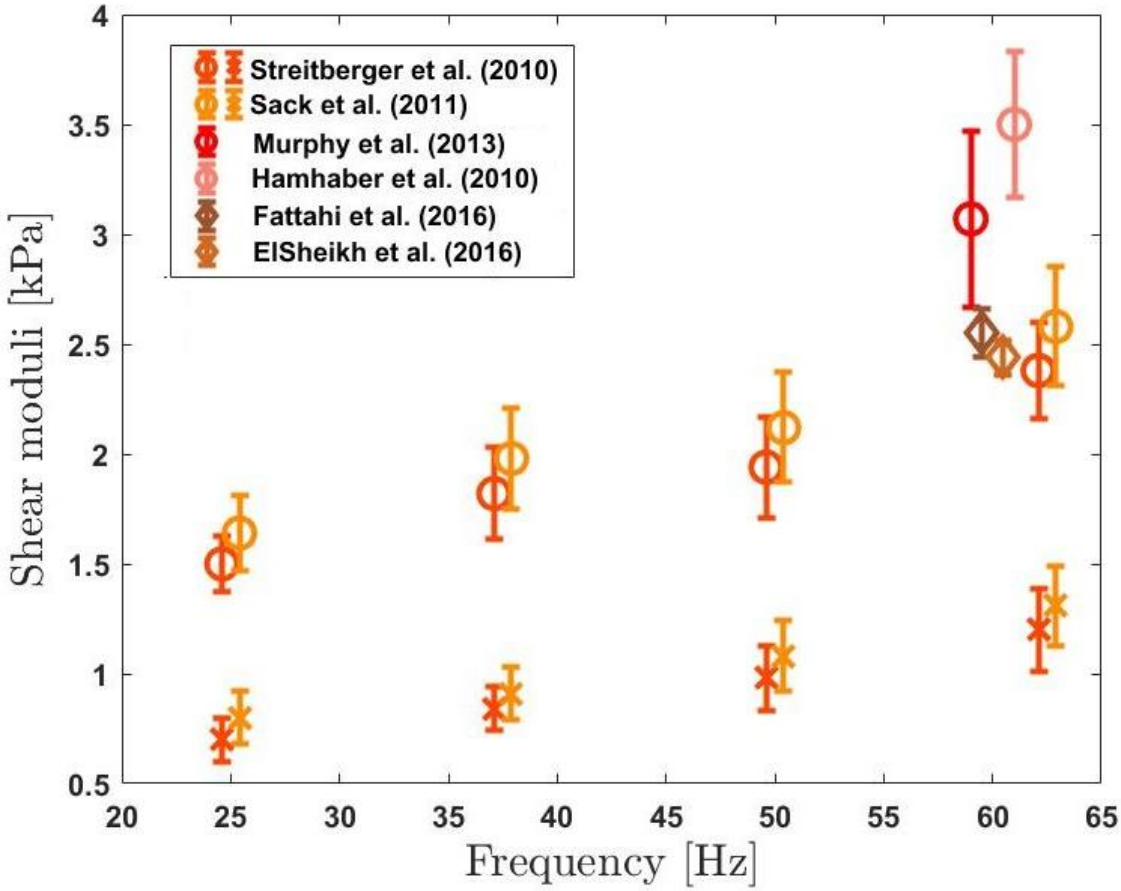

Figure g: Shear stiffness $|G^*|$ (diamond), shear elasticity G'(round) and shear viscosity G'' (cross) mean values and associated standard deviations obtained in the cerebrum by different research groups at excitation frequencies 25 Hz, 37.5 Hz, 50 Hz, 60 Hz, and 62.5 Hz (data acquired at the same excitation frequency slightly shifted for the sake of visualization). The shear viscoelasticity moduli increase with the excitation frequency for the two main datasets that were obtained with the same acquisition and reconstruction methods. The shear elasticity modulus obtained by other research groups does not match these results as they fall largely above.

Different moduli of shear stiffness G^*, shear elasticity G' and shear viscosity G'', whenever provided, were collected from the literature and are plotted in a single graph (Figure g). These studies performed brain MRE with mechanical excitations in the cerebrum in the frequency range between 25 Hz and 62.5 Hz. All these studies used an isotropic reconstruction algorithm. Streitberger et al. [32] and Sacks et al. [13] performed multi-frequency MRE between 25 Hz and 62.5 Hz with the same excitation device and similar acquisitions parameters. For both studies, we observe a linear increase of the shear elasticity G' and viscosity G'' with the excitation frequency and similar standard deviations values. Fattahi et al. [28] and ElSheikh et al. [23] who also used the same excitation device and similar acquisitions parameters obtained G^* mean values in the cerebrum in the same range. However, Murphy et al. [14] and Hamhaber et al. [15] obtained much higher values at 60 Hz than Streitberger et al. [32] and Sacks et al. [11]

and they used other excitation devices and different acquisition parameters and reconstruction algorithms than the ones implemented above. The overall mean values remain in the same range provided the excitation device as well as the acquisition and reconstruction parameters are similar.

Regional analysis

Healthy brain

Mechanical differentiation of white and grey matters

A number of groups [6], [16]–[22], [33] compared the shear elasticity G' values in the segmented white and grey matters of the cerebrum considering an isotropic reconstruction algorithm model. All these mechanical values with their respective standard deviations are reported in Figure h. for the white matter (blue) and grey matter (grey) for each research group. The spread of the shear viscoelasticity values does not only reflect the dispersive mechanical trend of brain tissues but largely the variety of the results obtained by the different research (Figure h). The reported values span an order of magnitude from (1.08 ± 0.15) kPa at 50 Hz to (10.7 ± 1.4) kPa at 80 Hz. In addition, some results presented in Figure h exhibit very large standard deviations for both G' or G^*. For example at 50 Hz, Johnson et al. [17] found $G'_{WM} = (2.43 \pm 1.04)$ kPa in the white matter and $G'_{GM} = (1.81 \pm 1.02)$ kPa in the grey matter which not only makes it difficult to determine a precise value of the elasticity modulus G' in each segmented region but also makes it impossible to discriminate grey and white matters which mechanical difference, if any, falls below the sensitivity of the technique at 50 Hz. Even if small standard deviations were reported for G' by Zhang et al. [18] (0.23 kPa in white matter and 0.22 kPa in grey matter), the estimated mean values are so close (2.41 kPa in white matter versus 2.34 kPa in grey matter) that grey and white matters cannot mechanically differentiated at the region scale and much less at the voxel scale.

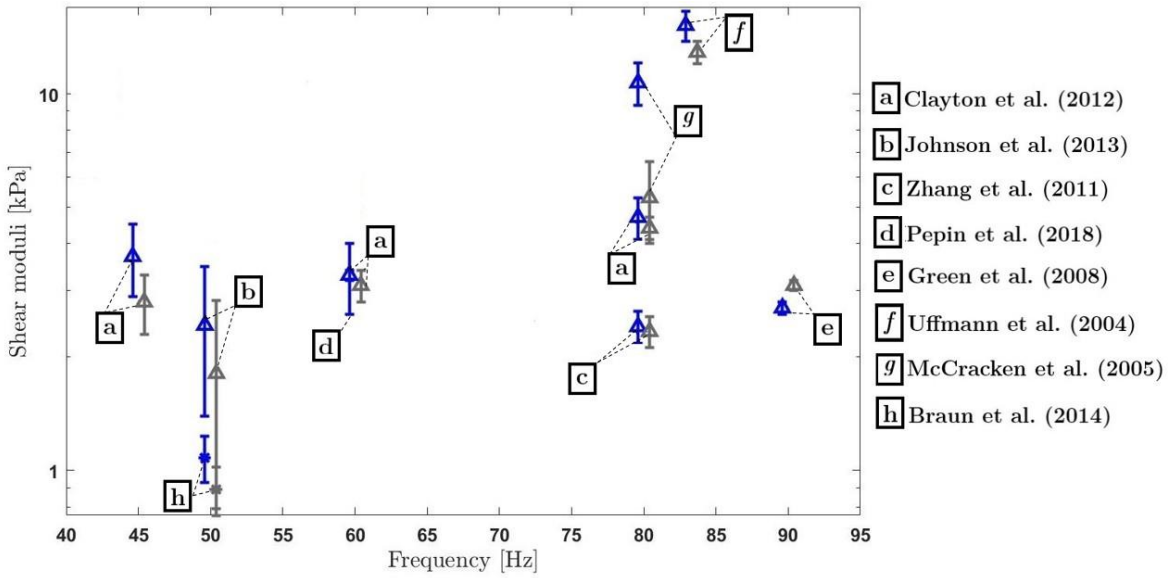

Figure h: Shear elasticity G' in the white matter (blue triangles) and the grey matter (grey triangles), shear modulus G^* in the white matter (blue stars) and the grey matter (grey stars) obtained by different research groups (from **a** to **h**) at excitation frequencies ranging from 25 Hz to 90 Hz. Even at Beside the expected dispersion with the frequency, the distribution of the reported modulus values is widespread among the research groups and regional standard deviations are large so white and grey matters cannot be significantly mechanically discriminated by MRE.

Mechanical differentiation of brain regions

Other studies compared the shear stiffness G^* in different segmented regions of healthy subjects' brain. Four of them are reported in Figure i. They were performed at 60 Hz with similar acquisition parameters to compare healthy and pathological brains with regional affections. Mean G^* values are provided in Figure i for six regions: frontal lobes (FL), occipital lobes (OL), parietal lobes (PL), temporal lobes (TL), deep cerebral grey matter (GM) and cerebral white matter (WM) as well as the cerebellum ($Cblum$) [14], [23], [24], [26], [28]. G^* was also evaluated in the sensory motor region (SM) [23], [26].

For the primary six brain regions (FL, OL, PL, TL, Deep GM/WM, and $Cblum$), the shear stiffness values vary by more than 40% from 2.15 kPa to 3.1 kPa with standard deviations between 0.1 kPa and 0.3 kPa except in the deep grey and white matters where it is around 0.6 kPa. The cerebellum region ($Cblum$) exhibits lower G^* mean values than the other regions for the four reported studies. The shear stiffness values of Murphy et al. [14] are always higher but the lack of reported standard deviation values for this study does not allow to compare the precision of these results with those obtained by the other groups.

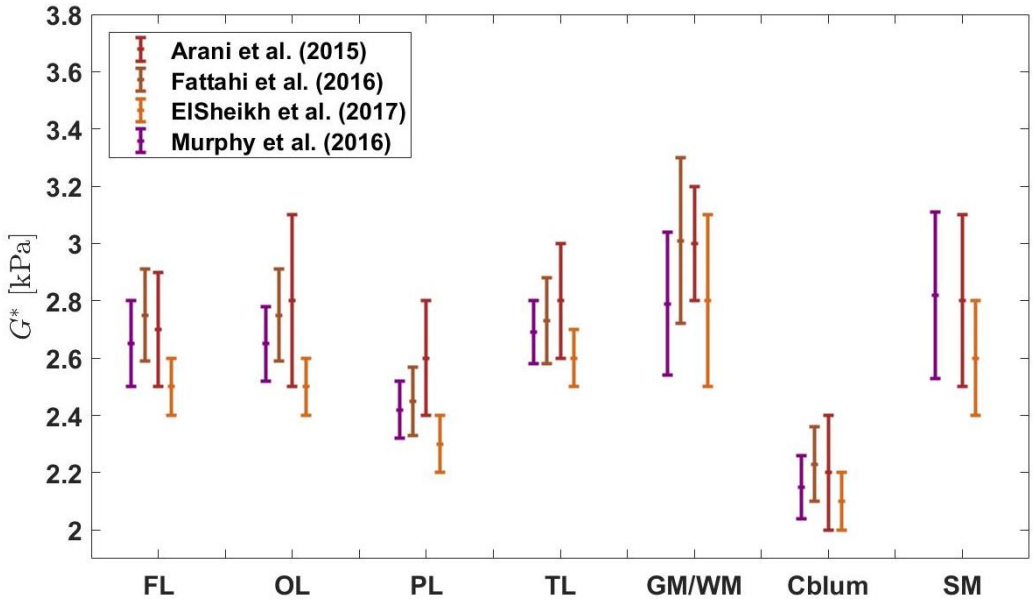

Figure i: Shear stiffness G^* in seven brain regions (FL: frontal lobes, OL: occipital lobes, PL: parietal lobes, TL: temporal lobes, GM/WM: deep grey and white matters, $Cblum$: cerebellum, SM: sensorimotor cortex) obtained by different research groups at 60 Hz [14], [23], [24], [26], [28]. Shear stiffness values largely overlap between regions except with the cerebellum where the stiffness values are significantly lower.

Pathological brain

Recent studies attempted to discriminate healthy from pathological tissue with MRE. Figure j reports the shear stiffness values obtained in tumors such as glioblastoma (GB), gliomas, meningioma ($Mening.$), pituitary adenomas ($P.A.$) and vestibular schwannoma ($V.S.$) [12], [14], [19], [26], [29], [32]–[34] as well as in different regions of the brain (frontal (FL), occipital (OL), parietal (PL), temporal (TL) lobes, deep grey and white matters (GM/WM), cerebrum, cerebellum and sensorimotor cortex) for diseases such as normal pressure hydrocephalus (NPH), Alzheimer disease (AD), frontotemporal dementia (FTD) and dementia with Lewis bodies (DLB).

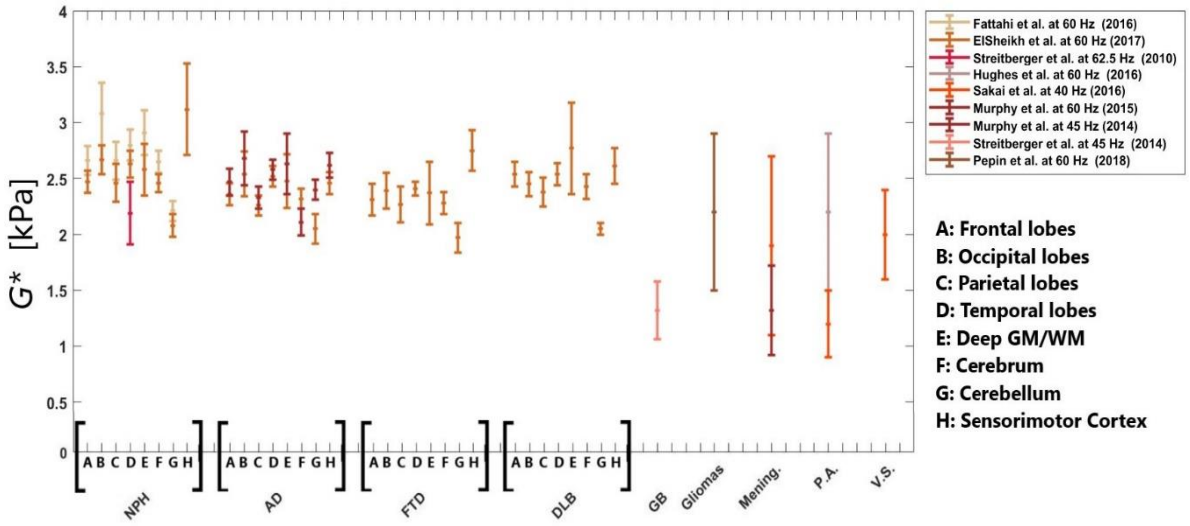

Figure j: Mean shear stiffness G^* of different studies measured in different regions of the brain for patients with various diseases (normal pressure hydrocephalus (NPH), Alzheimer disease (AD), frontotemporal dementia (FTD), dementia with Lewis bodies (DLB)) as well as with different tumor types such as glioblastomas (GB), gliomas, miningiomas ($Mening.$), pituitary adenomas ($P.A.$), vestibular schwannomas ($V.S.$). Large standard deviations make it difficult to discriminate between different types of disease although NPH, AD, FTD and DLB seem to all exhibit shear stiffness values greater than 2 kPa in contrast with tumors which exhibit lower shear stiffness values.

The shear stiffness values are spread between 1.32 kPa and 3.08 kPa for the different studied diseases. They are above 2 kPa for diseases like NPH, AD, FTD and DLB they are below 2 kPa for the different types of tumors such as glioblastomas, gliomas, meningioma, pituitary adenomas and vestibular schwannoma and soft tumors. The standard deviations associated with these diseases and these tumor stiffness values are so the different diseases cannot mechanically discriminated (Figure i).

In summary, for healthy brains, there is a broad distribution of shear stiffness and elasticity measurements in white and grey matters among the studies (Figure b). For pathological brains, it is difficult to distinguish different anatomical regions as well as to characterize different diseases based on shear modulus measurements (Figure h and Figure i).

The many results found in the literature question, first, the precision and the accuracy of brain MRE, second, the sensitivity and the specificity of MRE to characterize brain tissues and discriminate them. They point out the challenges MRE face in a complex remote organ like the brain: achieving robust measurements to mechanically differentiate one healthy brain region from another, one healthy brain region from a pathological one, and one pathology from another. They constitute the main problematic and they set the context of my thesis work, which purpose is the development of an

acquisition and reconstruction methodology to accurately and precisely estimate the mechanical parameter values which would fully characterize and discriminate with MRE healthy and pathological tissues in the brain.

Workflow

The first objective of my thesis work is to gradually determine the conditions of validity for MRE in increasingly mechanically complex media, from homogeneous phantoms (Chapter 2), heterogeneous phantoms (Chapter 3) to healthy human brains (Chapter 4). The second objective is to study under optimal conditions the sensitivity of brain MRE to mechanical changes between different anatomical regions and between different controlled pressure conditions (Chapter 5).

The first part of this manuscript provides the background and the basics of MRE applied to the brain toward accurate and precise measurements. More specifically, Chapter 1 describes the physical parameters for elastography by introducing the Hooke's law which allows to establish the wave equation governing the displacements of the tissue produced by the mechanical wave propagating throughout the medium. This chapter also introduces local inversion methods used to deduce the mechanical parameters describing the state of the targeted tissue. Then, the three elementary steps of the MRE experiments we implemented will be described, from the generation and transmission of guided pressure waves into the targeted tissue, through the registration of the displacement fields acquired by phase contrast MRI up to the computation of parametric maps with a reconstruction algorithm optimally conditioned to eventually provide precise and accurate quantification of the brain mechanical properties.

The second part of this manuscript is dedicated to the MRE experiments performed during my thesis, first, to find optimal conditions for brain MRE within which mechanical parameters can be estimated with the best precision and accuracy possible and, second, second, to investigate the sensitivity of brain MRE in optimal conditions such as to allow to significantly discriminate different tissue types. Optimal conditions were studied in heterogeneous and structured media so that MRE could be adequately applied to the brain. The three successive chapters 2 to 4 investigate different media both inside and outside the MRE optimal domain by analyzing multi-frequency and multi-scale MRE data. In this constrained framework, precision and accuracy of the estimated mechanical parameters were determined stepwise, first, in simple cases of homogeneous phantoms (Chapter 2), second in a heterogeneous breast phantom composed of inclusions stiffer than the breast parenchyma (Chapter 3) and, finally in the brain in vivo with attempts to discriminate different anatomical structures (Chapter 4).

The third and last part of this manuscript (Chapter 5) studies the sensitivity of MRE performed in optimal conditions with brain tissue under controlled gravity-driven

pressure variations. The evolution of the mechanical parameters during physical conditions analogous to microgravity are studied, allowing challenging MRE sensitivity to infer pressure and mechanical variations. The last chapter is thus the opportunity to test whether brain MRE could be advantageously used to detect mechanical alterations due to similar or inverse pressure changes in pathological processes like hemorrhage, hydrocephalus, or cancer with blood flow redistribution and cerebrospinal fluid accumulation or depletion.

The manuscript ends with a conclusion summarizing the various results obtained during this thesis through the various phantoms and in vivo MRE studies.

Chapter 1 Magnetic Resonance Elastography: toward accurate and precise measurements

1.1 Elastography as quantitative palpation

Mechanical properties of biological tissues reveal interesting characteristics which can be considered as biomarkers of the pathophysiological state of the tissue. One of the oldest concepts in medicine using this information is the principle of palpation, described by Hippocrates in ancient Greece over 2,000 years ago. The palpation technique involves massaging and pinching an organ of interest to find suspicious changes in the stiffness of the tissue. This method is still used today in order to obtain a subjective assessment of the tissue state, more particularly, to find nodules or cysts, for example in the detection of breast, prostate or thyroid cancer. However, this approach is limited to superficial organs, with global, qualitative and operator dependent results, which make it difficult to standardize this practice as a precise technique of quantification for modern medicine.

Over the past decades, objective palpation techniques have been developed using the theory of elastography associated to non-irradiating medical imaging technologies such as ultrasound or magnetic resonance imaging (MRI) to quantitatively probe the mechanical properties of human tissues. Two clinically available imaging methods have emerged which are known to be complementary: Ultrasound Shear Wave Elastography (SWE) and Magnetic Resonance Elastography (MRE).

Standard elastography relies on the recording of the tissue deformation induced by an external excitation. SWE and MRE are based on the resolution of the equation of the induced wave propagating through the tissues [35], [36] which depends on the medium where the wave propagates, more precisely, on the mechanical parameters of the tissue. By resolving the inverse problem of the wave equation, it is possible to access the mechanical parameters of the tissue such as the shear velocity, elasticity and viscosity.

In this chapter, notions of mechanics of continuous media will first be introduced (Section 1.2). Then, the three steps of the MRE protocol will be described with a review of existing approaches and in particular of reconstruction techniques used in the literature to derive the viscoelastic properties of the investigated medium (Section 1.3). In Section 1.4, the MRE protocol used during my thesis, from the excitation system to the reconstruction algorithm, will be described. Finally, in Section 1.4, the quantification

approach we chose to ensure a robust and reliable estimation of viscoelastic parameters will be presented.

1.2 Physical parameters for Elastography

Tissue stiffness is described by its elasticity. In a medical examination, the elasticity perceived by palpation or calculated by elastography is directly related to the stress applied to the tissue and to the resulting strain of the tissue through Hooke's law. This law describes the linear elastic behavior of a solid, that is to say, its response when subjected to a small amplitude distortion [37]. From appropriate common assumptions and equations defined in the reconstruction model of elastography, this part presents the method to calculate the value of the tissue elasticity submitted to mechanical excitation from Hooke's law [37], [38].

1.2.1 Hooke's law

Around 1660, Hooke discovered the proportional relationship between the force applied on a spring and its elongation in an elastic and linear domain. For an elastic medium under a small deformation such as a simple traction or compression, the original Hooke's law can be extended in scalar format by linking the applied stress σ and the resulting strain ε through the Young modulus, E:

$$\sigma = E \cdot \varepsilon \qquad 1.1$$

The stress and strain have multiple independent components and need to be locally defined by generalization of Hooke's law in tensor or matrix formats.

1.2.2 Stress tensor

The stress tensor $\boldsymbol{\sigma}$ is defined with nine components:

$$\boldsymbol{\sigma} = \begin{pmatrix} \sigma_{11} & \sigma_{21} & \sigma_{31} \\ \sigma_{12} & \sigma_{22} & \sigma_{32} \\ \sigma_{13} & \sigma_{23} & \sigma_{33} \end{pmatrix} \qquad 1.2$$

It can be decomposed into three normal (or longitudinal) stresses (σ_{ii} elements) which compose the diagonal of the stress tensor with positive values during traction and negative values during compression, and six tangential stresses (or shear) (σ_{ij} elements with $i \neq j$).

In static equilibrium, the reciprocity of tangential constraints associated with two perpendicular faces of the elementary volume induces the symmetry of the stress tensor : $\sigma_{ij} = \sigma_{ji}$ allowing to simplify the stress tensor with six independent components [37].

1.2.3 Strain tensor

The second parameter allowing to access the elasticity is the strain tensor, $\boldsymbol{\varepsilon}$. This tensor characterizes the local deformations resulting from forces applied to the elementary volume. The strain tensor can be written with nine components as:

$$\boldsymbol{\varepsilon} = \begin{pmatrix} \varepsilon_{11} & \varepsilon_{21} & \varepsilon_{31} \\ \varepsilon_{12} & \varepsilon_{22} & \varepsilon_{32} \\ \varepsilon_{13} & \varepsilon_{23} & \varepsilon_{33} \end{pmatrix} \qquad 1.3$$

As the stress tensor, the strain tensor is composed of three normal stress components ε_{ii} which compose the strain tensor diagonal, and six tangential strain components ε_{ij} with $i \neq j$. For the same reason of reciprocity of tangential constraints during static equilibrium, the strain tensor is symmetric ($\varepsilon_{ij} = \varepsilon_{ji}$) and can by simplified to six independent components.

1.2.4 Generalized Hooke's law

In an elastic solid, there is a one-to-one relationship between stresses and strains. Assuming small deformations and elastic behavior, any stress component σ_{ij} is well described by the following Taylor expansion:

$$\sigma_{ij}(\varepsilon_{kl}) = \sigma_{ij}(0) + \left(\frac{\partial \sigma_{ij}}{\partial \varepsilon_{kl}}\right)_{\varepsilon_{kl}=0} \varepsilon_{kl} + \frac{1}{2}\left(\frac{\partial^2 \sigma_{ij}}{\partial \varepsilon_{kl} \partial \varepsilon_{mn}}\right)_{\substack{\varepsilon_{kl}=0 \\ \varepsilon_{mn}=0}} \varepsilon_{kl}\varepsilon_{mn} + \cdots \qquad 1.4$$

Considering $\sigma_{ij}(0) = 0$, the first-order term of Equation 1.4 gives, for small deformations, the well-known relationship between the stress tensor σ_{ij} and the strain tensor ε_{ij} which is the Hooke's generalized law with $i, j, k, l \in \{1,2,3\}$:

$$\sigma_{ij} = C_{ijkl}\, \varepsilon_{kl} \qquad 1.5$$

where the coefficients C_{ijkl} are the stiffness tensor elements defined as:

$$C_{ijkl} = \left(\frac{\partial \sigma_{ij}}{\partial \varepsilon_{kl}}\right)_{\varepsilon_{kl}=0} \qquad 1.6$$

The coefficients C_{ijkl} given by Equation 1.6 are components of the stiffness tensor $\boldsymbol{C}$ of rank four which expresses the most general possible linear relationship between the second rank tensor σ_{ij} and ε_{kl}. As it is a tensor of rank four, the stiffness tensor $\boldsymbol{C}$ leads to $3^4 = 81$ components. However, it is possible to simplify Equation 1.6 as the tensors σ_{ij} and ε_{kl} are symetric: the components of $\boldsymbol{C}$ are unaffected when either the first two or the last two indices are interchanged: $C_{ijkl} = C_{jikl}$ and $C_{ijkl} = C_{ijlk}$.

The stiffness tensor $\boldsymbol{C}$ can thus be represented with 36 components only, leading to the following relationship between the stress and strain tensors:

$$\begin{pmatrix}\sigma_{11}\\ \sigma_{22}\\ \sigma_{33}\\ \sigma_{23}\\ \sigma_{13}\\ \sigma_{12}\end{pmatrix} = \begin{pmatrix}c_{11} & c_{12} & c_{13} & c_{14} & c_{15} & c_{16}\\ c_{12} & c_{22} & c_{23} & c_{24} & c_{25} & c_{26}\\ c_{13} & c_{23} & c_{33} & c_{34} & c_{35} & c_{36}\\ c_{14} & c_{24} & c_{34} & c_{44} & c_{45} & c_{46}\\ c_{15} & c_{25} & c_{35} & c_{45} & c_{55} & c_{56}\\ c_{16} & c_{26} & c_{36} & c_{46} & c_{56} & c_{66}\end{pmatrix}\begin{pmatrix}\varepsilon_{11}\\ \varepsilon_{22}\\ \varepsilon_{33}\\ \varepsilon_{23}\\ \varepsilon_{13}\\ \varepsilon_{12}\end{pmatrix} \qquad 1.7$$

1.2.5 Mechanical parameters in an isotropic medium

By definition, in an isotropic medium, the physical constants are independent of the choice of the coordinate axes assumed orthonormal. Especially, the stiffness tensor $\boldsymbol{C}$ must be invariant for any change of axis–rotation, or symmetry from a point or a plane. Only a scalar or the unit tensor $\boldsymbol{\delta}$ are unaffected by these orthogonal transformations. Thus, each component C_{ijkl} of the stiffness tensor $\boldsymbol{C}$ can be expressed in terms of components of the unit tensor $\boldsymbol{\delta}$. Moreover, because of the symmetry $\delta_{ij} = \delta_{ji}$, only three distinct combinations containing the four indices $ijkl$ are possible: $\delta_{ij}\delta_{kl}$, $\delta_{ik}\delta_{jl}$, $\delta_{il}\delta_{jk}$. Consequently, the stiffness tensor components C_{ijkl} can be written as:

$$C_{ijkl} = \lambda\delta_{ij}\delta_{kl} + \mu_1\delta_{ik}\delta_{jl} + \mu_2\delta_{il}\delta_{jk} \qquad 1.8$$

where λ, μ_1 and μ_2 are constants.

Moreover, as seen previously, the condition $C_{ijkl} = C_{jikl}$ induces the equality $\mu_1 = \mu_2 = \mu$ which allows to simplify the stiffness tensor:

$$C_{ijkl} = \lambda\delta_{ij}\delta_{kl} + \mu(\delta_{ik}\delta_{jl} + \delta_{il}\delta_{jk}) \qquad 1.9$$

Thus, two independent constants λ and μ named Lamé constants specify the properties of an isotropic medium. The second Lamé constant μ is also named the shear modulus. It characterizes the transverse deformation. The first Lamé constant λ characterizes the longitudinal deformation (or compression deformation).

In an isotropic medium, the Hooke's law can be simplified into:

$$\sigma_{ij} = \lambda(\varepsilon_{11} + \varepsilon_{22} + \varepsilon_{33})\delta_{ij} + 2\mu\varepsilon_{ij} \qquad 1.10$$

The Young modulus E, the bulk modulus K and the Poisson's ratio ν are related to the Lamé constants λ and μ as follow:

$E = \dfrac{\mu(3\lambda + 2\mu)}{\lambda + \mu}$	1.11
$K = \lambda + \dfrac{2}{3}\mu$	1.12
$\nu = \dfrac{\lambda}{2(\lambda + \mu)}$	1.13

Soft tissues are considered quasi-incompressible as there are mainly composed of water. Almost all classical materials have Poisson coefficients ranges of $\frac{1}{5} < \nu < \frac{1}{2}$ [39]. For isotropic weakly compressible materials such as liquids, the Poisson's ratio approaches the upper bound $\nu = \frac{1}{2}$. In that case the Young modulus equals three times the shear modulus μ (Equation 1.14) and the bulk modulus is much larger than the Young's modulus.

$$\begin{matrix} E \approx 3\mu \\ K \gg \mu \end{matrix} \qquad 1.14$$

1.3 MRE principle and protocol

MRE can be summarized by three successive steps: the first step consists of inducing the propagation of a mechanical wave in the targeted tissue by the application of an external stress. The second step consists of acquiring the displacement field induced by the wave propagating in the tissue. Finally, the last step aims at extracting the mechanical properties of the tissue by inverting the wave equation from the displacement maps obtained with MRI.

In this section, the three MRE steps are described, from the generation of mechanical waves in the targeted tissue to the computing of maps of mechanical properties.

1.3.1 Generation of a mechanical excitation

Since the emergence of MRE in the 1990s, a variety of excitation techniques have been developed by different research groups to perform measurements of mechanical properties. There are two ways to apply an external constraint in a medium that correspond to two kinds of MRE approaches, namely static MRE which was first developed and dynamic MRE which is the most common approach nowadays.

Static (or quasi-static) elastography consists of applying a stress on the tissue at one frequency (~Hz) and imaging tissue before and after being stressed [40]–[42]. Although encouraging results were obtained for quasi-static MRE approaches, this measurement requires a uniform stress over the entire volume, which is difficult to achieve especially for deep organs. Moreover, it is difficult to measure the tensor components of Hooke's law (equation 1.5) and therefore to quantify the mechanical parameters of the tissue. This technique can thus only give qualitative information because of the difficulty to know the stress applied to the tissue. As a result, the quasi-static MRE approaches have not been widely spread and accepted.

Dynamic elastography involves applying a mechanical excitation in the tissue in order to generate a shear wave synchronized with the motion encoding gradients of the

MRI sequence [35], [43], [44] [35], [45], [46]. Most groups use the dynamic approach in their MRE practice because of the limits of static MRE. Different dynamic approaches can be distinguished depending on the type of excitation devices, type of imaging sequences, and choice of reconstruction methods. This dynamic excitation mode has been chosen to characterize the mechanical parameters in our work.

1.3.1.1 Wave generators

The MRE technique uses mechanical waves with low acoustic frequencies typically ranging from 40 Hz to 150 Hz and usually generated by a vibration device placed on the targeted body region. These devices must be designed so as to manage and control the generation of the mechanical waves. During thirty years of development, investigators have described successful MRE driver devices that are based on different transducers types: electromagnetic transducers which use the MR field to induce a motion [2], [43], [47], piezoelectric transducers placed in the MRI scanner tunnel against the targeted tissue [9], [10], and passive wave generators remotely activated by a transducer nearby the magnet [48]–[53].

The induction of a mechanical excitation by external transducers is submitted to the European directive for the exposure of workers to mechanical vibrations (*Directive EU2002/44/EC)*. The group of Richard Ehman [31] compared the wave amplitudes recorded by MRE in organs, such as the brain, liver, breast, kidney and skeletal muscle, and showed that these amplitudes were lower than the maximal authorized amplitude by the directive which varies from 700 µm (20 Hz) to 100 µm (140 Hz).

1.3.1.2 Excitation of deep organs

The brain is considered as a deep organ as it has the particularity of being protected by natural barriers such as the skull bone and the meninges. The anatomical barriers hinder access of the mechanical wave from the surface of the head to the brain parenchyma. However, several research groups have developed successful wave generators, principally electromagnetic transducers and passive wave generators, to stimulate the brain tissue.

The first transducers developed for brain MRE used electromagnetic coils. Kruse et al. [54], [55] used an electromechanical driver delivering mainly anteroposterior vibrations from an electromagnetic coil placed under the head or, to avoid artifacts, connected to a bite block (Figure 1.3.1.(a)) producing vibrations of the head mainly in the right–left direction [55]–[61].

Other wave generators as passive wave generators were developed from acoustic energy delivered by a loud speaker membrane connected to the head coil through a bar producing mechanical energy with anteroposterior pendulum swings [62]–[65]. (Figure

1.3.1.(b)). In [66], the acoustic energy of two loud speakers is transmitted to two polyethylene bottles through pneumatic tubes inflated with air pressure waveforms with a 180° mutual phase difference in order to induce side-to-side, cradle-like head motion (Figure 1.3.1.(c)).

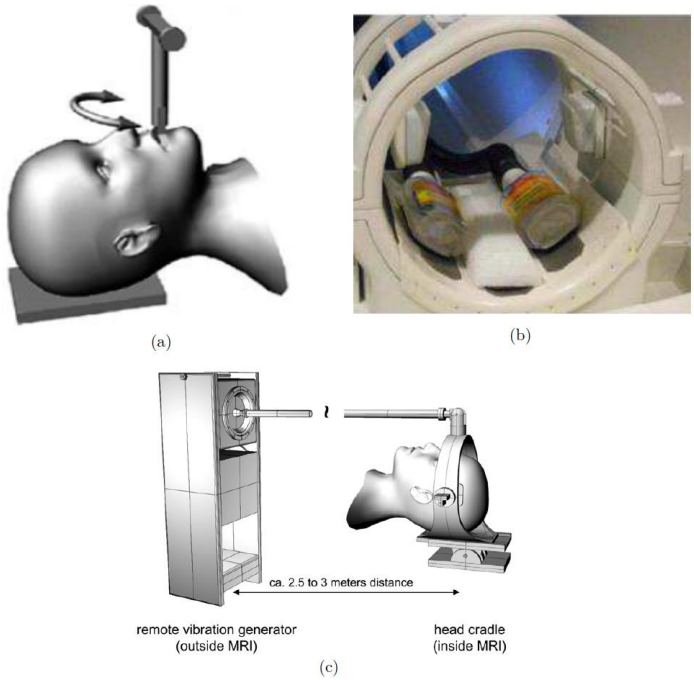

Figure 1.3.1: Actuators for brain MRE with (a) electromagnetic coils connected to a bar that the subject bites, initiating right-left movements [61], (b) passive generators using pressure waves to inflate two bottles placed under the subject's head with a phase shift of 180° [66], and (c) a bar connected to the membrane of a loudspeaker inducing movement of the head antenna placed on a cradle [62].

Apart from coils and passive generators, Gallichan et al. used gradient-induced table vibrations [67]. High intensity diffusion gradients mechanically bring the table into resonance in the low frequency range. This technique allows to eliminate the use of external actuators. It is also much more comfortable for the subject than the vibration systems used by the previously described generators which can be hard to tolerate by the patient. However, the main drawback of the proposed technique is that the excitation frequency is predetermined by the mechanical resonance of the existing scanner hardware. This removes the possibility to choose the driving frequency which is set to 23 Hz and induces a wavelength around 20 cm which is too large to reliably probe the mechanical parameters of the brain.

All these actuators provide the advantage of generating waves passing through the bone barrier. However, Green et al. and Sack et al. showed strong attenuation of the wave with recorded amplitudes from 30 µm in the peripheral part to a few microns in the center of the brain [56], [62].

To counter this limitation principally due to the wave attenuation through different anatomical barriers of the human brain, researchers have developed a technique of passive elastography which consists of using the pulses emitted by the human body as a wave generator [68], [69]. The specificity of noise fields induced by human activities allows to extract the information on mechanical properties of the medium by well-known time reversal physics approach. This method also called 'intrinsic activation' eliminates the requirement for external vibrations by measuring the motion generated by natural pulses. In human body, these pulses can be naturally created by activities like heart beating and artery pulsatility [70]–[73]. The resulting passive elastography permits to compute the viscoelastic parameters in the whole brain while avoiding the use of external transductors but with the limitation of not being able to choose the excitation frequency as for gradient-induced table vibrations and with still unclear in vivo outcomes today.

Standard magnetic resonance elastography is based on the generation of a steady-state periodic wave. During this mechanical excitation, each volume element of the excited tissue is continuously animated with a sinusoidal movement defined by an amplitude and a phase that can be measured by phase-contrast MRI. The following section describes the sequences used to acquire these displacement fields.

1.3.2 Acquiring the MR signal

1.3.2.1 Motion encoding

In standard MRI, the signal recorded by the receiving coils can be localized by frequency and phase encoding with a sequence of magnetic gradients, producing the k-space (Figure 1.3.2).

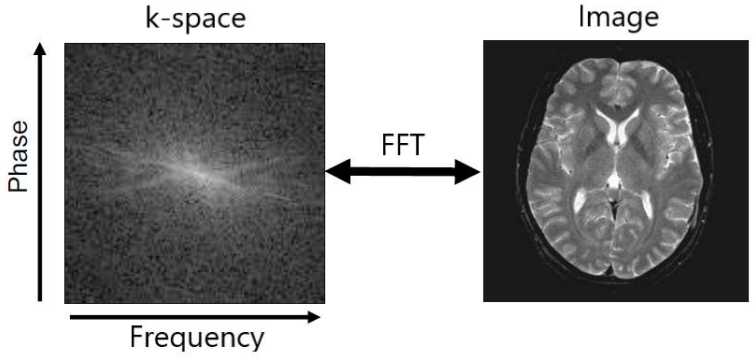

Figure 1.3.2: MR image of a brain obtained by Fourier transform of the k-space

The k-space information of all the acquired points can be translated into a complex image in the image-space through a Fourier transform:

$$S = M \cdot e^{i\varphi} \qquad 1.15$$

where S, the MR signal, is characterized by an amplitude M and a phase φ. The amplitude image M (Figure 1.3.3 left) is generally used for interpretation by the

radiologist. The phase image φ (Figure 1.3.3 right) can be used for recording and mapping the displacement fields induced in MRE.

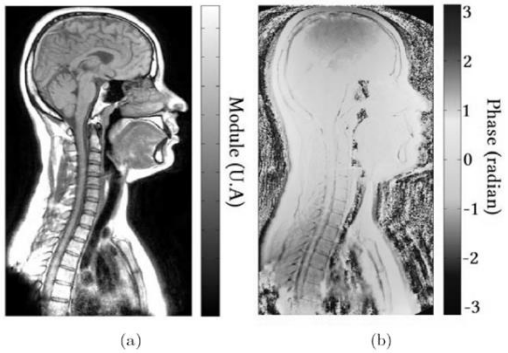

Figure 1.3.3: Amplitude image (a) and phase image (b) of the head and neck of a volunteer in the sagittal plane obtained by MRI

The recording of motion information is made possible by adding a motion encoding gradient along the selected motion direction in a phase contrast MRI sequence. By applying two intense magnetic field gradients with typically identical duration and amplitude but with opposite signs as illustrated in the second line of the sequence chronogram of Figure 1.3.4., moving spins accumulate an additional phase while static spins do not. These gradients are called bipolar gradients or motion encoding gradients (MEG).

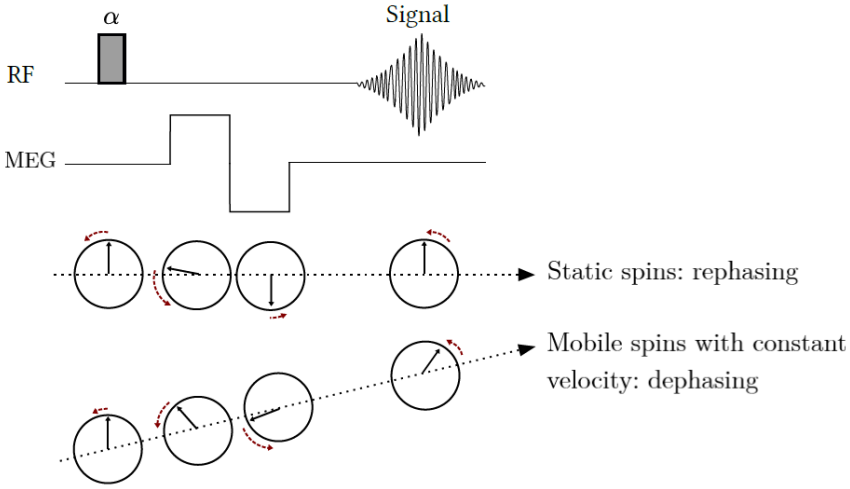

Figure 1.3.4: Zero phase accumulation for static spins and motion-related phase accumulation for mobile spins during a phase-contrast sequence with an additional bipolar gradient.

Figure 1.3.4 illustrates the principle of motion encoding by comparing the phase accumulation of static and mobile spins submitted to the MEG. Static spins are first outphased by the first gradient lobe and then rephased by the second gradient lobe, while mobile spins, moving at a constant velocity along the bipolar gradient direction during

the application of the two MEG lobes, acquire a phase proportional to their coherent motion.

1.3.2.2 Gradient echo based MRE sequence

Muthupillai et al. [2] first described in 1995 a gradient echo based MRE sequence to map and quantify the displacements corresponding to harmonic shear waves as illustrated in Figure 1.3.5.

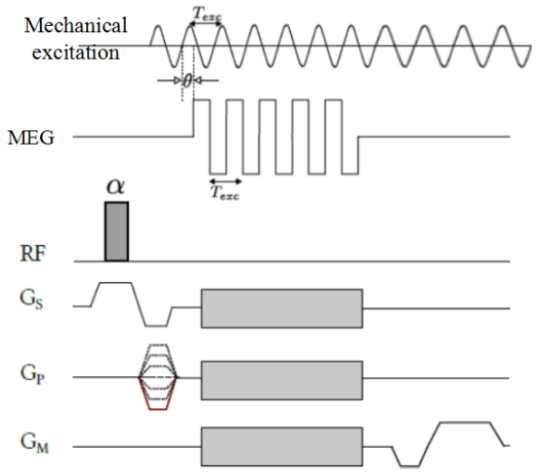

Figure 1.3.5: Elastography sequence developed by Mayo Clinic in 1995, based on a gradient echo sequence. The mechanical excitation is synchronized with the motion encoding gradients (MEG) applied along one of the three encoding axes (grey rectangle) explained in the equation 1.19 [74].

As illustrated in Figure 1.3.4, the application of a magnetic field gradient results in an additional phase shift $\boldsymbol{\varphi(r,t)}$ of the transverse magnetization that depends on the gradient amplitude and the spin position with time. This phase shift can be written as:

$$\varphi(\boldsymbol{r},t) = \gamma \int_0^t \boldsymbol{G}_{MEG}(t) \cdot \boldsymbol{r}(t) \cdot dt \qquad 1.16$$

with γ the gyromagnetic ratio of hydrogen, t the duration of gradient after excitation, $\boldsymbol{G}_{MEG}$ the time-dependent magnetic field gradient and $\boldsymbol{r}$ the position vector the considered spin population.

The shear waves propagating in the tissues to be analyzed are periodic waves. The position vector is therefore a sinusoid form:

$$\boldsymbol{r}(t) = \boldsymbol{r}_0 + \boldsymbol{A}\cos(\boldsymbol{k}\cdot\boldsymbol{r} - \omega_{exc}\cdot t + \theta) \qquad 1.17$$

with r_0 the mean position of the spins, $\boldsymbol{A}$ the amplitude of the displacement of the isochromat spins, $\boldsymbol{k}$ the wave vector, ω_{exc} the angular frequency of the mechanical excitation and θ the initial offset of the phase.

Thus, the phase shift given by equation 1.16 can be rewritten as:

$$\varphi(\boldsymbol{r},t) = \gamma \left(\boldsymbol{r_0} \int_0^{T_{MEG}} \boldsymbol{G}_{MEG}(t) \cdot dt + \boldsymbol{A} \int_0^{T_{MEG}} \boldsymbol{G}_{MEG}(t) \cdot \cos(\boldsymbol{k} \cdot \boldsymbol{r} - \omega_{exc} \cdot t + \theta) \cdot dt \right) \quad 1.18$$

with T_{MEG} the period of the bipolar gradient defined by $T_{MEG} = 2\pi/\omega_{MEG}$.

In the gradient echo-based sequence developed by Mayo Clinic, trapezoidal bipolar gradients (equation 1.19) are synchronized with the external mechanical excitation ($\omega_{MEG} = \omega_{exc}$) and can be applied along each of the spatial encoding axis to encode the three-dimensional displacement field.

$$\boldsymbol{G}_{MEG}(t) = \begin{cases} \boldsymbol{A}_{MEG} & if\ (n-1)T_{exc} < t < T_{exc} \\ -\boldsymbol{A}_{MEG}\ if\ (2n-1)\frac{T_{exc}}{2} < t < nT_{exc} \end{cases} \quad \text{with } n \in [1, N_{MEG}] \quad 1.19$$

with N_{MEG} the number of bipolar gradients.

The static first term in the phase equation 1.18 is effectively zeroed:

$$\int_0^{T_{MEG}} \boldsymbol{G}_{MEG}(t) \cdot dt = 0 \quad 1.20$$

The phase shift given by the equation 1.18 is then only dependent on the motion of the spins in the direction of the applied motion encoding gradient:

$$\varphi(\boldsymbol{r},t) = \gamma \boldsymbol{A} \int_0^{T_{MEG}} \boldsymbol{G}_{MEG}(t) \cdot \cos(\boldsymbol{k} \cdot \boldsymbol{r} - \omega_{exc} \cdot t + \theta) \cdot dt \quad 1.21$$

Successive phase offset values θ between the mechanical excitation and the motion encoding gradients are imposed in order to acquire the displacement field at different instants of the mechanical excitation period.

Finally, by integrating equation 1.21 and 1.19, the measured MR phase is:

$$\varphi(\boldsymbol{r}, N_{MEG}, T_{MEG}, \theta) = \frac{2\gamma N_{MEG} T_{exc} \boldsymbol{A}_{MEG} A}{\pi} \sin(\boldsymbol{k} \cdot \boldsymbol{r} + \theta) \quad 1.22$$

The gradient echo sequence is sensitive to the magnetic field inhomogeneities and introduces detrimental phase shifts which contaminate the phase accumulation originating from spin motion. One solution to cancel this bias is to reconstruct a final phase difference image from two phase images with opposite MEG polarities, which is at the cost of increasing acquisition time.

1.3.2.3 Gradient echo based fractional encoding MRE sequence

The gradient echo-based fractional encoding sequence has been developed to reduce the acquisition time but also to achieve a multi-frequency acquisition of the mechanical wave. This sequence developed by Ralph Sinkus' team [75] uses the principle of fractional elastography [63], [76] which consists in imposing a single bipolar gradient for encoding

trapezoidal motion with a frequency higher than that of the external excitation Figure 1.3.6.

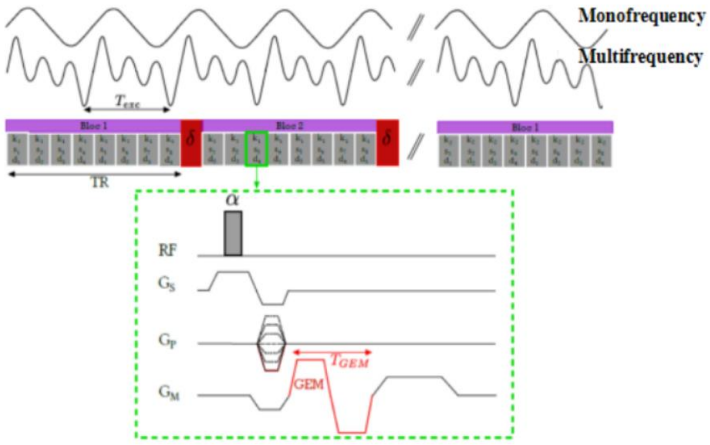

Figure 1.3.6: Fractional encoding based MRE sequence developed by Garteiser et al. [75].

This sequence is composed of imaging blocks where each block contains multiple shots with duration of an integer number of vibration cycles as illustrated in the Figure 1.3.6. The repeated element of a gradient echo based MRE sequence with fractional encoding is performed during each shot. Thus, only a fraction of one vibration cycle is encoded per repetition time, TR, so as to reduce the echo time, TE, and TR. In this case, the phase accumulation formula can be written as:

$$\varphi(\boldsymbol{r},\theta) = \gamma T_{MEG} A_{MEG} A \frac{\sin(\pi q)}{\pi(1-q^2)} \qquad 1.23$$

where $T_{MEG} < T_{exc}, q = \frac{T_{MEG}}{T_{exc}}$ and the phase accumulation reaches the maximum with $\theta = \pi(1-q)$ and $q = 0.84$.

The limit of the sequence lies in its reduced sensitivity at low amplitudes as the signal phase build-up is reduced because of the removal of the second bipolar gradient for motion encoding as well as the use of fractional encoding. However, this sequence makes it possible to reduce the acquisition time by a factor 5 compared to the spin echo sequence presented below and also to easily achieve multi-frequency acquisitions. In addition, the echo time TE is greatly reduced which allow to increase the SNR value.

1.3.2.4 Spin echo based MRE sequence

Another MRE sequence is the spin echo based MRE sequence developed by Sinkus et al. [77].

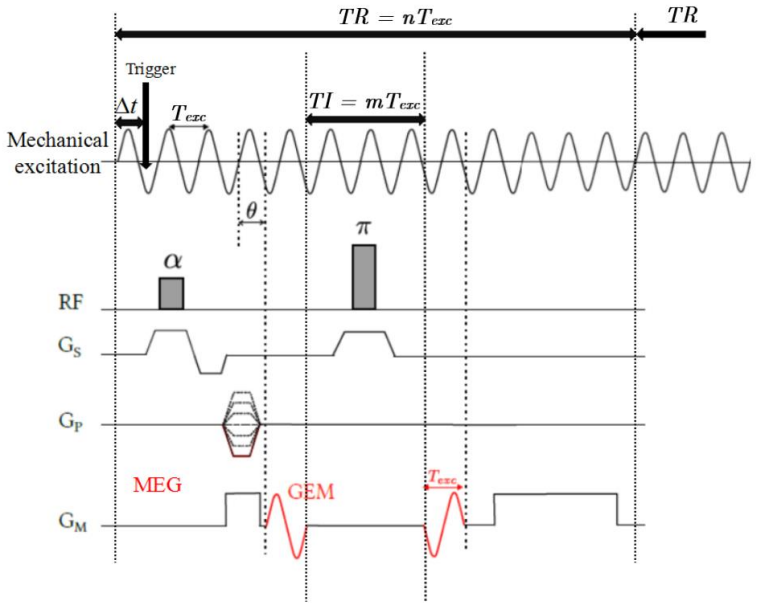

Figure 1.3.7: Chronogram of the spin echo based MRE sequence with the MRE specific time constraints.

As illustrated in Figure 1.3.7, this sequence is a standard spin echo sequence modified by the application of two sinusoidal MEG on both side of the π pulse. These two MEG have the same pattern and the same period as the mechanical wave induced in the tissue:

$$\boldsymbol{G}_{MEG}(t) = \boldsymbol{A}_{MEG}\cos(\omega_{exc}t) \qquad 1.24$$

To encode the three-dimensional displacement field, the associated phase shift is recorded along the three encoding axes usually named M (measurement axis), P (phase axis) and S (slice axis) by switching the application axis of the MEG for each acquisition.

By integration of the equation 1.21 with equation 1.24, the measured MR phase is:

$$\varphi(\boldsymbol{r}, 2T_{MEG}, \theta) = \gamma T_{exc}\boldsymbol{A}_{MEG}\boldsymbol{A}\sin(\boldsymbol{k}\cdot\boldsymbol{r} + \theta) \qquad 1.25$$

The motion sensitivity of the sequence can be increased by adding motion encoding bipolar gradients so equation 1.25 becomes:

$$\varphi(\boldsymbol{r}, 2T_{MEG}, N_{MEG}, \theta) = \gamma T_{exc}N_{MEG}\boldsymbol{A}_{MEG}\boldsymbol{A}\sin(\boldsymbol{k}\cdot\boldsymbol{r} + \theta) \qquad 1.26$$

where N_{MEG} is the number of bipolar gradients on each side of the refocusing RF-pulse in the sequence.

For each encoding axis, several measurement points during the motion period are made by dephasing the mechanical excitation by θ from the MEG which induces a time delay $\Delta t = \theta/\omega_{exc}$ between the excitation trigger generated by the imaging sequence and the imaging sequence. Thus, the displacement field is acquired at evenly distributed times of the oscillatory cycle of the excitation stored as and called the number of dynamics.

First, to ensure synchronization of the MEG with the mechanical excitation, the repetition time, TR, of the spin echo sequence must be an integer, n, of the period of the mechanical excitation, T_{exc}. Second, to ensure phase accumulation of the two sets of MEG on both sides of the refocusing RF-pulse, the time interval between them, TI, must be a half-integer number, m, (also called N_{GAP}) of the period of the mechanical excitation, T_{exc} (Figure 1.3.7).

From the recorded phase maps along each motion encoding direction $i \in \{1,2,3\}$, it is possible to calculate the components u_i, $i \in \{1,2,3\}$, of the displacement field induced in the tissue where the mechanical wave propagates:

$$u_i(\boldsymbol{r},\theta) = \frac{\varphi(\boldsymbol{r}, 2T_{MEG}, \theta)}{\gamma T_{exc} A_{MEGi}} \qquad 1.27$$

where $\boldsymbol{u}(\boldsymbol{r},\theta) = \boldsymbol{A}\sin(\boldsymbol{k}\cdot\boldsymbol{r}+\theta)$ and $i \in \{1,2,3\}$

Thanks to the refocusing RF-pulse, the spin echo based MRE sequence is lowly affected by the field inhomogeneity. However, this is at the expense of prolonged echo time TE and total acquisition time TA. One the one hand, the long TE can be a disadvantage for tissues showing transverse relaxation lower than the echo time ($T_2 < TE$) and, on the other hand, TA may be challenging for in vivo applications. One means of addressing these issues is to increase the excitation frequency f_{exc} and reduce the number of bipolar gradients N_{MEG} and the field-of-view (FOV).

1.3.2.5 From phase shift to displacement field

The displacement field components $u_i(\boldsymbol{r},t)$ are computed from the recorded phase values $\varphi_i(\boldsymbol{r},t)$ (Equation 1.27). The uncertainty of the displacement field Δu_i comes from the measurement uncertainty of the MRI signal phase which is related to the signal-to-noise ratio (SNR) of the acquired MR images.

As shown in Equation 1.15, the MR signal S is obtained in a complex form with a real part M_R and an imaginary part M_I or with a magnitude M (Equation 1.28) and a signal phase φ (Equation 1.29):

$$M = \sqrt{{M_R}^2 + i{M_I}^2} \qquad 1.28$$

$$\varphi = \operatorname{atan}\left(\frac{M_R}{M_{Im}}\right) \qquad 1.29$$

When extracted from the magnitude M, the MR noise σ_0 is biased and follows a Rician distribution, which is related to the Gaussian distribution of the noise σ, when extracted either from the real part M_R and the imaginary part M_I, by::

$$\sigma_0 = \sigma\sqrt{2 - \frac{\pi}{2}} \qquad 1.30$$

Thus, the SNR can be expressed as:

$$SNR = \frac{M}{\sigma} = \frac{M \cdot \sqrt{2 - \frac{\pi}{2}}}{\sigma_0} \quad 1.31$$

where σ_0 is the standard deviation measured in a region void of signal of the magnitude image.

The uncertainty of the phase measurement, noted $\Delta\varphi$, can be expressed as a function of the SNR:

$$\Delta\varphi = \operatorname{atan}\left(\frac{1}{SNR}\right) \quad 1.32$$

which, for large enough SNR, get simplified to [78]:

$$\Delta\varphi \simeq \frac{1}{SNR} \quad 1.33$$

Thus, the measured SNR value from the MR image allows to calculate the uncertainty of the phase measurement $\Delta\varphi$ according to Equation 1.33 as well as the error of the displacement measure Δu using Equations 1.63 and 1.64 which allow to deduce Δu for a spin echo sequence (equation 1.34) and for a gradient echo sequence (equation 1.35) respectively.

$$\Delta u = \frac{1}{\gamma T_{exc} A_{MEG}} \cdot \frac{1}{SNR} \quad 1.34$$

$$\Delta u = \frac{\pi(1 - q^2)}{\gamma T_{exc} A_{MEG} \sin(\pi q)} \cdot \frac{1}{SNR} \quad 1.35$$

The measurement uncertainty Δu_i along each i motion-encoding direction can be propagated to calculate the uncertainty Δq_i on the amplitude q_i of the curl of the displacement field. The ratio of these last two quantities (Δq_i and q_i) define the quality of the computed curl of the displacement field: It is higher when the amplitude q_i is bigger and when the uncertainty Δq_i is smaller; It is lower when q_i is smaller and Δq_i, bigger. It sets the data quality for $\boldsymbol{q}$-field based reconstruction as we will see below.

1.3.3 Reconstruction algorithms

In order to derive the mechanical parameters from the acquired displacement fields, the wave equation governing the displacements of the tissue induced by the mechanical wave must be written. The mechanical parameters can then be extracted by inversion of the wave equation.

1.3.3.1 Mechanical wave equation

In the case of a purely elastic medium, the mechanical wave equation can be written as:

$$\rho \partial_t^2 u_i(\boldsymbol{r}, t) = C_{ijkl} \frac{\partial^2 u_l}{\partial x_j \partial x_k} \qquad 1.36$$

Assuming an isotropic and locally homogeneous medium, the wave equation governing the displacement field $\boldsymbol{u}(\boldsymbol{r}, t)$ can be written as:

$$\rho \partial_t^2 \boldsymbol{u}(\boldsymbol{r}, t) = \mu \nabla^2 \boldsymbol{u}(\boldsymbol{r}, t) + (\lambda + \mu) \boldsymbol{\nabla}(\boldsymbol{\nabla u}(\boldsymbol{r}, t)) \qquad 1.37$$

This equation relies on spatial and time derivatives. The mechanical wave propagation consists of three components: the compression wave, the shear wave and the coupling term between the two previous components (Figure 1.3.8). Deformations due to shear components are characterized by the second Lamé constant μ while deformations due to compression components are characterized by the first Lamé constant λ. The displacement field $\boldsymbol{u}$ is mainly composed of the compression wave and shear wave components as the coupling is negligible due to its amplitude which decreases more rapidly than the two others components.

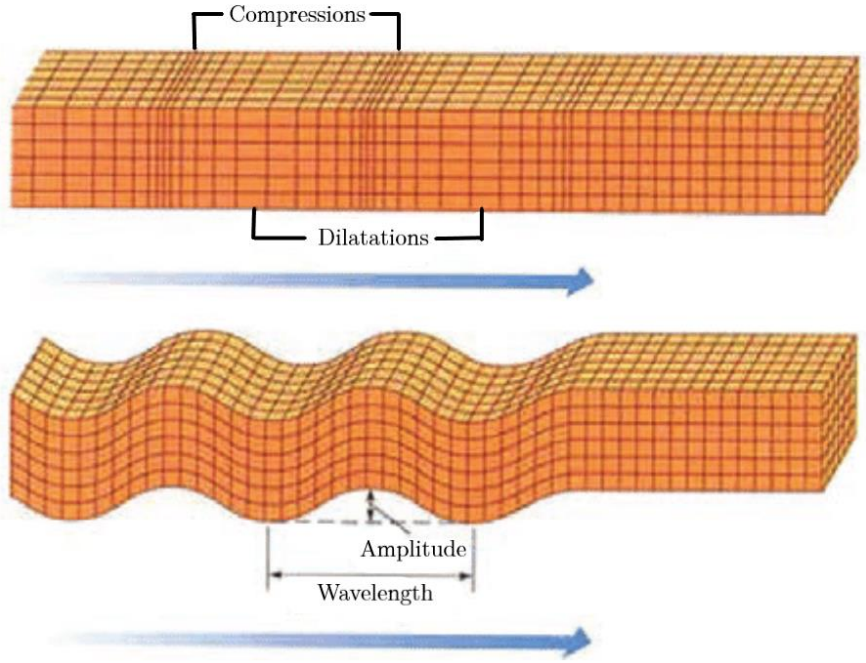

Figure 1.3.8: Illustration of the propagation characteristics of the compression wave component (top) and the shear wave component (below). For the compression wave, the medium deformation (u_L) is parallel to the wave propagation. For the shear wave, the medium deformation (u_T) is perpendicular to the wave propagation

Thus, $\boldsymbol{u}$ can be decomposed into a transversal ($\boldsymbol{u_T}$) and a longitudinal displacement ($\boldsymbol{u_L}$):

$$\boldsymbol{u} = \boldsymbol{u_T} + \boldsymbol{u_L} \quad 1.38$$

where:

$$\nabla \cdot \boldsymbol{u_T} = \boldsymbol{0} \quad 1.39$$

$$\nabla \times \boldsymbol{u_L} = \boldsymbol{0} \quad 1.40$$

Equation 1.38 can be decomposed into two equations, the first one for the compression wave (Equation 1.41) and the second one for the shear wave (Equation 1.42) :

$$\frac{\partial \boldsymbol{u_L}}{\partial t^2} = \frac{\lambda + 2\mu}{\rho} \nabla^2 \boldsymbol{u_L} \quad 1.41$$

$$\frac{\partial \boldsymbol{u_T}}{\partial t^2} = \frac{\mu}{\rho} \nabla^2 \boldsymbol{u_T} \quad 1.42$$

The two equations allow to deduce the compression wave velocity V_L and the shear wave velocity V_T:

$$V_L = \sqrt{\frac{\lambda + \mu}{\rho}} \quad 1.43$$

$$V_T = \sqrt{\frac{\mu}{\rho}} \quad 1.44$$

For soft tissues considered as non-Newtonian fluids, the elastography technique exploits the displacement field resulting from the shear wave component and not the compression wave. This is because the compression wave velocity V_L travels much faster; it is about 1500 $m \cdot s^{-1}$ while the shear wave velocity usually ranges from 1 to 10 $m \cdot s^{-1}$ depending on the tissue.

The hypothesis of elastic tissue which has been assumed so far is not sufficient as human tissue are generally characterized by their elasticity but also their viscosity. Shear and stress moduli are composed of a real part, the elasticity, which reflects the rigidity of the material and therefore the ability to conserve and restore energy, and, an imaginary part, the viscosity, which reflects the resistance of the material and therefore the ability to dissipate energy. Measuring the viscosity modulus of an organ allows to observe certain pathologies or their evolution, for which the elasticity practically does not undergo any modification.

Rheological models help modeling the mechanical behaviors of materials and allow to combine the stiffness tensor and the viscosity tensor

The Voigt model, which is represented as a damper and a spring placed in parallel, is usually chosen to rewrite the Hooke's law (Equation 1.5) by adding an extra viscosity tensor η_{ijkl} for a viscoelastic medium:

$$\sigma_{ij} = C_{ijkl}\varepsilon_{kl}(t) + \eta_{ijkl}\frac{\partial \varepsilon_{kl}}{\partial t} \qquad 1.45$$

Using this model, the wave equation in an isotropic, homogeneous, and viscoelastic medium is written as:

$$\begin{aligned}\rho\partial_t^2\boldsymbol{u}(\boldsymbol{r},t) = \; & \mu\nabla^2\boldsymbol{u}(\boldsymbol{r},t) + (\lambda+\mu)\boldsymbol{\nabla}\big(\boldsymbol{\nabla u}(\boldsymbol{r},t)\big) \\ & + \; \zeta\partial_t\nabla^2\boldsymbol{u}(\boldsymbol{r},t) + (\xi+\zeta)\partial_t\boldsymbol{\nabla}\big(\boldsymbol{\nabla u}(\boldsymbol{r},t)\big)\end{aligned} \qquad 1.46$$

where ζ is the shear viscosity accounting for attenuation within the medium and ξ, the viscosity of the compressional wave. From Equation 1.46, the shear viscoelastic moduli can be deduced by Helmholtz decomposition. Because they both use temporal and spatial derivatives of the displacement fields $\boldsymbol{u}(\boldsymbol{r},t)$, the equations for an elastic medium (Equation 1.37) and for a viscoelastic medium (Equation 1.46) can be simplified by applying the Fourier transform on $\boldsymbol{u}(\boldsymbol{r},t)$. This Fourier transform leads to a time independent wave equation in the frequency space for an elastic medium (Equation 1.47) and for a viscoelastic medium (Equation 1.48):

$$\rho\omega^2\boldsymbol{u}(\boldsymbol{r},\boldsymbol{\omega}) = \; \mu\nabla^2\boldsymbol{u}(\boldsymbol{r},\boldsymbol{\omega}) + (\lambda+\mu)\boldsymbol{\nabla}\big(\boldsymbol{\nabla u}(\boldsymbol{r},\boldsymbol{\omega})\big) \qquad 1.47$$

$$\begin{aligned}\rho\omega^2\boldsymbol{u}(\boldsymbol{r},\boldsymbol{\omega}) = \; & \mu\nabla^2\boldsymbol{u}(\boldsymbol{r},\boldsymbol{\omega}) + (\lambda+\mu)\boldsymbol{\nabla}\big(\boldsymbol{\nabla u}(\boldsymbol{r},\boldsymbol{\omega})\big) \\ & + \; j\omega_{exc}\zeta\nabla^2\boldsymbol{u}(\boldsymbol{r},\boldsymbol{\omega}) \\ & + j\omega_{exc}(\xi+\zeta)\boldsymbol{\nabla}\big(\boldsymbol{\nabla u}(\boldsymbol{r},\boldsymbol{\omega})\big)\end{aligned} \qquad 1.48$$

The two equations above govern the basic reconstruction of dynamic elastography which presents the advantage that the stress and strain tensors are independent contrarily to static elastography. Thus, quantitative mechanical properties can be deduced from displacement fields assessed through MRI.

To extract the viscoelastic moduli, it is necessary to inverse the wave equation established in a viscoelastic medium. As explained in section 1.2.5, the shear wave and the compression wave are the two principal components of the mechanical wave propagation. The velocity of the shear wave is much lower (1 to 10 $m \cdot s^{-1}$) than the velocity of the compression wave (~1500 $m \cdot s^{-1}$) with wavelengths in the range of meters that varies little with the mechanical alterations of the tissue. On the contrary, the shear wave presents shear wavelengths in the range of centimeters allowing measurable variations in tissues and providing thus good contrast between different tissue types and

different pathophysiological tissue conditions. Therefore, only viscoelastic moduli relating to the shear wave are accessible and relevant with MRI.

1.3.3.2 Algorithms to solve the wave equation

The mechanical parameters are estimated by solving the wave equation. MRE reconstruction can be globally divided into two approaches. The first kind of approaches are iterative methods also called Nonlinear Inversion (NLI) methods. It consists of minimizing the difference between the measured wave field and simulated wave fields found from solving the forward problem. A solution to the inverse problem is found when reaching a minimum or satisfying some convergence criteria. This approach is dependent on model assumptions (boundary conditions and initial value) as they only consider displacement fields that satisfy the governing equation. In the literature, several iterative methods have been developed such as: gradient-descent methods [79], 3D-Subzone [80], Gauss-Newton methods combining Subzone technique [81], traveling-wave expansion [3].

The second approach is the direct inversion method which consists of resolving a linear minimization problem and performing a pixel-wise inversion of the homogeneous time-harmonic linear viscoelasticity equations. Contrary to the first approach, the direct inversion method leaves the linearly dependent viscoelastic variables as unknowns available to minimize the system. Direct methods require much less computational effort than iterative methods but they are more dependent on data quality.

In the literature, several algorithms based on direct inversion methods have been developed: heterogeneous direct methods [82]–[85], Local Frequency Estimation (LFE) [46], [86]–[88] Algebraic Inversion of the Differential Equation (AIDE) [3], [35], [89]–[92], as well as other direct inversion methods using a derived approach of the direct inversion [93]–[98]

As they are the most frequently used in the literature, the LFE and AIDE algorithms are briefly described in the next part.

1.3.4 Local inversion techniques

During the acquisition for elastography, the propagating wave induced in the targeted tissue can be locally considered as a monochromatic wave plane:

$$\boldsymbol{u_i}(\boldsymbol{r},t) = \boldsymbol{A_0}.\, e^{j(\omega_{exc}t - \boldsymbol{k_i r_i})} \qquad 1.49$$

with ω_{exc} the angular frequency of the mechanical wave and k_i the wave vector component along the direction i, $i \in \{1,2,3\}$.

Equation 1.47 turns into a purely local inversion problem. However, due to the quasi-incompressibility of soft tissue, there is an unbalanced magnitude between μ which lies in the range of kPa and λ which lies in the range of GPa. The hypothesis of $\nabla \boldsymbol{u} \approx 0$

is thus considered which involves neglecting the second and fourth terms on the right-hand side of Equation 1.48.

$$\rho\partial_t^2\boldsymbol{u}(\boldsymbol{r},t) = \mu\nabla^2\boldsymbol{u}(\boldsymbol{r},t) + \zeta\partial_t\nabla^2\boldsymbol{u}(\boldsymbol{r},t) \quad 1.50$$

which can be also written in the frequency space as:

$$\rho\omega^2\boldsymbol{u}(\boldsymbol{r},\boldsymbol{\omega}) = \mu\nabla^2\boldsymbol{u}(\boldsymbol{r},\boldsymbol{\omega}) + j\omega_{exc}\zeta\nabla^2\boldsymbol{u}(\boldsymbol{r},\boldsymbol{\omega}) \quad 1.51$$

This assumption is examined in the next part of this chapter as it raises questions about its rightfulness.

1.3.4.1 Local frequency Estimation (LFE) algorithm

The local frequency estimation (LFE) method [86] consists of only taking the local wavelength into account without considering the wave attenuation. Thus, the shear modulus is deduced from the measured wavelength λ in the Equation 1.44 of the shear wave velocity with the hypothesis of a homogeneous tissue density close to the water density ($\rho\sim1$ kg$\cdot$s^{-1}):

$$\mu_{LFE} = \left(\frac{\omega_{exc}}{2\pi}\right)^2 \cdot \lambda^2 \quad 1.52$$

The LFE algorithm has proven to be a robust and fast approach because of the sophisticated multi-scale data averaging in the estimation. It yields accurate and isotropic local frequency estimates, which is relatively insensitive to noise [99]. However, this algorithm presents some resolution limitations, and at sharp boundaries the LFE estimate is blurred and the correct estimate is reached only half a wavelength into a given region. It is essentially a 2D approach which favors the acquisition and reconstruction times so it remains inherently biased by the choice of the slice orientation with respect to the direction of the wave propagation [84], [91]. Moreover, this algorithm approach cannot be extended to viscoelastic media.

1.3.4.2 Algebraic Inversion of the Differential Equation (AIDE)

The AIDE algorithm assumes local homogeneity and allows to measure the mechanical parameters via direct inversion of the wave equation 1.48. Contrary to the LFE algorithm, the AIDE algorithm can take the attenuation into account and thus the viscosity of the medium.

As explained previously, the simplifying assumption $\nabla\boldsymbol{u} \approx 0$ have allowed to obtain Equation 1.50. by removing the second and the fourth terms of Equation 1.48. Neglecting the fourth term is legitimate because the compressional viscosity (ξ) can be ignored at MRE low frequencies. However, this hypothesis does not hold for the second term. According to Equation 1.48, the high value of the compression wave velocity is related to the very large Lamé constant λ which outweighs very small $\nabla(\nabla\boldsymbol{u})$.

One possibility to simplify Equation 1.48 was proposed by Sinkus et al. [35]. It consists of decomposing the plane wave $\boldsymbol{u}$ (Equation 1.50) into the transverse wave $\boldsymbol{u_T}$ and the longitudinal wave $\boldsymbol{u_L}$ according to the Helmholtz-Hodge theorem. As the curl of the longitudinal wave ($\nabla \times \boldsymbol{u_L}$) and also the divergence of the transverse wave ($\nabla \boldsymbol{u_T}$) are equal to zero, the term $\nabla(\nabla \boldsymbol{u})$ can be simplified as:

$$\nabla(\nabla \boldsymbol{u}) = \nabla(\nabla(\boldsymbol{u_T} + \boldsymbol{u_L})) \quad 1.53$$

$$\nabla(\nabla \boldsymbol{u}) = \boldsymbol{\nabla^2 u_L} + \nabla \times (\nabla \times \boldsymbol{u_L}) \quad 1.54$$

$$\nabla(\nabla \boldsymbol{u}) = \boldsymbol{\nabla^2 u_L} \quad 1.55$$

The application of the curl operator on the displacement field $\boldsymbol{u}$:

$$\boldsymbol{q} = \nabla \times \boldsymbol{u} \quad 1.56$$

can be used to remove any compressional contribution [35] and Equation 1.48 is simplified by only keeping the shear components μ_i and ζ_i along i:

$$-\rho \partial_t^2 \boldsymbol{q_i}(\boldsymbol{r}, \omega) = \mu_i \nabla^2 \boldsymbol{q}(\boldsymbol{r}, \omega) + \zeta_i \, \partial_t \nabla^2 \boldsymbol{q}(\boldsymbol{r}, \omega) \quad 1.57$$

with ∂_t the time derivative and $i \in \{1,2,3\}$.

Computing the curl adds noise along the data processing. To fully address the 3D nature of the displacement field in the tissues and to properly apply the curl operator, the displacement field components along the three spatial directions are usually acquired so higher acquisition times are required. However, this approach does not need any particular assumption but linear elasticity, local homogeneity, local plane wave, and isotropy once the solutions of the equations 1.57 along $i \in \{1,2,3\}$ are averaged.

According to Equation 1.49, the curl component of the displacement field along i can also be written as a plane wave:

$$\boldsymbol{q_i} = |\boldsymbol{q_i}| \cdot e^{j(\omega_{exc} t + \boldsymbol{k_i} \boldsymbol{r_i})} \quad 1.58$$

with ω_{exc} the angular frequency of the mechanical wave, $\boldsymbol{k_i}$ the wave vector, and $i \in \{1,2,3\}$..

Thus, Equation 1.57 can also be written as the Helmholtz equation over $\boldsymbol{q}$:

$$-\rho \omega_{exc}^2 \boldsymbol{q_i}(\boldsymbol{r}, \omega_{exc}) = \mu_i \nabla^2 \boldsymbol{q_i}(\boldsymbol{r}, \omega_{exc}) + j\omega_{exc} \zeta_i \nabla^2 \boldsymbol{q_i}(\boldsymbol{r}, \omega_{exc}) \quad 1.59$$

The above Helmholtz equation provides the complex shear modulus with real part, G', being the dynamic shear modulus and, imaginary part, G'', being the loss shear modulus:

$$G^* = \mu + j\omega_{exc}\zeta \quad 1.60$$

$$G^* = G' + jG'' \quad 1.61$$

1.4 MRE approach for precise and accurate quantification

In my thesis work, MRE studies were carried over with guided pressure waves in phantoms and in human brains along basic but specific methodologies that favor the validity of both acquisition and reconstruction data at the expense of time in order to derive as precise and accurate mechanical parameters as possible within the simplifying assumptions of linear elasticity, local homogeneity, local plane wave, and isotropy of the probed media.

1.4.1 Acquisition protocol

1.4.1.1 Pressure wave generation

As seen above, any mechanical excitation is *fortunately* limited in the brain mainly by the protective barriers of the cranial bone and meninges. Wave amplitudes achieved in the brain may easily be low to reliably infer the viscoelastic moduli from the recorded displacement fields.

To perform brain MRE in this thesis work, we used pressure waves generated by a loudspeaker and directly guided into the oral cavity of the subject *via* waveguides (Figure 1.4.1). This method allows to bypass the protective barriers by guiding the pressure wave directly into the head through the natural mouth input and along inner natural pathways to further access the brain all the way to the extreme top lobes of the cerebrum. This method only requires from the subject to spontaneously breath through the nose so the uvula is kept closed and the pressure wave is not directed along the airways down to the lung but kept up in the buccal and cranial cavities.

Maitre et al. [100] and Hagot et al. [101] demonstrated the efficiency of this technique that allowed to reach wave amplitudes up to 70 µm with mean values over the whole brain of 14 µm.

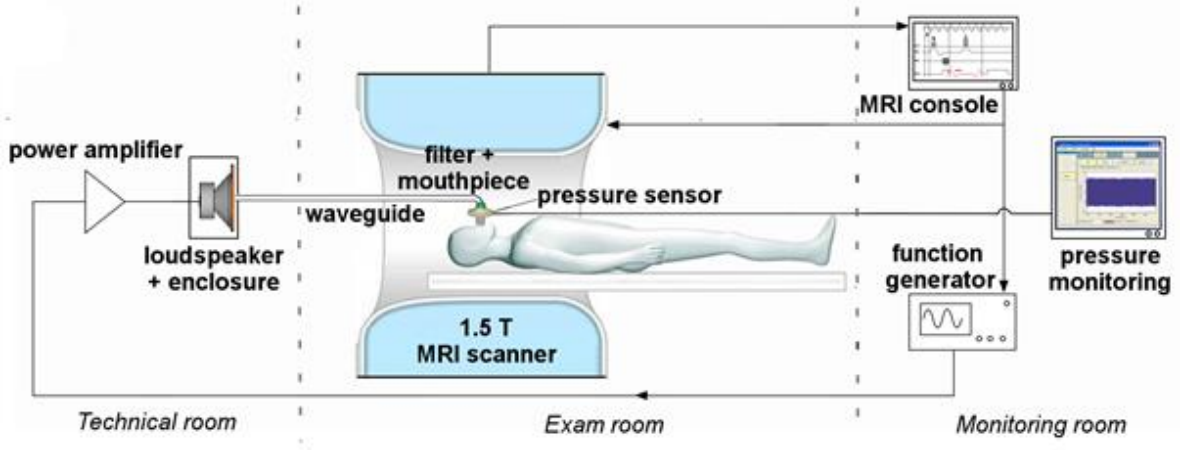

Figure 1.4.1: Experimental setup for brain MRE with guided pressure waves. The subject lies in a 1.5 T Achieva MR system with the head placed in a standard head SENSE coil. Remotely generated and amplified pressure waves are guided to the center of the MRI magnet into the subject's buccal cavity. Pressure wave level is monitored at the mouth via an optical fiber sensor. Pressure wave are synchronized to the MRI acquisition sequence.

Pressure waves are remotely generated from the technical room behind the MRI exam room (Figure 1.4.1) with a function generator (AFG 3021B, Tektronix, OR, USA; Figure 1.4.2.(a)) before being amplified with a power amplifier (P5000S, Yamaha, Japan, Figure 1.4.2.(b)), transduced with a 300 W 12" woofer (PHL Audio 4530, France, Figure 1.4.2.(c)), and guided through the Faraday cage along Altuglas® tubes and adapting hoses to the mouthpiece (Figure 1.4.1). The generation of pressure waves is trigged by the MRI system for synchronization with the MRE acquisition and monitored from the MRI console (Figure 1.4.1) with an oscilloscope (TDS 2014, Tektronix, USA, Figure 1.4.3.(a)). The generated pressure is recorded on site with an optical fiber sensor at 5 kHz (EVO-RM-8, FISO, Canada, Figure 1.4.3.(c)) connected to the mouthpiece in case of brain acquisition or to an acoustic adapter in case of phantom acquisition. It is monitored from the MRI console room *via* the pressure measurement modules (Figure 1.4.3.(b) and Figure 1.4.3.(d)). The main advantages of this type of wave generation reside in the gas transmission of the excitation, in the flexibility of the orientation and of the size of the excitation source with appropriate acoustic end adapters.

Figure 1.4.2: (a) Function generator (AFG 3021B, Tektronix, USA), (b) power amplifier (P2500S, Yamaha, Japan), (c) 300 W 12" woofer (PHL Audio 4530, France), (d) rolling wooden cabinet comprising the power amplifier, the woofer and a cooling pump on top to prevent loudspeaker overheating.

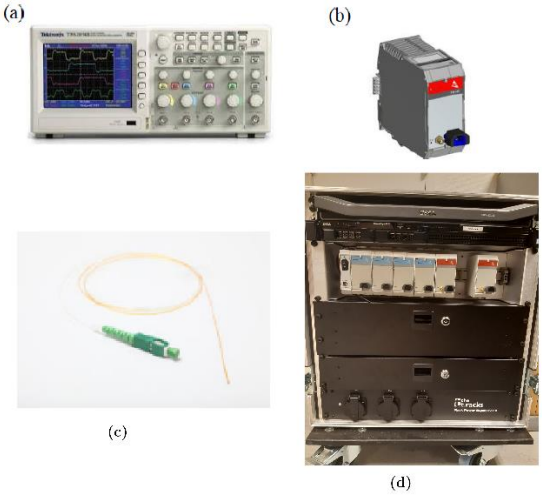

Figure 1.4.3: Wave generation monitoring system:(a) oscilloscope, (b) optical measurement module, (c) optical fiber pressure sensor and (d) rolling rack with optical modules and monitoring computer.

1.4.1.2 Automated acoustic pressure monitoring

When I started my PhD in the laboratory, the pressure wave monitoring system was limited to one MRI site (SHFJ, Philips 1.5 T MRI). I optimized and automated the pressure wave calibration and monitoring so we could control the pressure wave amplitude at the subject's mouth or at the surface of the probed phantom from the console room during MRE acquisitions. The system was mounted onto a rolling flight case so it could be easily transported and used on different MRI platforms for multisite experiments.

The system was calibrated and the resonant guiding modes of the close system from the loudspeaker to the probed subject or phantom were characterized by wobulation. An acquisition and generation code was developed with Matlab® to control, via a laptop computer, the function generator in order to sweep the input excitation frequency and to record the output pressure level measured by the optical fiber sensor. The resulting system frequency response was used for optimizing and selecting the excitation at the resonant mode highest pressure peaks (Figure 1.4.4). The pressure wave amplitude was then adjusted by the output amplitude of the function generator between 1 V to 8 V. The ultimate applied pressure wave amplitude was limited by the subject's comfort.

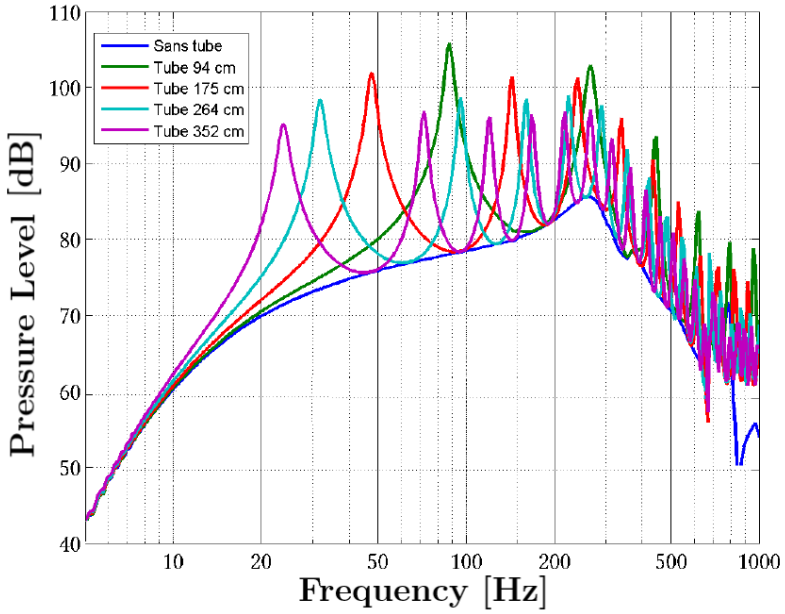

Figure 1.4.4: Wobulation curve showing the resonance modes of the excitation system obtained using waveguide with 32 mm diameter with different lengths. The resonant frequency peaks depend on the length of the waveguide. Any frequency can be matched by tuning the length of the waveguide.

The frequencies of the system resonant modes depend on the length L of the waveguide as shown in Figure 1.4.4 for L ranging from 94 cm to 352 cm. According to Equation 1.62, it is possible to determine the system resonant frequencies from the waveguide length L and sound velocity in the air $c_0 = 340.5\ \mathrm{m \cdot s^{-1}}$ [74], [102].

$$f_n = \frac{(2n-1)\cdot c_0}{4L} \qquad 1.62$$

where $n \in \mathbb{N}$ is the harmonic number of the resonant mode.

We used this guided pressure wave system for MRE acquisitions in phantoms (Chapter 2 and Chapter 3) and in human brain (Chapter 4 and Chapter 5). The air-tight 1 mm diameter acoustic adapter for phantom MRE was replaced by a mouthpiece for in vivo brain MRE.

1.4.2 MRE data acquisition

1.4.2.1 MRE sensitivity

Both gradient echo and spin echo based MRE sequences were used in this work. However, most MRE studies were performed with spin echo based MRE sequences to avoid as much as possible any distortion and artefact in the acquired phase maps (Section 1.3.2.4 page 30).

The motion sensitivity for gradient and spin echo based sequences is given by the phase shift accumulated during the application of the encoding bipolar gradients

respectively set by Equations 1.23 and 1.27. From these two equations, it is possible to write the relationship between the resulting uncertainty, Δu, on the displacement field and the measurement uncertainty, $\Delta\varphi$, on the phase shift and to infer the associated sensitivities, S_{SE}, for spin echo, and S_{GE}, for gradient echo:

$$\begin{aligned} u(\boldsymbol{r},\theta) &= \frac{\varphi(\boldsymbol{r},2T_{MEG},\theta)}{\gamma T_{exc}\boldsymbol{A}_{MEG}} \\ \Leftrightarrow\ \Delta u(\boldsymbol{r},\theta) &= \frac{\Delta\varphi(\boldsymbol{r},2T_{MEG},\theta)}{\gamma T_{exc}\boldsymbol{A}_{MEG}} \\ \Leftrightarrow \Delta u(\boldsymbol{r},\theta) &= S_{SE}\cdot\Delta\varphi(\boldsymbol{r},2T_{MEG},\theta) \end{aligned} \quad 1.63$$

$$\begin{aligned} u(\boldsymbol{r},\theta) &= \varphi(\boldsymbol{r},\theta)\cdot\frac{\pi(1-q^2)}{\gamma T_{exc}A_{MEG}\sin(\pi q)} \\ \Leftrightarrow\ \Delta u(\boldsymbol{r},\theta) &= \Delta\varphi(\boldsymbol{r},\theta)\cdot\frac{\pi(1-q^2)}{\gamma T_{exc}A_{MEG}\sin(\pi q)} \\ \Leftrightarrow \Delta u(\boldsymbol{r},\theta) &= S_{GE}\cdot\Delta\varphi(\boldsymbol{r},\theta) \end{aligned} \quad 1.64$$

which allows to identify the motion sensitivity of the acquisition sequences as:

$$S_{SE} = \frac{\varphi(\boldsymbol{r},2T_{MEG},\theta)}{u(\boldsymbol{r},\theta)} = \gamma N_{MEG}T_{exc}A_{MEG} \quad 1.65$$

$$S_{GE} = \frac{\varphi(\boldsymbol{r},\theta)}{u(\boldsymbol{r},\theta)} = \frac{\gamma T_{exc}A_{MEG}\sin(\pi q)}{\pi(1-q^2)} \quad 1.66$$

1.4.2.2 Anatomical acquisitions for brain segmentation

During brain MRE acquisitions, we also acquire anatomical brain images (such as T1-weighted and T2-weighted) before and after MRE acquisitions in order to check potential alteration of brain tissues after the MRE mechanical excitation.

In a post processing step, we make use of these anatomical images to segment specific brain regions. This segmentation is performed with SPM12 (*The Wellcome Centre for Human Neuroimaging, UCL, London, United-Kingdom*). It relies on an a priori that intensity variations due to MR physics are spatially smooth while those due to different tissue types tend to contain more high frequency information. By including prior knowledge about the distribution of the fields likely to be encountered by the correction algorithm, data are classified into a number of different tissue types which are defined according to tissue probability maps defining the prior probability of finding a tissue type at a particular location. This segmentation allows to identify the grey matter, white matter, CSF, bone, soft tissue and air/background in the cerebrum and white matter/grey matter in the cerebellum. To evaluate the mechanical behavior of the different tissues, means and standard deviations of the mechanical parameters are then

calculated on inferred masks of cerebral white matter and cerebral grey matter and of integrated cerebellar white and grey matters (Figure 1.4.5).

Figure 1.4.5: T1-weighted based segmentation using SPM12 to produce masks of cerebral grey and white matters and a mask of the cerebellar tissues.

Finally, together with the extracted parametric maps and the regional masks, brain images were spatially normalized to conduct multi-frequency, multi-resolution, multi-position analysis over the various datasets that were acquired over the last years.

1.4.3 Conditioning of data for reconstruction

In this section, we will see how to achieve MRE in optimal conditions so to compute the shear elasticity G' and the shear viscosity G'' AIDE reconstruction algorithm while minimizing the uncertainty.

1.4.3.1 Mechanical parameters for elastic medium

The q-based AIDE algorithm may theoretically be flawless upon proper joint assumptions and equation [103].

As shown earlier, in order to remove the compressional wave components, Sinkus et al. [4] applied the curl operator and simplified the wave equation (Equation 1.47) to obtain the Helmholtz equation (Equation 1.59).

Thus, the complex shear modulus (G^*) which is related to the dynamic shear modulus (G') and the loss shear modulus (G'') can be deduced from Equation 1.67 by inverting the q-field based Helmholtz equation (Equation 1.59) obtained without rheological assumptions along the three i motion-encoded direction:

$$\begin{aligned} G_i^* &= G_i^{'} + jG_i^{''} \\ G_i^* &= \mu_i + j\omega_{exc}\zeta_i \\ G_i^* &= -\rho\omega_{exc}^2 \frac{\boldsymbol{q_i}(\boldsymbol{r},\omega_{exc})}{\boldsymbol{\nabla^2 q_i}(\boldsymbol{r},\omega_{exc})}, \text{with } i \in \{1,2,3\} \end{aligned} \quad 1.67$$

As we have assumed an isotropic, homogeneous and linearly-elastic medium, the Helmholtz equation 1.67 which describes the differential equations for the three components of the $\boldsymbol{q}$-field can be simplified to extract the shear elasticity $G_i^{'}$ as:

$$G_i^{'} = -\rho\omega_{exc}^2 Re\left(\frac{\boldsymbol{q_i}(\boldsymbol{r},\omega_{exc})}{\boldsymbol{\nabla^2 q_i}(\boldsymbol{r},\omega_{exc})}\right), \text{with } i \in \{1,2,3\} \quad 1.68$$

Equation 1.44 giving the transverse velocity V_T can be derived along the three i motion-encoded directions for the shear velocity $V_{s,i}$ such as:

$$V_{s,i} = \sqrt{\frac{\mu_i}{\rho}} \quad \text{or } V_{s,i} = \sqrt{\frac{G_i'}{\rho}} \tag{1.69}$$

Then, the shear velocity can be deduced along the three spatial directions i from the three components of the q-fields such as:

$$V_{s,i}(r, \omega_{exc}) = \frac{\omega_{exc}}{Re\left(\sqrt{\frac{\boldsymbol{\nabla^2 q_i}(\boldsymbol{r}, \omega_{exc})}{\boldsymbol{q_i}(\boldsymbol{r}, \omega_{exc})}}\right)}, \text{with } i \in \{1,2,3\} \tag{1.70}$$

For a mechanically-isotropic medium, the three shear velocity values along the three i motion-encoded directions are expected to be the same and could be averaged ($V_s \approx V_{s_1} \approx V_{s_2} \approx V_{s_3}$). To get a more robust velocity estimation than the one we would get from the mean average, we can advantageously weight each direction by the data quality along this direction. As developed by Jin Long Yue in the course of his PhD [103], the average velocity V_s is weighted for each voxel over the three directions by the squared q-field quality (qQW):

$$V_s = V_{s,qQW} = \frac{1}{Q^2} \sum_i \left(\left(\frac{q_i}{\Delta q_i} \right)^2 V_{s,i} \right) \tag{1.71}$$

where $Q = \sqrt{\sum_i \left(\frac{q_i}{\Delta q_i} \right)^2}$ is the q-field quality (1.72)

with Δq_i, the uncertainty on the amplitude q_i of the curl component of the displacement field $\boldsymbol{q_i}(\boldsymbol{r}, \omega_{exc})$. The Q-weighted average velocity V_s defined in equation 1.71 minimizes the minimum absolute percentage error ($MAPE$) and thus provides the most accurate and precise estimation of the local shear velocity with AIDE [103].

1.4.3.2 Mechanical parameters for viscoelastic medium

In the MRE studies of Chapter 4 and Chapter 5, we assume that the medium is isotropic, homogeneous and linearly viscoelastic. The shear dynamic, G_i', and loss, G_i'', moduli are deduced along each spatial dimension i by algebraic inversion of the Helmholtz equation 1.67.

By combining the equation given by the local planar wave assumption (Equation 1.58) with Equation 1.67, the complex shear modulus can be written as:

$$G_i^* = G_i' + jG_i''$$
$$G_i^* = \frac{\rho\omega_{exc}^2}{k_i^2} \quad 1.73$$

with k_i the complex wave number such as:

$$k_i = \beta_i - j\alpha_i. \quad 1.74$$

with: $\beta_i = \frac{2\pi}{\lambda_{shear}} = \frac{\omega_{exc}}{V_s}$, λ_{shear} the shear wavelength, V_s the shear wave velocity calculated from the qQW methods given by the equation 1.76 [103] and α_i the attenuation parameter calculated from the q-fields from Equation 1.67.

Equation 1.58 giving the q-field based on an assumption of local planar wave can thus be written with each component $\boldsymbol{q_i}$ such as:

$$\boldsymbol{q_i} = |\boldsymbol{q_i}| \cdot e^{j(\boldsymbol{\beta_i r_i} - \omega_{exc} t)} e^{-\boldsymbol{\alpha_i r_i}} \quad 1.75$$

Thereafter, the complex shear modulus can be rewritten as:

$$G_i^* = G_i' + jG_i''$$
$$G_i^* = \frac{\rho\omega_{exc}^2}{k_i^2} \quad 1.76$$
$$G_i^* = \frac{\rho\omega_{exc}^2}{(\beta_i - j\alpha_i)^2}$$

It is possible to express the dynamic shear modulus G' and the shear loss modulus G'' by separating real from imaginary parts in the above equation 1.76:

$$G_i' = \rho\omega_{exc}^2 \frac{{\beta_i}^2 - {\alpha_i}^2}{\left({\beta_i}^2 - {\alpha_i}^2\right)^2 + 4(\alpha_i\beta_i)^2} \quad 1.77$$

$$G_i'' = \rho\omega_{exc}^2 \frac{2\alpha_i\beta_i}{({\beta_i}^2 - {\alpha_i}^2)^2 + 4(\alpha_i\beta_i)^2} \quad 1.78$$

In Chapter 4 and Chapter 5, as the studied media are considered viscoelastic, the mechanical parameters were calculated from Equations 1.77 and 1.78.

1.4.4 MRE absolute quantification

As seen in the Introduction, it is difficult to provide reference values for the mechanical properties because of the wide dispersion of the viscoelastic moduli found in the literature. To estimate and compare the mechanical parameters obtained with MRE, it is necessary to establish the conditions of validity of the MRE measurements. To this end, it is necessary to study the impact of the acquisition and reconstruction parameters which are decisive to yield precise and accurate MRE measurements.

1.4.4.1 Key parameters of q-AIDE algorithm

Although today there is no consensus on which model is the most appropriate for describing the tissue response under a mechanical excitation, hence which reconstruction method is to be used, I have used the $\boldsymbol{q}$-based AIDE algorithm during my thesis work to reconstruct the mechanical properties as it is a model-independent algorithm. The chosen $\boldsymbol{q}$-based AIDE algorithm allows to compute mechanical parameters in each voxel of the acquisition volume by local inversion of the wave equation in a viscoelastic medium. Mechanical parameters then depend on the mechanical excitation frequency f_{exc}, the voxel size a, the amplitude of the curl of the displacement field $\boldsymbol{q}$ and the associated measurement uncertainty Δq. Furthermore, recent works [103] have shown that the factors determining the accuracy and precision of MRE measurement can ultimately be subsumed with two parameters that essentially characterize how well the propagating shear wave is sampled: the spatial sampling factor (or number of voxels per wavelength), $s = \lambda/a$, where λ is the shear wavelength which is linearly related to the excitation frequency f_{exc}; and the amplitude sampling factor (or data quality factor), $Q = q/\Delta q$ where $1/\Delta q$ is the $\boldsymbol{q}$-field measurement uncertainty, which is related to the signal-to-noise ratio, SNR. Q, along SNR, should be maximized. For SNR values between 5 and 30, in mechanically homogeneous media, it was also shown that s should range between 6 and 9 to establish MRE conditions of validity [103]. These findings were demonstrated on simulated data by varying the spatial sampling factor s with f_{exc}. Inside the s optimal range, the estimated mechanical parameters were more accurate and exhibited minimal standard deviation values so they were also more precise. Outside the s optimal range, they were either overestimated ($s \lesssim 6$) or underestimated ($s \gtrsim 9$) with increasing standard deviations away from the s optimal range.

At a set excitation frequency, namely for a given wavelength in a mechanically homogeneous medium, the spatial sampling factor s is increased by reducing the voxel size so the signal-to-noise ratio is usually expected to be degraded (Figure 1.4.6 right). It results a greater uncertainty on the local estimate of the second derivatives and an increase in the error on the local curve of the displacement field. Increasing the amplitude of the induced displacement fields, or Q, can alleviate this issue (Figure 1.4.6 right). The spatial sampling factor s can also be decreased by increasing the voxel size so the signal-to-noise ratio is improved but the determination of the wavelength may then be obliterated by the poorer spatial resolution (Figure 1.4.6 left). Thus, a compromise needs to be found between the spatial resolution and the excitation frequency to achieve optimal sampling of the displacement field with the available SNR or the data quality.

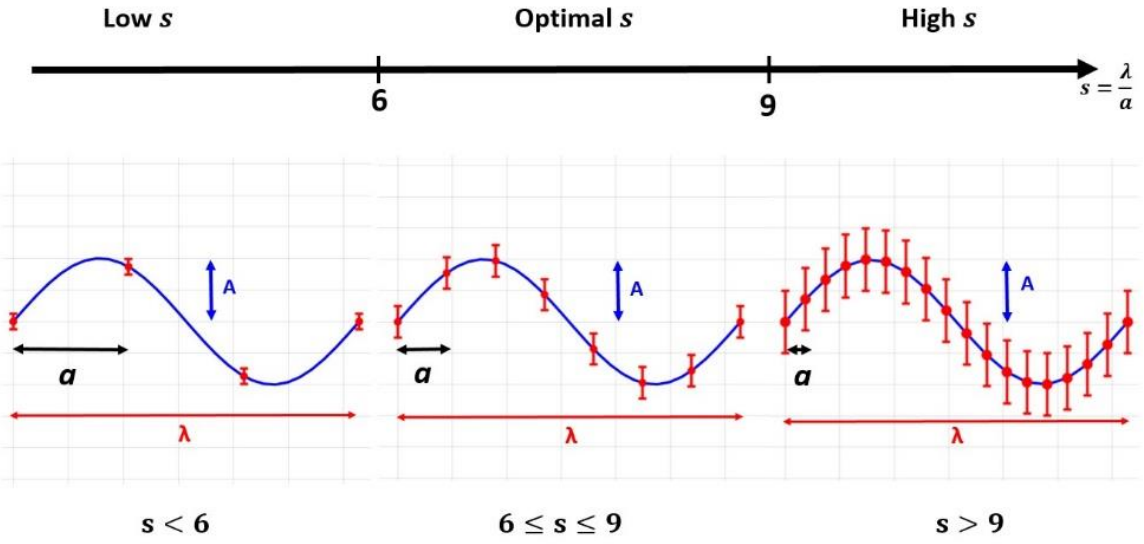

Figure 1.4.6: Spatial sampling with voxel size a of the displacement field produced in the medium by a propagating wave with wavelength λ. When $a > \lambda/6$ (or $s < 6$), despite enhanced SNR, the displacement field is undersampled and the wavelength λ is overestimated. When $a < \lambda/9$ (or $s > 9$), the SNR is degraded, the displacement field is oversampled, the displacement field amplitude is smeared out between neighboring voxels, and the wavelength λ is underestimated. In between, when $6 \leq s \leq 9$, that is to say, when there is between 6 and 9 voxels per wavelength, the displacement field is optimally sampled and the measurement uncertainty is minimal with best wavelength precision and accuracy.

The evolution of the s factor and the mean absolute percentage error (MAPE) for different Q factors were simulated by Jinlong Yue [103] as illustrated in Figure 1.4.7. The higher the quality factor is, the less s affects the precision and accuracy of the shear velocity measurement, the larger the s optimal domain is.

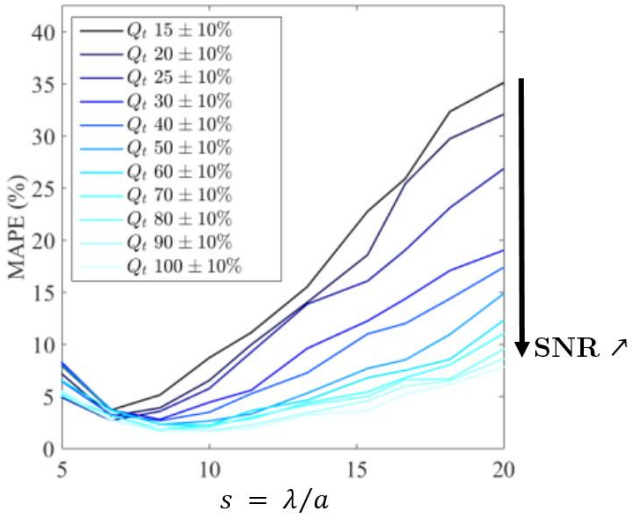

Figure 1.4.7: Simulated data from Yue PhD works [104] for appropriate s prediction using the q-field quality weighted method for different Q values. Optimal s is found

between 6 and 9 where the MAPE (Mean Absolute Percentage Errors) is minimized. The MAPE is minimized over a larger range of s ($6 < s < 11$) for the highest Q values.

1.4.4.2 Data conditioning

In practice, the shear wavelength, hence s, is not known before starting the MRE acquisition. Optimal spatial sampling must then be implemented either (1) with an estimation of the expected mechanical properties of the probed medium with preliminary acquired phase data, (2) with prospective multi-frequency or multi-resolution MRE covering the possible range for optimal s, or (3) with standard MRE at a single frequency and with a single voxel size but with retrospective multi-resampling of the acquired displacement field to find the optimal s domain.

The study presented in Chapter 2 proposes to explore with multi-frequency acquisitions the influence of s using a voxel-wise reconstruction quality criterion. Retrospective data multi-resampling could then be compared to actual prospective multi-frequency acquired data with constant frequency-voxel size product $f \cdot a$.

In Chapter 3 and Chapter 4, other constraints are taken into account to adequately probe and visualize the heterogeneity of the medium. First, the voxel size needs to be smaller than the size of the inclusions, the tumors, or the heterogeneity so it sets a frequency lower bound to reach the optimal s domain. Second, the reconstruction kernel size needs to be smaller than the size of the inclusions, the tumors, or the heterogeneity to reveal. Fulfilling these two conditions are necessary to allow the reconstruction algorithm to reliably reveal the mechanical heterogeneity associated to the medium. Moreover, as the mechanical properties differ from one region to another, the shear velocity is expected to be similarly heterogeneous and spatial sampling needs to be regionally optimized throughout the tissue either by prospective multi-frequency or multi-resolution MRE acquisitions or by retrospective resampling.

In summary, s and Q factors have been determined for four homogeneous phantoms (Chapter 2), a heterogeneous phantom (Chapter 3) and in the human brain (Chapter 4) in order to establish optimal conditions where best precision and accuracy of MRE measurements can be achieved.

1.5 Conclusion

In this chapter, MRE has been introduced. Existing MRE approaches and the original approach undertaken in this work have been described from the choice of the wave generator to the choice of the acquisition and reconstruction methods. According to former simulations, we showed that the latter choice is critical as it highly influences the measurement results. The variability of these key parameters has been weighted when the conditions of acquisition and reconstruction were not appropriately chosen. In the

next chapters, these key parameters will be monitored. We will see how it is possible to perform MRE both on phantom and in vivo on the brain with the most precise and accurate measurement possible.

Chapter 2 Homogeneous phantom study at multi-frequency MRE for elasticity quantitation and optimal tissue discrimination

2.1 Introduction

As described in the Chapter 1, MRE aims at mapping the mechanical properties of biological tissues by recording the displacement fields generated by a mechanical wave travelling through them. The extracted viscoelasticity moduli can be advantageously used in clinical diagnosis as the development of most pathological processes comes with an alteration of the tissue mechanical properties [8], [105]–[107]. In spite of successful applications in the clinic, the spread of MRE is undermined by the lack of accuracy and precision of the measurement on a voxel basis.

This chapter addresses some pitfalls in establishing MRE mechanical parameters by highlighting that MRE outcomes are conditioned by the mechanical waves travelling throughout the targeted tissue (their frequency, amplitude, and pattern within the definite boundary conditions), the acquisition parameters (the voxel size, the motion sensitizing gradients, and the resulting signal-to-noise ratio for a given MR pulse sequence), and the reconstruction method. In the framework of algebraic inversion of the differential equation of motion, AIDE [108], [109], once temporal sampling is set, the factors determining the accuracy and precision of MRE measurements can ultimately be subsumed with two parameters that essentially characterize how well the propagating shear wave is sampled: the spatial sampling factor (or number of voxels per wavelength), $s = \lambda/a$, and the amplitude sampling factor (or data quality factor), $Q = q/\Delta q$, where λ is the shear wavelength, a, the voxel size, q, the amplitude of the curl of the displacement field, and Δq, the associated measurement uncertainty [103]. These two dimensionless factors can be extracted for any voxel. If the spatial sampling factor, s, is too small (generally smaller than 6) then the shear wave pattern is undersampled and the shear velocity and the shear elasticity are overestimated. If it is too big (generally greater than 9) then the shear wave pattern is oversampled and the shear velocity and the shear elasticity are underestimated. Otherwise, when it stands in between (generally between 6 and 9), the shear wave pattern is optimally sampled and the measurement uncertainty is minimized [4], [103], [110]. The amplitude sampling factor, Q, increases with q and SNR (along with $1/\Delta q$). For a given shear wave amplitude, the higher the SNR, the smaller the measurement uncertainty is and the less influence s has on this

uncertainty. The lower the SNR, the higher the measurement uncertainty and the more the measurement precision and accuracy are sensitive to s. With a rather low SNR of 8, simulations predicted and experiments recorded relative velocity biases of 45% and threefold standard deviations when the voxel size, all things being equal otherwise, was either halved or doubled with respect to the optimal size for proper wave spatial sampling at 2 kHz, respectively leading to $s \simeq 12$ and $s \simeq 3$ [111]. Similarly, with a rather standard SNR of 30, simulations predicted relative biases of 10% and sixfold standard deviations when the excitation frequency, all things being equal otherwise, was halved, namely when the wavelength was doubled and the wave spatial sampling departed from the optimal conditions with $s = 20$ [103]. As a consequence, special care should be taken when performing MRE either using different voxel sizes and different excitation frequencies [112], [113], or simply probing tissues at different stages of a disease [114], [115] and mapping mechanically heterogeneous tissues [6], [8]. All those cases exhibit different wavelengths, leading to different spatial sampling conditions with different measurement bias and precision. Furthermore, additional mechanical features are expected to be revealed by the biological tissue dispersive behaviour [116], [117]. In this framework, MRE rheological studies carried out by merely sweeping the excitation frequency present dispersion laws that are inherently flawed by frequency-dependent measurement bias and precision.

In order to further confirm these results for a wider spectrum of situations, the first stage of my thesis focussed on investigating the repeatability, reproducibility, robustness, accuracy and precision of MRE along optimal sampling conditions across two MRI platforms at 1.5 T and 3 T in two different sites. For that purpose, multi-frequency experiments were carried out on mechanically-calibrated phantoms that mimic liver fibrosis.

This Chapter 2 is divided into five parts. The first part describes the protocol of the MRE experiments performed in the two MRI platform. The second part is a description of the process to obtain the mechanical outcomes parameters, from MRE acquisitions parameters to the MRE reconstruction description. Then, the third part reports the analysis of the mechanical parameters in order to study the repeatability of our measurements and the reproducibility between the two platforms. The fourth part of the Chapter 2, presents a reproducibility analysis between the two MRI platforms, based on data acquired with optimal excitation frequencies for each of the four calibrated phantoms. The third part and the fourth part of this chapter allowed to evaluate the ability to discriminate between shear velocity estimates in optimal and non-optimal conditions, and a re-conditioning strategy was considered to cope for non-optimally acquired datasets. Finally, resulting shear velocity estimates were compared with values obtained with the optimally pre-conditioned datasets. The last part of this chapter

presents a global discussion which allowed, first, to step back on our results and, then, to discuss about some MRE pitfalls already faced in the literature.

2.2 Protocol description

2.2.1 Phantom description

The MRE acquisitions of this study were performed on the set of the test phantoms (C1, C2, C3, C4) consisting of four cylinders housing 10 cm diameter, 12 cm height, homogeneous Zerdine® solid elastic hydrogel (Model 039, CIRS, VA, USA). As specified by the manufacturer, differing Zerdine® concentrations provided Young's moduli of 3.5 kPa, 11.4 kPa, 28.6 kPa and 44.8 kPa that matched various stages of liver fibrosis from normal state to mild, moderate and severe grades (Figure 2.2.1). The phantoms are characterized by an average compressional velocity of 1540 m·s-1, a density of 1030 kg·m-3, and a Poisson's ratio of 0.5. These phantoms were developed and validated in a study sponsored by the Quantitative Imaging Biomarker Alliance. They served as reference standards to evaluate shear wave velocity measurements with quasi-static compression dynamic mechanical analysis, vibration-controlled transient elastography, and hyper-frequency viscoelastic spectroscopy. They were shown to be more elastic than viscous [118].

Figure 2.2.1: Set of CIRS test phantoms {C1,C2,C3,C4} calibrated for liver fibrosis staging and grading at 3.5 kPa, 11.4 kPa, 28.6 kPa, and 44.8 kPa.

2.2.2 MRE bench setup

The experimental setup of the MRE acquisitions required a lot of attention to be able to provide a good reproducibility of the experiments on the two platforms. Indeed, it was necessary to reproduce the same waveguide length as it constitutes the intermediary piece between the source represented by the loudspeaker and the target to be excited, represented by the phantom. This waveguide length adjustment step is critical since it allows to define the different resonance frequencies as explained in the Chapter 1 section 1.4.1.1. However, in order to provide a good reproducibility of the experiments, it is important to obtain the same resonant excitation frequencies on the two platforms

by a wobulation (method explained in Chapter 1 section 1.4.1.1). The first constraint was therefore to reproduce the length of the waveguides (from the loudspeaker to the phantom) since the two MRI platforms are not structured and organized in the same way. Despite this experimental setup constraint, MRE acquisitions were carried out in the same way on Achieva 1.5 T and Ingenia 3 T MR systems (Philips Healthcare, Netherlands). Phantoms were placed at the center of the magnet bore into a 8 channel SENSE knee coil (Philips Healthcare, Netherlands) with their axis horizontally aligned with the directing magnetic field (Figure 2.2.2).

Point source mechanical excitation was induced in the phantom by guided pressure waves through an air-tight 1 mm diameter acoustic adapter. The pressure waves were remotely generated from the technical room (Figure 2.2.2) with a function generator (AFG 3021B, Tektronix, OR, USA) before being amplified with a power amplifier (P5000S, Yamaha, Japan), transduced with a 300 W 12" woofer (PHL Audio 4530, France), and guided through the Faraday cage along 22 mm inner diameter 6.24 m long altuglas® tubes and adapting hoses to the surface of the phantom (Figure 2.2.2) [19]. The generation of pressure waves was trigged by the MRI system for synchronization with the MRE acquisition and monitored with an oscilloscope (TDS 2014, Tektronix, USA).

The source pressure generated at the surface of the phantom was recorded onsite with an optical fiber sensor at 5 kHz (EVO-RM-8, FISO, Canada) and monitored from the MRI console room in order to keep a close eye on the real time evolution of the amplitude of the wave sent via the pressure measurement system communicating with the technical room.

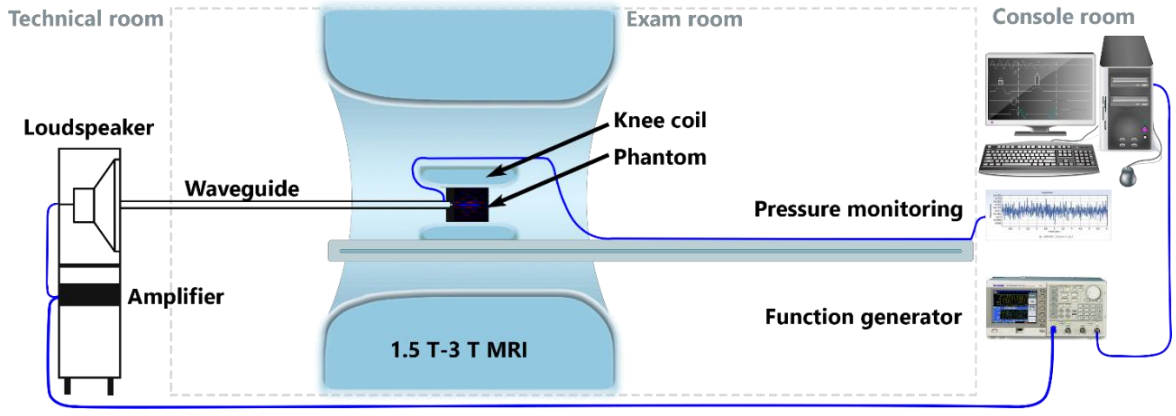

Figure 2.2.2: Schematic of the MRE bench setup at 1.5 T and 3 T. Remotely generated and amplified pressure waves are guided in the center of the MRI magnet bore to the phantom placed in a knee coil. Pressure level is monitored via an optical fiber sensor. Pressure wave are synchronized to the MRI acquisitions sequence.

2.2.3 SWE bench setup

SWE acquisitions were carried out on an Aixplorer ultrasound system (Supersonic Imagine, Aix-en-Provence, France). An artificial arm was used to steadily hold the

ultrasound probes on the surface of the phantoms in order to minimize the operator dependent influence. The phantoms were mechanically characterized using three different probes (XC6-1, SL10-2, and SL15-4) leading to respective pixel sizes of (0.8×0.6) mm^2, (0.35×0.20) mm^2 and (0.21×0.20) mm^2. The depth of the insonification window was placed in the center of the phantoms and adapted to the frequency bandwidth of each probe.

2.3 MRE acquisition and reconstruction

2.3.1 MRE acquisition parameters

For the different MRI platforms, the acoustic resonances of the wave-guiding close system were characterized by wobulation from 10 Hz to 400 Hz. The amplitude of the pressure waves was then set for each frequency to provide easily measureable waves within the phantoms while avoiding as much as possible reflections on the cylindrical walls. Selected pressure amplitudes were recorded at the surface of the phantoms, repeated and reproduced for every experiment performed at the same frequency. Upon the expected shear wavelengths at 3.5 kPa, 11.4 kPa, 28.6 kPa and 44.8 kPa, four optimal frequencies were selected, close to these resonances, at $f_{\mathrm{opt}} = \{60; 175; 207; 320\}$ Hz to prospectively optimize the spatial sampling factor s with $a = 1.25$ mm in each phantom. Three additional frequencies were picked up, again close to the resonances of the system, at $f = \{40; 90; 130\}$ Hz to prospect measurement outcomes for one of the four phantoms, C2, at 11.4 kPa, when s was not optimized. For repeatability, measurements on C2 were also repeated at 130 Hz at the end of the experimental runs. Moreover, data were acquired at 60 Hz for the four phantoms as most of liver MRE is reported in the literature at this frequency.

A standard multi-slice motion-encoding spin-echo sequence was implemented with a field of view FOV = $(120 \times 120 \times 30)$ mm^3 covering the upper part of the cylindrical phantoms, a matrix size of $(96 \times 96 \times 24)$, and an isotropic voxel of size $a = 1.25$ mm. The amplitude of the motion-encoding gradients was set to the default value of MR systems, which were very close: 21 mT · m^{-1} at 1.5 T and 22.5 mT · m^{-1} at 3 T. Hence the motion sensitivity could be considered similar for the different MR systems. Besides, the number of bipolar motion encoding gradients was increased sixfold while the frequency of the mechanical excitation varied from 40 Hz to 320 Hz. Thus, the motion sensitivity could compensate, at least partly, the lower motion amplitudes at higher frequencies. The echo time TE was maintained between 27 ms and 62 ms, while the repetition time TR, was concomitantly varied between 1,049 ms and 1,800 ms in order to maintain a relatively consistent SNR (Table 2.3.1).

CIRS	Fs [T]	TR/TE [ms]	a [mm]	f [Hz]	$\langle s \rangle$	$\langle SNR \rangle$	$\langle A \rangle$ [µm]	$\langle Q \rangle$	$\langle V_s \rangle$ [m·s^{-1}]	$\langle G_d \rangle$ [kPa]
C2	1.5	1800/62	1.25	40	30.2	29	12.36 ± 3.74	117 ± 44	1.47±0.47	2.38±3.30
C2	3.0	1800/62	1.25	40	30.2	45	4.50 ± 1.32	63 ± 31	1.48±0.40	2.34±1.60
C2	1.5	1600/58	1.25	60	20.1	29	15.03 ± 4.78	137 ± 51	1.44±0.12	2.10±0.35
C2	3.0	1333/39	1.25	60	20.1	40	1.93 ± 0.66	30 ± 11	1.44±0.33	2.20±1.50
C2	1.5	1600/50	1.25	90	13.4	30	13.99 ± 6.06	274 ± 124	1.46±0.05	2.15±0.16
C2	3.0	1200/42	1.25	90	13.4	45	3.27 ± 0.73	43 ± 17	1.46±0.10	2.14±0.30
C2	1.5	1477/46	1.25	130	9.3	30	3.57 ± 1.23	67 ± 26	1.48±0.04	2.19±0.12
C2	3.0	923/27	1.25	130	9.3	34	3.36 ± 0.86	37 ± 17	1.49±0.05	2.23±0.16
C2	1.5	1477/46	1.25	130	9.3	30	3.27 ± 1.83	68 ± 27	1.48±0.04	2.19±0.12
C2	3.0	923/27	1.25	130	9.3	34	3.04 ± 1.34	40 ± 17	1.50±0.05	2.25±0.16
C2	1.5	1370/46	1.25	175	6.9	27	4.46 ± 2.18	104 ± 42	1.51±0.02	2.27±0.07
C2	3.0	1096/37	1.25	175	6.9	41	0.46 ± 0.15	17 ± 7	1.51±0.04	2.30±0.13
C2	1.5	1158/36	1.25	207	5.8	24	2.03 ± 1.36	34 ± 17	1.53±0.04	2.33±0.12
C2	3.0	1042/36	1.25	207	5.8	39	0.53 ± 0.19	15 ± 6	1.56±0.05	2.42±0.16
C2	1.5	1049/34	1.25	320	3.8	22	1.63 ± 0.55	5 ± 3	2.53±0.50	6.64±3.80
C2	3.0	1049/34	1.25	320	3.8	39	3.15 ± 0.93	9 ± 10	2.13±0.40	4.40±2.50

Table 2.3.1: MRE acquisition parameters and MRE mechanical outcomes for the CIRS liver fibrosis phantoms C2 at 1.5 T and 3 T. The voxel size is 1.25 mm for all experiments; Fs: Field strength; TR/TE: repetition and echo times, a: voxel size, f: excitation frequency, s: sampling factor or number of voxels per wavelength, SNR, A: displacement field amplitude, Q: quality factor, V_s: shear velocity, and G': shear elasticity.

2.3.2 MRE reconstruction

The components of the 3D displacement field u_i (r, t), with $i = \{x, y, z\}$, of a voxel located at r and taken at time t can be computed from the recorded MRI phase values $\varphi_i(\mathbf{r}, t)$:

$$\varphi_i(\boldsymbol{r}, t) = \gamma \frac{N}{2} T \cdot A_{MEG,i} \cdot u_i(\boldsymbol{r}, t) \qquad 2\text{-}1$$

where γ is the gyromagnetic ratio of hydrogen nuclei, N, the number of bipolar motion-encoding gradient of duration $T = 1/f$, and $A_{MEG,i}$, the amplitude of the motion-encoding gradient along the three directions $i = \{x, y, z\}$.

The components $q_i(\mathbf{r}, t)$ of the rotational of $\mathbf{u}(\mathbf{r}, t)$ satisfy the Helmholtz equation 2-2 for shear wave in a locally homogeneous isotropic viscoelastic medium with complex shear modulus G^*.

$$\rho\omega^2 q_i(\mathbf{r}, t) = G^* \nabla^2 q_i(\mathbf{r}, t) \text{ with } \omega = 2\pi f \qquad 2\text{-}2$$

$$\text{where } \mathbf{q}(\mathbf{r}, t) = \nabla \times \mathbf{u}(\mathbf{r}, t) \text{ and } i = \{x, y, z\} \qquad 2\text{-}3$$

By algebraic inversion, AIDE, the shear dynamic, G_i', and loss, G_i'', moduli can be deduced along each spatial dimension i before being averaged for each voxel. As the phantoms are essentially elastic, we will here focus on G_i' as well as on the shear wave

velocity, $V_i = \sqrt{G_i'/\rho}$. The average over the directions was weighted by the data quality according to:

$$V_s = \frac{1}{Q^2}\sum_i \left(\left(\frac{q_i}{\Delta q_i}\right)^2 V_{s,i}\right) \text{ with } i = \{x, y, z\} \qquad 2\text{-}4$$

where Q is the data quality factor defined in every voxel:

$$Q = \sqrt{\sum_i \left(\frac{q_i}{\Delta q_i}\right)^2} \qquad 2\text{-}5$$

where Δq_i is the uncertainty on the amplitude q_i of the rotational component of the displacement field $q_i(\mathbf{r}, t)$ and $\frac{1}{\Delta q_i}$ corresponds to the signal-to-noise ratio SNR, so the Q values increase with the SNR. Moreover, the SNR values being proportional to total magnetic moment M_0, the Boltzmann statistic allowed to show the signal is proportional to the magnetic field B_0 according to the equation 2-6:

$$M_0 \approx \frac{N\gamma\hbar}{4kT} \cdot B_0 \qquad 2\text{-}6$$

With N, the number of spins.

The Q-weighted average velocity V_s defined in equation 2-4 minimizes the minimum absolute percentage error (MAPE) and thus provides the most accurate and precise estimation of the local shear velocity with AIDE [103].

Masks were automatically generated by magnitude thresholding for the different acquisitions. They were eroded by six voxels to exclude possible reconstruction biases at the boundaries before their intersection so 65,343 voxels were used for final data analysis. Both the mean value and the standard deviation of the amplitudes of the generated displacement fields, $\langle A \rangle$ and σ_A, were considered at every frequency for a fair evaluation of the inhomogeneous amplitude of the spherical wave throughout each phantom. Similarly, mean values and standard deviations of Q were considered to reflect this inherent inhomogeneity. Mean values, $\langle \mathrm{SNR} \rangle$, $\langle V_s \rangle$, $\langle G' \rangle$ and associated standard deviations were calculated over the resulting phantom mask to exhibit the accuracy and the precision of the MRE acquisition and reconstruction. For the sake of simplicity, we will only refer from now on to the shear velocities but the corresponding shear dynamic moduli could have been used instead.

In order to compare MRE outcomes to the manufacturer's calibration values as well as to the SWE values, the Young's modulus E was deduced for each phantom using the simple relationship for homogeneous, isotropic, elastic, and incompressible media:

$$E = 3G' \qquad 2\text{-}1$$

Then the Young's modulus, E, is deduced from MRE and SWE for each phantom and compared to the manufacturer's specification values. Relative differences were calculated with respect to MRE or SWE values.

MR raw data acquired at 60 Hz for the four phantoms were additionally resampled to retrospectively achieve optimal s conditions before extraction of the displacement fields and computation of the mechanical properties. Downsampling was performed through a Lanczos kernel and a low-pass anti-aliasing filter. The downsampling factors $\{1.00,2.91,3.43,5.33\}$ were given by the ratio $f_{\mathrm{exc}}/f_{\mathrm{opt}}$ between the excitation frequency, $f_{\mathrm{exc}} = 60$ Hz, and the optimal frequencies, f_{opt}, for the four phantoms C1, C2, C3, and C4 respectively. The Lanczos kernel widths, $\{1.00,3.06,3.45,4.16\}$ were adapted to each downsampling factor to match expected SNR gain one would obtain with Gaussian noise by mere averaging over downsampled voxels.

2.3.3 SWE Reconstruction

SWE velocity maps were processed together with the corresponding quality maps. Quality map values ranged from 0 to 1, 1 expressing a perfect confidence in the estimated shear velocity. Regions with quality below 0.7 were masked out before calculating the shear velocity mean and standard deviations values for the three ultrasound probes. (section 4.4.1.1 SSI using different ultrasound probes in [104])

2.3.4 Data analyses

Statistical analyses were performed using the shear velocity mean values, $\langle V_s \rangle$, as the primary outcomes. Boxplots of V_s measurements were computed to visually represent the dispersion of the data, both within and between experiments conducted with differing acquisition and reconstruction conditions. Non-parametric unpaired two-samples Wilcoxon tests were performed within R [119]. A result was deemed statistically significant if the probability was lower than 1% or p-value < 0.01.

Measurement repeatability and reproducibility were quantified with two-way random effects single-measure intra-class correlation coefficients (ICCs) and coefficients of variation (CVs). These coefficients were computed for the shear velocity mean and standard deviation values in order to access both accuracy and precision of the measurements.

2.4 MRE optimal conditions

For both MRE platforms, the 11.4 kPa calibrated phantom (C2) was first imaged and mechanically characterized at seven different excitation frequencies (f_{exc} = {40, 60, 90, 130, 175, 207, 320} Hz). Then, it was imaged again at 130 Hz for assessing the

measurement repeatability. The excitation frequencies were chosen so as to cover a corresponding s range of 3.5 (at 320 Hz) to 28 (at 40 Hz) (Table 2.3.1). The voxel size a was 1.25 mm and the wavelength λ was estimated from V_s at f_{opt}.

2.4.1 Analysis of mechanical outcomes

In the C2 phantoms, the SNR maps were rather homogeneous and consistent for any excitation frequency (Figure 2.4.1). Mean SNRs ranged between 22 and 30 at 1.5 T and between 34 and 45 at 3 T (Table 2.3.1). They were expectedly higher at higher field according to the equation 2-6. They were also slightly higher for longer TRs and shorter TEs.

Total amplitudes of the displacement fields ranged on average between 1.63 µm and 15.03 µm at 1.5 T and 0.46 µm and 4.5 µm at 3 T but they can reach 40.6 µm at 90 Hz and 1.5 T and 58.3 µm at 130 Hz and 3 T depending on how far from the source the measurements were performed. Mean values $\langle \mathrm{A} \rangle$ and $\langle Q \rangle$ were roughly twice higher at 1.5 T than at 3 T for each frequency, except at 320 Hz where $\langle \mathrm{A} \rangle$=1.63 µm and $\langle \mathrm{Q} \rangle$ fell down to 5 at 1.5 T, which was twice lower than at 3 T. Except at 320 Hz, $\langle Q \rangle$ values ranged between 15 and 274. The Q maps (Figure 2.4.1) exhibited patterns that were analogous to those of the q maps (Figure 2.4.1), which were mainly induced by the residual wave interferences onto the curl of the displacement field.

2.4.2 Measurement repeatability

Repeated measurements at 130 Hz on C2 yielded identical shear velocities at 1.5 T: $\langle V_s \rangle_{130\,\mathrm{Hz}}^{\mathrm{C2\text{-}1.5\,T}} = (1.48 \pm 0.04)$ m · s^{-1} and very similar values at 3 T: $\langle V_s \rangle_{130\,\mathrm{Hz}}^{\mathrm{C2\text{-}3\,T}} = (1.49 \pm 0.05)$ m · s^{-1} and $\langle V_s \rangle_{130\,\mathrm{Hz}}^{\mathrm{C2\text{-}3\,T}} = (1.50 \pm 0.05)$ m · s^{-1} (Table 2.3.1). With a relative dispersion of 3%, velocity maps at 130 Hz were fairly homogeneous.

2.4.3 Measurement reproducibility

As mention previously, SNR, A, q, and Q at 1.5 T and 3 T differed. In contrast, except at 320 Hz, shear velocity mean values and standard deviations followed the same trends at both fields: They were fairly homogeneous between 90 Hz and 207 Hz (recorded mean values stayed within less than 1% (Table 2.3.1)), whereas the velocity map homogeneity was degraded either at lower or higher frequencies (Figure 2.4.1): For the two field strengths the standard deviations of the shear velocity are higher at 40 Hz (eight times higher) 60 Hz (three to six times higher) and 320 Hz (ten times higher) than between 90 Hz and 207 Hz.

The voxel-wise velocity represented for C2 as a function of Q in Figure 2.4.2 also followed the same trend at both fields with a distribution that similarly evolved with f:

It narrowed between 90 Hz and 207 Hz whereas it changed its shapes and spread at lower and higher frequencies. The shear velocity dispersion in C2 was minimized at 175 Hz as clearly depicted on Figure 2.4.1. It sets the optimal conditions, $s = 6.9$, for the phantom from which the shear velocity, $\langle V_s \rangle_{175\,\mathrm{Hz}}^{\mathrm{C2}} = (1.51 \pm 0.02)\ \mathrm{m \cdot s^{-1}}$, can be extracted with the best confidence.

The overall mean CVs between 1.5 T and 3 T of $\langle V_s \rangle$ and σ_{V_s}, all phantoms and frequencies combined, were 1.62% (0–12.1%) and 1.95% (0-10.3%) respectively. The ICCs were 0.98 (95% confidence interval $0.943 < \mathrm{ICC} < 0.995$) and 0.89 (95% confidence interval $0.660 < \mathrm{ICC} < 0.966$) for $\langle V_s \rangle$ and σ_{V_s} respectively.

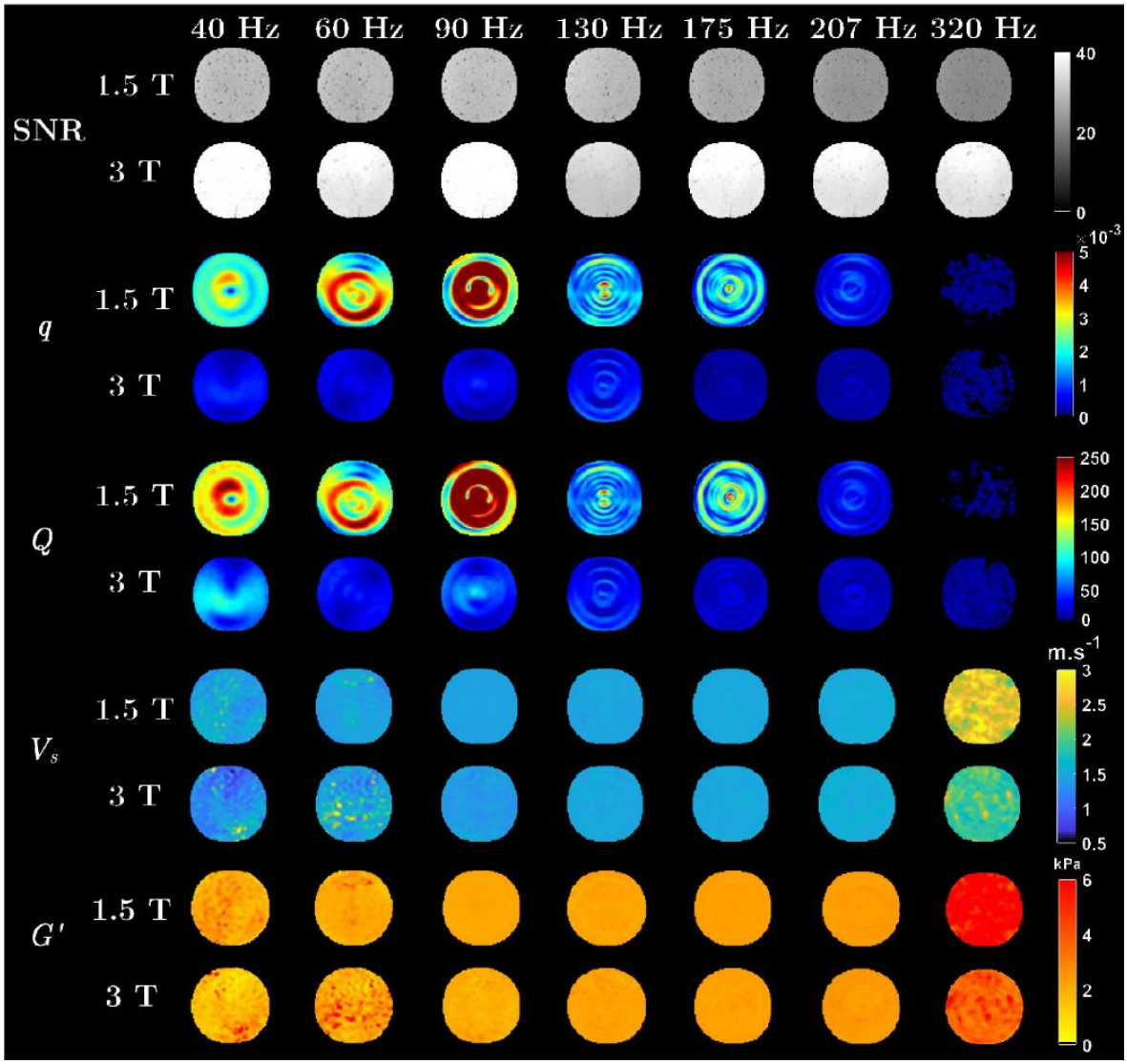

Figure 2.4.1: SNR, amplitude of the curl of the displacement field q, data quality Q, shear velocity V_s, and shear elasticity G' maps for the CIRS liver fibrosis phantoms C2 with MRE at excitation frequencies $f = \{40,60,90,130,175,207,320\}$ Hz. With consistent SNR but inhomogeneous q and Q maps, MRE is well conditioned and provides homogeneous V_s and G' maps in the 90 Hz-207 Hz frequency range.

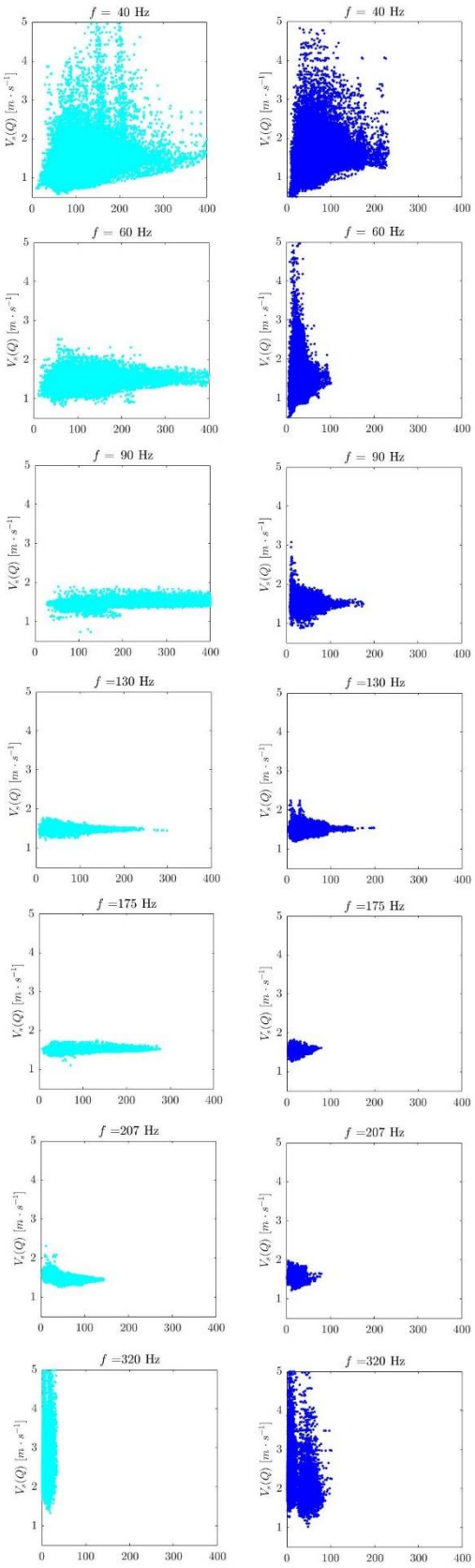

Figure 2.4.2: MRE voxel-wise shear velocity V_s as a function of data quality Q in the CIRS liver fibrosis phantom C2 at excitation frequencies $f = \{40,60,90,130,175,207,320\}$ Hz at 1.5 T (top row) and 3 T (bottom row). Velocity values increase with the frequency. Velocity

distributions are narrowed in the optimal s domain between 130 Hz and 207 Hz ($6 \lesssim s \lesssim 9$) where the measurements are expected to be the most accurate and precise.

2.4.4 Measurement conditioning

For C2, when data sets are resampled to approach optimal spatial sampling, a_{opt}, at frequencies ranging between 40 Hz and 320 Hz (Figure 2.4.3 (c)), the extracted shear velocity mean values fall down in a much narrower range with a standard deviation that is reduced from 0.40 at 1.5 T – and 0.23 at 3 T – to 0.02 at 1.5 T (Table 2.5.1). Concurrently, the measurement precisions are improved. The effects are negligible when data were already in the optimal s domain, at 130 Hz and 207 Hz, but they are radical when data were away from it, at 40 Hz, 60 Hz and 320 Hz, with revealed relative biases between 3% and 62% and precision gains between 4 and 23.5. Exemplarily at 320 Hz, we have $\langle V_s \rangle_{\text{MRE}}^{\text{C2-320 Hz}} = (2.53 \pm 0.50)$ m · s^{-1} at $a = 1.25$ mm while $\langle V_s \rangle_{\text{MRE-opt}}^{\text{C2-320 Hz}} = (1.59 \pm 0.12)$ m · s^{-1} at $a_{\text{opt}} = 0.68$ mm.

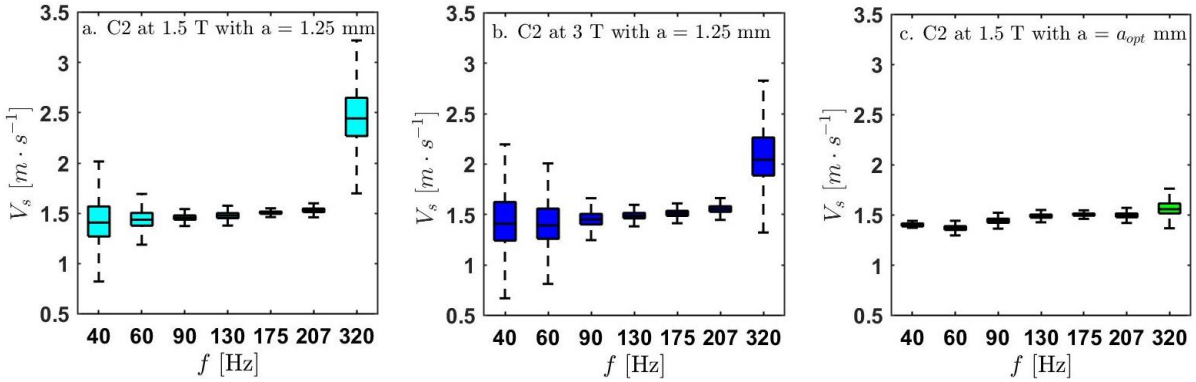

Figure 2.4.3: MRE shear velocity V_s as a function of the excitation frequency, f, in the CIRS liver fibrosis phantom C2 at 1.5 T (light blue), 3 T (blue) and after data resampling at 1.5 T (green). At both fields, MRE optimal conditions are reached at $f = 175$ Hz where measurement uncertainty is minimized (a and b). At other excitation frequencies, MRE accuracy and precision are regained by data resampling.

2.5 Optimal tissue discrimination

2.5.1 Outcomes analyses

In the Figure 2.5.1, for the four phantoms at optimal frequency and at both fields, the SNR maps were rather homogeneous and consistent. Mean SNRs ranged between 24 and 30 at 1.5 T and between 38 and 41 at 3 T (Table 2.5.2). They were expectedly higher at higher field. They were also slightly higher for longer TRs and shorter TEs.

Total amplitudes of the displacement fields ranged on average between 2.85 µm and 10.13 µm at 1.5 T and 0.46 µm and 5.37 µm at 3 T. Mean values $\langle A \rangle$ and $\langle Q \rangle$ were

higher at 1.5 T than at 3 T for each optimal frequency, except at 320 Hz where $\langle A \rangle$ were in the same range for both field. The Q maps (Figure 2.5.1) exhibited patterns which were mainly induced by the residual wave interferences onto the curl of the displacement field.

2.5.2 Measurement reproducibility at f_{opt}

As described in the Table 2.5.2, SNR, A, q, and Q at 1.5 T and 3 T differed. In contrast, shear velocity mean values and standard deviations remained similar between the two field strengths. Recorded mean values stayed within less than 1% (Table 2.5.2). A slight discrepancy occurred at the highest frequencies (207 Hz for C3 and 320 Hz for C2 and C4) but this variation remained well below the maximal measurement standard deviation of 8.3%. MRE shear velocity measurements in the optimal conditions for each phantom (C1 at 60 Hz, C2 at 175 Hz, C3 at 207 Hz, and C4 at 320 Hz) are represented as boxplots on Figure 2.4.3 for 1.5 T (a) and 3 T (b). The corresponding mean values and standard deviations are listed in Table 2.5.2. Measurements are also positively reproduced at both fields. The agreement of the mean values and the standard deviations was fair for C3 and C4 and excellent for C1 and C2.

For the four phantoms, the maps were homogeneous in their respective expected optimal conditions was set by the excitation frequency (Figure 2.5.1).

The voxel-wise velocity represented for the four phantoms as a function of Q in Figure 2.5.2 also followed the same trend at both fields with a distribution that similarly evolved with f: It narrowed for each optimal frequency used and it sets the optimal conditions, $6.9 < s < 11.1$ depending on the phantom (Table 2.5.2).

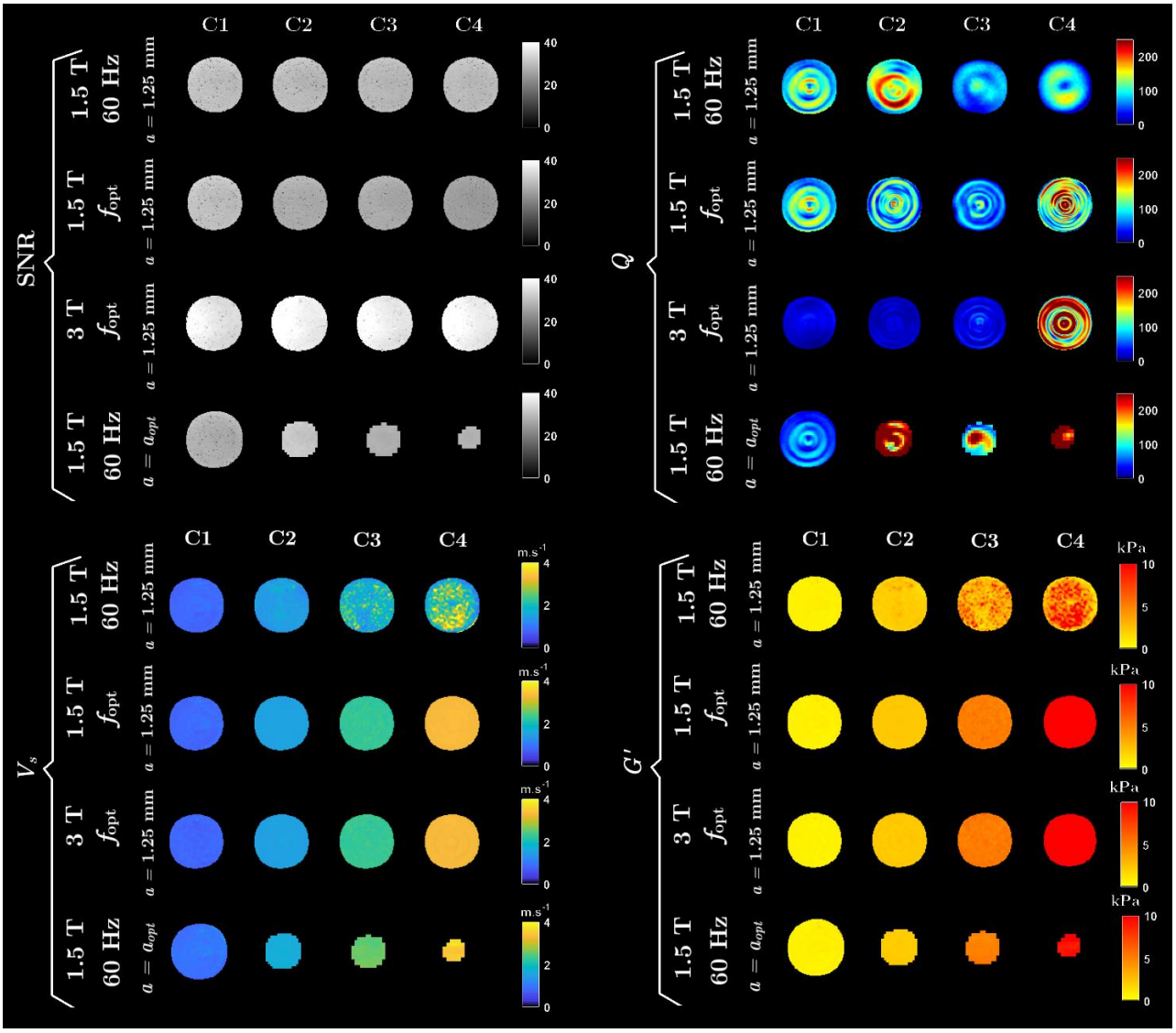

Figure 2.5.1: SNR, data quality Q, shear velocity V_s, and shear elasticity G' maps for the four CIRS liver fibrosis phantoms {C1,C2,C3,C4} with MRE at standard excitation frequency (f = 60 Hz), optimal excitation frequencies f_{opt} = {60,175,207,320} Hz at 1.5 T and 3 T and at 60 Hz with resampling. Despite different and inhomogeneous Q maps, MRE at f_{opt} is well conditioned and provides homogeneous V_s and G' maps for the four phantoms whereas at f = 60 Hz, MRE is only well conditioned and provides homogeneous V_s and G' maps for C1. It is degraded when departing from these optimal s conditions as the elasticity increases for the three other phantoms {C2,C3,C4}

CIRS	Fs [T]	TR/TE [ms]	a [mm]	f [Hz]	$\langle s \rangle$	$\langle SNR \rangle$	$\langle A \rangle$ [µm]	$\langle Q \rangle$	$\langle V_s \rangle$ [m·s^{-1}]	$\langle G_d \rangle$ [kPa]	$\langle E \rangle$ [kPa]
C1	1.5	1600/58	1.25	60	11.1	30	10.13 ± 4.35	114 ± 40	0.83 ± 0.06	0.69 ± 0.12	2.07
C1	3.0	1200/42	1.25	60	11.1	38	1.25 ± 0.59	21 ± 8	0.84 ± 0.07	0.71±0.12	2.13
C2	1.5	1370/46	1.25	175	6.9	27	4.49 ± 2.17	105 ± 43	1.51±0.02	2.27±0.07	6.81
C2	3.0	1096/37	1.25	175	6.9	41	0.46 ± 1.15	17 ± 7	1.51±0.04	2.30±0.13	6.9
C2	1.5	1600/58	1.25	60	20.1	26	15.03 ± 4.78	137 ± 51	1.44 ± 0.12	2.10 ± 0.35	6.30
C2	1.5	1096/37	3.63	60	6.9	31	0.46 ± 1.15	17 ± 7	1.51±0.04	2.30±0.13	6.9
C3	1.5	1158/36	1.25	207	8.7	26	2.85 ± 1.10	65 ± 26	2.27 ± 0.08	5.15 ± 0.37	15.45
C3	3.0	1042/36	1.25	207	8.7	40	0.92 ± 0.34	32 ± 16	2.30 ± 0.08	5.32±0.39	15.96
C3	1.5	1200/42	1.25	60	29.9	29	8.69 ± 4.13	59 ± 24	1.76 ± 0.50	3.34 ± 2.13	10.02
C3	1.5	1200/42	4.29	60	8.7	29	7.24 ± 2.79	173 ± 70	2.20 ± 0.07	4.82 ± 0.31	14.46
C4	1.5	1049/34	1.25	320	8.3	24	6.49 ± 2.55	132 ± 60	3.32 ± 0.09	11.03 ± 0.59	33.30
C4	3.0	1049/34	1.25	320	8.3	41	5.37 ± 2.09	179 ± 106	3.30 ± 0.06	10.09 ±0.39	30.27
C4	1.5	1200/42	1.25	60	44.4	29	12.59 ± 8.00	61 ± 37	1.88 ± 0.77	4.13 ± 4.5	12.39
C4	1.5	1200/42	5.70	60	9.7	29	17.38 ± 6.09	348 ± 95	2.96 ± 0.19	8.81 ± 1.11	26.43

Table 2.5.1: MRE acquisition parameters for the four CIRS liver fibrosis phantoms C1-C4 at 1.5 T (light blue highlight) and 3 T (dark blue highlight) at optimal frequencies $f_{\text{opt}} = \{60,175,207,320\}$ Hz as well as at 1.5 T, 60 Hz without (blue font) and with resampling (green font). Fs: Field strength; f: excitation frequency, TR/TE: repetition and echo times, a: voxel size, s: sampling factor or number of voxels per wavelength, SNR, A: displacement field amplitude, Q: quality factor, V_s: shear velocity, G': shear elasticity, and E: Young's modulus.

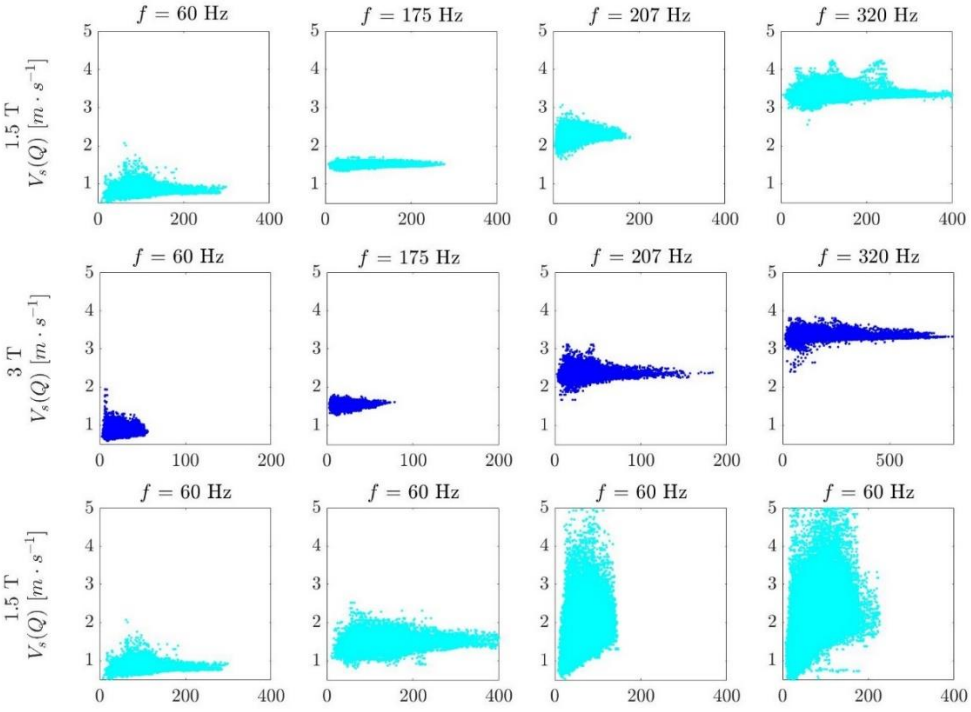

Figure 2.5.2: MRE shear velocity V_s as function of Q for the four CIRS liver fibrosis phantoms {C1,C2,C3,C4} at optimal excitation frequencies $f_{\text{opt}} = \{60,175,207,320\}$ Hz for both magnetic field at 1.5 T (upper row) and 3 T (middle row) and at standard excitation frequency $f = 60$ Hz (bottom row). For both magnetic field strengths, the measurement uncertainties are best when optimal conditions are matched ($6 \lesssim s \lesssim 9$), here at f_{opt} for each phantom, irrespective of the data quality.

2.5.3 Comparison of MRE at f_{opt} and at $f = 60$ Hz

For each phantom, the MRE shear velocity at 60 Hz is represented on Figure 2.5.3.(c). The corresponding mean values and standard deviations are listed in Table 2.5.3. Measurements taken at $f = 60$ Hz largely differed from the measurements taken at f_{opt} (Figure 2.5.3 (a) or Figure 2.5.3 (b)). The mean relative difference was only 4.6% for C2 but went up to 21% for C3 and to 43% for C4. The measurement uncertainty, away from the optimal condition, at $f = 60$ Hz, was also three to sixfold higher than at f_{opt}.

Nonetheless, in any configuration, the mean shear velocity increased with the phantom grade. But at $f = 60$ Hz, it only increases over the four phantom stiffness from $\langle V_s \rangle_{MRE}^{C1\text{-}60\ Hz} = 0.83\ m \cdot s^{-1}$ to $\langle V_s \rangle_{MRE}^{C4\text{-}60\ Hz} = 1.88\ m \cdot s^{-1}$ whereas, at f_{opt}, it varied from $\langle V_s \rangle_{MRE}^{C1\text{-}60\ Hz} = 0.83\ m \cdot s^{-1}$ to $\langle V_s \rangle_{MRE}^{C4\text{-}320\ Hz} = 3.32\ m \cdot s^{-1}$. Similar results were observed at 3 T. The measurements for different phantoms did not overlap at f_{opt} while they did at $f = 60$ Hz.

Each measurement at f_{opt} provided a clear discrimination on a voxel-basis of the four phantoms with highly significant statistical differences (with infinitesimal p-values and low ranks 268 for C2-C3, 2780 for C3-C4, and 0 otherwise) but measurements at $f = 60$ Hz failed to discriminate between C3 and C4 with $p \simeq 0.14$ (rank 212,150). Although the Wilcoxon tests revealed significant differences between the other phantoms, they showed high ranks (100 for C1-C2, 117,990 for C2-C3, and 142,430 for C2-C4).

2.5.4 Measurement conditioning

For downsampled datasets acquired at $f = 60$ Hz, MRE shear velocities increased and the associated dispersion reduced towards the values found at f_{opt} (Table 2.5.2). The Wilcoxon tests revealed statistically significant differences between the four phantom measurements with infinitesimal p-values for any combination of phantom results. Henceforth, after appropriate downsampling, the phantoms could be discriminated (Figure 2.5.3 (d)).

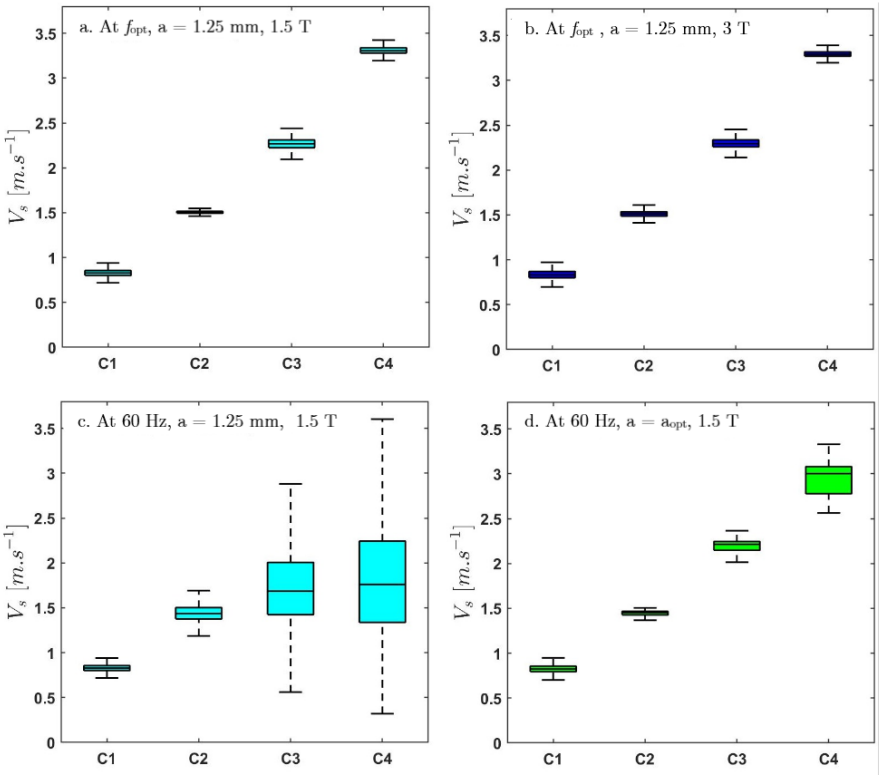

Figure 2.5.3 : MRE shear velocity V_s in four CIRS liver fibrosis phantoms {C1,C2,C3,C4} at optimal excitation frequencies $f_{opt} = \{60,175,207,320\}$ Hz at 1.5 T (a) and 3 T (b) and at standard excitation frequency $f = 60$ Hz without (c) and with data resampling (d). When properly conditioned, either prospectively by multi-frequency acquisition in the optimal s domain (a and b), or retrospectively by multi-resampling of the data to the optimal s domain (d), MRE measurement sensitivity and specificity are improved with regard to standard MRE at $f = 60$ Hz (c).

CIRS	Fs [T]	TR/TE [ms]	a [mm]	f [Hz]	$\langle s \rangle$	$\langle SNR \rangle$	$\langle A \rangle$ [µm]	$\langle Q \rangle$	$\langle V_s \rangle$ [m·s^{-1}]	$\langle G_d \rangle$ [kPa]	$\langle E \rangle$ [kPa]
C1	1.5	1600/58	1.25	60	11.1	30	10.13 ± 4.35	114 ± 40	0.83 ± 0.06	0.69 ± 0.12	2.07
C1	3.0	1200/42	1.25	60	11.1	38	1.25 ± 0.59	21 ± 8	0.84 ± 0.07	0.71±0.12	2.13
C2	1.5	1370/46	1.25	175	6.9	27	4.49 ± 2.17	105 ± 43	1.51±0.02	2.27±0.07	6.81
C2	3.0	1096/37	1.25	175	6.9	41	0.46 ± 1.15	17 ± 7	1.51±0.04	2.30±0.13	6.9
C2	1.5	1600/58	1.25	60	20.1	26	15.03 ± 4.78	137 ± 51	1.44 ± 0.12	2.10 ± 0.35	6.30
C2	1.5	1096/37	3.63	60	6.9	31	0.46 ± 1.15	17 ± 7	1.51±0.04	2.30±0.13	6.9
C3	1.5	1158/36	1.25	207	8.7	26	2.85 ± 1.10	65 ± 26	2.27 ± 0.08	5.15 ± 0.37	15.45
C3	3.0	1042/36	1.25	207	8.7	40	0.92 ± 0.34	32 ± 16	2.30 ± 0.08	5.32±0.39	15.96
C3	1.5	1200/42	1.25	60	29.9	29	8.69 ± 4.13	59 ± 24	1.76 ± 0.50	3.34 ± 2.13	10.02
C3	1.5	1200/42	4.29	60	8.7	29	7.24 ± 2.79	173 ± 70	2.20 ± 0.07	4.82 ± 0.31	14.46
C4	1.5	1049/34	1.25	320	8.3	24	6.49 ± 2.55	132 ± 60	3.32 ± 0.09	11.03 ± 0.59	33.30
C4	3.0	1049/34	1.25	320	8.3	41	5.37 ± 2.09	179 ± 106	3.30 ± 0.06	10.09 ±0.39	30.27
C4	1.5	1200/42	1.25	60	44.4	29	12.59 ± 8.00	61 ± 37	1.88 ± 0.77	4.13 ± 4.5	12.39
C4	1.5	1200/42	5.70	60	9.7	29	17.38 ± 6.09	348 ± 95	2.96 ± 0.19	8.81 ± 1.11	26.43

Table 2.5.2: MRE acquisition parameters for the four CIRS liver fibrosis phantoms C1-C4 at 1.5 T (light blue highlight) and 3 T (dark blue highlight) at optimal frequencies $f_{\text{opt}} = \{60,175,207,320\}$ Hz as well as at 1.5 T, 60 Hz without (blue font) and with resampling (green font). Fs: Field strength; f: excitation frequency, TR/TE: repetition and echo times, a: voxel size, s: sampling factor or number of voxels per wavelength, SNR, A: displacement field amplitude, Q: quality factor, V_s: shear velocity, G': shear elasticity, and E: Young's modulus.

2.5.5 MRE and SWE comparison

As expected in the four phantoms, both ultrasound Bmode images and elasticity maps were homogeneous. Only regions outside the trapezoidal insonification window for the XC6-1 probe and the deepest regions for the SL15-4 probe were found below 0.7 on the quality maps. Measurement dispersions were small and below 6 % except for C1 where it reached 10% with the SL10-2 probe. Shear velocities obtained with SWE were similar regardless of the probe used (Table 2.5.3). Small differences only appeared for the softest phantoms C1 and C2. The overall mean shear velocities were $\langle V_s \rangle_{\text{SWE}}^{\text{C1}} = (0.98 \pm 0.04)$ m · s^{-1}, $\langle V_s \rangle_{\text{SWE}}^{\text{C2}} = (1.63 \pm 0.05)$ m · s^{-1}, $\langle V_s \rangle_{\text{SWE}}^{\text{C3}} = (2.46 \pm 0.03)$ m · s^{-1} and $\langle V_s \rangle_{\text{SWE}}^{\text{C4}} = (3.46 \pm 0.06)$ m · s^{-1}. The MRE observables, averaged at 1.5 T and 3 T, compared rather well with the SWE values with $\langle V_s \rangle_{\text{MRE}}^{\text{C1}} = (0.84 \pm 0.05)$ m · s^{-1}, $\langle V_s \rangle_{\text{MRE}}^{\text{C2}} = (1.51 \pm 0.03)$ m · s^{-1}, $\langle V_s \rangle_{\text{MRE}}^{\text{C3}} = (2.29 \pm 0.06)$ m · s^{-1} and $\langle V_s \rangle_{\text{MRE}}^{\text{C4}} = (3.31 \pm 0.05)$ m · s^{-1}. Relative discrepancies were below 8% except for C1, where it reached 18%. This trend propagated to the shear elasticities with twice as large relative discrepancies, ranging from 10% to 39% (Table 2.5.3).

The MRE and SWE Young's moduli ranged between $\langle E \rangle_{\text{MRE}}^{\text{C1}} = 2.07$ kPa and $\langle E \rangle_{\text{MRE}}^{\text{C4}} = 33.3$ kPa and between $\langle E \rangle_{\text{SWE}}^{\text{C1}} = 3.0$ kPa and $\langle E \rangle_{\text{SWE}}^{\text{C4}} = 36.9$ kPa, which were well below the CIRS calibrated values between $\langle E \rangle_{\text{CIRS}}^{\text{C1}} = 3.5$ kPa and $\langle E \rangle_{\text{CIRS}}^{\text{C2}} = 44.8$ kPa.

The CIRS measurements differed from SWE by 17% to 53% and from MRE by 34% to 80%.

CIRS	$\langle V_s \rangle_{\mathrm{MRE}}$ [m · s^{-1}]				$\langle V_s \rangle_{\mathrm{SWE}}$ [m · s^{-1}]		
	1.5 T	1.5 T	1.5 T	3 T			
	$a = 1.25$ mm $f = 60$ Hz	$a = a_{\mathrm{opt}}$ $f = 60$ Hz	$a = 1.25$ mm $f = f_{\mathrm{opt}}$	$a = 1.25$ mm $f = f_{\mathrm{opt}}$	Probe XC6-1 MHz	Probe SL10-2 MHz	Probe SL15-4 MHz
C1	0.83 ± 0.07	0.83 ± 0.07	0.83 ± 0.06	0.84 ± 0.07	0.96 ± 0.03	1.01 ± 0.11	0.97 ± 0.05
C2	1.44 ± 0.12	1.44 ± 0.03	1.51±0.02	1.51±0.04	1.60 ± 0.02	1.66 ± 0.10	1.61 ± 0.10
C3	1.76 ± 0.50	2.20 ± 0.07	2.27 ± 0.08	2.30 ± 0.08	2.43 ± 0.04	2.47 ± 0.06	2.48 ± 0.08
C4	1.88 ± 0.77	2.96 ± 0.19	3.32 ± 0.09	3.30 ± 0.06	3.51 ± 0.11	3.43 ± 0.12	3.43 ± 0.10

Table 2.5.3: Shear velocity mean values and standard deviations for the four CIRS liver fibrosis phantoms C1-C4 reported with MRE at 1.5 T and 3 T at standard excitation frequency $f = 60$ Hz, without and with data resampling, and at optimal excitation frequencies $f_{\mathrm{opt}} = \{60,175,207,320\}$ Hz; and by SWE with three ultrasound probes at 3.5, 6, and 7.5 MHz.

2.6 Discussions

MRE was repeated and reproduced in two sites at different magnetic field strengths on four phantoms mechanically excited from 40 Hz to 320 Hz. Although the amplitude of the mechanical waves and the SNRs differed between the platforms, the shear velocities and elasticities matched within the measurement uncertainty for each excitation frequency. Both mean values and standard deviations agreed at 1.5 T and 3 T (Table 2.5.2). Despite an average factor three in data quality between 1.5 and 3 T, the voxel-wise velocities followed the same distribution with respect to Q (Figure 2.4.3 and Figure 2.5.3). Such robustness effectively held when the data were well conditioned but failed otherwise. When $6 \lesssim s \lesssim 9$, both measurement accuracy and precision were preserved at 1.5 T and 3 T with dissimilar Q whereas, when $s \lesssim 6$ or $s \gtrsim 9$, they were degraded. These results fully corroborate the simulations carried out in a purely elastic, isotropic, homogeneous medium [103]. Here, the shear viscosity could be neglected and the four phantoms could be considered as purely elastic in the range of frequencies explored by both MRE and SWE. Indeed, the phase velocities measured at a single excitation frequency with MRE were similar to the group velocities measured within a broadband excitation with SWE. Moreover, the SWE measurements were rather independent of the ultrasound probe, XC6-1, SL10-2 or SL15-4, with respective central frequencies (3.5 MHz, 6 MHz, and 7.5 MHz) to which the excitation bandwidths are related. We may thus fairly assume that the phantoms are not dispersive as formerly stated on similar Zerdine® solid elastic hydrogels [120]. Therefore, the dispersion law should be a constant and not a monotonically increasing function of frequency as reported here for C2 between 40 Hz and 320 Hz (Figure 2.4.3 (a) and Figure 2.4.3 (b)). This dispersion is only apparent as the increasing trend vanishes provided optimal spatial sampling is carried over before

data processing (Figure 2.4.3 (c)). Hence, the increase of shear velocity from 1.44 m · s^{-1} to 2.53 m · s^{-1} consequently may not reflect the mechanical response of the medium but instead the bias added along the reconstruction, which depends on the spatial sampling.

In our study, this bias was negative when $s \gtrsim 9$ – here when $f \lesssim 90$ Hz – and positive when $s \lesssim 6$ – here when $f \gtrsim 207$ Hz. Furthermore, this reconstruction bias came with an escalating measurement dispersion. Even with high Q, the measurement precision was progressively degraded as we moved away from the optimal s conditions (Table 2.3.1). At 3 T, it lost a factor 10 when $s = 3.8$ or $s = 30.2$. At 1.5 T, the loss in measurement precision reached an even higher factor of 25 because, Q being roughly twice higher at 1.5 T than at 3 T, due to differing excitation wave amplitudes, the data quality influenced the observables in a much lesser extent. This is exemplified at both fields where the lowest standard deviations that the measurements exhibited were found at 175 Hz (1.3% at 1.5 T and 2.6% at 3 T), compared to much higher standard deviations at 40 Hz, (32% at 1.5 T and 27% at 3 T), or even at 90 Hz, (3.4% at 1.5 T and 6.8% at 3 T), although $Q_{\mathbf{175}\,\mathrm{Hz}}^{\mathrm{C2\text{-}1.5\text{-}3\ T}}$ were smaller than $Q_{\mathbf{40}\,\mathrm{Hz}}^{\mathrm{C2\text{-}1.5\text{-}3\ T}}$ and $Q_{\mathbf{90}\,\mathrm{Hz}}^{\mathrm{C2\text{-}1.5\text{-}3\ T}}$.

The comparison at different fields might have been weakened by reproducibility issues. The SNR gain of 40% was expected at 3 T but the wave amplitude loss was disappointing. Despite the dissimilar configurations of the MRI systems, we made sure that the waveguides were of the same length to obtain identical resonant modes and frequencies were identical on both platforms. Moreover, we verified that the applied pressures, as optically recorded at the surface of the phantoms, were the same for each frequency on both sites. Yet, the displacement fields measured with MRE did not exhibit the same amplitudes at 1.5 T and 3 T (Table 2.3.1). We assume that the 1 mm diameter acoustic adapter was not properly sealed at 3 T and pressure leaked. Therefore, data quality was reduced in average by a factor 3 at 3 T.

The higher amplitudes at 1.5 T revealed underlying interference patterns that resulted from wave reflections on the cylindrical wall boundary. Geometric dispersion did not suffice to attenuate the waves before they bounced onto the wall and too little if any attenuation came from the viscosity of the phantoms. This corroborates the purely elastic behavior of the phantoms.

These interferences wave patterns have been well described by Okamoto et al. in a similar setup with the sum of Bessel functions of the first and second kinds [121]. However, in our study, patterns were not carried over the reconstruction and they were barely seen on the inferred maps of shear velocity and elasticity (Figure 2.4.1 and Figure 2.5.1). These results underscore the robustness of AIDE with respect to boundary conditions, multiple reflections, and interferences provided the waves do not get fully annihilated [122]. The robustness is confirmed by the agreement between MRE and SWE, for which the extraction of the shear velocity is not subjected to any boundary condition.

It is obtained here when MRE is performed in optimal conditions and because the phantoms are largely elastic and negligibly viscous [103].

The MRE shear velocity mean values stand below the SWE mean values, within 8% for C2-C4, at the limit of the added measurement uncertainties. The main underestimation we report for C1, 18%, might partly originate from the over-optimal conditioning ($s = 11.1$) as the optimal conditioning was only estimated for C1, C3, and C4 while it had been experimentally determined for C2. Moreover, the general negative bias might mainly originate not from MRE underestimation but from SWE overestimation. The SWE overestimation has already been by Oudry et al. [123] and by Urban et al. [124] with relative differences of up to 22% at 400 Hz. Our results question the calibrated Young's moduli provided by the phantom manufacturer, which match neither SWE nor MRE inferred values. Indeed, the manufacturer Young's moduli do increase with the phantom stiffness but largely overestimate SWE Young's moduli by 15% to 35% and MRE Young's moduli by 25% to 44%.

In [123], MRE and ultrasound transient elastography (TE) measurements were averaged over multi-frequency acquisitions on four styrene-ethylene/butylene-styrene phantoms between 60 Hz and 220 Hz. The phantoms were considered more elastic than viscous and shear elasticities were averaged over the frequency range for MRE-TE comparison. Yet, we can estimate that, over the explored ranges, s roughly spans from 17.2 down to 6.5 for the softer phantom and from 17.7 down to 12.9 for the stiffer phantom. Namely, while sweeping the frequency spectrum, the optimal conditions are not always fulfilled and MRE shear elasticities are biased negatively and positively with respect to the effective s at the applied excitation frequency. No special spectral trend shows up for the stiffer phantom as all shear elasticity values are recorded outside the optimal domain with expectedly measurement uncertainties overwhelming the trend. Yet, noticeable increasing trends come as a rather clear signature for the other three phantoms.

Bigot et al. carried out a thorough comparative study on agarose phantoms with inclusions of two types of cerebral fibrils and bovine serum albumin (BSA) [117]. MRE was performed at multiple frequencies between 400 and 1200 Hz. Shear velocities increased over the frequency span from (2.01 ± 0.77) m · s-1 to (2.59 ± 0.42) m · s-1 in average in fibrils and from (2.28 ± 0.69) m · s-1 to (2.57 ± 0.48) m · s-1 in BSA. The voxel size of the acquisitions was 0.391 mm and the spatial sampling factors below 800 Hz ranged out of the optimal domain ($s \gtrsim 10.3$) as substantiated by nearly twice larger associated measurement standard deviations. Therefore, we do speculate that part of the reported dispersive behaviors of fibrils and BSA could be explained by the positive measurement bias expected in these conditions.

In this framework, we could interestingly review a pioneering work that was carefully performed by Green et al. with roughly $s \simeq 7$ at a single frequency in a gelatin phantom with four mechanically different regions [6]. Nevertheless, the reported shear elasticities were systematically lower with MRE at 200 Hz, $G'_{\mathrm{MRE}} = \{6.6; 12.0; 16.2; 23.0\}$ kPa, than with rheometry at 50 Hz, $G'_{\mathrm{Rheo}} = \{6.7; 14.2; 24.2; 33.2\}$ kPa. The negative MRE measurement bias remained effectively small, within 15%, as long as s remained within the optimal domain, which held for the two softer regions of the phantom ($s \lesssim 9$). However, for the two stiffer regions, s was beyond 10 and the measurement bias was above 30%. Our interpretation is also confirmed by the increasing measurement deviations for stiffer regions – from 2% to 5% and 10%.

The data conditioning pitfall is exemplified in this work by the comparison between MRE at 60 Hz (Figure 2.5.3 (c)), which is currently established as the reference procedure for diagnosing liver fibrosis [125]–[127], and the proposed s-optimized multi-frequency MRE (Figure 2.5.3 (a) or (b)) or multi-sampling MRE (Figure 2.5.3 (d)). When data are not well conditioned, namely here, at 60 Hz, when s goes farther away from the optimal domain from $s \simeq 11.1$ for C1 up to $s \simeq 43.9$ for C4 (Table 2.5.2), the shear velocity mean value gets so underestimated, down to 43.2%, and the measurement dispersion gets so large, up to fivefold, that the rather far apart fibrosis severity mimicked by the C3 and C4 phantoms cannot be mechanically discriminated (Figure 2.5.3 (c)). When data are well conditioned, either prospectively by adjusting the excitation frequencies and the voxel size with respect to the expected shear wavelengths or retrospectively by resampling the recorded MRI data with respect to the estimated shear wavelengths, then MRE measurement uncertainty is minimized; and shear velocity values are as much accurate and precise as they can be with the available data quality. In these conditions only, correct quantitative MRE can be achieved at the voxel level.

The prospective adjustment of a single excitation frequency may not be clinically applicable, since the tissue stiffness is not known a priori and is in contrary the unknown under consideration. Yet it is possible to set a broad spectrum of optimal conditions that would cover the expected mechanical range of an organ or a disease by implementing multi-frequency acquisitions [112], [128]–[132]. Complementarily, or alternatively with standard single frequency MRE, multi-resampling iterations could be implemented before reconstruction. Thus, composite multi-frequency and/or multi-sample accurate and precise velocity maps could be produced with optimal conditions being fulfilled for every voxel.

The retrospective approach may hinder the effective spatial resolution of MRE when data downsampling is required. In our study, we even reached the bottom line at 40 Hz as we were left with only a single reconstructed slice after reconditioning the data

set from 1.25 mm to 5.70 mm. In this case, measurement accuracy and precision come at the expense of spatial resolution and the trade-off should be thoroughly studied on heterogeneous media before deciding upon optimal parameters to implement for MRE acquisition.

2.7 General conclusion

This Chapter 2 allowed to highlight that calculation by MRE of mechanical parameters in homogeneous phantom does not come without any pitfall and this is why it is important to ensure that similar acquisition conditions have to be used when making inter-study comparisons.

The different results of this chapter showed that, preferably, the data should be of high quality and the displacement fields induced in the targeted homogeneous tissue at a single frequency should be sampled with the optimal number of voxels per expected wavelength ($6 \lesssim s \lesssim 9$). Yet, acquired data are usually of acceptable but not exceptional quality and the tissue is generally heterogeneous requiring multiple optimal s domains throughout the tissue that cannot be achieved altogether.

This chapter showed that absolute quantification can only be completed when optimal conditions are fulfilled either prospectively by adequate multi-frequency excitation or retrospectively by data multi-resampling. Once achieved, wherever stands the quality of available data, MRE measurement accuracy and precision will be optimal such that intra-subject or inter-subject regional or temporal tissue mechanical variations can be quantified and discriminated as shown here at the voxel level on phantoms mimicking liver fibrosis.

Chapter 3 MRE optimal conditions in a heterogeneous medium

3.1 Introduction

In Chapter 2, the extraction of the mechanical parameters was performed in homogeneous, elastic and isotropic phantoms and optimal spatial sampling conditions were determined to minimize the measurement uncertainty. *In vivo*, the tissue mechanical response is not expected to be homogenous over the probed region of interest. Quite the contrary, when it is locally afflicted by a disease, the organic medium is more likely heterogenous and different shear velocities are to be extracted to discriminate healthy and pathological regions.

In the literature, pathological regions were effectively revealed by MRE in organs such as the breast [4], [133]–[135] and the brain [12] [14], [19], [29], [33], [136]–[138]. The specific stiffness values recorded by MRE for tumours were corroborated by the associated histopathological findings [29], [137], [138]. Yet, the diagnosis based on MRE is made difficult and questionable in complex tissues as pointed out by the review performed on ten different brain MRE studies by Benevicius et al. [8]. They showed that, in the selected studies, the shear modulus was not significantly different neither in pathological and surrounding healthy tissues nor among the various diseases. Only meningiomas could be discrminated from glioblastomas, anaplastic astrocytomas, gliomas, and metastatic tumors by their stiffest.

In all these studies, MRE displacement fields were acquired at a single excitation frequency and MRE reconstruction was carried out with the given acquisition spatial sampling. Hence, MRE data might have been well conditioned for one type of tissue – either healthy or pathological – but not the other and for a type of tumor but not for the others. MRE accuracy and precision were thus necessarily degraded in some regions as the optimal spatial sampling factor $s = \lambda/a$ varies with the local shear velocity and the extracted values, which are biased in those regions, cannot be fairly compared with those in the other regions. Thus, it would be necessary to set different optimal sampling factors either by prospectively acquiring with multiple excitation frequencies or multiple voxel sizes or by restrospectively resampling the acquired displacement field data as pointed out in the former chapter.

In this Chapter 3, we studied a heterogeneous breast phantom with inclusions mimicking tumoral lesions stiffer than the surrounding parenchyma. Optimal s values were regionally achieved everywhere in the phantom with multi-frequency MRE acquisitions so data were properly conditioned for the healthy and pathological tissues

with the corresponding frequency datasets. Thus, best precise and accurate mechanical measurements could be extracted in each of the regions.

In this chapter, we start describing the MRE protocol by the heterogenous breast phantom and the acquisition MRE pulse sequence. Then, the acquisition and reconstruction processes are depicted to reach the mechanical outcomes. Finally, computed MRE outcomes are presented through maps, graphs, and histograms in order to compare them in every region of interest as a function of the excitation frequency.

3.2 Protocol description

3.2.1 Phantom description

MRE acquisitions were carried out in the framework of Marion Tardieu's doctoral work [74] on a breast phantom (Model 051, CIRS, Arlington, VA, USA), originally designed for biopsy and made of Zerdine. The phantom contained dense masses (Figure 3.2.1 (a)) with diameters ranging from 2 to 8 mm and cystic-like masses with diameters ranging from 3 to 10 mm. These masses are visible with low signal on MR magnitude images as shown in the central slice of the phantom in Figure 3.2.1 (b). With Zerdine viscoelastic properties close to those of human tissues, the phantom is a fair model of an heteregenous medium. It presents mechanically-different regions with inclusions showing viscoelastic properties different than the surrounding homogeneous parenchyma.

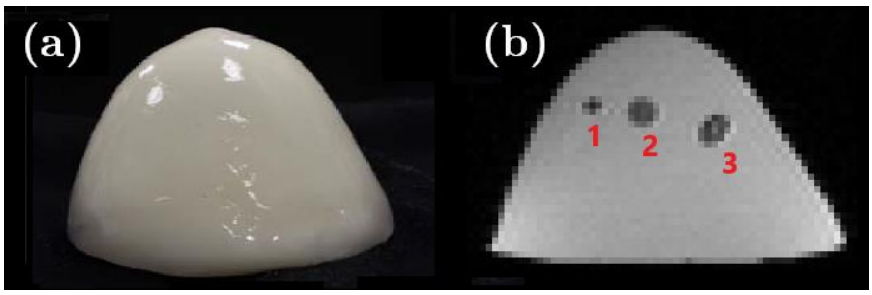

Figure 3.2.1 (a): Breast phantom (Model 051); (b): Central axial slice of MR magnitude image of the phantom. Inclusions are easily exhibited with low signal. They are numbered from one to three.

3.2.2 MRE setup

The acquisitions were performed by Marion Tardieu on a 1.5 T MRI (Achieva, Philips Healthcare, The Netherlands) [74]. The phantom was placed between two flexible SENSE coils (SENSE Flex-M, Philips Healthcare, The Netherlands) with its axis vertically perpendicular to the directing magnetic field as if the subject was lying supine.

The MRE acquisitions were carried out at five excitation frequencies: $f_{exc} = \{155,225,296,327,399\}$ Hz. A standard multi-slice spin-echo sequence with motion-encoding was implemented with a field of view FOV $= (128 \times 104 \times 84)$ mm^3 covering the whole breast phantom, a matrix size of $(64 \times 64 \times 42)$, and an isotropic voxel of size $a = 2$ mm. The amplitude of the motion-encoding gradients was 21 mT $\cdot$ m^{-1}. The number of bipolar motion encoding gradients, N_{MEG}, was increased by up to a factor twelve while the frequency of the mechanical excitation varied from 155 Hz to 399 Hz. The echo time, TE, ranged between 26 ms and 74 ms, while the repetition time, TR, ranged between 1492 ms and 4742 ms in order to maintain a relatively consistent SNR (Table 3.2.1).

The experimental setup and materials used to carry out the MRE acquisitions on the breast phantom are the same as described in Chapter 2 Section 2.2.2. It is composed of three parts: the first part takes place behind the MRI exam room in the technical room where pressure waves are remotely generated by the excitation generator. The second part takes place in the MRI exam room where the pressure waves are guided through the Faraday cage along a waveguide to the surface of the breast phantom in the center of the magnet bore. Then, the third part takes place in the console room where we monitor the amplitude of the induced mechanical wave, we implement the MRI and MRE sequences and we acquire the MRI and MRE datasets (Figure 4.2).

f_{exc} [Hz]	155	225	296	327	399
N_{MEG}	2	2	2	20	24
TR/TE [ms/ms]	1626/26	1492/27	1561/27	4240/75	4742/74
TA	5 min 43 s	5 min 15 s	5 min 29 s	14 min 50 s	16 min 35 s
SNR	8	9	9	6	6
$\langle A \rangle$ [µm]	28.98 ± 33.04	7.53 ± 14.86	4.74 ± 11.21	32.75 ± 40.86	18.71 ± 31.18
$\langle Q \rangle$	104.57 ± 96.27	23.04 ± 39.12	10.69 ± 22.80	395.5 ± 412.8	192.1 ± 274.5
$\langle V_s \rangle_{BP}$ [m·s^{-1}]	2.86 ± 0.13	2.93 ± 0.11	3.11 ± 0.12	3.29 ± 0.22	4.16 ± 0.81
$\langle V_s \rangle_{inc,1}$ [m·s^{-1}]	3.32 ± 1.04	3.35 ± 0.52	3.50 ± 0.37	3.62 ± 0.32	4.08 ± 0.38
$\langle V_s \rangle_{inc,2}$ [m·s^{-1}]	3.30 ± 1.11	3.31 ± 0.50	3.61 ± 0.60	3.74 ± 0.58	4.50 ± 0.82
$\langle V_s \rangle_{inc,3}$ [m·s^{-1}]	3.07 ± 0.22	3.15 ± 0.18	3.28 ± 0.15	3.41 ± 0.16	4.05 ± 0.42
$\langle G' \rangle_{BP}$ [kPa]	8.19 ± 0.77	8.61 ± 0.68	9.67 ± 0.76	10.88 ± 1.48	18.00 ± 7.44
$\langle G' \rangle_{inc,1}$ [kPa]	12.80 ± 12.60	11.52 ± 4.15	12.42 ± 2.78	13.21 ± 2.46	16.78 ± 3.32
$\langle G' \rangle_{inc,2}$ [kPa]	12.40 ± 13.73	11.21 ± 4.49	13.42 ± 6.12	14.32 ± 5.10	20.09 ± 8.03
$\langle G' \rangle_{inc,3}$ [kPa]	9.50 ± 1.59	9.96 ± 1.18	10.80 ± 1.03	11.60 ± 1.07	16.57 ± 3.55
s_{BP}	9.2 ± 0.4	6.5 ± 0.2	5.3 ± 0.2	5.0 ± 0.3	5.0 ± 0.8
$s_{inc,1}$	11.3 ± 3.4	7.4 ± 1.1	6.0 ± 0.6	5.5 ± 0.5	5.1 ± 0.4
$s_{inc,2}$	11.0 ± 3.9	7.4 ± 1.1	6.1 ± 1.0	5.7 ± 0.8	5.4 ± 0.8
$s_{inc,3}$	10.0 ± 0.7	7.0 ± 0.4	5.5 ± 0.3	5.2 ± 0.2	5.1 ± 0.4

Table 3.2.1: MRE acquisition parameters in the breast phantom: excitation frequency f_{exc}, number of MEG N_{MEG}, repetition time TR, echo time, TE, acquisition time TA and MRE outcomes: signal-to-noise, SNR, amplitude of displacement field A, shear velocity V_s, shear elastic modulus G' and spatial sampling factor $s\,(=\lambda/a)$ in: the breast parencyma, s_{BP}, the inclusion 1, $s_{inc.1}$, the inclusion 2, $s_{inc.2}$, the inclusion 3, $s_{inc.3}$ at five excitation frequencies {155, 225, 296, 327, 399} Hz. Minimal standard deviations are highlighted in red.

3.2.3 MRE reconstruction

Both the mean value and the standard deviation of the amplitudes of the generated displacement fields, $\langle A \rangle$ and σ_A, were considered at each excitation frequency for a fair evaluation of the highly inhomogeneous wave amplitude throughout the phantom.

Similarly, mean values and standard deviations of Q, were considered to reflect this inherent inhomogeneity.

As the studied regions of interest in the breast phantom are essentially elastic, we focus here on the Q-weighted average velocity V_s defined in equation 1.71 by the data quality factor Q in equation 4-5. As seen before, it minimizes the minimum absolute percentage error (MAPE) and thus provides the most accurate and precise estimation of the local shear velocity with AIDE [103]. For broader comparison, G' was then inferred as $G' = \rho V_s^2$.

The mean values $\langle V_s \rangle$ and $\langle G' \rangle$ and the standard deviations of the shear velocity V_s and the elastic modulus G' were computed for every excitation frequency in four different regions: the parenchyma and three inclusions. Mechanically homogeneous regions of interest were composed of 279 voxels in the inclusion 1, 707 voxels in the inclusion 2 and 472 voxels in the inclusion 3. The size of the region taken in the breast parenchyma was adapted to the size of the inclusion in order to ease fair statistical comparisons among the regional distributions and histograms.

The inclusions were chosen near the excitation source, where the amplitude was maximum in order to maximize the quality factor and therefore to minimize the measurement uncertainty. Regional mean signal-to-noise ratio, $\langle \mathrm{SNR} \rangle$, and its associated standard deviations were also calculated over the four regions of interest (Table 3.2.1).

Like in Chapter 2, for the sake of simplicity, we will only refer from now on to the shear velocities but the corresponding shear dynamic moduli could have been used instead.

3.2.4 MRE data analyses

First, errorbar voxel-by-voxel shear velocity was plotted as a function of the excitation frequency for the four regions of interests (parenchyma, inclusion 1, inclusion 2 and inclusion 3). Thus, the optimal frequency domain, leading to optimal spatial sampling ($6 < s < 9$) for which the shear velocity in the breast parenchyma and in the inclusions presents the best precision and accuracy, could be determined when the errobars are the smallest.

Then, the shear velocity distributions were plotted for the four regions of interests with gaussian fits after having tested the normal distribution of the data sets. The mean values and standard deviations of each fitted gaussian curves were used to respectively quantify the tissue discrimination power of MRE (the bigger μ differences between parenchyma and inclusions, the better the discrimination) and the precision of the measurements (the smaller the standard deviation σ, the better the precision of the measurement).

Non-parametric unpaired two-samples Wilcoxon tests were performed with Matlab® to quantify the shear velocity differences between the breast parenchyma and the inclusions. A result was deemed statistically significant if the probability was lower than 1% or p-value $< 10^{-3}$.

3.3 MRE optimal conditions

3.3.1 MRE optimal domain determination

In the breast phantom, the SNR maps are rather homogeneous and consistent for any excitation frequency (Figure 3.3.1). Mean SNR ranges between 6 and 9 (Table 3.2.1) with TR and TE values almost threefold higher at 327 Hz and 399 Hz than at 155 Hz, 225 Hz and 296 Hz.

The mean total amplitude of the displacement fields ranges between 4.74 µm at $f_{exc} = 296$ Hz and 32.25 µm at $f_{exc} = 327$ Hz. Mean amplitudes, $\langle A \rangle$, at frequencies 155 Hz, 327 Hz and 399 Hz are roughly four to eight times higher than the mean amplitudes at 225 Hz and 296 Hz (Table 3.2.1).

The maps of the quality factor, Q, exhibit patterns that are analogous to those found in the maps of the displacement field amplitude A (Figure 3.3.1) as those were mainly induced by the residual wave interference onto the curl of the displacement field. Q drops down at 296 Hz with $\langle Q \rangle_{296\,Hz} = 10.7$ whereas it reaches very high values at 327 Hz with $\langle Q \rangle_{327\,Hz} = 395.5$ as the pressure wave was increased in order to achieve reasonable wave amplitude at higher frequencies (Table 3.2.1).

The mean shear velocity maps showed in Figure 3.3.1 increases with the excitation frequency (from 155 Hz to 399 Hz) regardless of the region of interest (breast parenchyma, BP, or inclusions $inc, 1\text{-}3$): from $\langle V_s \rangle_{BP} = 2.86$ m·s^{-1} to $\langle V_s \rangle_{BP} = 4.16$ m·s^{-1} in the breast parenchyma, from $\langle V_s \rangle_{inc,1} = 3.32$ m·s^{-1} to $\langle V_s \rangle_{inc,1} = 4.08$ m·s^{-1} in inclusion 1, from $\langle V_s \rangle_{inc,2} = 3.30$ m·s^{-1} to $\langle V_s \rangle_{inc,2} = 4.50$ m·s^{-1} in inclusion 2 and from $\langle V_s \rangle_{inc,3} = 3.07$ m·s^{-1} to $\langle V_s \rangle_{inc,3} = 4.05$ m·s^{-1} for inclusion 3 (Table 3.2.1).

The standard deviations of the shear velocities in the four regions of interest, σ_{BP}, $\sigma_{inc,1}$, $\sigma_{inc,2}$, $\sigma_{inc,3}$ show a minimum at 225 Hz for the breast parenchyma with $\sigma_{BP} = 0.11\ \mathrm{m \cdot s^{-1}}$, at 327 Hz for inclusion 1 with $\sigma_{inc,1} = 0.32\ \mathrm{m \cdot s^{-1}}$, at 225 Hz for inclusion 2 with $\sigma_{BP} = 0.50\ \mathrm{m \cdot s^{-1}}$ and at 296 Hz for inclusion 3 with $\sigma_{BP} = 0.15$ m·s^{-1}. The velocity map in the breast parenchyma is more homogeneous at 225 Hz where the standard deviation σ_{BP} is minimal ($\sigma_{BP} = 0.11\ \mathrm{m \cdot s^{-1}}$). Moreover, the velocity maps show more clearly mechanically-delineated inclusion shapes where the standard deviation is minimized.

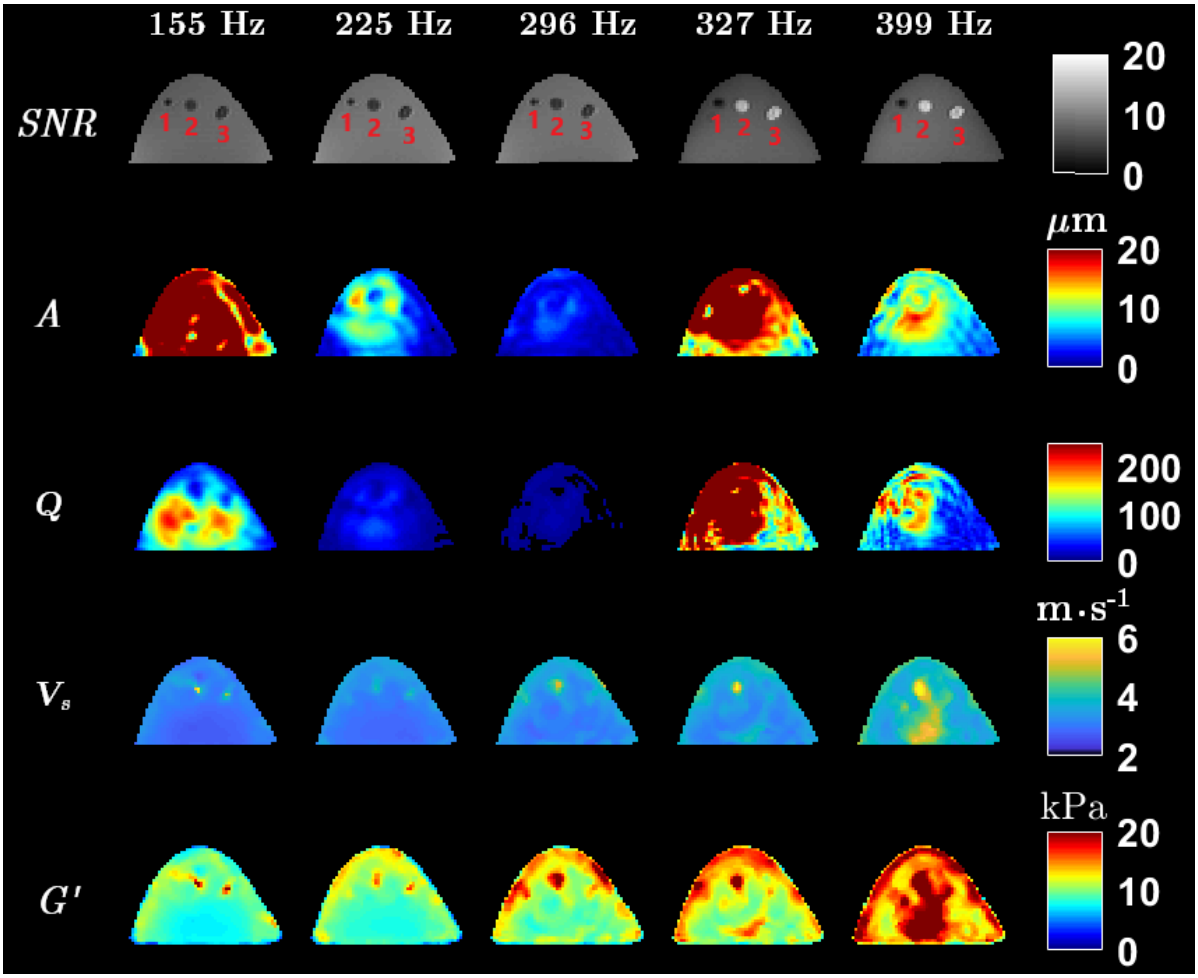

Figure 3.3.1: Central axial MRE parametric maps in the breast heterogenous phantom: SNR, amplitude of the displacement field, A, data quality factor Q, shear velocity V_s, and shear elasticity G' at excitation frequencies $f_{exc} = \{155,225,296,327,399\}$ Hz. With consistent an d rather homogenous SNR but inhomogeneous A and Q maps, MRE is well conditioned and provides homogeneous V_s and G' maps in the breast parenchyma and inclusion 2 at 225 Hz, in inclusion 3 at 296 Hz, and in inclusion 1 at 327 Hz.

The voxel-wise velocities in the parenchyma (blue), inclusion 1 (khaki), inclusion 2 (sea green) and inclusion 3 (lime) are represented as a function of Q in Figure 3.3.2.(1). The distributions in the four regions of interest shift towards higher velocity values with the excitation frequency f. They narrow at 225 Hz for the breast parenchyma and inclusion 2, at 327 Hz for inclusion 1 and at 296 Hz for inclusion 3 whereas they spread for the other excitation frequencies. The distributions are more easily distinguised between 225 Hz and 327 Hz.

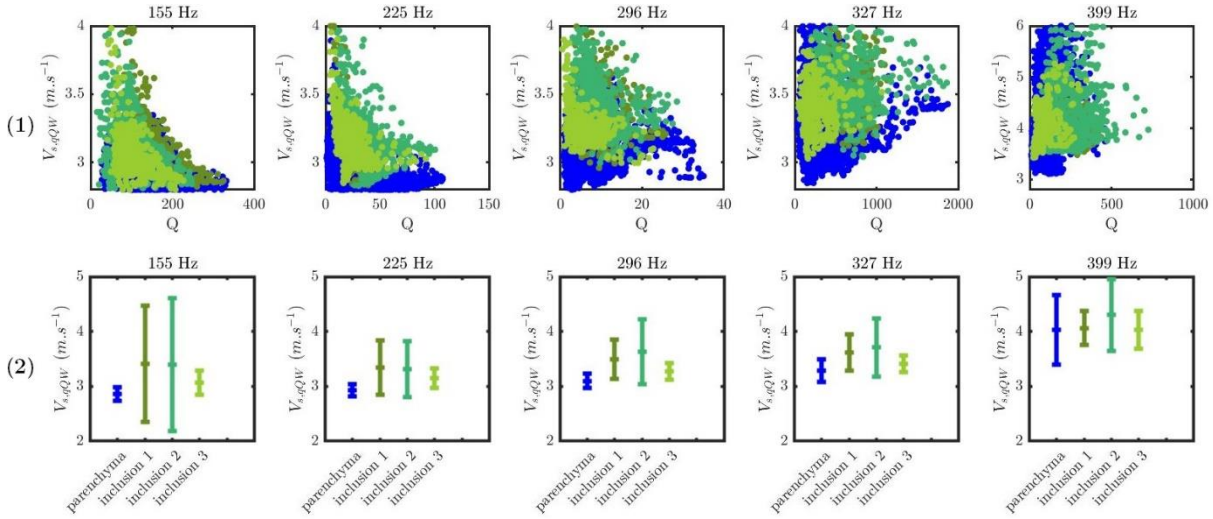

Figure 3.3.2: (1) MRE voxel-wise shear velocity, V_s, as a function of the data quality factor, Q, in the four regions of interest: the breast phantom parenchyma (blue), inclusion 1 (khaki), inclusion 2 (sea green) and inclusion 3 (lime) at excitation frequencies $f = \{155,225,296,327,399\}$ Hz. Velocity values increase with the frequency. Velocity distributions narrow in the optimal s domain between 225 Hz and 327 Hz ($6 \lesssim s \lesssim 9$) where the measurements are expected to be the most accurate and precise.
(2) MRE shear velocity V_s in the four regions of interest as a function of the excitation frequency f. Measurement uncertainty is minimized at 225 Hz in the breast parenchyma (blue), at 327 Hz in inclusion 1, at 225 Hz in inclusion 2, at 296 Hz in inclusion 3 (see Table 3.2.1).

Figure 3.3.3 to Figure 3.3.6 show the Gaussian fits of the shear velocity distributions in each region of interest over the excitation frequency range. These Gaussian fits explicit the observations made on the basis of Figure 3.3.2. First, the central mean values of the Gaussian curves increase by +38.2% in the parenchyma (from $\mu_{BP}^{225\,\mathrm{Hz}}$= 2.88 m·s^{-1} to $\mu_{BP}^{399\,\mathrm{Hz}}$ = 3.98 m·s^{-1}), by +28.7% in inclusion 1 (from $\mu_{inc,1}^{225\,\mathrm{Hz}}$ = 3.17 m·s^{-1} to $\mu_{inc,1}^{399\,\mathrm{Hz}}$ = 4.08 m·s^{-1}), by +34.8% in inclusion 2 (from $\mu_{inc,2}^{225\,\mathrm{Hz}}$ = 3.10 m·s^{-1} to $\mu_{inc,2}^{399\,\mathrm{Hz}}$= 4.18 m·s^{-1}), and by +33% in inclusion 3 (from $\mu_{inc,3}^{225\,\mathrm{Hz}}$ = 3.06 m·s^{-1} to $\mu_{inc,3}^{399\,\mathrm{Hz}}$= 4.03 m·s^{-1}).

The Gaussian fitting curves clearly spread out – σ increases – when the conditions depart from the optimal domain either at lower or higher frequencies (Figure 3.3.3 to Figure 3.3.6. Whitout considering the variations of s into account, these Gaussian fitting curves suggest, first, that data at 399 Hz exhibit the worst measurement precisions with the largest standard deviations ($\{\sigma_{BP}^{399\,\mathrm{Hz}}; \sigma_{inc,1}^{399\,\mathrm{Hz}}; \sigma_{inc,2}^{399\,\mathrm{Hz}}; \sigma_{inc,3}^{399\,\mathrm{Hz}}\} = \{0.57; 0.31; 0.49; 0.34\}\,\mathrm{m \cdot s^{-1}}$), second, that there is not a single optimal frequency but rather a range of optimal frequencies, which fulfills optimal spatial sampling for a = 2 mm ($6 \lesssim s \lesssim 9$). Slightly different ranges of minimal standard deviations are found in the parenchyma (between 155 Hz and 296 Hz), inclusion 1 (between 155 Hz and 327 Hz), and the inclusions 2 and 3 (between 225 Hz and 327 Hz) with:

$\{\sigma_{BP}^{155\,\mathrm{Hz}}; \sigma_{BP}^{225\,\mathrm{Hz}}; \sigma_{BP}^{296\,\mathrm{Hz}}\} = \{0.14; 0.10; 0.13\}\,\mathrm{m \cdot s^{-1}}$, $\{\sigma_{inc,1}^{155\,\mathrm{Hz}}\text{-}\sigma_{inc,1}^{327\,\mathrm{Hz}}\} = \{0.23; 0.24; 0.25; 0.21\}\,\mathrm{m \cdot s^{-1}}$, $\{\sigma_{inc,2}^{225\,\mathrm{Hz}}\text{-}\sigma_{BP}^{327\,\mathrm{Hz}}\} = \{0.20; 0.20; 0.18\}\,\mathrm{m \cdot s^{-1}}$, $\{\sigma_{inc,3}^{225\,\mathrm{Hz}}\text{-}\sigma_{inc,3}^{327\,\mathrm{Hz}}\} = \{0.16; 0.16; 0.15\}\,\mathrm{m \cdot s^{-1}}$.

The shear elastic modulus G' maps - calculated from the shear velocity maps (V_s) – expectedly follow the same trends with the excitation frequency (Figure 3.3.1). For every acquisition, the mean elastic modulus in the breast parenchyma $\langle G' \rangle_{BP}$ is lower than $\langle G' \rangle_{inc,1}$, $\langle G' \rangle_{inc,2}$ and $\langle G' \rangle_{inc,3}$ in the inclusions. When optimal conditions are fullfilled, shear elastic difference reaches 4.6 $\pm$ 2.5 kPa between parenchyma and inclusion 1, 2.6 $\pm$ 4.5 kPa between parenchyma and inclusion 2 and 2.2 $\pm$ 1.2 kPa between parenchyma and inclusion 3 (Table 3.2.1).

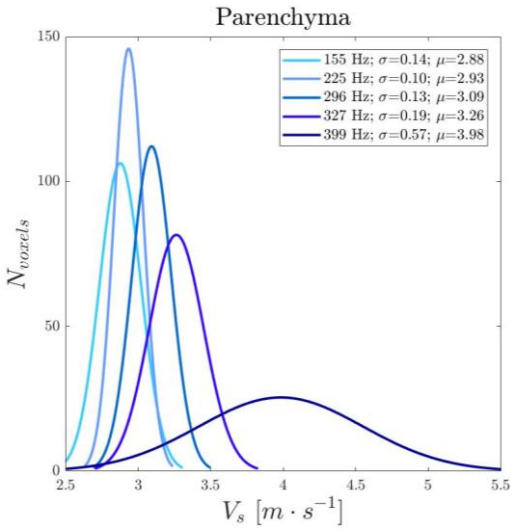

Figure 3.3.3: Gaussian fits of the shear velocity histograms at five excitation frequencies {155,225,296,327,399} Hz in the breast parenchyma. The measurement precision on the shear velocity is worst at 399 Hz and best between 155 Hz and 296 Hz.

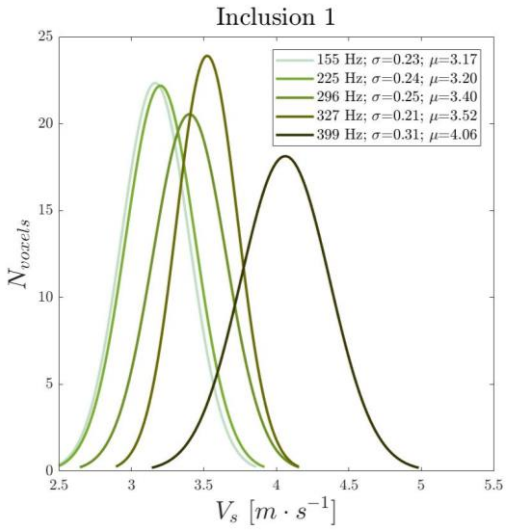

Figure 3.3.4: Gaussian fits of the shear velocity histograms at five excitation frequencies {155,225,296,327,399} Hz in the inclusion 1. The measurement precision on the shear velocity is worst at 399 Hz and best between 155 Hz and 327 Hz.

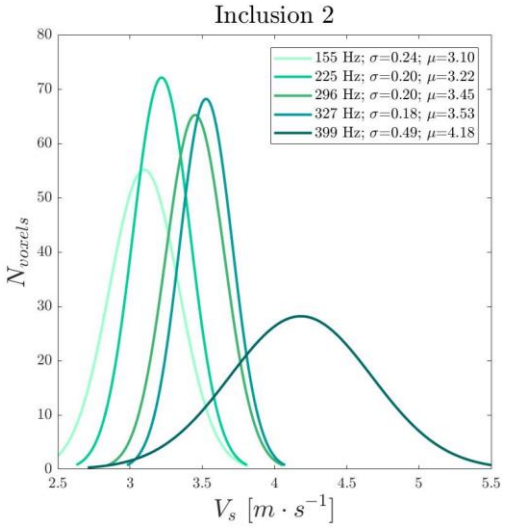

Figure 3.3.5: Gaussian fits of the shear velocity histograms at five excitation frequencies {155,225,296,327,399} Hz in inclusion 2. The measurement precision on the shear velocity is worst at 399 Hz and best between 225 Hz and 327 Hz.

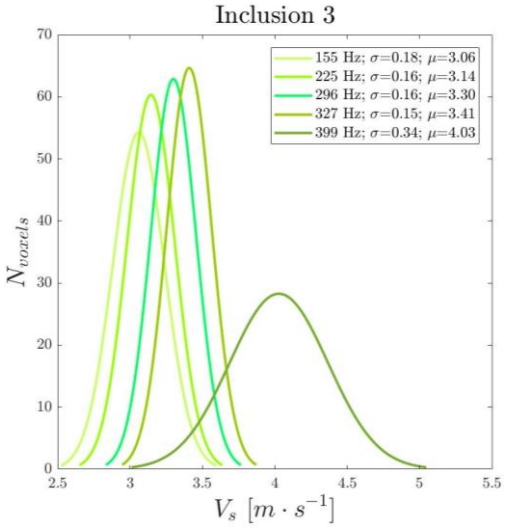

Figure 3.3.6: Gaussian fits of the shear velocity histograms at five excitation frequencies {155,225,296,327,399} Hz in inclusion 3. The measurement precision on the shear velocity is worst at 399 Hz and best between 225 Hz and 327 Hz.

3.3.2 MRE discrimination power

Shear velocity histograms are represented for the four regions of interest and the five excitation frequencies in Figure 3.3.7 (1)-(3).

The breast phantom parenchyma is mechanically different from the inclusions with statistical significance ($p < 10^{-3}$) for every excitation frequency but 399 Hz. At 399 Hz, MRE measurements stand outside the optimal domain except for inclusion 1, which remains statistically different from the parenchma with $p \simeq 0.6$ (Figure 3.3.7 (1)).

The shear velocity peak-to-peak differences of the Gaussian fits, δV_{pp}, between the breast parenchyma and the inclusions exhibit different values with the excitation frequency. The higher median differences stand between 155 Hz and 296 Hz for inclusion 1 with $\delta V_{pp} = 0.39\ \mathrm{m \cdot s^{-1}}$ at 155 Hz and 225 Hz. It is at 296 Hz for inclusion 2 with $\delta V_{pp} = 0.46\ \mathrm{m \cdot s^{-1}}$ and at 225 Hz for inclusion 3 with $\delta V_{pp} = 0.21\ \mathrm{m \cdot s^{-1}}$.

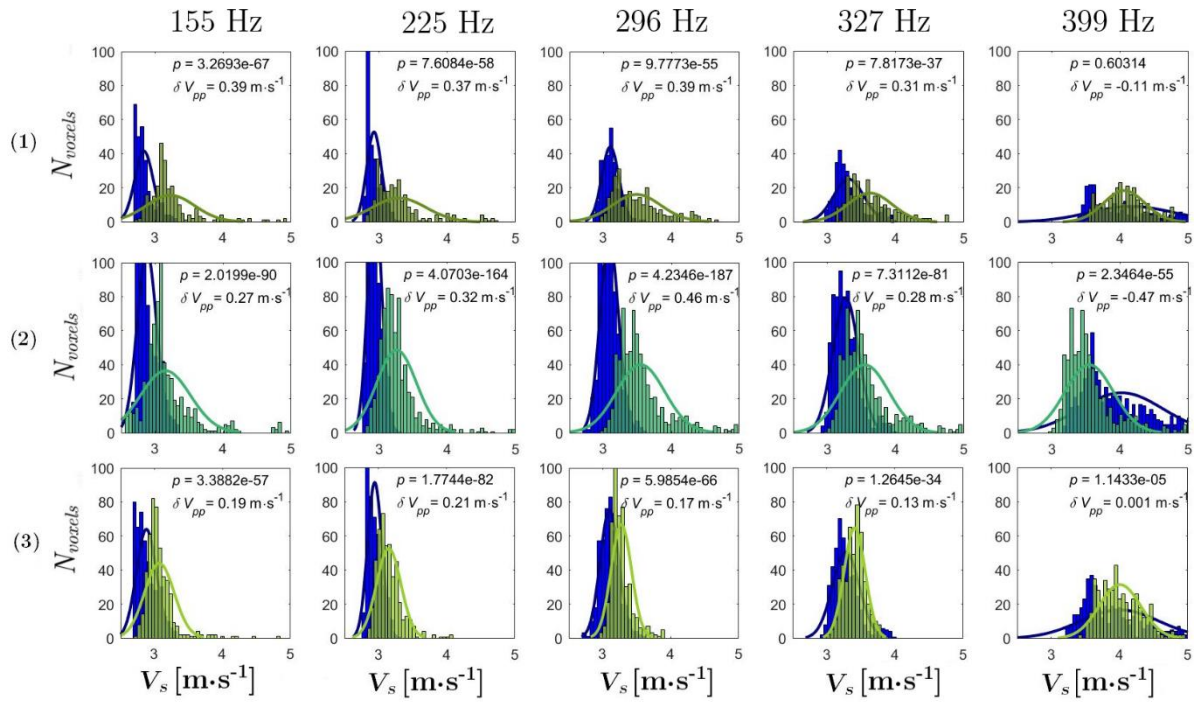

Figure 3.3.7: Voxel-wise velocity distributions in the breast parenchyma (blue) and inclusion 1 (first row in khaki), inclusion 2 (second row in sea green), and inclusion 3 (third row in lime). The sizes of the selected region in the breast parenchyma were adapted to the size of the inclusions for running Wilcoxon tests and histogram analyses. The best compromise to mechanically discriminate the different regions and to determine the shear velocity with minimal standard deviation is reached at 296 Hz for the three inclusions. δV_{pp} is the shear velocity peak-to-peak of the Gaussian fits and p is the p-value associated to the Wilcoxon tests ($p < 10^{-3}$ allow to conclude that the difference between the population median and the hypothesized median is statistically significant).

3.3.3 Discussion

This study was implemented in a heterogeneous breast phantom originally developed by CIRS for biopsy training. The phantom was not necessarily purely elastic but its viscosity was neglected in the framework of this study. MRE shear velocity measurements were found different in the breast parenchyma and the three selected inclusions. The differences were small though as this phantom was not especially intended for tissue mechanical characterization. It is not ideal to show the importance of performing discriminative MRE within the optimal s domain. However, this limitation allowed to model early concrete clinical cases where the disease is not fully developed and the tissue mechanical alteration is still light in the pathological tissue.

As demonstrated in Chapter 1, the quality factor Q depends on the amplitude of the rotational of the displacement field and the associated measurement uncertainty, namely indirectly on the total amplitude A of the displacement field and the SNR. It can

be noticed in the graphs of Figure 3.3.2 and in the mean $\langle Q \rangle$ values listed in Table 3.2.1 that the quality factor is not constant over the excitation frequency range whereas the mean SNR values remain similar (Table 3.2.1). Therefore, the variation of the quality factors with the excitation frequency is almost due to the applied sound level pressure and the resulting wave amplitude at the different frequencies (Table 3.2.1 and Figure 3.3.1). Care was not really taken to ensure a constant excitation pressure at the surface of the breast phantom. However, this experimental limitation sustains the robutsness of the optimal domain approach, which matters more in the given range of SNR and A than the SNR and A themselves. The analysis with a Gaussian model may be unsatisfactory here as the shear velocity distributions are noisy and not necessarily normal as the goodness of the fits suggested not only visually but also statistically with small p-values ($p < 10^{-3}$) obtained with the test on normal law. Nevertheless, it was still possible to determine, with a voxel size of $a = 2$ mm, an optimal frequency domain for the breast phantom parenchyma ($155\,Hz \leq f_{exc} \leq 296$ Hz), for inclusion 1 ($155\,Hz \leq f_{exc} \leq 327$ Hz), and for the inclusions 2 and 3 ($225\,Hz \leq f_{exc} \leq 327$ Hz).

These slightly different MRE optimal domains involve a necessary compromise between them to best mechanically discriminate the regions of interest: The pair regional velocity distributions must be as narrow as possible (ideally both in their optimal domains) while their respective mean values must be spread apart as much as possible (with the largest δV_{pp}). Here, even if s was reasonably in the optimal domain at 225 Hz for the four regions of interest ($\boldsymbol{s_{BP} = 6.5 \pm 0.2}$; $\boldsymbol{s_{inc.1} = 7.4 \pm 1.1}$; $\boldsymbol{s_{inc.2} = 7.4 \pm 1.1}$; $\boldsymbol{s_{inc.3} = 7.0 \pm 0.4}$), the shear velocity voxel values between the parenchyma and the inclusions could be best differentiated at 296 Hz where $\boldsymbol{s_{BP} = 5.3 \pm 0.2}$; $\boldsymbol{s_{inc.1} = 6.0 \pm 0.6}$; $\boldsymbol{s_{inc.2} = 6.1 \pm 1.0}$; $\boldsymbol{s_{inc.3} = 5.5 \pm 0.3}$ and $\delta V_{pp} = 0.39\ \mathrm{m \cdot s^{-1}}$ for inclusion 1, $\delta V_{pp} = 0.46\ \mathrm{m \cdot s^{-1}}$ for inclusion 2, and $\delta V_{pp} = 0.17\ \mathrm{m \cdot s^{-1}}$ for inclusion 3. Henceforth, MRE measurements should be carried at 296 Hz to favour tissue discrimination.

3.4 Conclusion

MRE data were acquired in a heterogeneous breast phantom over a range of frequencies (155 Hz-399 Hz) covering the optimal s conditions for a voxel size of $a = 2$ mm in three targetted inclusions and the surrounding parenchyma. This study showed the expected shift of the shear velocity distribution towards higher mean values when the excitation frequency increased while the velocity distributions spread away when the optimal conditions were degraded at lower and higher frequencies.

Despite the small mechanical differences between heterogeneous regions, we could significantly discriminate them by MRE over different frequency ranges ($155\ \mathrm{Hz} \leq f_{exc} \leq 327\ \mathrm{Hz}$) within the different optimal domains. Tissue discrimination could be found

optimal at $f_{exc} = 296$ Hz by compromising the MRE shear velocity measurement uncertainty in the different tissues and the shear velocity gap between them. Outside the optimal domains for the breast phantom parenchyma and the inclusions, above 327 Hz and below 155 Hz, MRE measurement uncertainties are so degraded – with shifted and spread shear velocity distributions – that characterization and discrimination of *healthy* and *diseased* tissues become unachievable. In a MRE clinical setting at typically 60 Hz, both tissues would be indistinguisable with mixed low shear viscoelastic moduli in the same as shown here at 399 Hz in Figure 3.3.1. Even retrospective resampling could not cope with the ill-condtionned problem as keeping the product $f_{exc} \cdot a$ would require, with $f_{exc} = 60$ Hz downsampling at $a = 7.5$ mm, which would result in detrimental spatial smearing by leaving us with only a couple of voxels per inclusion at most.

Chapter 4 Optimal conditions for brain MRE

4.1 Introduction

We saw in the previous chapters the multiple dependence of the MRE results on acquisition parameters and reconstruction methods (Chapter 2 and Chapter 3). The approximations of homogeneity previously carried out on phantoms (Chapter 2) are a priori questionable in a structured and complex organ such as the brain.

In the animal brain, post-mortem MRE [139] and in vivo MRE [16], [140] revealed different viscoelastic regions through the brain. In the case of post-mortem MRE, a stiffness increase of the brain tissue was found and, according to Weickenmeier et al. [139], this phenomenon is probably a manifestation of alterations in polarization, oxidation, perfusion, and metabolism immediately after death. These expected findings support the importance of characterizing brain tissue in vivo and question the relevance of ex vivo brain tissue testing as a whole.

In the human brain, several groups probed the mechanical parameters of the different brain regions with MRE [6], [16]–[18], [20], [21], [24]–[26], [28]. Brain white matter is composed of anisotropic myelin fibers, which foster the transmission of the electrical signals along the axons. Brain grey matter is mainly located at the periphery of the brain. It is the cortical tissue that contains the cell bodies of neurons. White matter is consequently expected to be more rigid than grey matter. However, as we saw in the previous Chapter 1 Figure h, the mechanical parameters reported in white and grey matters by the different research groups are widely dispersed. The viscoelastic parameters obtained for two different anatomical regions of the brain were found both too close and too dispersed to be significantly different [16], [17]. For instance, in the study by Clayton et al. , the mean shear elasticity modulus obtained at 60 Hz was (3.3 ± 0.1) kPa in the white matter and (3.1 ± 0.3) kPa in the grey matter which, given the closeness of the values and the associated standard deviations, does not allow any mechanical differentiation of the structures based on their shear elasticity as claimed since the first MRE measurements were initiated in the brain [55].

Previously, in Chapter 2 and Chapter 1, we have shown the importance of adapting the frequency of the mechanical excitation wave to the mechanical type of analyzed tissue in order to obtain the most accurate and precise measurement of the mechanical parameters. The main objectives of this chapter is to determine whether such optimal conditions could be found for brain MRE and to test the sensitivity of MRE to actually detect anatomical structures within the brain. For that purpose, the viscoelastic

properties of a human brain were determined in three different segmented regions (white matter, WM, grey matter, GM, and cerebellum, $Cblum$). Optimal spatial sampling conditions were regionally explored with multifrequency MRE acquisitions so data could eventually be conditioned for each segmented anatomical brain regions.

This chapter is divided into three parts. The first part is a presentation of the MRE protocol with a description of the human brain acquisitions. Then, the second part is a description of the process to extract the mechanical parameters, from MRE acquisition to MRE reconstruction. The third part compares regionally segmented MRE outcomes obtained at four different excitation frequencies. The optimal sampling conditions are determined in each of the segmented regions of the brain to produce the most precise and accurate measurements therein.

4.2 Methods

4.2.1 MRE setup

In the framework of Marion Tardieu's PhD work [74], in vivo acquisitions were carried out on a healthy volunteer on a 1.5 T Achieva system using a standard SENSE head coil (Philips Healthcare, Best, The Netherlands). The mechanical excitation systems used for the brain generally tend in the literature to induce mechanical waves through the brain protective barriers: cranial vault, cranial floor, and meninges [66]. These physical barriers yield mechanical wave attenuation in deep brain tissue which could lead to an underestimation of the measurements when the amplitude wave is too weak (Figure 4.2.4).

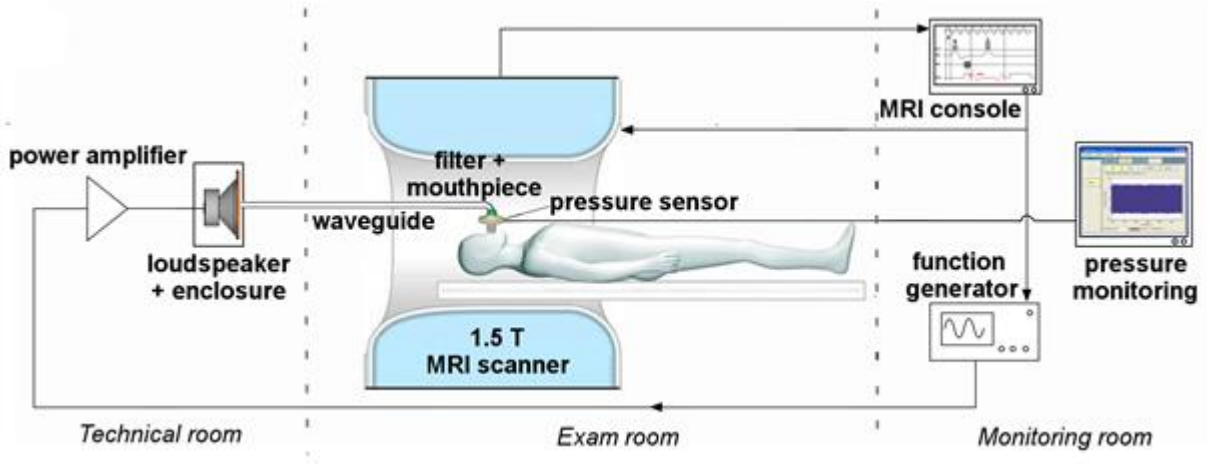

Figure 4.2.1: Schematic of the MRE setup on a Philips Achieva MRI 1.5 T from Marion Tardieu's PhD work [74]. Remotely generated and amplified pressure waves are guided in the center of the MRI magnet bore to the volunteer placed in a head coil. Pressure level is monitored via an optical fiber sensor. Pressure waves are synchronized to the MRI acquisitions sequence.

In this work, pressure waves were generated by a loudspeaker and guided directly into the subject's oral cavity to circumvent this limitation (Figure 4.2.1). These pressure waves were then guided to the brain along the brain stem while the subject was spontaneously breathing through the nose with a closed uvula. The efficacy of this technique was shown by Maître et al. [100] and Hagot et al. [101] with wave amplitudes up to 70 µm and average amplitudes over the whole brain up to 14 µm.

During MRE acquisitions, sinusoidal waves were generated by a function generator (AFG 3021B, Tektronix, USA, Figure 4.2.2.(a)), then amplified (P2500S, Yamaha, Hamamatsu, Japan, Figure 4.2.2.(b) 1) to be finally transformed into acoustic pressure waves by a loudspeaker placed in a wooden enclosure (12NW100, B&C Speakers, Bagno A Ripoli, Italy, Figure 4.2.2.(b) 2). The acoustic wave was guided to the oral cavity using an Altuglas® waveguide (Altuglas, La Garenne-Colombes, France), 3.5 m long and 22 mm internal diameter (Figure 4.2.2.(b) 3) and an antibacterial filter and an adaptation part or mouthpiece (Intersurgical, Wokingham, United Kingdom).

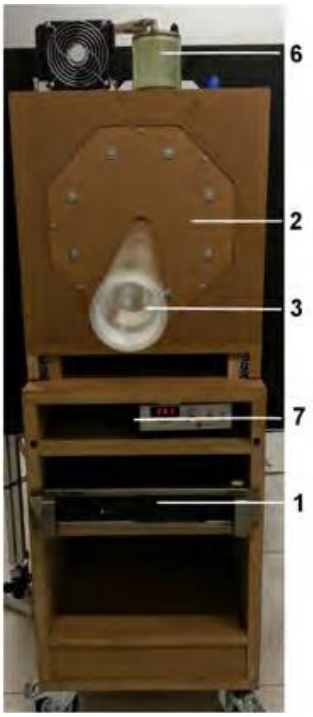

(a) (b)

Figure 4.2.2: Guided pressure wave generation: Mechanical vibrations are induced in the brain by guided pressure waves, remotely generated by an enclosed subwoofer (2) connected to a power amplifier (1), driven from the console room by a function generator (a). The subwoofer is cooled down (6) and its temperature is monitored (7). The system is placed in a rolling cabinet (b) in the technical room, behind the examination room. Pressure waves are transmitted to the subject's buccal cavity by a waveguide (3) through an antibacterial filter and a mouthpiece.

4.2.2 MRE acquisitions parameters

Before MRE acquisitions, the acoustic resonances of the wave-guiding close system were characterized by wobulation from 10 Hz to 500 Hz. The amplitude of the pressure waves was set for each frequency to provide, from the MR-phase images, easily and qualitatively measurable waves throughout the brain while preserving the subject's comfort. The spatial sampling factor s was studied over four frequencies $f_{exc} = \{43; 50; 84; 113\}$ Hz with an isotropic voxel size, $a = \{2.75; 3.00; 2.94; 2.75\}$ mm.

f_{exc} [Hz]	43	50	84	113
a [mm]	2.75×2.75×2.75	2.67×2.67×3.00	2.94×2.94×2.94	2.75×2.75×2.75
$FOV_x \times FOV_y \times FOV_z$	264×264×118	256×256×129	235×235×147	264×264×118
N_{MEG}	2	2	2	4
N_{dyn}	8	8	4	8
TR/TE [ms/ms]	5000/70	4301/70	2976/42	3803/49
TA / encoding direction	37 min 30 s	28 min 50 s	11 min 12 s	28 min 31 s

Table 4.2.1: Acquisition parameters for the standard MRE spin echo sequence at frequency $f_{exc} = \{43,50,84,113\}$ Hz. f_{exc}: excitation frequency, a: voxel size, $\mathrm{FOV_x} \times \mathrm{FOV_y} \times \mathrm{FOV_z}$: field of view, N_{MEG}: number of MEG, N_{dyn}: number of dynamic, TR/TE: repetition and echo times, TA: acquisition time per encoding direction.

A standard multi-slice motion-encoding spin-echo sequence was implemented with a field of view covering the whole brain with the parameters reported in Table 4.2.1. The amplitude of the motion-encoding gradients was 21.5 mT · m^{-1}. The number of bipolar motion encoding gradients N_{MEG} was limited to 2 except for the highest excitation frequency $f_{exc} = 113$ Hz increased twofold to partially compensate for the reduction of the wave amplitude with the frequency. As reported in Table 4.2.1, the echo time TE ranged between 42 ms and 70 ms, while the repetition time ranged roughly between 3000 ms and 5000 ms.

4.2.3 MRE reconstruction

As explained in Chapter 3 and Chapter 4, the components of the 3D displacement field u_i (r, t), with $i = \{x, y, z\}$, of a voxel located at r and taken at time t were computed from the recorded MRI phase values $\varphi_i(\mathbf{r}, t)$ (equation 1.23) for the four MRE acquisitions. The Q-weighted average velocity V_s and the quality factor Q were calculated according to the equation 1.71 and equation 1.72.

As the brain is assumed to be viscoelastic, the Helmholtz equation reported in the equation 1.59 for a locally homogeneous isotropic viscoelastic medium was used to reconstruct the shear dynamic, G_i', and loss, G_i'', moduli from the complex shear moduli G^* along each spatial dimension i before being averaged for each voxel. In this study, a model-independent approach developed by Sinkus et al. [4] was used to calculate the complex shear modulus which can be written as:

$$G^* = -\rho\omega_{exc}^2 \frac{q_i(r, \omega_{exc})}{\nabla^2 q_i(r, \omega_{exc})} \qquad 4\text{-}1$$

The local planar wave assumption used for the displacement field and thus also for each q-field component, q_i, can be written as:

$$q_i = |q_i| \cdot e^{k_i \cdot r_i}, \qquad 4\text{-}2$$

where:

- $k_i = \beta_i - j\alpha_i$ is the complex wave number
- $\beta_i = \frac{\omega_{exc}}{V_s}$ with V_s the quality Q-weighted shear velocity (equation 1.72).
- α_i the attenuation parameter

The equation 4-1 can be written as:

$$G^* = G_i' + jG_i'' = \frac{\rho\omega_{exc}^2}{k_i^2} = \frac{\rho\omega_{exc}^2}{(\beta_i - j\alpha_i)^2} \qquad 4\text{-}3$$

The shear dynamic, G_i', and loss, G_i'', moduli can be inferred by:

$$G_i' = \rho\omega_{exc}^2 \frac{{\beta_i}^2 - {\alpha_i}^2}{\left({\beta_i}^2 - {\alpha_i}^2\right)^2 + 4(\alpha_i\beta_i)^2} \qquad 4\text{-}4$$

$$G_i'' = \rho\omega_{exc}^2 \frac{2\alpha_i\beta_i}{\left({\beta_i}^2 - {\alpha_i}^2\right)^2 + 4(\alpha_i\beta_i)^2} \qquad 4\text{-}5$$

Additional T_1-weighted whole brain images were used as anatomical references (Figure 4.2.1). They were segmented and registered to the MRE magnitude images with SPM12 *(The Wellcome Centre for Human Neuroimaging, UCL, London, United-Kingdom)* and masks of white matter (black blue), grey matter (blue), and cerebellum (light blue) were inferred after removal of CSF, bone, background tissue and air (Figure 4.2.3).

Figure 4.2.3: Sagittal view of T1-Weighted map from which white matter, WM in black blue, grey matter, GM in blue, and cerebellum, $Cblum$ in light blue, were segmented and associated masks were extracted.

MRE data were reconstructed to extract maps of the signal-to-noise ratio, SNR, the displacement fields, A, the quality factor, Q, the shear velocity, V_s, and the shear viscoelastic moduli, G' and G''. Every map was eventually registered to the T_1-weighted image acquired together with the MRE at 113 Hz with the smallest FOV.

Finally, masks of the brain parenchyma were eroded by six voxels to exclude possible reconstruction biases at the boundaries before their intersection so 17,573 voxels in the white matter, 20,341 voxels in the grey matter and 3109 voxels in the cerebellum were used for final data analysis.

SNR mean values were calculated over the brain parenchyma for comparison purposes between the four MRE acquisitions. Both the mean value and the standard deviation of the amplitudes of the generated displacement fields, $\langle A \rangle$ and σ_A, were considered at every excitation frequency in order to evaluate the inhomogeneous wave amplitude throughout the subject's brain.

As the brain is expected to be mechanically inhomogeneous, mean values, $\langle Q \rangle$, $\langle V_s \rangle$, $\langle G' \rangle$ and their associated standard deviations were calculated over the whole brain parenchyma and over each segmented region (white matter, grey matter and cerebellum) to exhibit, in each segmented region, the related uncertainty of the MRE acquisition and reconstruction.

4.2.4 Data analyses

Maps of SNR, A, Q, V_s, G' and G'' were plotted for the four excitation frequencies $f = \{43, 50, 84, 113\}$ Hz in the axial, sagittal, and coronal planes of the subject's brain.

The voxel-by-voxel mechanical behavior was studied with respect to the quality factor Q for each excitation frequency in the three segmented regions of the brain (white matter, grey matter and cerebellum).

Strong enough pressure waves are required in order ensure stable and linear MRE outcomes. As showed with the dataset acquired in the framework of Marion Tardieu's PhD work [74] a low displacement field amplitude, A, and therefore low data quality, Q, leads to underestimated measured values. To avoid this estimation bias, it is possible to establish a threshold either on the uncertainty-normalized amplitude, UNA, [141] or, more adequately, on the data quality, Q, such that, above $Q_{threshold}$, MRE results could be fairly considered as valid. Below $Q_{threshold}$, MRE results were discarded. $Q_{threshold}$ was defined on the voxel-wise shear velocity distribution when the initial increasing trend of the upper envelop is reversed, that is when the shear velocity values are not governed anymore by the increasing data quality.

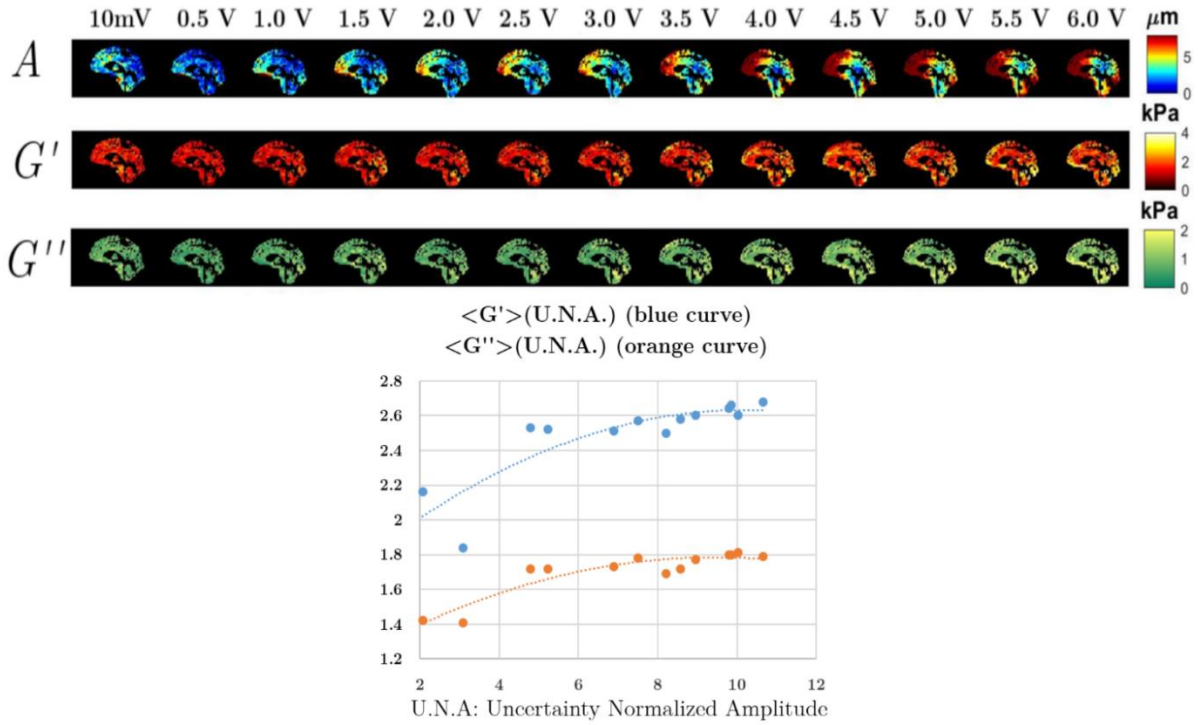

Figure 4.2.4: Amplitude A, shear elasticity G' and viscosity G'' maps in the brain of a healthy subject in the sagittal plane. MRE data were acquired at 87 Hz. The wave amplitude was adjusted via the function generator amplitude from 0.01 V to 6 V. Mean shear elasticity G' and viscosity G'' were plotted as function of the uncertainty-normalized amplitude UNA, which is the ratio between the total amplitude and the measurement uncertainty of the total amplitude ($UNA = A/\Delta A$). Mean values of G' and G'' increase with the wave amplitude until a plateau is reached where their mean values are consistent [141].

Statistical analyses were performed using the shear velocity mean values, $\langle V_s \rangle$, and the shear elastic modulus $\langle G' \rangle$ as the primary outcomes. Boxplots of V_s and G' measurements were built in the cerebral white and grey matters, and in the cerebellum to, first, visually represent the regional means and the related standard deviations of the datasets and, then, to compare the mechanical behavior in each of the three segmented brain regions, both within and between experiments conducted with differing acquisition and reconstruction conditions. Non-parametric unpaired two-samples Wilcoxon tests were performed within Matlab. A result was deemed statistically significant if the probability was lower than 1% or p-value < 0.01.

4.3 Results

4.3.1 MRE outcomes

The SNR maps were rather homogeneous for every excitation frequency (Figure 4.3.1, Figure 4.3.2, and Figure 4.3.3). Different TR and TE values between the four MRE acquisitions led to different mean SNRs values ranged between 34 at 43 Hz and 102 at 84 Hz. They were expectedly higher for longer TRs and shorter TEs as reported in Table 4.2.1.

f_{exc} [Hz]	43	50	84	113
$\langle SNR \rangle_{Brain}$	34	95	102	45
$\langle A \rangle_{Brain}$ [µm]	9.4 ± 4.7	12.3 ± 6.1	3.4 ± 1.6	4.3 ± 2.8
$\langle Q \rangle_{Brain}$	460 ± 255	1511 ± 887	167 ± 144	181 ± 197
V_{Brain} [m·s^{-1}]	1.46 ± 0.32	1.57 ± 0.31	1.99 ± 0.19	2.14 ± 0.21
s_{Brain}	16.8 ± 2.7	14.9 ± 2.3	8.1 ± 0.8	6.4 ± 0.7
V_{WM} [m·s^{-1}]	1.46 ± 0.34	1.55 ± 0.33	2.09 ± 0.20	2.15 ± 0.21
s_{WM}	17.7 ± 2.9	13.4 ± 2.5	8.5 ± 0.8	6.7 ± 0.7
V_{GM} [m·s^{-1}]	1.47 ± 0.29	1.59 ± 0.29	1.97 ± 0.18	2.14 ± 0.21
s_{GM}	16.7 ± 2.5	14.2 ± 2.1	8.0 ± 0.7	6.3 ± 0.7
V_{Cblum} [m·s^{-1}]	1.19 ± 0.29	1.30 ± 0.17	1.92 ± 0.32	2.13 ± 0.40
s_{Cblum}	11.0 ± 2.5	9.4 ± 1.2	5.3 ± 1.3	4.2 ± 1.3
G'_{Brain} [kPa]	1.38 ± 0.46	1.57 ± 0.47	3.08 ± 0.57	3.52 ± 0.67
G'_{WM} [kPa]	1.34 ± 0.48	1.50 ± 0.48	3.13 ± 0.60	3.56 ± 0.68
G'_{GM} [kPa]	1.44 ± 0.43	1.64± 0.45	3.01 ± 0.53	3.46 ± 0.66
G'_{Cblum} [kPa]	0.94 ± 0.33	1.17 ± 0.37	2.74 ± 0.87	3.44 ± 1.06
G''_{Brain} [kPa]	1.02 ± 0.51	1.18 ± 0.55	1.78 ± 0.53	2.07 ± 0.66
G''_{WM} [kPa]	1.02 ± 0.52	1.16 ± 0.56	1.76 ± 0.56	2.00 ± 0.67
G''_{GM} [kPa]	1.02 ± 0.51	1.21 ± 0.54	1.80 ± 0.51	2.15 ± 0.63
G''_{Cblum} [kPa]	0.79 ± 0.35	0.78 ± 0.27	1.60 ± 0.68	1.88 ± 0.94

Table 4.3.1: MRE outcomes in the whole brain ($Brain$), the cerebral white matter (WM in dark blue), the cerebral grey matter (GM in blue), and the cerebellum ($Cblum$ in light blue) at excitation frequencies $f_{exc} = \{43,50,84,113\}$ Hz. f_{exc}: excitation frequency, s: sampling factor or number of voxels per wavelength, SNR, A: displacement field amplitude, Q: quality factor, V_s: shear velocity, G': shear elasticity, and G'': shear viscosity. MRE optimal conditions (in red) are achieved for the cerebrum for both white and grey matters at $f_{exc} = 84$ Hz ($s \simeq 8\text{-}8.5$) and for the cerebellum at $f_{exc} = 50$ Hz ($s \simeq 9.4$).

Total amplitudes of the displacement fields ranged on average between (3.4 ± 1.6) µm at 84 Hz and (12.3 ± 6.1) µm at 50 Hz where they can reach 46.5 µm. Mean values $\langle A \rangle$ and $\langle Q \rangle$ were roughly twice higher at 43 Hz and 50 Hz than at 84 Hz and

113 Hz as reported in Table 4.3.1. $\langle Q \rangle$ values ranged between 167 at 84 Hz and 1511 at 50 Hz but they can reach around 2000 at 43 Hz, 84 Hz and 113 Hz and 6000 at 50 Hz.

A and Q maps reveal higher values in the frontal lobe (FL) ($\langle A \rangle_{FL} \approx \{10,20,5,9\}$ µm) and in the occipital lobe (OL) $\langle A \rangle_{FL} \approx \{10,15,5,5\}$ µm for $f_{exc} = \{43,50,84,113\}$ Hz). With the frequency-dependent wave attenuation, they fall deeper inside the brain ($\langle A \rangle \approx \{7,5,2,2\}$ µm for $f_{exc} = \{43,50,84,113\}$ Hz) (Figure 4.3.3). As illustrated in Figure 4.3.1 and Figure 4.3.2, A and Q maps exhibit maximal values at the tentorial surface of the cerebellum ($\langle A \rangle_{Tentorial\ Cb} \approx \{17,18,4,6\}$ µm for $f_{exc} = \{43,50,84,113\}$ Hz).

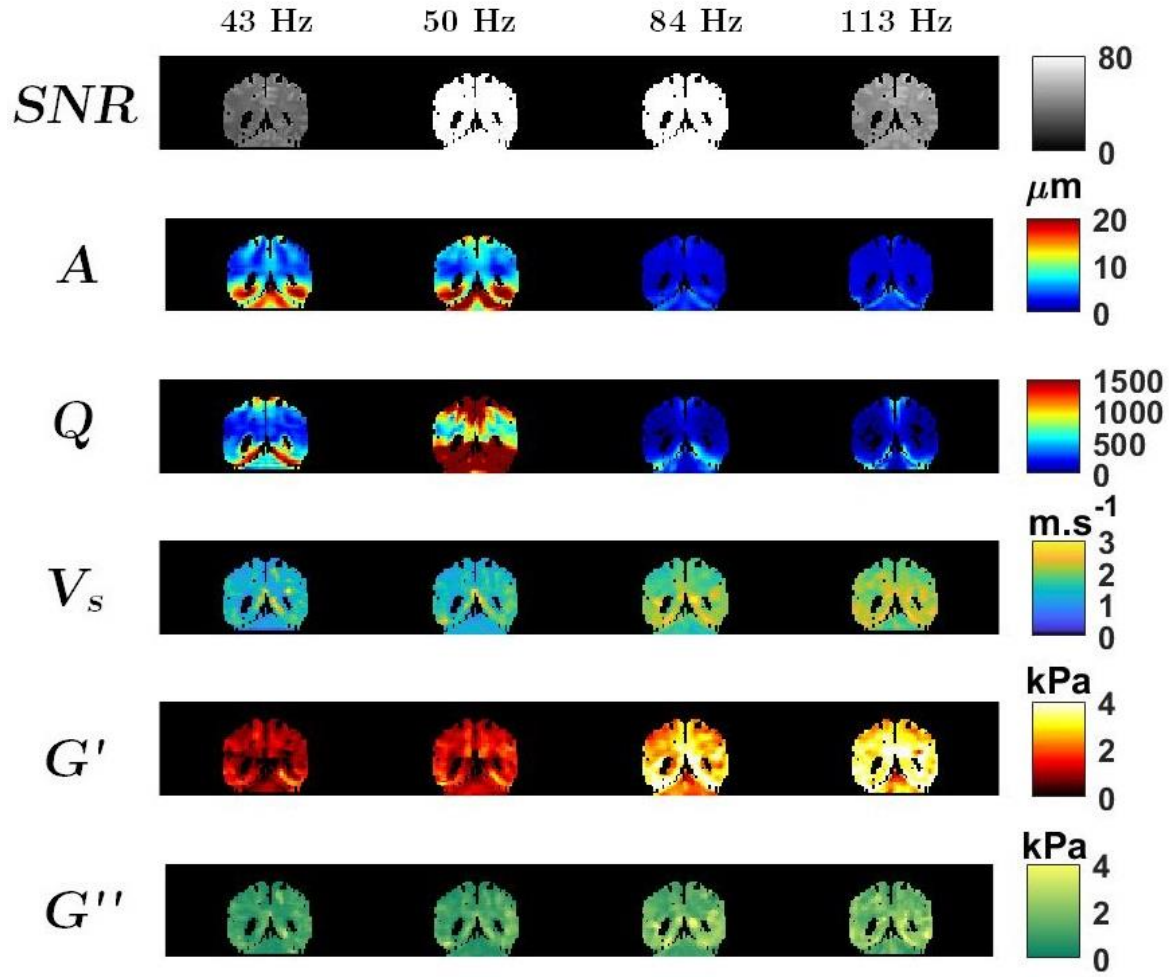

Figure 4.3.1: SNR, wave amplitude A, data quality Q, shear velocity V_s, shear elasticity G' and viscosity G'' maps in coronal slice number 65 from whole brain MRE at four excitation frequencies $f_{exc} = \{43,50,84,113\}$ Hz on one healthy subject. V_s, G', G'' values increase with the frequency. Frontal lobe, occipital lobe and the region above the tentorial surface of the cerebellum are more rigid and viscous.

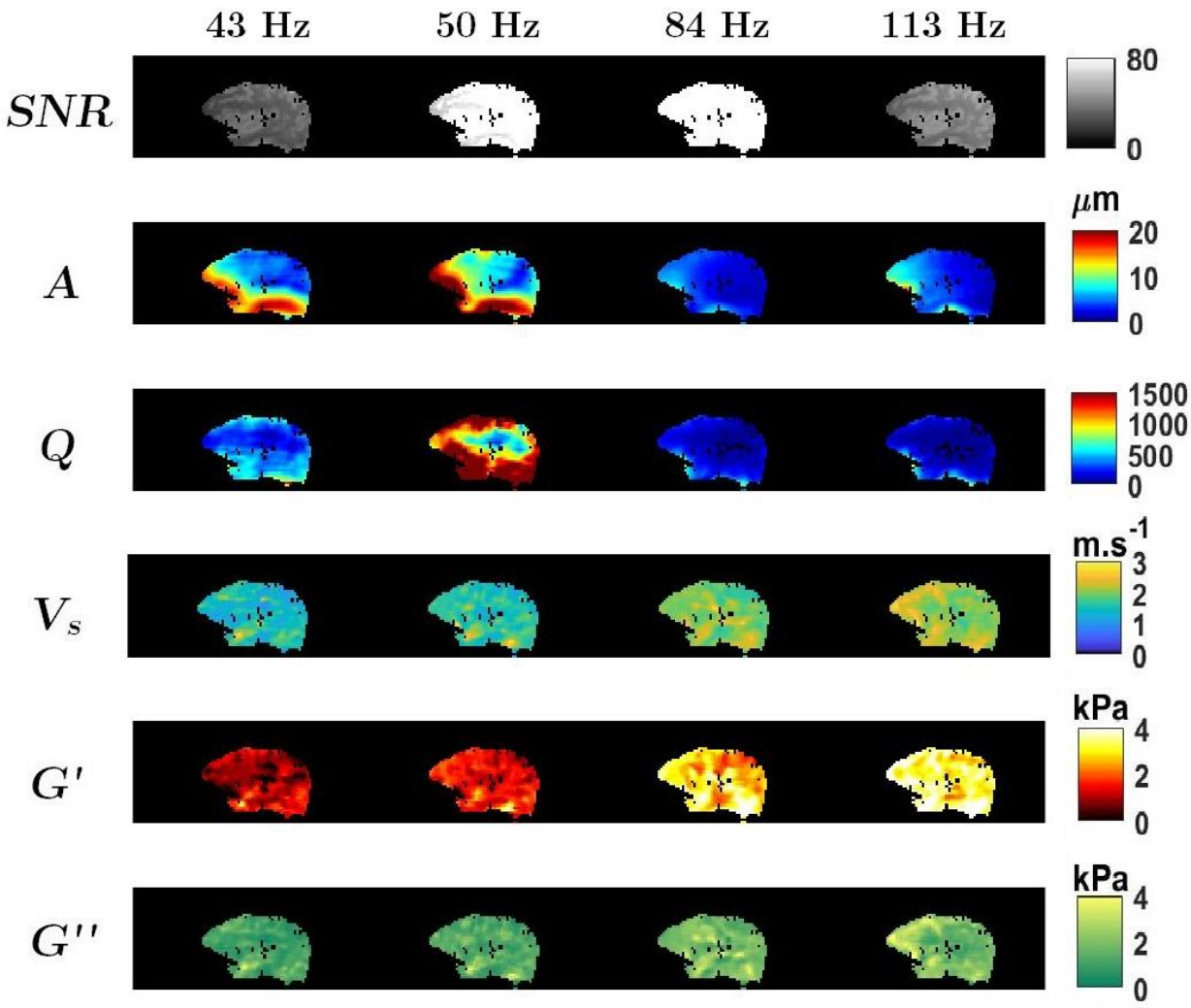

Figure 4.3.2: SNR, wave amplitude A, data quality Q, shear velocity V_s, shear elasticity G' and viscosity G'' maps in sagittal left brain at slice number 35 from whole brain MRE at excitation frequencies $f_{exc} = \{43,50,84,113\}$ Hz on one healthy subject. Mean values of V_s, G', G'' increase with the frequency. Frontal lobe, occipital lobe and the region above the tentorial surface of the cerebellum are more rigid and viscous.

The shear velocity, V_s, and the viscoelastic moduli, G' and G'', all increase with the excitation frequency everywhere throughout the brain. As reported in Table 4.3.1, the mean values $\langle V_s \rangle$, $\langle G' \rangle$ and $\langle G'' \rangle$ calculated in the brain respectively range from 1.45 ± 0.34 m·s^{-1} at 43 Hz to 2.13 ± 0.23 m·s^{-1} at 113 Hz, from 1.12 ± 0.45 kPa at 43 Hz to 3.41 ± 0.71 kPa at 113 Hz and from 1.02 ± 0.47 kPa at 43 Hz to 2.08 ± 0.74 kPa at 113 Hz. V_s exhibits higher values in the frontal lobe (1.58 ± 0.30 m·s^{-1} at 43 Hz to 2.25 ± 0.40 m·s^{-1} at 113 Hz) and in the region above the tentorial surface of the cerebellum (1.91 ± 0.40 kPa at 43 Hz to 2.28 ± 0.55 kPa at 113 Hz) as illustrated in the three planes of Figure 4.3.1, Figure 4.3.2 and Figure 4.3.3.

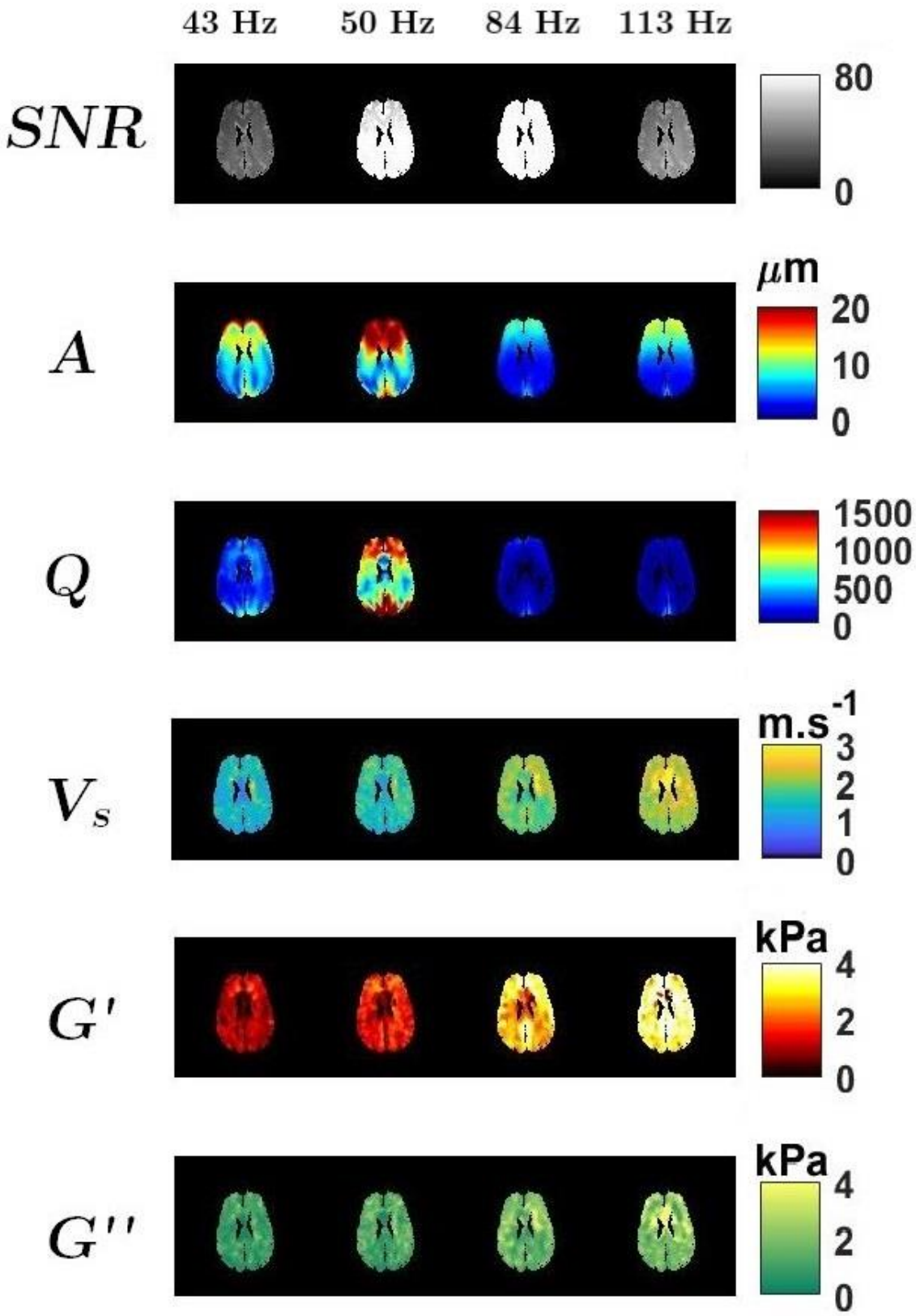

Figure 4.3.3: SNR, wave amplitude A, data quality Q, shear velocity V_s, shear elasticity G' and viscosity G'' maps in slice number 23 at axial direction from four spin echo sequences with the four excitation frequencies $f_{exc} = \{43,50,84,113\}$ Hz on one healthy subject. Mean values of V_s, G', G'' increase with the frequency. Frontal lobe,

occipital lobe and the region above the tentorial surface of the cerebellum are more rigid and viscous.

In Figure 4.3.4, the voxel-wise velocity, elasticity and viscosity distributions for the cerebral white matter (dark blue), the cerebral grey matter (blue) and the cerebellum (light blue) as a function of Q share a similar shape. They are asymmetric and present a wider dispersion towards higher mechanical values at low Q with strong correlation to Q. As Q increases, they get narrower and become symmetrical around a central value, which increases with the excitation frequency. Correlations to Q then vanish. In the cerebral tissues, away from the optimal conditions, either at lower ($f_{exc} = \{43,50\}$ Hz) or higher ($f_{exc} = 113$ Hz)frequencies, the velocity distributions are clearly more spread and exhibit higher values than in the optimal conditions ($f_{exc} = 84$ Hz). Similarly in the cerebellar tissues, the velocity distribution is narrower at 50 Hz and becomes wider at the other excitation frequencies.

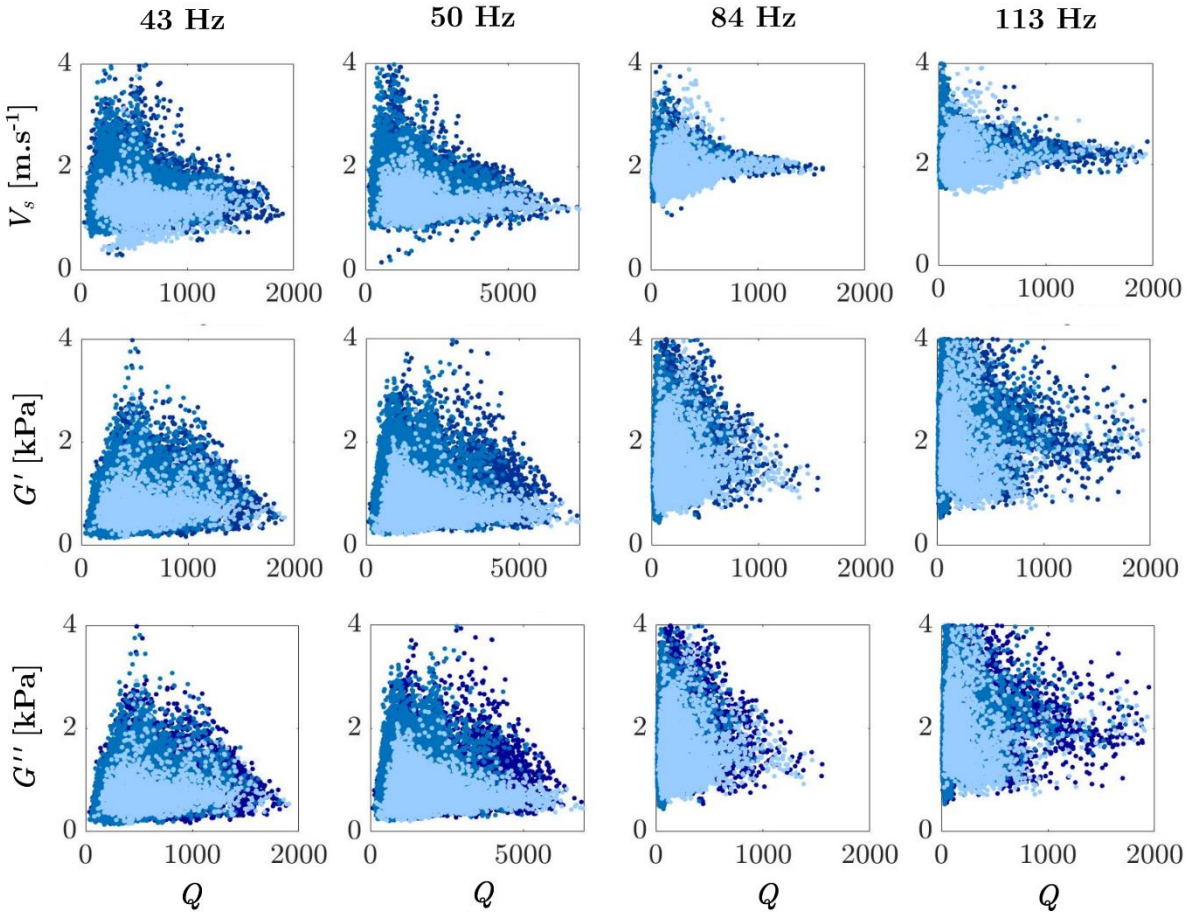

Figure 4.3.4: Brain MRE voxel-wise shear velocity V_s (upper row), G' (middle row), G''(bottom row) as a function of data quality Q in one healthy subject at excitation frequencies $f_{exc} = \{43,50,84,113\}$ Hz. V_s, G' and G'' values increase with the frequency. Velocity distributions are the narrowest at 84 Hz in the cerebellar white and grey

matter ($s_{WM}^{84\,\mathrm{Hz}} = 8.5 \pm 0.8$ and $s_{GM}^{84\,\mathrm{Hz}} = 8.0 \pm 0.7$) and at 50 Hz in the cerebellum ($s_{Cb}^{50\,\mathrm{Hz}} = 9.4 \pm 1.2$).

The mean values of the velocity, elasticity and viscosity distributions in each segmented regions all increase with f_{exc} (Table 4.3.1). The measured minimal shear velocity standard deviations in both cerebral white and grey matters occur at 84 Hz with $\sigma_{84\,\mathrm{Hz}}^{WM} = 0.20$ m · s^{-1} and $\sigma_{84\,\mathrm{Hz}}^{GM} = 0.18$ m · s^{-1}. The minimal shear velocity standard deviation in the cerebellum occurs at 50 Hz ($\sigma_{50\,\mathrm{Hz}}^{Cb} = 0.17$ m · s^{-1}) as clearly depicted below by the boxplots in Figure 4.3.5.(a).

The amplitudes of the mechanical waves and a fortiori the quality factors obtained between the different acquisitions are different but the shapes remain the same: the voxel-wise shear velocity converge for higher quality factors at 50 Hz with $Q_{max}^{50\,Hz} = 5000$ than at 43 Hz, 84 Hz and 113 Hz for $Q_{max}^{43\,Hz} = 2000$, $Q_{max}^{84\,Hz} = 1800$ and $Q_{max}^{113\,Hz} = 2000$.

The threshold values of quality factor for each excitation frequency were estimated at $Q_{threshold}^{43\,Hz} = 200$, $Q_{threshold}^{50\,Hz} = 1000$, $Q_{threshold}^{100\,Hz} = 100$ and $Q_{threshold}^{113\,Hz} = 100$ (Table 4.3.2). Despite an obvious increasing trend of the velocity upper envelop (Figure 4.3.4), the correlation coefficient $R(Q < Q_{threshold}, V_s)$ calculated between V_s and Q does not revealed any dependence of the velocity values with the data quality (Table 4.3.2).

f_{exc} [Hz]	$R(Q < Q_{threshold}, V_s)$	$Q_{threshold}$
43	0.0861	200
50	-0.0007	1000
84	-0.001	100
113	0.0472	100

Table 4.3.2: Correlation coefficient R between V_s and Q for $Q < Q_{threshold}$ and $Q_{threshold}$ for $f_{exc} = \{43,50,84,113\}$ Hz.

4.3.2 MRE inside and outside optimal conditions

Boxplots of the shear velocity, elasticity and viscosity represented for the cerebrum and the cerebellum in Figure 4.3.5.

In the cerebrum, the optimal conditions are best fulfilled at 84 Hz with $s_{84\,\mathrm{Hz}}^{Cbrum} \simeq 8.0\text{-}8.5$. As seen above, at this frequency, the shear velocity standard deviation is effectively minimal in the cerebral tissues, $\sigma_{84\,\mathrm{Hz}}^{Cbrum} = 0.18\text{-}0.20$ m · s^{-1}. For every excitation frequency, mean shear velocities are found to be roughly the same in the white and grey matters (Figure 4.3.5.(a)) whether or not the optimal conditions are fulfilled. Yet, at 43 Hz or 113 Hz, away from the optimal conditions with $s_{43\,\mathrm{Hz}}^{Cbrum} \simeq 16.7\text{-}17.7$ or $s_{113\,\mathrm{Hz}}^{Cbrum} \simeq 6.3\text{-}6.7$, the shear velocities are essentially indistinguishable ($p_{43\,\mathrm{Hz}}^{WM-GM} \simeq 0.006$ or $p_{113\,\mathrm{Hz}}^{WM-GM} \simeq 0.007$) between white and grey matters, even above $Q_{threshold}$: $\langle V_s \rangle_{43\,\mathrm{Hz}}^{WM} =$

(1.46 ± 0.34) m · s^{-1} and $\langle V_s \rangle_{43\,\mathrm{Hz}}^{GM} = (1.45 \pm 0.31)$ m · s^{-1}, $\langle V_s \rangle_{113\,\mathrm{Hz}}^{WM} = (2.15 \pm 0.21)$ m · s^{-1} and $\langle V_s \rangle_{113\,\mathrm{Hz}}^{GM} = (2.14 \pm 0.21)$ m · s^{-1} (Table 4.3.1). At 84 Hz, in the optimal condition range with $s_{84\,\mathrm{Hz}}^{Cbrum} \simeq 8.0\text{-}8.5$, the velocities in the cerebral tissues become significantly different ($p_{84\ Hz}^{WM-GM} \ll 0.001$) with $\langle V_s \rangle_{84\,\mathrm{Hz}}^{WM} = (2.09 \pm 0.20)$ m · s^{-1} and $\langle V_s \rangle_{84\,\mathrm{Hz}}^{GM} = (1.97 \pm 0.18)$ m · s^{-1}. This tissue discrimination remains significant at 50 Hz ($p_{84\ Hz}^{WM-GM} \ll 0.001$) but in a lesser extent and with larger relative standard deviations: $\sigma_{50\,\mathrm{Hz}}^{Cbrum} = 18\text{-}21\%$ instead of $\sigma_{84\,\mathrm{Hz}}^{Cbrum} \simeq 9\text{-}10\%$ (Table 4.3.3).

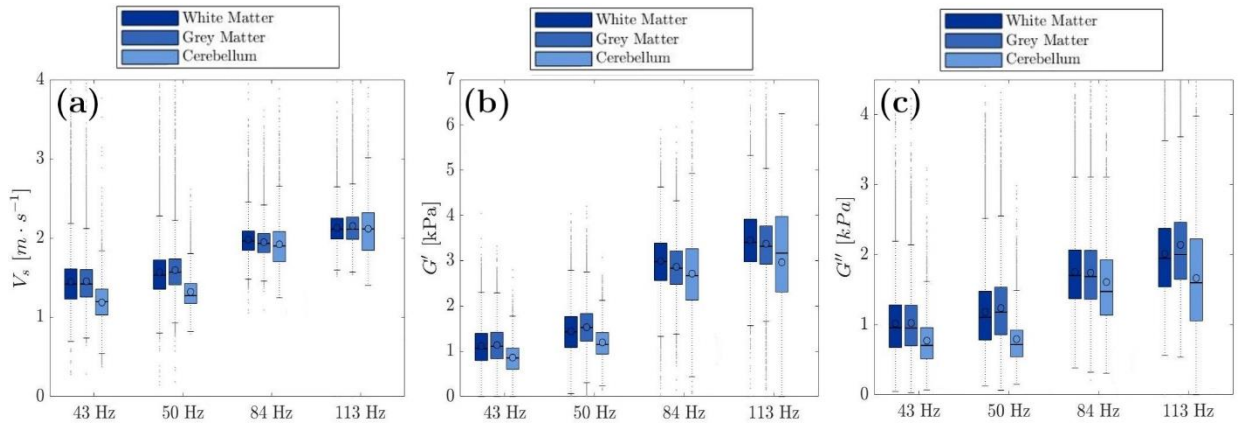

Figure 4.3.5: MRE shear velocity V_s (a), elasticity G' (b), and viscosity G'' (c) as a function of the excitation frequency, f_{exc}, in the cerebral white matter (dark blue), the cerebral grey matter (medium blue) and in the cerebellum (light blue). MRE optimal conditions are reached at $f_{exc} = 84$ Hz in the cerebrum and at $f_{exc} = 50$ Hz in the cerebellum where velocity measurement uncertainties are respectively minimized (a).

In the cerebellum, the optimal conditions are best fulfilled at 50 Hz with $s_{50\,\mathrm{Hz}}^{Cblum} \simeq 9.4$. It is then easier to mechanically discriminate the cerebrum and the cerebellum at 50 Hz than at the other excitation frequencies (Figure 4.3.5). Indeed, shear velocities significantly differ between the cerebellum and the cerebral white and grey matters ($p \ll 0.001$) with $V_{50\,\mathrm{Hz}}^{Cblum} = (1.30 \pm 0.17)$ m · s^{-1}, $\langle V_s \rangle_{50\,\mathrm{Hz}}^{WM} = (1.55 \pm 0.33)$ m · s^{-1} and $\langle V_s \rangle_{50\,\mathrm{Hz}}^{GM} = (1.59 \pm 0.29)$ m · s^{-1} (Figure 4.3.5.(a)). This tissue discrimination still holds at 43 Hz but with higher relative standard deviations than at 50 Hz: $\sigma_{43\,\mathrm{Hz}}^{Cbrum} \simeq 20\text{-}23\%$ and $\sigma_{43\,\mathrm{Hz}}^{Cblum} \simeq 24\%$ instead of $\sigma_{50\,\mathrm{Hz}}^{Cbrum} \simeq 18\text{-}21\%$ and $\sigma_{50\,\mathrm{Hz}}^{Cblum} \simeq 13\%$ (Table 4.3.3).

f_{exc} [Hz]	43	50	84	113
V_{WM} [m·s^{-1}]	1.46 ± 0.34	1.55 ± 0.33	2.09 ± 0.20	2.15 ± 0.21
s_{WM}	17.7 ± 2.9	13.4 ± 2.5	8.5 ± 0.8	6.7 ± 0.7
σ_{WM}	23.3%	21.3%	9.6%	9.8%
V_{GM} [m·s^{-1}]	1.47 ± 0.29	1.59 ± 0.29	1.97 ± 0.18	2.14 ± 0.21
s_{GM}	16.7 ± 2.5	14.2 ± 2.1	8.0 ± 0.7	6.3 ± 0.7
σ_{GM}	19.7%	18.2%	9.1%	9.8%
V_{Cblum} [m·s^{-1}]	1.19 ± 0.29	1.30 ± 0.17	1.92 ± 0.32	2.13 ± 0.40
s_{Cblum}	11.0 ± 2.5	9.4 ± 1.2	5.3 ± 1.3	4.2 ± 1.3
σ_{Cblum}	24.4%	13.1%	16.7%	18.8%

Table 4.3.3: Shear velocity in the cerebral white matter (WM in dark blue), the cerebral grey matter (GM in blue), and the cerebellum ($Cblum$ in light blue) at excitation frequencies $f_{exc} = \{43,50,84,113\}$ Hz. f_{exc}: excitation frequency, s: sampling factor or number of voxels per wavelength, σ: shear velocity relative standard deviation. MRE optimal conditions (in red) are achieved for the cerebrum for both white and grey matters at $f_{exc} = 84$ Hz and for the cerebellum at $f_{exc} = 50$ Hz where $6 \lesssim s \lesssim 9$ and σ is minimal.

4.4 Discussion

MRE was performed on the brain mechanically excited between 43 Hz and 113 Hz. The amplitude of the induced mechanical waves varied throughout the brain with the excitation frequency as the addressed acoustic modes change and because the input pressure level decreases and attenuation gets stronger in the viscous brain tissues at higher frequencies. It particularly affects the amplitude of the induced displacement fields in the deepest regions of the brain, as we can see around the lateral ventricles in the amplitude maps, A, and quality maps, Q, of Figure 4.3.1, Figure 4.3.2 and Figure 4.3.3.

The shear velocities and elasticities are expected to increase with the excitation frequency. This frequency dependence of the brain mechanical response is illustrated in the literature with shear elasticity values, G', in the grey matter that range between 2.8 kPa at 45 Hz and 4.4 kPa at 80 Hz [16]. Yet, the elasticities measured by the different research groups do not follow a general monotonically-increasing trend with the excitation frequency as reported in Table 4.4.1. Thus, higher values of the shear elasticity were measured in the grey matter at 45 Hz, $G'^{GM}_{45\,Hz} = 2.8$ kPa [16], than at 50 Hz, $G'^{GM}_{50\,Hz} = 1.9$ kPa [16], or even than at 80 Hz, $G'^{GM}_{80\,Hz} = 2.3$ kPa [18]. The modulus at 50 Hz turned to be smaller only than the one reported at 90 Hz: $G'^{GM}_{90\,Hz} = 3.1$ kPa [6]. MRE outcomes cannot reasonably be compared between different research groups when shear viscoelasticity moduli have been evaluated at different excitation frequencies with different reconstruction algorithms (LFE for [16], NLI (Non Linear Inversion) for [17] and AIDE [6] and [18]). Moreover, shear waves have been generated with different means and resulting displacement field amplitudes and patterns differ for every research group.

Indeed, as pointed out by Marion Tardieu in her PhD work [74] and reported in Figure 4.2.4, if the displacement field amplitude in the target organ is too low, the mechanical parameters are underestimated. It is not clear for every published work whether the displacement fields were induced in the brain with enough amplitude to reach the plateau where the mechanical parameters may be properly extracted, and thus, comparison between research groups, possible.

The optimal conditions determined here for the cerebral tissues with $a \simeq 2.94$ mm at 84 Hz are close to those achieved by Lynne Bilston' research group at 80 Hz [18] and at 90 Hz [6] with the same reconstruction algorithm. In their work, they explicitly made sure to roughly achieve $s \simeq 7$ with $a \simeq 3$ mm and $f_{exc} = 80\text{-}90$ Hz. Yet, they only acquired seven slices and the reported mean viscoelasticity moduli do not cover the whole cerebrum or cerebellum. Besides, at 90 Hz, they found significantly lower values in the cerebral white matter ($G'^{WM}_{90\,\mathrm{Hz}} \simeq 2.7$ kPa) than in the cerebral grey matter ($G'^{GM}_{90\,\mathrm{Hz}} \simeq 3.1$ kPa) whereas, at 80 Hz, they found the contrary with general lower values ($G'^{WM}_{80\,\mathrm{Hz}} \simeq 2.41$ kPa and $G'^{GM}_{80\,\mathrm{Hz}} \simeq 2.34$ kPa) (Table 4.4.1). On the basis of the available displacement fields in both references, we could assume that, at 90 Hz, the overall excitation amplitude was rather low except at the periphery of the organ so, deeper inside the brain, the data quality was degraded and viscoelastic moduli were more underestimated in the white matter. At 80 Hz, the overall excitation amplitude was more homogenous and tissues were effectively displaced in the center of the brain. They were able to mechanically differentiate white and grey matters according to the tissue structural expectations ($G'^{WM}_{80\,Hz} > G'^{GM}_{80\,\mathrm{Hz}}$) as well as cerebral and cerebellar tissues ($G'^{Cbrum}_{80\,\mathrm{Hz}} > G'^{Cblum}_{80\,\mathrm{Hz}}$). As we have also found, the white and grey differences are tenuous and they may be opposite at lower frequencies ($G'^{WM}_{43\,\mathrm{Hz}} < G'^{GM}_{43\,\mathrm{Hz}}$ and $G'^{WM}_{50\,\mathrm{Hz}} < G'^{GM}_{50\,\mathrm{Hz}}$) while the cerebellar and cerebral mechanical differences are enhanced at 50 Hz ($G'^{Cblum}_{113\,\mathrm{Hz}} \simeq 1.17$ kPa and $G'^{Cbrum}_{113\,\mathrm{Hz}} \simeq 1.5\text{-}1.64$ kPa) and mitigated at higher frequencies ($G'^{Cblum}_{113\,\mathrm{Hz}} \simeq 3.44$ kPa and $G'^{Cbrum}_{113\,\mathrm{Hz}} \simeq 3.46\text{-}3.56$ kPa). Hence, it is not easy to establish a clear mechanical behavior of the brain as, first, it is obviously heterogeneous, second, the MRE measurement uncertainty is itself heterogeneous – partly independently of the probed tissue with respect to the heterogeneity of the amplitude sampling factor, Q, and partly dependently on the tissue shear elasticity modulus with respect to the heterogeneity of the spatial sampling factor, s. MRE outcomes might also be obliterated by intrinsic differing rheological behavior of the different tissues along the excitation frequency. Nevertheless, we can knowingly assert the difference of shear elasticities between cerebral white and grey matters neither at low frequency ($\Delta G'^{WM\text{-}GM}_{43\,\mathrm{Hz}} \simeq 0.03$ kPa with $p \simeq 0.006$) nor at high frequency where the difference is higher ($\Delta G'^{WM\text{-}GM}_{113\,\mathrm{Hz}} \simeq 0.08$ kPa with $p \simeq 0.007$) but in the optimal conditions at 84 kHz where the difference becomes statistically significant with $\Delta G'^{WM\text{-}GM}_{84\,\mathrm{Hz}} \simeq 0.04$ kPa and $p \ll 0.001$. Similarly, the mechanical

difference between the cerebral and the cerebellar tissues is statistically significant at 43 Hz and 50 Hz (with $p \ll 0.001$) when the optimal conditions are matched for the cerebellum.

In any cases referring to cerebellum, cerebrum, white and grey matters, tissue discrimination is significant only because we are dealing with a large number of voxels. MRE is not sensitive enough today to mechanically differentiate healthy tissue types at the voxel level.

f_{exc} [Hz]	Ref.	G'_{WM} [kPa]	G'_{GM} [kPa]	G'_{Cblum} [kPa]		G''_{WM} [kPa]	G''_{GM} [kPa]	G''_{Cblum} [kPa]	
				$G'_{Cblum,WM}$ [kPa]	$G'_{Cblum,GM}$ [kPa]			$G''_{Cblum,WM}$ [kPa]	$G''_{Cblum,GM}$ [kPa]
45	[16]	3.7±0.8	2.8±0.5						
50	[17]	2.49±1.02	1.91±0.97						
60	[22]	3.3±0.1	3.1±0.3						
	[24]			2.2±0.2					
	[28]			2.23±0.13					
	[25]			2.36±0.16					
	[26]			2.15±0.11					
80	[16]	4.7±0.6	4.4±0.3			2.3±0.2	2.4±0.5		
	[18]	2.41±0.23	2.34±0.22	1.85±0.18	1.77±0.24	1.21±0.21	1.11±0.03	1.10±0.23	0.94±0.17
	[21]	10.7±1.4	5.3±1.3						
83.3	[20]	15.2±1.4	12.9±0.9						
90	[6]	2.7±0.1	3.1±0.1			2.5±0.2	2.5±0.2		

Table 4.4.1: MRE studies investigating shear elasticity, G', and viscosity, G'', moduli in segmented brain regions (white matter, WM, and grey matter, GM, of the cerebrum, $Cbrum$, and cerebellum, $Cblum$) of healthy volunteers at different excitation frequencies, $f_{exc} = \{45,50,60,80,83.3,90\}$ Hz. Measurements are largely spread between 1 kPa and 15 kPa with a factor 2 or 4 between studies for a same region and even the same excitation frequencies. Mechanical differences between brain regions are not obvious for each study. Works by Green et al. [6] and Zhang et al. [18] were carried out in similar conditions to the current study. They are used for comparison.

The MRE optimal domain determined over our datasets for the shear velocity was not easily extendable to the shear viscoelasticity moduli as they depend on other parameters than the wavelength – and the associated wavelength scaling factor s – as showed on equation 4-4 and equation 4-5, including attenuation and the square of the excitation frequency. Thus, the standard deviations of the shear elasticity and viscosity moduli increase with the excitation frequency up to the highest value (Figure 4.3.5 (b) and (c)) whereas those of the shear velocity are minimal when s is in the optimal domain ($6 \lesssim s \lesssim 9$)(Figure 4.3.5 (a)).

4.5 Conclusion

In spite of the natural protective barriers of the skull and the meninges, which are hardly trespassed by mechanical waves, multi-frequency brain MRE was performed here with robust motion-encoding spin-echo based sequences and guided pressure waves. Fair

displacement field amplitudes were found from 43 Hz up to 113 Hz. Surprisingly enough, data conditioning could be optimized within the simple assumptions made in the former chapters for homogeneous and isotropic media.

In this chapter, we saw how it is important to perform brain MRE within the optimal conditions in order to provide precise and accurate mechanical properties and better discriminate brain tissues. The major difference was not found between white and grey matters as one could expect but between cerebral and cerebellar tissues. Hence, optimal conditions in healthy brain tissues were found at 50 Hz in the cerebellum and at 84 Hz in the cerebrum, for either white or grey matters. The cerebral tissue could be more easily discriminated from the cerebellar tissue when optimal conditions were fulfilled at 50 Hz in the cerebellum.

For the sake of the available displacement field amplitude, the clinical practice has favored so far low frequency acquisitions (25 Hz-60 Hz) with a voxel size of a few millimeters, which, in the upper range (50 Hz-60 Hz), should yield the most accurate and precise measurement possible in the cerebellum. With an isotropic voxel size of 3 mm, brain MRE should preferably be performed even at higher frequencies – between 50 Hz and 80 Hz or with accordingly larger voxel sizes – in the cerebellum, and at even higher frequencies – between 80 Hz and 120 Hz or again larger voxel sizes – in the cerebrum to minimize the measurement uncertainty in healthy brain tissues. In diseased tissues, the viscoelastic moduli are usually higher and even higher frequencies (or accordingly larger voxel sizes) should be considered to avoid local mechanical underestimation and negative diagnosis. Alternatively, retrospective downsampling could be performed but (like with smaller matrix acquisitions) it would be at the expense of the spatial resolution of the affected regions.

Anyhow, prospective multi-frequency or retrospective multi-resampling MRE should advantageously be promoted to mechanically characterize the different tissues in healthy and pathological brains.

Chapter 5 Brain MR-Elastography in micro-gravity analogous conditions

5.1 Introduction

In the preceding chapters, we have shown the difficulty to mechanically discriminate stiffer inclusions from the surrounding parenchyma in a phantom or to distinguish different tissues in the brain. Previous MRE studies have also shown the difficulty to distinguish healthy from pathological tissues [8] and to discriminate different grades of tumors [19] or different neurodegenerative pathologies [23], [24], [26], [28] because estimated mechanical parameters of these different tissues are both too close to each other and too dispersed. These findings show that we do not really know whether the current MRE technique is able to significantly, precisely and accurately measure tissue changes due to pathological processes.

It is known that the astronauts' exposure to microgravity leads to various physiological responses such as headward fluid shift, body unloading, and cardiovascular deconditioning [142]. One of the most obvious and consistent effect of the fluid alterations seen in space flight is facial edema. These fluid alterations most probably come from cerebral autoregulation set out of balance by the effects of microgravity [143]–[146]. The cerebral autoregulation is the homeostatic mechanism for maintaining constant cerebral blood flow during changes in cerebral pressure by adjusting vascular tone and cerebral vessel diameter [147]. It was shown that during spaceflights, gravity-induced hydrostatic pressure gradients, normally present on Earth, vanish, which induces a fluid shift in tissues of the head and the neck [147]–[149]. This cephalad fluid shift may increase intracranial pressure due to impaired cerebral venous drainage [13],[16], which may in turn alter the mechanical properties of the tissues. To study these physiological changes in spaceflight conditions, head-down tilt (HDT) position is frequently used as a ground-based analog in order to induce a cephalad fluid shift. HDT involves placing the body in a tilted position to induce a positive hydrostatic pressure gradient towards the head relative to the heart. HDT position was well documented in recent works [143], [144], [146], [148], [151], [152].

The effects of microgravity on the brain have often been visualized with MRI by acquiring T1-weighted [153], [154] or T2-weighted images [151], [155] which are both sensitive to water content. In the following study, we propose for the first time to probe the mechanical properties of the brain under controlled gravity-driven pressure variations

with MRE in optimal conditions. For that purpose, we will first review the effects of microgravity on the brain MR signal lifetime as already studied by several teams in the literature, then we will probe the brain mechanical properties (shear velocity V_s, elasticity G' and viscosity G'') at 104 Hz in 0°Supine and 17°HDT positions following a gravity-dependence protocol inspired by previous works [155].

Chapter 5 is divided into four parts. The first part establishes a state of the art of the different results found by exposure of the human brain to spaceflights and spaceflight analogs. This part highlights the physiological changes on cerebral hemodynamics and the fact that, although physiological differences are observed during exposure to microgravity, consequences on the brain remain complex and poorly understood. The second part describes the experimental protocol of optimal human brain MRE performed in ground and microgravity-analog conditions. Then, the third part shows the measured changes on the brain MR signal lifetime and on the mechanical parameters during 0°Supine and 17°HDT positions in the whole brain as well as in the segmented brain regions including the cerebral white and grey matters and the cerebellum. This part aims, first, at underlining the modifications of the mechanical parameters and the MR signal lifetime in microgravity experiments, and then, at establishing whether MRE is significantly sensitive to these pressure and mechanical variations. Finally, a comparative study of our results and the added value of brain MRE with those found in the literature is proposed in the fourth part together with a discussion about the contributions and limitations of the study.

5.2 Microgravity effects on human brain structure

The physiological effects of spaceflights and space environment upon the human body are well documented in the literature with models of microgravity frequently used for reproducing the symptomatology of facial puffiness, nasal congestion, headache, and decrease in calf size associated with microgravity [149], [156]–[159].

In 1990, Maurice et al. made serial estimates of total brain water volume (TBW) and CSF volume by spectral imaging of four women at 6°HDT [160]. They showed that TBW increased linearly during the 1st hour of HDT by approximately 25%, with CSF volume increasing by approximately 10% compared to that measured with subjects upright. Thereafter, in 1999, Caprihan et al. [155] showed in MRI a T_2 reduction of 21% in the subarachnoid cerebrospinal fluid compartment and 11% in the eyes between ground supine position and space analogous 13°HDT position. Such T_2 reductions were interpreted as a local reduction of the water content.

In 2015, Roberts et al. [152] studied the evolution of brain volumes by analyzing structural pre- and post- bed rest brain MR images. They found a distinct change in ventricular volume for some subjects between pre- and post-bed rest but it was not

statistically significant on the group analysis due to the variability of responses across individuals. Nevertheless, they obtained significant increases in brain tissue density in regions at the vertex in the frontoparietal lobes with contraction of adjacent extra-axial *CSF* spaces, and significant decreases of the tissue density in areas along the base of the brain in the orbitofrontal cortex. In 2017, by analyzing the astronauts' brain after long-duration flights, they showed a significant narrowing of the central sulcus, an upward shift of the brain, and a significant narrowing of *CSF* spaces at the vertex [153]. In 2019, they demonstrated a significant increase in the percentage of total ventricular volume change after long-duration spaceflights [161].

In 2016, Koppelmans et al. [151] assessed with MRI the effects of spaceflights on segmented brain volumetric structures. They found significant volume decreases in the grey matter, *GM*, around the frontal and temporal poles and the orbits. Moreover, comparisons with long duration HDT bed rest studies allowed to find similar results in terms of *GM* changes which were attributed to an upward shift of the center of mass of the brain.

In the same year, Marshall-Goebel et al. [147] evaluated the effect of both the HDT angle on cerebral arterial and venous hemodynamic and the exposure to 1% CO_2 during 12°HDT position. They showed a decrease in total arterial blood flow and an increase of venous cross-sectional area accompanied with a decrease of venous outflow when increasing the angle of HDT from 0° to 18° HDT. Moreover, a comparison from 12°HDT at ambient atmosphere and 12°HDT with 1% CO_2 allowed to show an increase in total arterial blood flow and jugular outflow.

In 2020, Kramer et al. [154] investigated with MRI the intracranial effect of microgravity on astronauts' brain by measuring combined changes in intracranial volumetric parameters, pituitary morphologic structure and aqueductal *CSF* hydrodynamics relative to spaceflight. They found that long-duration spaceflights came with an increased pituitary deformation, an augmented aqueductal *CSF* hydrodynamics, and an expansion of brain parenchyma and *CSF* volumes. Moreover, they suggested that those alterations became permanent when brain parenchyma and *CSF* volumetric expansion persisted during recovery over a year.

As this state-of-the-art indicates, clear evidence of changes in brain structure due to microgravity have been highlighted in the literature of space medicine. Particularly, most of these studies underline the important role of the cerebral hemodynamic adaptation in order to overcome the cephalad fluid shift due to the removed or minimized hydrostatic gradients during either spaceflight or ground-based simulated spaceflight such as HDT bed rest. All these findings show the complexity of the physiological brain changes and the need to explore the different processes involved in the adaptation and alteration of the brain to microgravity to better understand the pathology behind normal

pressure hydrocephalus, hemorrhage or cancer where intracranial overpressure, cerebrospinal fluid accumulation, or depletion play a central role and which present similar brain symptoms.

5.3 Protocol description

It takes several hours for the fluid translocation and the capillary and interstitial pressures to restore the baseline reference values when a subject is submitted to the HDT position. Therefore, to achieve comparative acquisition conditions on Earth and in space, like in the work of Caprihan et al. [155], a healthy volunteer (male, 49 y/o) was first imaged in the supine position after a 40 min rest in this position (Figure 5.3.1 a). Then, the subject was removed from the magnet and allowed to sit up, stand, and walk briefly for 30 min. The subject was then returned to the MRI bed and placed onto a padded board titled by an angle of 17° from the horizontal plane of the MRI bed (Figure 5.3.1 b). After 40 min in this position, the subject was imaged in the head down tilt position following the same acquisition protocol as when in the supine position. MRI and MRE acquisitions were performed using a standard head SENSE coil in a 1.5 T Achieva MR system (Philips, Best, Netherlands) at SHFJ.

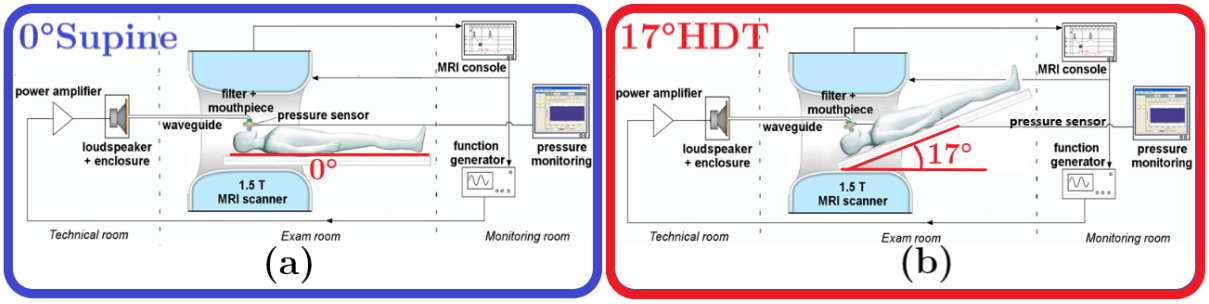

Figure 5.3.1: Schematic of the MRE setup in (a) 0°Supine position and (b) 17°HDT position. The subject lies in a 1.5 T Achieva MR system with the head placed in a standard head SENSE coil. Remotely generated and amplified pressure waves are guided in the center of the MRI magnet to the subject's buccal cavity. Pressure wave level is monitored at the mouth via an optical fiber sensor. Pressure wave are synchronized to the MRI acquisition sequence.

5.3.1 MRI acquisitions

For the two positions 0°Supine and 17°HDT, T_2-mapping in the brain was achieved with a multi spin-echo multi-slice sequence implemented with $FOV = (210 \times 210 \times 154)$ mm^3, Matrix $= (105 \times 105 \times 77)$, Voxel $= (2 \times 2 \times 2)$ mm^3, $TE/TR = \{20, 40, 60, 80, 100\}/10{,}000$ ms.

5.3.2 MRE acquisitions

Remotely generated pressure waves were guided into the subject's buccal cavity to induce shear waves throughout the brain while applying a synchronized motion-sensitized spin-echo sequence as described in Section 4.2.1.

Displacement fields were acquired in the 0°Supine and 17°HDT positions (Figure 5.3.1) with a field of view $FOV = (210 \times 210 \times 152)$ mm^3 covering the whole brain and a matrix size of $(80 \times 80 \times 52)$. An isotropic voxel of size $a = 2.94$ mm and an excitation frequency $f_{exc} = 104$ Hz were used to optimize the wavelength sampling in the cerebrum for the subsequent reconstruction of the MRE outcomes as demonstrated in Chapter 4.

The amplitude of the motion-encoding gradients was increased to 42 mT · m^{-1} to double the MRE sensitivity to the displacement field (with respect to the acquisition protocol presented in Chapter 4) with 4 temporal samples along the mechanical period. The echo time TE was 29 ms and the repetition time TR was 1999 ms for the two acquisitions at 0°Supine and 17°HDT position. The total acquisition time was 7 min 33 s per encoding direction.

5.3.3 Data processing

T_2 maps were computed by exponential fitting of the brain images acquired at five echo times: $TE = \{20, 40, 60, 80, 100\}$ ms. To avoid high T_2 values and biased exponential fitting due to the low signal decay like in the eyes, T_2 maps were clipped at an arbitrary value of $5 \times TE_{\max} = 500$ ms. After registering the image sets at 0° and 17°, T_2 variation maps, $\Delta T_2 = T_2^{17°} - T_2^{0°}$, were computed.

Shear velocity maps, $\mathrm{V_s}$, were extracted according equation 1.71, MRE data quality, Q, was calculated upon $\mathbf{q}$ along equation 1.72 and the shear dynamic and loss moduli, $\mathrm{G'}$ and G'', were deduced from equations 1.77 and 1.78.

For each position, the image with the shortest echo time ($TE = 20$ ms) was segmented using SPM12 (*The Wellcome Centre for Human Neuroimaging, UCL, London, United-Kingdom*) to infer masks of the cerebral grey matter (GM), the cerebral white matter (WM), the cerebellar white and grey matters (Cb), and the cerebrospinal liquid (CSF). Regional volume variations were calculated on the basis of the number of voxels reported in each segmented brain region for 0°Supine and 17°HDT positions. MR relaxometry was performed in every segmented regions of the brain whereas MR elastography was restricted to soft tissues as shear waves are not expected to propagate in the CSF. Regional comparison between MR relaxometry and MR elastography was then carried out on cerebral regions (including white and grey matters) close to the eyes

(Region A, Figure 5.3.2), the lateral ventricle (Region B, Figure 5.3.2) and the subarachnoid CSF (Region C, Figure 5.3.2).

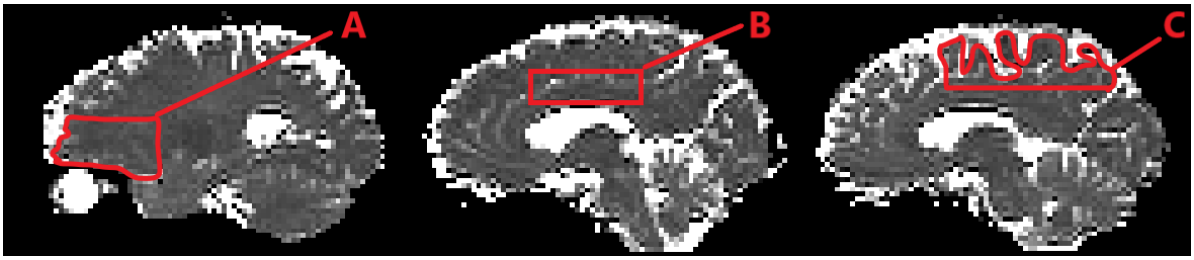

Figure 5.3.2: Regions A, B, and C selected in the brain for comparison with results found in the CSF by Caprihan et al. [155]. Region A is near the eyes, Region B is near the lateral ventricle and Region C is near the subarachnoid CSF.

Relative variations of the median values of the MR signal relaxivity, $\Delta R_2 = (R_2^{17°} - R_2^{0°})/R_2^{0°}$ with $R_2 = 1/T_2$, and relative variations of the mean values of V_s, G' and G'' were calculated in every slice to compare the outcomes in the 0°Supine and 17°HDT positions along the inferior-superior axis. Only voxels with high quality factor, $Q \geq Q_{th}$, were considered. The threshold value, Q_{th}, was determined after the correlations $R(Q, V_s)$ between V_s and Q over bins of 1000 voxels. Q_{th} corresponded to the convergence of the correlation fitting around zero (when $R < 0.025$).

In relation to the gravity, the effects onto the brain of the HDT position are expected to vary along the inferior-superior axis and be enhanced by regional volume changes of the CSF. Thus, the mechanical parameters were studied as a function of the axial slice number and in regions surrounding the CSF.

5.4 Results

5.4.1 MR morphometry

Very little volume changes between 0°Supine and 17°HDT positions can be reported in the cerebellum and the cerebral grey matter with respective relative variations of $\delta N_{Cblum} = -0.83\,\%$ and $\delta N_{GM} = +0.02\,\%$ (Table 5.4.1). More noticeable increases occurred in the CSF and the cerebral white matter with respective relative variations $\delta N_{WM} = +3.53\,\%$ and $\delta N_{CSF} = +3.36\,\%$. These latter variations correspond to a volume increase of +16 mL in the CSF and +22.2 mL in the WM.

	0°Supine	17°HDT	ΔN	$\Delta\vartheta$ [mL]	δN
N_{Brain}	94,919	96,353	+1,434	+36.4	+1.51%
N_{Cbrum}	66,808	67,691	+883	+22.4	+1.32%
N_{WM}	24,757	25,631	+874	+22.2	+3.53%
N_{GM}	42,051	42,060	+9	+0.2	+0.02%
N_{Cblum}	9,365	9,287	-78	-2.0	-0.83%
N_{CSF}	18,746	19,375	+629	+16.0	+3.36%

Table 5.4.1: Voxel number in the whole brain ($Brain$), the cerebrum ($Cbrum$), the cerebral white (WM) and grey (GM) matters, the cerebellum ($Cblum$), and the cerebrospinal fluid (CSF). Mean and relative variations, ΔN and δN, with corresponding volume variation in mL, $\Delta\vartheta$.

5.4.2 MR relaxometry

Figure 5.4.1 shows the T_2 variation maps, ΔT_2, between the 0°Supine and 17°HDT positions for different axial, sagittal, and coronal slices. These maps indicate both regional increase and decrease at tissue boundaries.

	0°Supine	17°HDT	ΔT_2	$\Delta\sigma$	δT_2
$T_{2_{Brain}}$	125±73	127±73	+2	±103	+1.6%
$T_{2_{Cbrum}}$	112±58	113±57	+1	±81	-0.9%
$T_{2_{WM}}$	110±31	112±34	+2	±46	+1.8%
$T_{2_{GM}}$	89±12	91±14	+2	±18	+2.2%
$T_{2_{Cblum}}$	107±36	108±35	+1	±50	+0.9%
$T_{2_{CSF}}$	209±107	205±106	-4	±150	-1.9%

Table 5.4.2: MR signal lifetime, T_2, in the whole brain ($Brain$), the cerebrum ($Cbrum$), the cerebral white (WM) and grey (GM) matters, the cerebellum ($Cblum$), and the cerebrospinal fluid (CSF). Mean and relative variations, ΔT_2 and δT_2 with associated standard deviation, $\Delta\sigma$.

T_2 is essentially the same for both positions in the cerebral tissues ($\Delta T_2 \simeq +2$ ms) and in the cerebellar tissues ($\Delta T_2 \simeq +1$ ms). It slightly decreases at 17° in the CSF compartment ($\Delta T_2 \simeq -4$ ms) but it is not clearly depicted in any specific region and (Figure 5.4.1, Figure 5.4.2, and Figure 5.4.3).

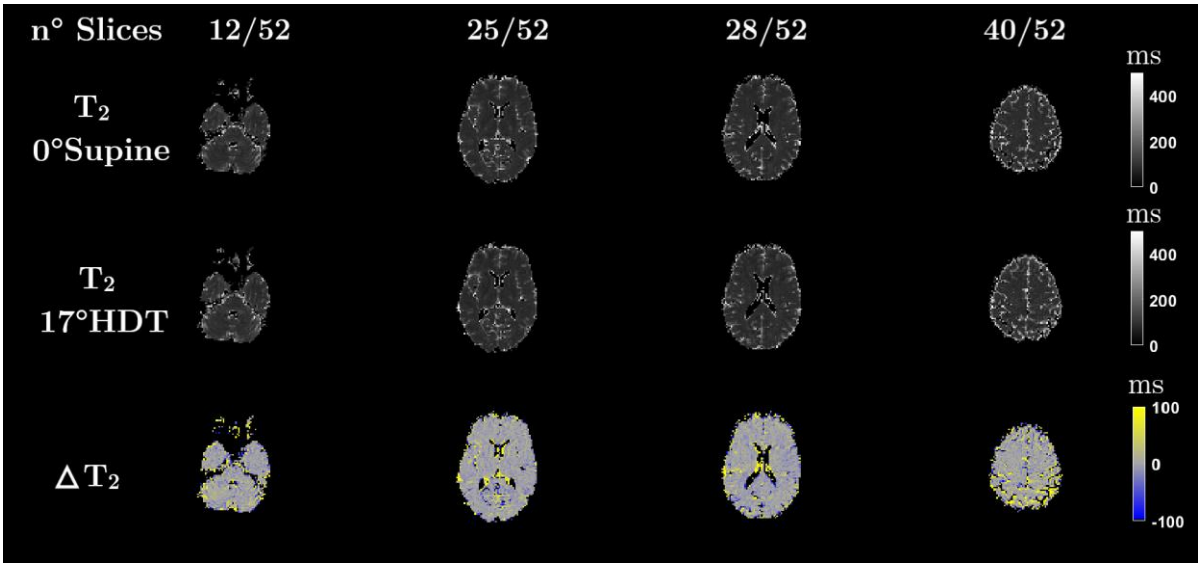

Figure 5.4.1: Axial maps at slices 12, 25, 28, and 40 of the MR signal lifetime (T_2) in supine position (first row), in HDT position (second row) and the variation of the MR signal lifetime, ΔT_2, between 0° and 17° positions. ΔT_2 is essentially zero everywhere but at tissue boundaries.

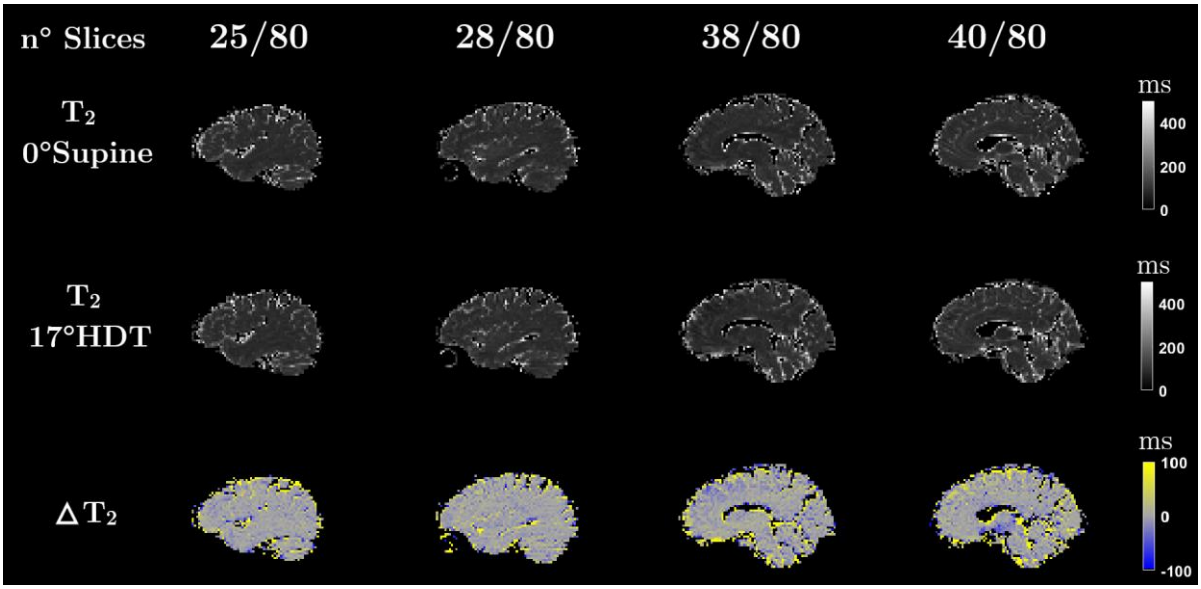

Figure 5.4.2: Sagittal maps at slices 25, 28, 38, and 40 of the MR signal lifetime (T_2) in supine position (first row), in HDT position (second row) and the variation of the MR signal lifetime, ΔT_2, between 0° and 17° positions. ΔT_2 is essentially zero everywhere but at tissues boundaries.

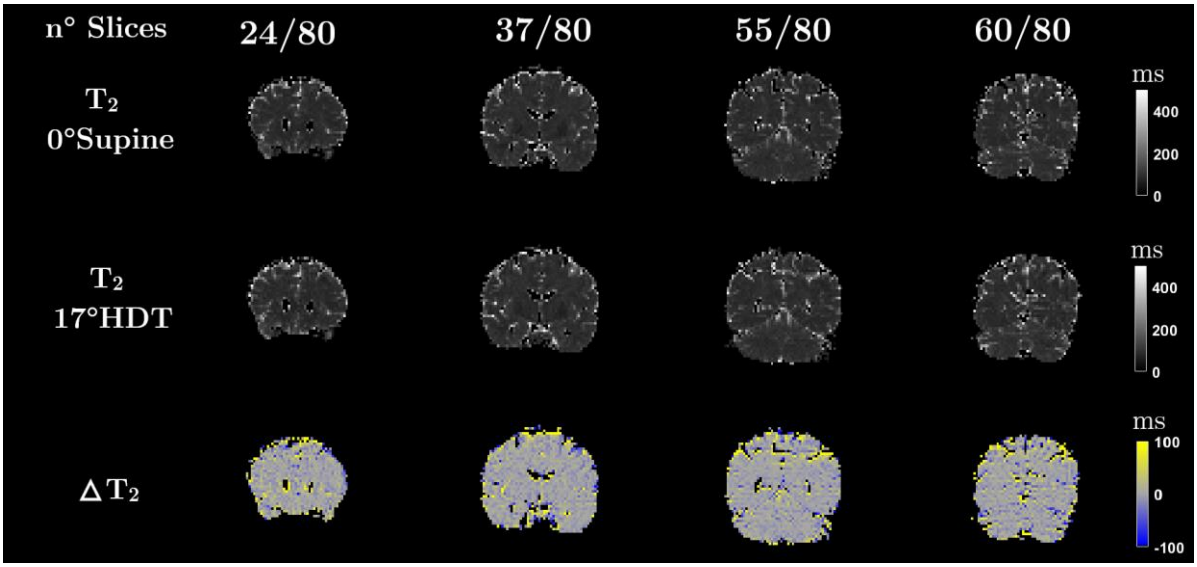

Figure 5.4.3: Coronal maps at slices 24, 37 55, and 60 of the MR signal lifetime (T_2) in supine position (first row), in HDT position (second row) and the variation of the MR signal lifetime, ΔT_2, between 0° and 17° positions. ΔT_2 is essentially zero everywhere but at tissue boundaries.

5.4.3 MRE data quality

MRE datasets in supine and HDT positions exhibit the same mean SNR value of 45 as expected for acquisitions with identical parameters (Table 5.4.6). They also exhibit essentially the same mean displacement field amplitude with $\langle A \rangle_{104\,\mathrm{Hz}}^{0^\circ} = 7.67 \pm 2.93$ µm in supine position and $\langle A \rangle_{104\,\mathrm{Hz}}^{17^\circ} = 7.84 \pm 2.79$ µm in HDT position, and consequently the same quality factors with $\langle Q \rangle^{0^\circ} \simeq 47$, $\langle Q \rangle^{17^\circ} \simeq 44$ (Table 5.4.6).

	0°SUPINE	17°HDT
$\langle SNR \rangle_{Brain}$	45±3	46±3
$\langle A \rangle_{Brain}$ [µm]	7.67±2.93	7.84±2.79
$\langle Q \rangle_{Brain}$	47±32	44±31

Table 5.4.3: Signal-to-noise ratio $\langle SNR \rangle$, wave amplitude $\langle A \rangle$, quality factor $\langle Q \rangle$ averaged over the whole brain ($Brain$).

They reach roughly the same maximal Q values with 384 at 0°Supine and 378 at 17°HDT (Figure 5.4.4). As seen in the former Chapter 4 and clearly delineated in the coronal and sagittal maps (Figure 5.4.8 and), maximal A and Q values show up around the tentorium cerebelli for both positions {0°Supine ,17°HDT}: $\langle A \rangle_{Tent\,Cb} \approx \{23,21\}$ µm, $\langle Q \rangle_{Tent\,Cb} \approx \{305,275\}$ and in the anterior part of the frontal lobe $\langle A \rangle_{Frontal\,lobe} \approx \{15,16\}$ µm and $\langle Q \rangle_{Frontal\,lobe} \approx \{98,103\}$.

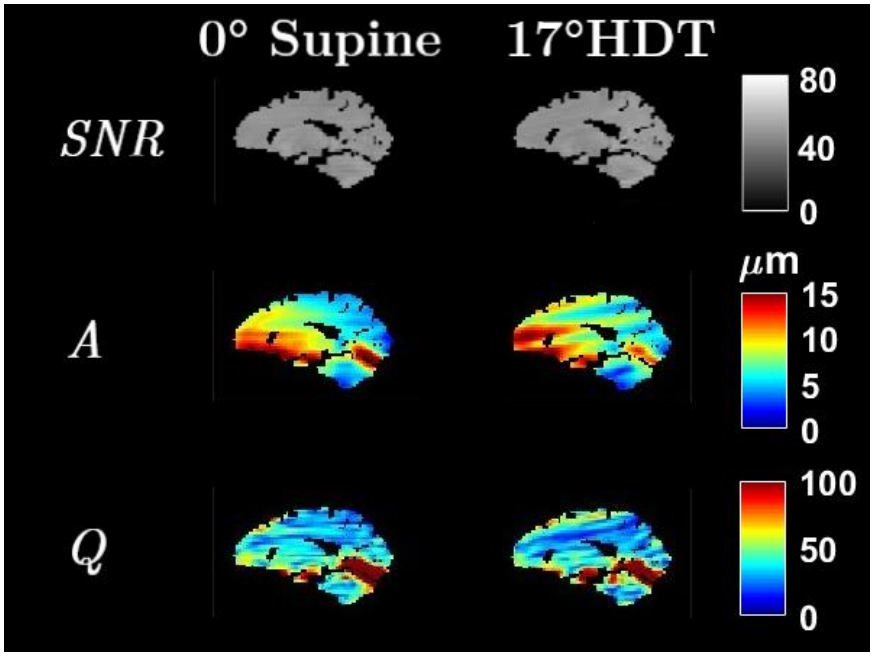

Figure 5.4.4: MRE maps of signal-to-noise, SNR, displacement field amplitude, A, and data quality factor, Q, in a lateral sagittal plane of the left hemisphere (slice 35/52) in 0°Supine and 17°HDT positions at 104 Hz in one healthy subject. SNR, A, and Q are similar for both 0°Supine and 17°HDT positions whereas V_s, G', G'' globally increase from 0°Supine to 17°HDT positions (Figure 5.4.8, Figure 5.4.9 and Figure 5.4.10).

The whole brain voxel-by-voxel distributions, $V_s(Q)$, represented in Figure 5.4.5 show the correlation coefficients $R(Q, V_s)$ of the successive bins of 1000 voxels (black points) and the fitting curve (black line). The threshold value was the same for both 0°Supine and 17°HDT positions: $Q_{th} = 13$. Above Q_{th}, the mean velocity value in the cerebrum increases by 9% from $\langle V_{Cbrum}^{0°\text{Supine}} \rangle = 2.10 \pm 0.26$ m·s^{-1} to $\langle V_{Cbrum}^{17°\text{HDT}} \rangle = 2.29 \pm 0.30$ m·s^{-1} whereas it remains the same in the cerebellum with $\langle V_{Cb}^{0°\text{Supine}} \rangle = 2.19 \pm 0.44$ m·s^{-1} and $\langle V_{Cb}^{17°\text{HDT}} \rangle = 2.19 \pm 0.44$ m·s^{-1}.

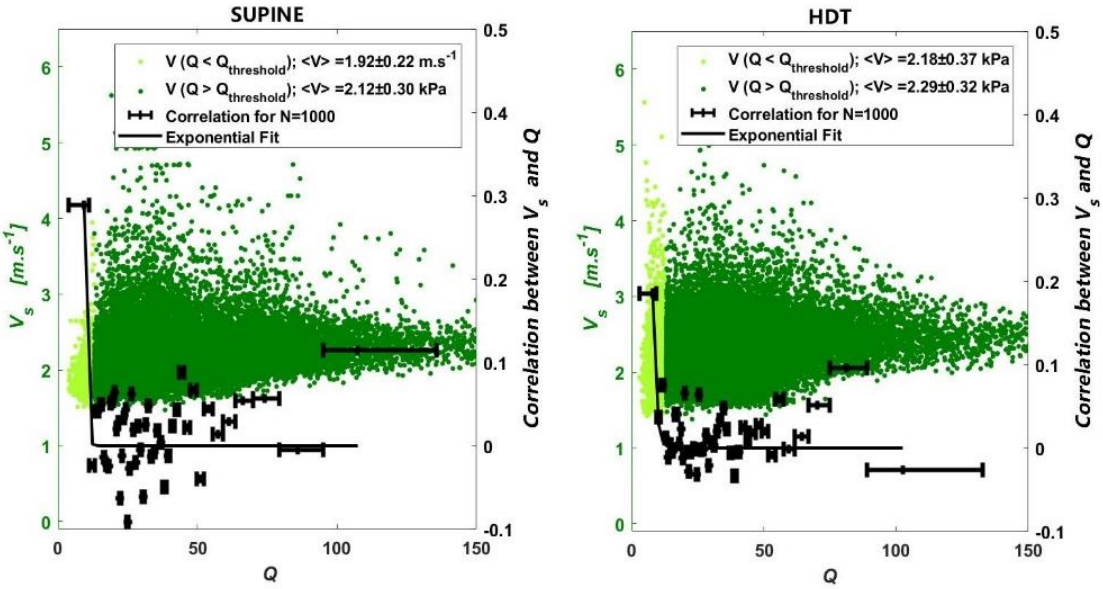

Figure 5.4.5: MRE voxel-wise shear velocity, V_s, as a function of the quality factor, Q, in 0°Supine (left) and 17°HDT (right) positions with an exponential correlation curve (black line) fitted to the correlation points $R(Q, V_s)$ calculated over bins of N=1000 voxels between the shear velocity V_s and the quality factor Q (black points). When the correlation fitting curve approaches zero (i.e. $R(Q, V_s) < 0.025$ into the right scale), then $Q = Q_{th}$. Here, $Q_{th} = 13$. Only voxel velocities with $Q \geq Q_{th}$ (dark green) are considered in the subsequent analysis. Voxel velocities with $Q < Q_{th}$ are discarded (light green).

5.4.4 MRE shear velocity distributions

The voxel-wise distributions of the cerebral shear velocity, elasticity and viscosity are represented in Figure 5.4.6 in dark blue for the white matter and in blue for the grey matter as a function of Q. They noticeably shift towards higher values from the 0°Supine position to the 17°HDT position (Table 5.4.4). They are narrower in the cerebrum ($\Delta V_{Cbrum} \simeq \pm 0.2$ m·s^{-1}) than in the cerebellum ($\Delta V_{Cblum} \simeq \pm 0.4$ m·s^{-1}) as, with $a = 2.94$ mm and $f_{exc} = 104$ Hz, the spatial sampling factor, s, is expectedly in the optimal range in the cerebral tissues whereas the measurement uncertainty is expectedly degraded in the cerebellar tissues for which s would be optimal at lower excitation frequencies, $f_{exc} \sim 50$ Hz (Chapter 4).

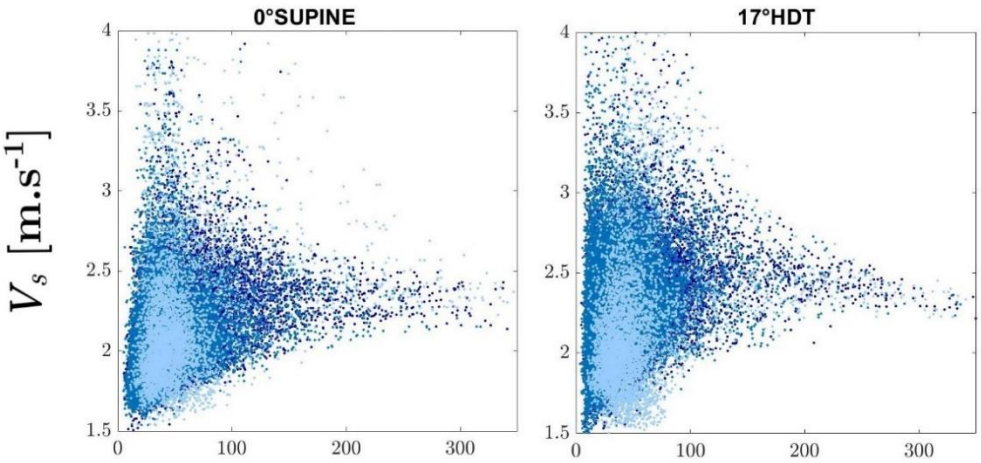

Figure 5.4.6 : MRE voxel-wise shear velocity, V_s, as a function of data quality, Q, in a healthy subject's brain at excitation frequency 104 Hz. V_s increases in the cerebral white matter, WM (dark blue), and grey matter, GM (blue), in 17°HDT position with respect to 0°Supine position but they remain in the same range in the cerebellum, $Cblum$ (light blue). For both positions, velocity distributions are narrower in the cerebrum – for which s is expectedly in the optimal range – than in the cerebellum – for which s is well above the optimal domain (Chapter 4).

	0°Supine	17°HDT	Variation	Relative
$\langle V_s \rangle_{Brain}$ [m·s^{-1}]	2.11±0.29	2.28±0.32	+0.17	+8.1%
$\langle G' \rangle_{Brain}$ [kPa]	3.68±0.66	4.12±0.83	+0.44	+12.0%
$\langle G'' \rangle_{Brain}$ [kPa]	1.79±0.78	2.26±0.91	+0.47	+26.3%
$\langle V_s \rangle_{Cbrum}$ [m·s^{-1}]	2.09±0.26	2.28±0.30	+0.19	+9.0%
$\langle G' \rangle_{Cbrum}$ [kPa]	3.69±0.65	4.15±0.80	+0.48	+13.0%
$\langle G'' \rangle_{Cbrum}$ [kPa]	1.74±0.70	2.28±0.87	+0.52	+29.7%
$\langle V_s \rangle_{WM}$ [m·s^{-1}]	2.12±0.27	2.30±0.30	+0.18	+8.5%
$\langle G' \rangle_{WM}$ [kPa]	3.75±0.69	4.25±0.80	+0.51	+13.6%
$\langle G'' \rangle_{WM}$ [kPa]	1.82±0.73	2.25±0.87	+0.41	+22.4%
$\langle V_s \rangle_{GM}$ [m·s^{-1}]	2.08±0.26	2.28±0.30	+0.20	+9.6%
$\langle G' \rangle_{GM}$ [kPa]	3.66±0.63	4.09±0.80	+0.46	+12.5%
$\langle G'' \rangle_{GM}$[kPa]	1.70±0.68	2.30±0.87	+0.59	+34.7%
$\langle V_s \rangle_{Cblum}$ [m·s^{-1}]	2.19±0.43	2.19±0.43	+0.00	+0.0%
$\langle G' \rangle_{Cblum}$ [kPa]	3.55±0.74	3.66±0.93	+0.12	+3.4%
$\langle G'' \rangle_{Cblum}$ [kPa]	2.11±1.15	2.17±1.26	+0.06	+2.8%

Table 5.4.4: Shear velocity (V_s), shear elasticity (G' in light orange), and shear viscosity (G'' in light green) averaged over the whole brain ($Brain$), the cerebrum ($Cbrum$), the cerebral white matter (WM), the cerebral grey matter (GM) and the cerebellum ($Cblum$). Variations (in [m·s^{-1}]) and relative variations (in percentage) between 0°Supine and 17°HDT positions.

In a lesser extent, the cerebral shear velocities at high Q ($Q > 150$) support the global tissue stiffening in the cerebrum with a 6.1% increase from $\langle V_{Cbrum}^{0°\text{Supine}}(Q > 150) \rangle = 2.31 \pm 0.13$ m·s^{-1} to $\langle V_{Cbrum}^{17°\text{HDT}}(Q > 150) \rangle = 2.45 \pm 0.16$ m·s^{-1}. In both 0°Supine and 17°HDT positions, Q values are limited but, for $Q > 150$, the cerebellar shear velocities tend to similar values with even a small mean value decrease of -4.0%: $\langle V_{Cblum}^{0°\text{Supine}}(Q > 150) \rangle = 2.49 \pm 0.30$ m·s^{-1} and $\langle V_{Cblum}^{17°\text{HDT}}(Q > 150) \rangle = 2.39 \pm 0.13$ m·s^{-1} (Figure 5.4.6, Table 5.4.5).

	0°Supine	17°HDT	Variation	Relative
$\langle V_s(Q>150)\rangle_{Cbrum}$ [m·s^{-1}]	2.31±0.13	2.45±0.16	+0.14	+6.1%
$\langle G'(Q>150)\rangle_{Cbrum}$ [kPa]	4.75±0.52	5.27±0.66	+0.52	+10.9%
$\langle G''(Q>150)\rangle_{Cbrum}$ [kPa]	1.79±0.42	2.15±0.62	+0.84	+22.0%
$\langle V_s(Q>150)\rangle_{WM}$ [m·s^{-1}]	2.32±0.12	2.45±0.13	+0.13	+5.6%
$\langle G'(Q>150)\rangle_{WM}$ [kPa]	4.89±0.42	5.36±0.53	+0.47	+9.6%
$\langle G''(Q>150)\rangle_{WM}$ [kPa]	1.73±0.42	2.06±0.62	+0.33	+19.1%
$\langle V_s(Q>150)\rangle_{GM}$ [m·s^{-1}]	2.28±0.15	2.45±0.18	+0.17	+7.4%
$\langle G'(Q>150)\rangle_{GM}$ [kPa]	4.53±0.58	5.12±0.53	+0.59	+13.0%
$\langle G''(Q>150)\rangle_{GM}$[kPa]	1.88±0.40	2.30±0.69	+0.42	+22%
$\langle V_s(Q>150)\rangle_{Cblum}$ [m·s^{-1}]	2.49±0.30	2.39±0.13	-0.10	-4.0%
$\langle G'(Q>150)\rangle_{Cblum}$ [kPa]	4.92±0.50	4.99±0.47	+0.07	+1.4%
$\langle G''(Q>150)\rangle_{Cblum}$ [kPa]	2.39±1.02	2.05±0.71	-0.34	-14.2%

Table 5.4.5: Shear velocity (V_s), shear elasticity (G' in light orange), and shear viscosity (G'' in light green) averaged over the whole brain ($Brain$), the cerebrum ($Cbrum$), the cerebral white matter (WM), the cerebral grey matter (GM) and the cerebellum ($Cblum$). Variations (in [m·s^{-1}]) and relative variations (in percentage) between 0°Supine and 17°HDT positions.

The trends on the shear velocity are somewhat followed by the shear elasticity distributions in the cerebrum with a large 10.9% increase in the cerebrum from $\langle G'^{0°\text{Supine}}_{Cbrum}(Q>150)\rangle = 4.75 \pm 0.52$ kPa to $\langle G'^{17°\text{HDT}}_{Cbrum}(Q>150)\rangle = 5.27 \pm 0.66$ kPa. In the cerebellum, it is slightly opposite though with a small +1.4% increase from $\langle G'^{0°\text{Supine}}_{Cblum}(Q>150)\rangle = 4.92 \pm 0.50$ kPa to $\langle G'^{17°\text{HDT}}_{Cblum}(Q>150)\rangle = 4.99 \pm 0.47$ kPa (Figure 5.4.7, top row, Table 5.4.5). The tissue stiffening is accompanied by a +22.0% increase of the cerebral shear viscosity from $\langle G''^{0°\text{Supine}}_{Cbrum}(Q>150)\rangle = 1.79 \pm 0.42$ kPa to $\langle G''^{17°\text{HDT}}_{Cbrum}(Q>150)\rangle = 2.15 \pm 0.62$ kPa and an accordingly important -14.2% decrease of the cerebellar shear viscosity from $\langle G''^{0°\text{Supine}}_{Cblum}(Q>150)\rangle = 2.39 \pm 1.02$ kPa to $\langle G''^{17°\text{HDT}}_{Cblum}(Q>150)\rangle = 2.05 \pm 0.71$ kPa (Figure 5.4.7, bottom row, Table 5.4.5).

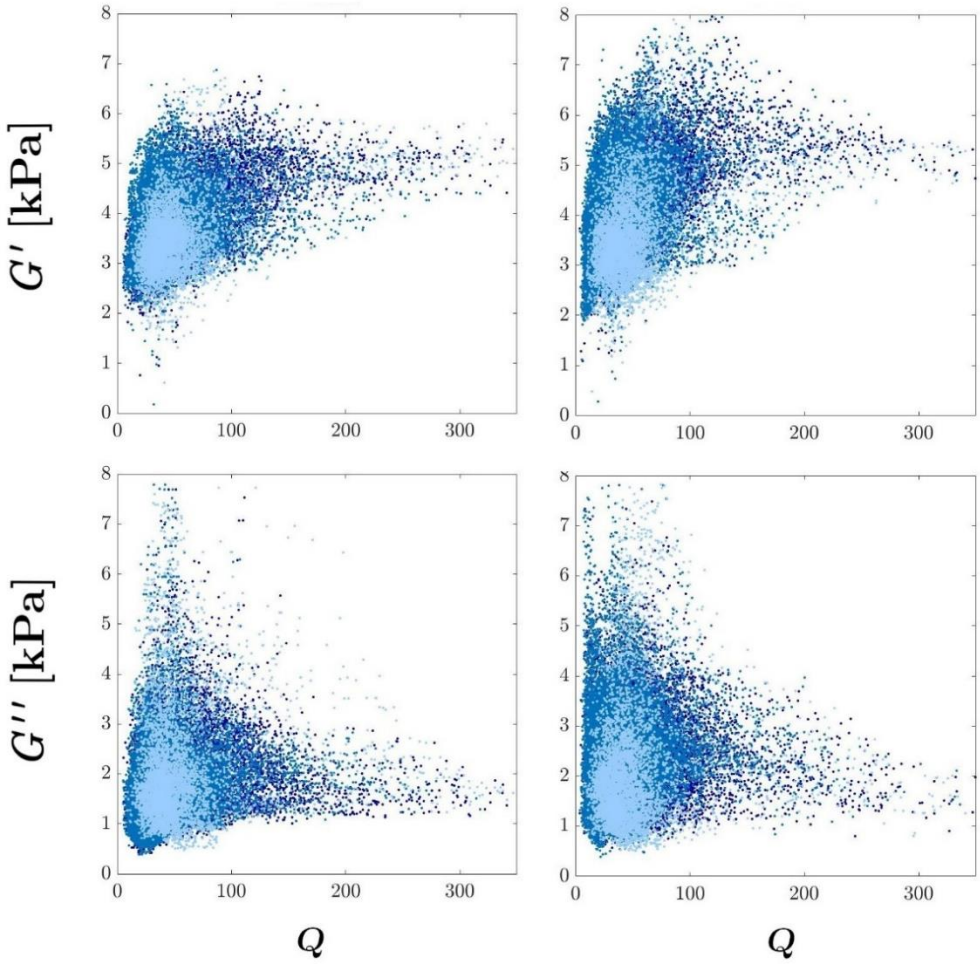

Figure 5.4.7 : MRE voxel-wise shear elasticity G' (top row), and viscosity G''(bottom row) as a function of data quality, Q, in a healthy subject's brain at excitation frequency 104 Hz. G' and G'' values increase in the cerebral white matter, WM (dark blue), and grey matter, GM (blue), in 17°HDT position with respect to 0°Supine position but they remain in the same range in the cerebellum, Cb (light blue).

5.4.5 MRE parametric maps

The different slices of the shear viscoelastic moduli Figure 5.4.9 and Figure 5.4.10 show that the mean increase of the mechanical parameters is hardly related to the segmented regions such as white and grey matters. Actually, the increase is heterogeneous across the parenchyma and even though the value of the mean shear velocity in the cerebrum is 2.28 ± 0.6 m·s^{-1}, it can reach 3 m·s^{-1} in the vertex region during 17°HDT position. Similarly, the mean shear elasticity (and viscosity) in the cerebrum is 4.2 ± 0.8 kPa (2.3 ± 0.9 kPa) but it can reach 6.2 ± 1.4 kPa (4.2 ± 2.3 kPa) in the vertex region.

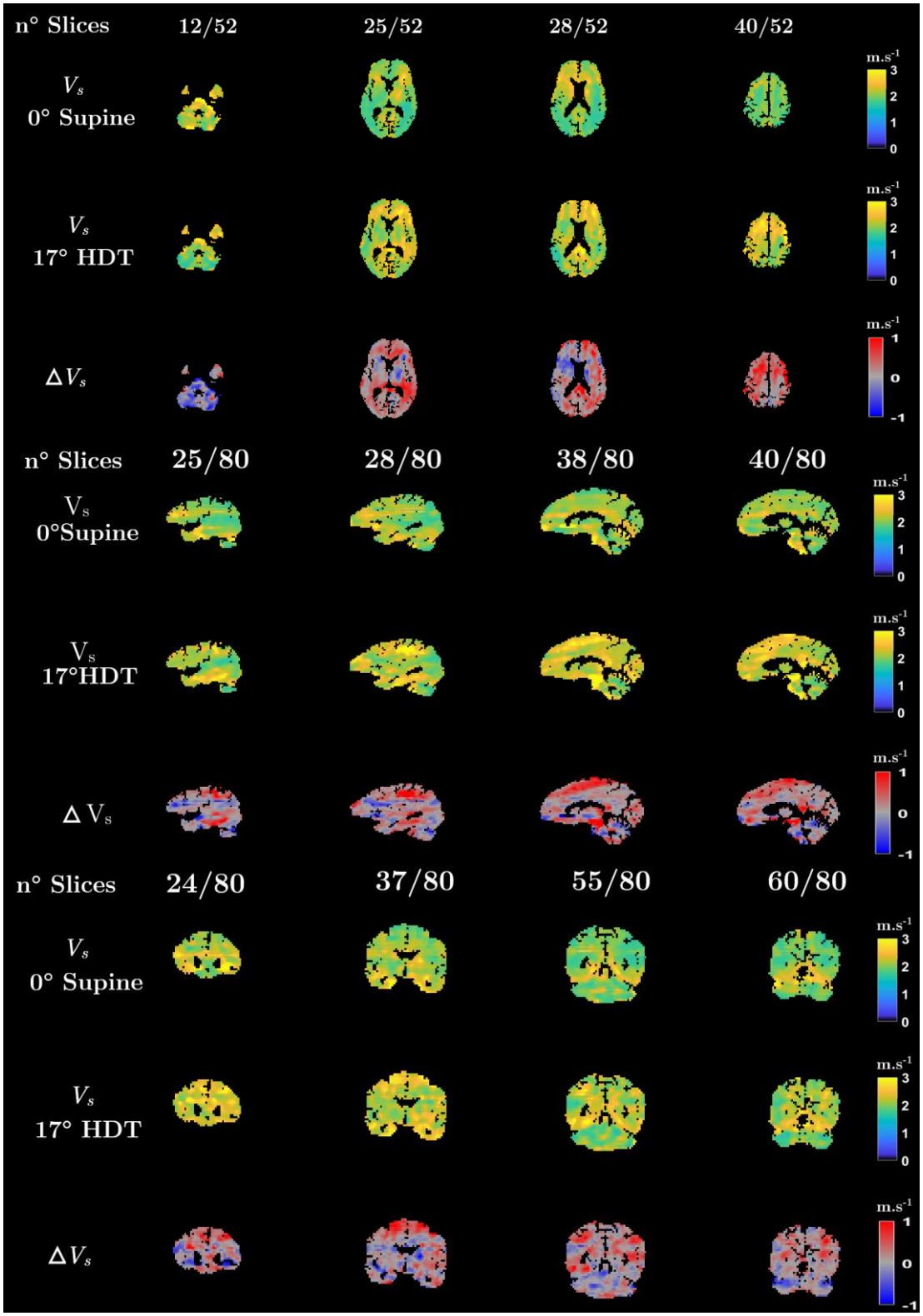

Figure 5.4.8: Axial maps at slices 12, 25, 28 and 40, sagittal maps at slices 25, 28, 38 and 40 and coronal map at slices 24, 37, 55, 60 of the shear velocity, V_s in 0°Supine position (first row), in 17°HDT position (second row) and of the shear velocity variation $\Delta V_s = V_s^{17°HDT} - V_s^{0°Supine}$ (third row) between 0° and 17° positions. A global mechanical increase between 0° supine and 17° HDT is revealed in the cerebral soft tissues.

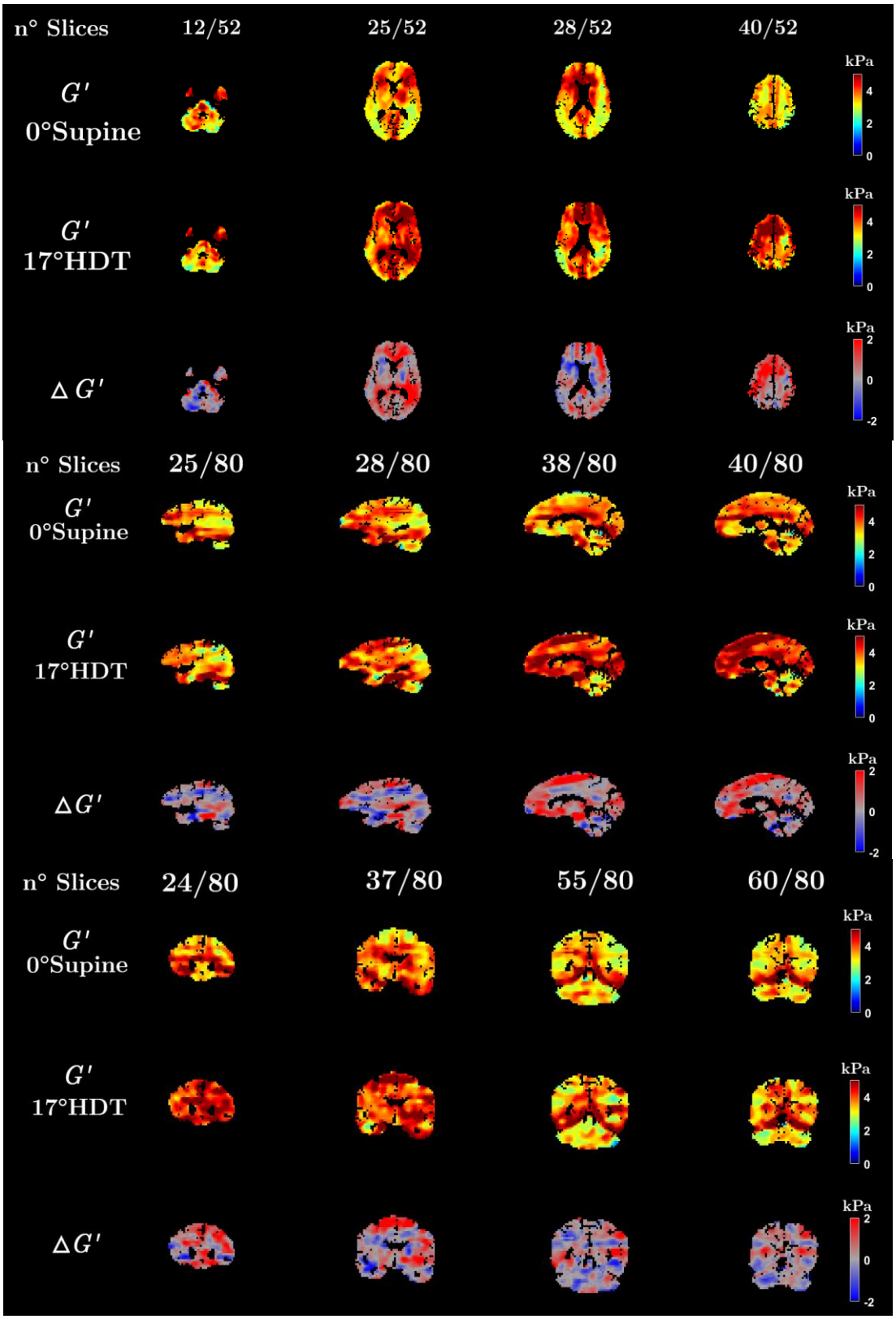

Figure 5.4.9: Axial maps at slices 12, 25, 28 and 40, sagittal maps at slices 25, 28, 38 and 40 and coronal map at slices 24, 37, 55, 60 of the shear elastic modulus, G' in 0° Supine position (first row), in 17° HDT position (second row) and of the shear velocity variation $\Delta G' = G'^{\,17°HDT} - G'^{\,0°Supine}$ (third row) between 0° and 17° positions . A global mechanical increase between 0° supine and 17° HDT is revealed in the cerebral soft tissues.

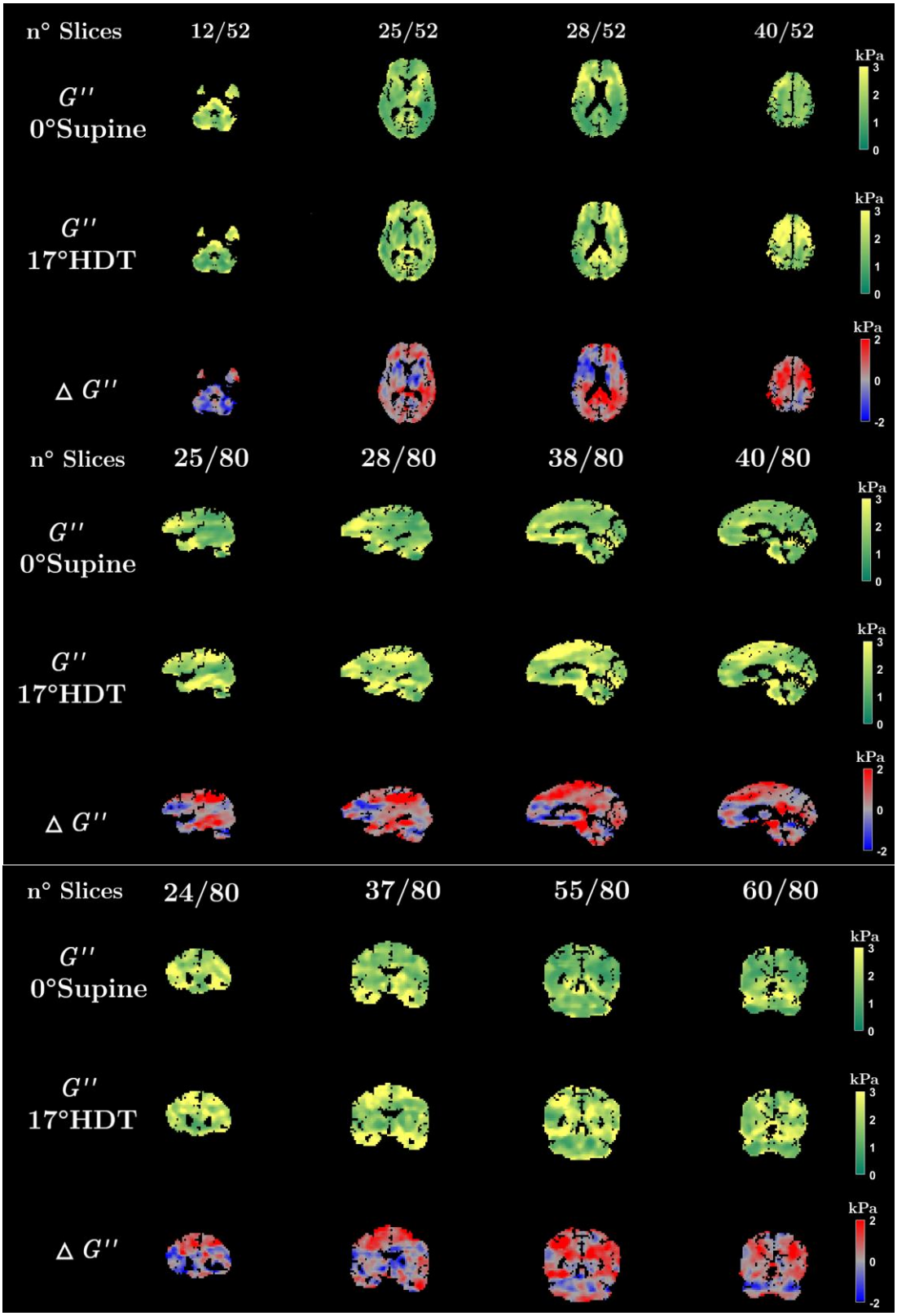

Figure 5.4.10: : Axial maps at slices 12, 25, 28 and 40, sagittal maps at slices 24, 37, 55 and 60 of the shear viscous modulus, G'' in 0° Supine position (first row), in 17° HDT position (second row) and of the shear velocity variation $\Delta G'' = G''^{17°HDT} - G''^{0°Supine}$ (third row) between 0° and 17° positions A global mechanical increase between 0° supine and 17° HDT is revealed in the cerebral soft tissues.

5.4.6 Gravity inferior-superior axis

The relative variation *between 0°Supine and 17°HDT positions* of the median values per axial slice of R_2, *and of the mean values* per axial slice of V_s, G' *and* G'' *are represented* along the inferior-superior axis in Figure 5.4.11. The relative variation of the median relaxivity, R_2, displays clear positive peaks around the fourth ventricle (slices 5-7), the eyes (slices 9-13), the third ventricle and the lateral ventricles (slices 25-31), and the subarachnoid *CSF* (slices 41-43) which implies a T_2 decrease at 17° in these regions.

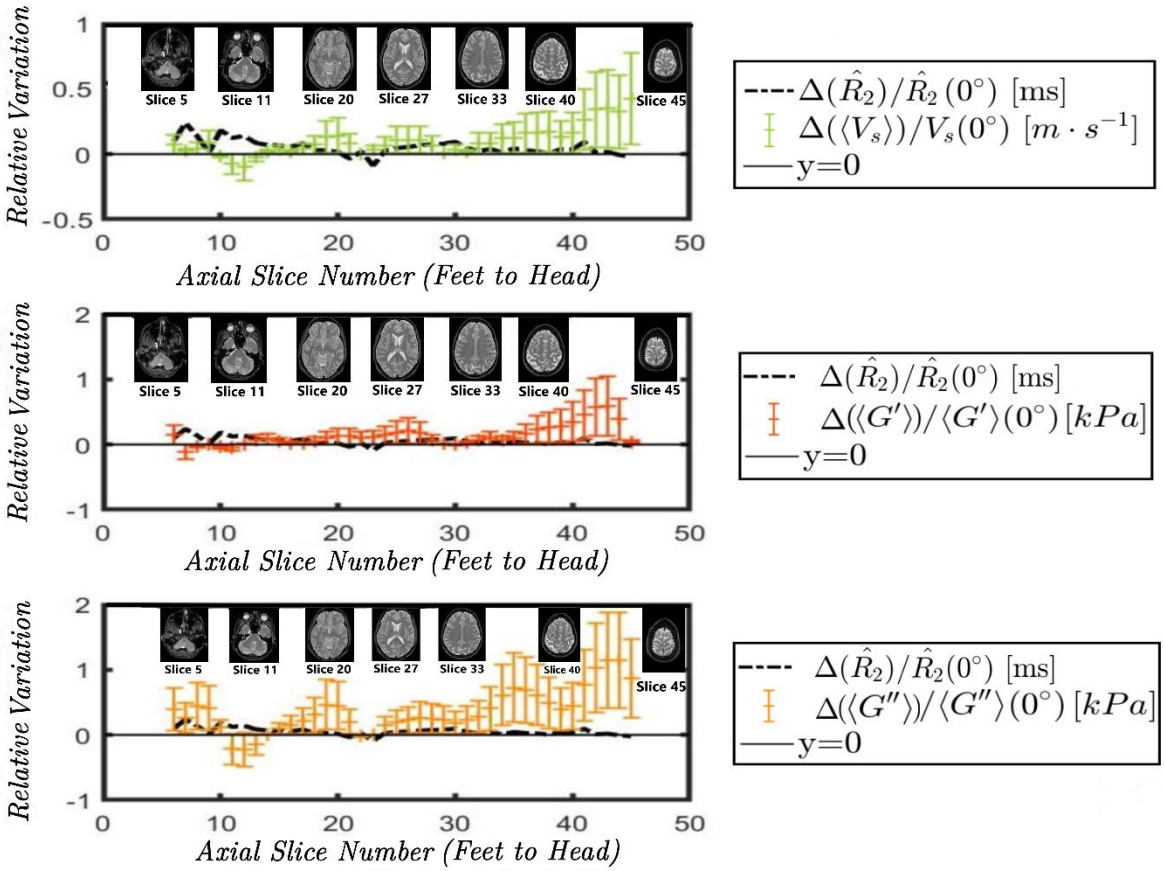

Figure 5.4.11: Relative variation of the median MR transverse relaxivity ($R_2 = 1/T_2$) (black), of the mean shear velocity, $\langle V_s\rangle_{sl}$, (green), the mean shear elasticity $\langle G'\rangle_{sl}$ (dark orange) and shear viscosity $\langle G''\rangle_{sl}$ (light orange) across the feet-head axial slices (sl). While $\hat{R}_2$ positively varies only locally in the *CSF* and orbital compartments, $\langle V_s\rangle_{sl}$, $\langle G'\rangle_{sl}$ and $\langle G''\rangle_{sl}$ increase everywhere in the cerebral tissues, remain rather constant in cerebellum ($1 \leq sl \leq 9$) and decrease around the tentorium ($10 \leq sl \leq 13$).

The curves of the relative variation of the mechanical parameters, V_s, G', *and* G'' follow a general positive gradient from slice 15 to slice 47 which implies an increase everywhere in the cerebrum. This cerebral mechanical increase is rather spread between voxels but the positive gradient becomes more pronounced towards the superior part of the brain (vertex region) from slice 40 to 47 (Figure 5.4.11). In contrast, the extracted

shear velocity and viscoelastic moduli remain the same in the cerebellum and they are even lessened around the tentorium cerebelli (Figure 5.4.11).

5.4.7 MR relaxometry and elastography

The average relative variations of the shear velocity are largely positive in the cerebral white and grey matters ($\delta V_s^{WM} = +8.5\%$ and $\delta V_s^{GM} = +9.6\%$) while it is negligible in the cerebellum ($\delta V_s^{Cblum} = +0.0\%$). Close to the CSF, in each of the three selected cerebral regions (Figure 5.3.2), they are enhanced: $\delta V_s^{A} = +15\%$ in Region A, $\delta V_s^{B} = +14\%$ in Region B, and even doubled in the superior part of the brain: $\delta V_s^{C} = +31\%$ in Region C (Table 5.4.6).

Tissue	ΔV_s [m·s^{-1}]	δV_s
White matter WM	+0.18	+8.4%
Grey matter GM	+0.20	+13.0%
Region A	+0.31	+15.1%
Region B	+0.29	+14.3%
Region C	+0.75	+31.4%

Table 5.4.6: Variations and relative variations of the shear velocity, $\Delta V_s = V_s^{17^\circ} - V_s^{0^\circ}$ and $\delta V_s = (V_s^{17^\circ} - V_s^{0^\circ})/V_s^{0^\circ}$, in cerebral white and grey matters and three regions selected near the eyes (Region A), the lateral ventricle CSF (Region B), and the subarachnoid CSF (Region C) defined in Figure 5.3.2 for comparison with results found in the CSF by Caprihan et al. [155].

Overall, they are much higher than the T_2 relative variations, which are, in comparison, negligible in the cerebral soft tissues: $\delta T_2^{WM} = +1.8\%$ and $\delta T_2^{GM} = +2.2\%$ (Table 5.4.2).

5.5 Discussions

5.5.1 MR morphometry

Roberts et al. [153] suggested a “crowding of sulcus” in the vertex regions of astronauts’ brain when back from long-duration spaceflights. In line with these results [155] and [160], Koppelmans et al. [151] additionally showed a volume decrease of the grey matter around the frontal and temporal poles and the orbits which they related to CSF redistribution. This hypothesis is sustained by studies on patients suffering from idiopathic normal pressure hydrocephalus for whom voxel-based morphometry associated CSF increases with GM decreases (and vice versa) in specific regions [162], [163].

In this study, voxel-based morphometry have led to global volume increases of $+22.4$ mL in cerebral WM (i.e. +3.53%), $+16$ mL in the CSF (+3.36%), and $+5.2$ mL in the inferior half of the cerebral GM between 0°Supine and 17°HDT positions. These results are consistent with Kramer et al. [154] who found, after long-duration spaceflight, a preserved volume of brain grey matter, volume increases in the brain white matter ($+26$ mL), lateral ventricles ($+2.2$ mL), and in the CSF (+33 mL). The overall brain values have to be nuanced, especially in the GM for which, in the inferior half of the brain (axial slices 1 to 26, and Figure 5.4.11), the relative volume variation is effectively negative with a volume decrease of -4.7 mL (-0.8%) but, in the superior half (axial slices 27 to 52, Figure 5.4.8 and Figure 5.4.11), it is positive with a volume increase of $+5.2$ mL ($+1\%$). These volume variations are corroborated by the findings of Roberts et al. [153]. First, they found significant volume increases in cerebral tissues at the vertex, along the central frontoparietal lobes, with a corresponding contraction of the adjacent CSF spaces where we have recorded a volume increase of cerebral WM and GM. Second, they found a significant decrease in GM volume in areas along the base of the brain and an expansion of the basal extra-axial CSF space volume where we have found a decrease of GM in the cerebellum and in the inferior part of the cerebrum.

Kubíková et al. [164] quantified brain vascularization and established that the numerical density of vessels, N_v, was 6-fold higher in the grey matter ($N_v^{GM} = 1350 \pm 445$ mm^{-3}) than in the white matter ($N_v^{WM} = 222 \pm 147$ mm^{-3}). Yet, first, the overall GM volume barely changed ($\delta_{GM} = +0.02\ \%$) while the overall WM volume largely increased ($\delta_{WM} = +3.53\ \%$). Second, the overall mechanical behavior of the cerebral GM and WM tissues, as recorded here, both followed very similar global increasing trends between 0°Supine and 17°HDT positions with $\Delta V_s^{WM} = +0.18$ m·s^{-1} and $\Delta V_s^{GM} = +0.20$ m·s^{-1}. Therefore, we might assume that the vascular system is rather well adjusted to microgravity-analogous conditions with little effect, if any, on the overall GM and WM overpressure. As reported by Marshall et al. [16], arterial and venous blood flows are reduced and the cross-sectional area of the internal jugular veins is largely increased in HDT positions. It might not be the case for the CSF system. With a slight volume increase ($\delta N_{CSF} = +3.38\ \%$) and an apparent loss of water content ($\delta T_2^{CSF} = -3\ \%$), the CSF might be the major source of structural and mechanical alterations of the brain in microgravity-analogous conditions. To support the implication of the vascularization in the cerebral autoregulation, blood flows could be measured as formerly performed by Marshall et al. and Asai et al. [147], [165].

5.5.2 MR relaxometry and elastography

In this study, T_2 values have been found non-significantly-lower at 17°HDT than at 0°Supine position in the CSF: $\Delta T_2 = -4$ ms or $\delta T_2 = -1.9\%$ (Table 5.4.6). T_2 reductions in CSF regions were much more significantly highlighted by Caprihan et al. [155] who found a maximum $|\Delta T_2| = 28.8$ ms ($\delta T_2 = -18\%$) in the subarachnoid CSF close to the vertex region. They had also reported a relative variation δT_2 of -14% in the eyes and 4% in the lateral ventricle (Table 5.4.6). In any case, the relative variations obtained with MRE are higher everywhere but in the cerebellum than those obtained with MR relaxometry here or by Caprihan et al. [155] (Table 5.4.6).

	ΔV_s [m·s^{-1}]	δV_s	ΔT_2 [ms]		δT_2	
Study	Current	Current	Cur	[155]	Cur	[155]
Cerebrum *Cbrum*						
White matter *WM*	+0.18	+8.5%	+2		+1.8%	
Grey matter *GM*	+0.20	+9.4%	+2	-2.6	+2.2%	-4%
Cerebrospinal fluid *CSF*						
Eyes *CSF*				-25.2		-14%
Region A (*Cbrum*)	+0.31	+15.1%				
Lateral ventricle *CSF*				-9.7		-2%
Region B (*Cbrum*)	+0.29	+14.3%				
Subarachnoid *CSF*				-28.8		-18%
Region C (*Cbrum*)	+0.75	+31.4%				
Cerebellum *Cblum*	**+0.01**	**+0.4%**	**+1**	+1.2	**+0.9%**	**+2%**

Table 5.5.1: Variations and relative variations of the shear velocity, $\Delta V_s = V_s^{17°} - V_s^{0°}$ and $\delta V_s = (V_s^{17°} - V_s^{0°})/V_s^{0°}$, and of the signal lifetime, $\Delta T_2 = T_2^{17°} - T_2^{0°}$ and $\delta T_2 = (T_2^{17°} - T_2^{0°})/T_2^{0°}$, in cerebral white and grey matters, cerebellum and three regions selected near the eyes (Region A), the lateral ventricle CSF (Region B), and the subarachnoid CSF (Region C) defined in Figure 5.3.2 for comparison with results found in the CSF by Caprihan et al. [155]. The relative variations obtained with MRE are higher everywhere but in the cerebellum than those obtained with MR relaxometry here or by Caprihan et al. [155].

5.5.3 MRE conditionning

MRE acquisitions were performed for both 0°Supine and 17°HDT positions with a unique excitation frequency ($f_{exc} = 104$ Hz) and a unique isotropic voxel ($a = 2.94$ mm) to properly sample the displacement fields in the cerebrum of a healthy subject as established in Chapter 4. Shear velocity distributions are rather narrow ($\Delta V_{Cbrum}^{0°\text{Supine}} = \pm 0.26$ m·s^{-1} and $\Delta V_{Cbrum}^{0°\text{HDT}} = \pm 0.30$ m·s^{-1}) (Table 5.4.4) so optimal conditioning can fairly be assumed everywhere in the cerebral tissues. MRE measurements can be considered as

accurate and precise as possible with a spatial sampling factor directly inferred from the extracted shear velocity averaged over the cerebrum for 0°Supine and 17°HDT positions: $s^{0°\text{Supine}} = 6.9 \pm 0.9$ and $s^{17°\text{HDT}} = 7.5 \pm 1.0$. Datasets are both well-conditioned ($6 \lesssim s_{\text{opt}} \lesssim 9$) and any mechanical alteration should be best revealed.

It is not the case in the cerebellum for which the spatial sampling factor was expected to be outside the optimal domain at $f_{exc} = 104$ Hz: $s_{Cblum}^{104\,Hz} \simeq 4.3$ (Chapter 4). The shear velocity and the associated viscoelastic moduli are thus overestimated in this study either at 0°Supine or 17°HDT positions. Such suboptimal conditions are reflected in the width of the velocity distributions in the cerebellar tissues ($\Delta V_{Cblum}^{0°\text{Supine}} = \pm 0.43$ m·s^{-1} and $\Delta V_{Cblum}^{0°\text{HDT}} = \pm 0.44$ m·s^{-1}). However, it was possible to alleviate this issue by selecting only high quality data for which MRE measurements are less sensitive to appropriate spatial sampling and the associated measurement uncertainty is reduced. For $Q \geq 150$, we have $\Delta V_{Cblum}^{0°\text{Supine}}(Q \geq 150) = \pm 0.30$ m·s^{-1} and $\Delta V_{Cblum}^{17°\text{HDT}}(Q \geq 150) = \pm 0.13$ m·s^{-1} while the mean shear velocity at $Q \geq 150$ slightly decreases from 0°Supine and 17°HDT positions in the cerebellar tissues: $\Delta V_{Cblum}^{0°\text{-}17°}(Q \geq 150) = -0.10$ m·s^{-1}. With such a high Q threshold, different voxels are selected at 0° and 17° within the cerebellum so the comparison between the two positions fails.

5.5.4 General limitations

This study presents several general limitations. First, we could not perform a local study with voxel-to-voxel comparisons of the brain volume in both 0°Supine and 17°HDT positions because as demonstrated in [152], there is a shift of the brain center of mass with upward and posterior rotation of the brain relative to the skull. Second, a comparison of the T_2 maps obtained in both position (0°Supine and 17°HDT) showed that the brain position in the head antenna had been slightly shifted during the acquisition probably because of the tilted head position in the antenna. These aspects prevented us from properly differentiating extracted voxel-by-voxel T_2 values with enhanced regional boundary artefact and from regionally comparing the modification of the number of voxels and thus of the volume in each segmented region of the brain. This would necessitate a registration of the skull as well as of the brain parenchyma as demonstrated in [152]. Moreover, the small volume changes that we observed in the cerebellum could reflect focal changes in each segmented region due to the imperfect nature of the segmentation algorithm as it is based on template images which encodes the average probability of finding different kind of tissues at each spatial location [166] [167].

Second, we only performed MRE at a single frequency, $f_{exc} = 104$ Hz, which was optimal in the cerebrum but not in the cerebellum. A prospective multi-frequency acquisition, with at least $f_{exc} = \{52,104\}$ Hz, should be implemented to further characterize the mechanical behavior of the cerebellar tissues in microgravity-analogous conditions. Or, data could be retrospectively interpolated to resample the acquired displacement fields down to $a \simeq 1.5$ mm and improve the measurement precision and accuracy in the cerebellum.

Third, the analysis at $Q \geq 150$, reported in Table 5.4.5, is questionable as voxels with high Q values are not necessarily representative of the selected brain region. In the cerebrum for example, they are essentially located in the basal region where the microgravity effect is weakened and the overall mean velocity increase $\delta V_{Cbrum}^{0°\text{-}17°} = +9\%$ (Table 5.4.4) drops down to $\delta V_{Cbrum}^{0°\text{-}17°}(Q \geq 150) = +6.1\%$ (Table 5.4.5).

Last but not least limitation is the fact that this study was performed on only one subject with bed rest and not on an astronaut cohort.

5.6 Conclusion

In this study, we used short-term bed rest, in supine (0°Supine) and head-down-tilt (17°HDT) positions, to assess MRE sensitivity to mechanical changes of the human brain. Under optimal conditions in the cerebrum and largely suboptimal conditions in the cerebellum, we could produce new insights on the overall mechanical response of brain tissues in microgravity analogous conditions:

1. A global increase of the shear velocity and the viscoelasticity moduli in the cerebrum during 17°HDT which indicate tissue stiffening with a positive gradient along the inferior-superior axis.

2. A local decrease of the shear velocity and the viscoelasticity moduli around the tentorium cerebelli.

These mechanical alterations come with:

3. A global increase of WM and CSF volumes in 17°HDT position, and increase of GM volumes in the bottom half of the brain and a decrease of GM in the top half of the brain.

4. No measurable significant difference of MR T_2 signal values between 17°HDT and 0°Supine position.

MRE provides a sensitive measurement of the changes of brain tissue under overpressure conditions everywhere in the brain but in the CSF. It is a powerful complementary approach to MR volumetry which records weakly-changing anatomical structures an MR relaxometry which only works in the CSF.

We demonstrated for the first time with MRE that microgravity exposure leads to temporary alterations of brain mechanical parameters. These findings should contribute to the interpretation of the consequences of microgravity exposure onto the human brain. They also assess the high potential of MRE for studying the mechanical response of the brain to pathological state like normal pressure hydrocephalus, hemorrhage or cancer They set the ground for advanced brain MRE at different strain amplitude given by the subject's tilt on the MRI bed [168].

Conclusion

Magnetic Resonance Elastography is an advanced imaging technique for characterizing the mechanical properties of human tissues in vivo. This thesis work aimed at establishing the optimal conditions of MRE acquisition and reconstruction in media of increasing complexity in order to ultimately address the challenging subject of MRE in the brain. The review of the literature on brain MRE presented in the introduction chapter questioned the sensitivity of the MRE technique to characterize or discriminate healthy and pathological brain tissues. The high discrepancies between MRE measurements of grey and white matter regions observed by different research groups questioned the measurement bias. The large standard deviations of MRE measurements, which are prejudicial for discriminating structurally different regions of the brain or healthy and pathological brain tissues, questioned the measurement precision. This led us to search for a MRE protocol that would allow to reproducibly achieve the most accurate and precise estimation of the mechanical parameters so to produce relevant clinical diagnostic upon consistent MRE outcomes.

For that purpose, optimal conditions of acquisition and reconstruction must be fulfilled. These conditions were introduced in Chapter 2 with the protocol of acquisition and reconstruction that was used during my thesis. We efficiently made use of the findings of a former PhD work carried in the lab by Jinlong Yue [104] in the case of mechanically homogeneous and isotropic media, which, once excited at a single frequency, can be characterized by a single shear wavelength. In the framework of algebraic inversion of differential equation (AIDE) applied to the curl of the displacement fields, two factors must be optimized: (1) the spatial sampling factor s related to the excitation frequency and the voxel size and (2) the amplitude sampling factor Q combining the amplitude of the rotational of the recorded displacement field and the measurement signal-to-noise ratio. As most organs in the human body are structured tissues, the assumption of homogeneity and isotropy does not generally hold. The aim of this thesis was to study the optimal conditions in heterogeneous and structured media to extend the approach for application to the brain.

A gradual approach was implemented in this work, starting by establishing optimal MRE conditions in the simple case of homogeneous phantoms of various stiffness (Chapter 2), then developing the analysis into a heterogeneous phantom (Chapter 3) before checking its validity onto the complex, structured, heterogeneous, and anisotropic medium that is the brain (Chapter 4 and Chapter 5). For every study presented in Chapter 2 to Chapter 4, the evaluation of the mechanical parameters obtained by MRE such as the shear velocity, elasticity, and viscosity, was carried out while optimizing the spatial sampling factor s, which, for common SNR values, should be ranging between 6

and 9, and the amplitude sampling factor Q, which should ideally be as high as possible. We showed that the optimal conditions on s and Q must be fulfilled to produce repeatable, reproducible, and robust, say valid, MRE results. These studies were carried inside and outside the optimal condition domains using either multi-frequency acquisitions or multi-scale reconstructions that allowed to determine lower bounds of Q optimal domain and the frequency-voxel size products to reach s optimal domain. For data acquired outside of the optimal s domain, appropriate resampling of the displacement field maps was performed when possible to match the frequency-voxel size product required for optimal sampling. We showed here that the resulting measurement uncertainty was then largely improved with important precision and accuracy gain – with no drawback in the case of upsampling but at the expense of a loss of spatial resolution in the case of downsampling.

The first study presented in Chapter 2 proposed optimal spatial sampling strategies by performing multi-frequency experiments on a set of four mechanically calibrated phantoms, which represented different stages of hepatic fibrosis. These phantoms could be considered as mechanically homogeneous, isotropic, and dominantly elastic. Thus, a single scalar value for every mechanical parameters was expected throughout each of the phantoms at every frequency within the associated measurement uncertainty. When the standard deviation of the shear velocity was found minimal, the spatial sampling factor always felt into the optimal domain ($6 \lesssim s \lesssim 9$) and the mean shear velocity could thus be considered as the most accurate and precise as possible within the frequency-spanned measurements. We demonstrated that, by fulfilling optimal MRE conditions, we could efficiently achieve absolute quantification and significant gradation of the different *fibrosis* stage of the four phantoms either prospectively by adequate multi-frequency acquisitions, or retrospectively by data multi-resampling conditioning. Away from the optimal conditions, MRE shear velocities are smeared out and wide of the mark. They are imprecise and either underestimated or overestimated so full gradation simply fails.

MRE data conditioning can be optimal only for a given type of tissue. It is degraded in mechanically different regions for which the spatial sampling factor necessarily differs. In order to establish optimal conditions for heterogeneous media, a second study was performed in Chapter 3 on a heterogeneous mammary phantom containing inclusions modeling tumoral lesions stiffer than the surrounding homogeneous parenchyma. The analysis approach consisted in defining, for each mechanically-different region, different optimal sampling factors through a set of acquisitions at different excitation frequencies. The challenge was to estimate the mechanical parameters in each region with the best possible precision and accuracy which would subsequently allow to best discriminate the different mechanical regions of the phantom. We were able to identify a frequency range over which the estimated mechanical parameters presented reduced standard deviations

such that the discrimination between the parenchyma and the inclusions could be effectively improved.

In a third study, multi-frequency brain MRE was performed to establish the best conditions for accurately and precisely discriminating white matter, grey matter and cerebellum in a healthy subject (Chapter 4). The cerebellum was found to be less elastic and viscous than the cerebrum whereas cerebral white and grey matters exhibited similar viscoelastic shear moduli despite their different anatomical structures. Yet, they could be better discriminated at 84 Hz for which the shear velocities of these two types of tissue presented minimal standard deviations. For the cerebellar tissues, the shear velocity standard deviation was minimized in a lower frequency range, around 50 Hz, for which and the cerebellum could be mechanically differentiated from the cerebrum. At higher frequencies, the shear velocity distributions of the different brain tissues become indistinct. We showed in this study that the simple approach developed for homogeneous and isotropic media still holds in the brain with multi optimal s domain and high enough Q. The mechanical similarity between white and grey matters, despite their different anatomical structures, corroborates the results found in the literature and question the general ability of MRE to discriminate and mechanically characterize cerebral diseases.

In order to study the sensitivity of optimally conditioned MRE data to mechanical alterations, we conducted a last MRE study in the brain in microgravity analogous conditions, which modify the intracranial pressure, hence the mechanical response of the brain. Presented in Chapter 4, this study revealed an increase of cerebral tissue stiffening with a positive gradient along the inferior-superior axis as well as a local decrease of the shear velocity and viscoelasticity moduli around the tentorium cerebelli. These increases come with a global increase of WM and CSF volumes and a formerly recorded decrease of the MR signal T_2 values in the CSF region.

All the studies presented in this thesis in phantoms or in the brain support the requirements of fulfilling MRE optimal conditions to critically improve the measurement uncertainty and produce a valid mechanical response of the targeted tissues. They obviously question the current approaches implemented today in clinical routine where the reported values of the shear viscoelasticity moduli in difficulty-addressed organs like the brain may often be biased and imprecise in a complex way that intermingles the measurement and the measured systems. In such situations, the mechanically-differing tissues or healthy and pathological tissues might be mechanically-confused and the diagnosis, might be inconclusive or, even worse, produce false positives and false negatives. In the optimal conditions ascertained here, multi-frequency MRE might be advantageously applied beyond space medicine to general brain pathology.

References

[1] J. Ophir, I. Céspedes, H. Ponnekanti, Y. Yazdi, and X. Li, "Elastography: A quantitative method for imaging the elasticity of biological tissues," *Ultrasonic Imaging*, vol. 13, no. 2, pp. 111–134, Apr. 1991, doi: 10.1016/0161-7346(91)90079-W.

[2] R. Muthupillai, D. J. Lomas, P. J. Rossman, J. F. Greenleaf, A. Manduca, and R. L. Ehman, "Magnetic resonance elastography by direct visualization of propagating acoustic strain waves," *Science*, vol. 269, no. 5232, pp. 1854–1857, Sep. 1995, doi: 10.1126/science.7569924.

[3] A. Baghani, S. Salcudean, M. Honarvar, R. S. Sahebjavaher, R. Rohling, and R. Sinkus, "Travelling wave expansion: a model fitting approach to the inverse problem of elasticity reconstruction," *IEEE Trans Med Imaging*, vol. 30, no. 8, pp. 1555–1565, Aug. 2011, doi: 10.1109/TMI.2011.2131674.

[4] R. Sinkus, M. Tanter, T. Xydeas, S. Catheline, J. Bercoff, and M. Fink, "Viscoelastic shear properties of in vivo breast lesions measured by MR elastography," *Magn Reson Imaging*, vol. 23, no. 2, pp. 159–165, Feb. 2005, doi: 10.1016/j.mri.2004.11.060.

[5] L. Huwart *et al.*, "Magnetic resonance elastography for the noninvasive staging of liver fibrosis," *Gastroenterology*, vol. 135, no. 1, pp. 32–40, Jul. 2008, doi: 10.1053/j.gastro.2008.03.076.

[6] M. A. Green, L. E. Bilston, and R. Sinkus, "In vivo brain viscoelastic properties measured by magnetic resonance elastography," *NMR in Biomedicine*, vol. 21, no. 7, pp. 755–764, Aug. 2008, doi: 10.1002/nbm.1254.

[7] S. Chatelin, A. Constantinesco, and R. Willinger, "Fifty years of brain tissue mechanical testing: from in vitro to in vivo investigations," *Biorheology*, vol. 47, no. 5–6, pp. 255–276, 2010, doi: 10.3233/BIR-2010-0576.

[8] A. Bunevicius, K. Schregel, R. Sinkus, A. Golby, and S. Patz, "REVIEW: MR elastography of brain tumors," *NeuroImage: Clinical*, vol. 25, p. 102109, Jan. 2020, doi: 10.1016/j.nicl.2019.102109.

[9] S. Chatelin, A. Constantinesco, and R. Willinger, "Fifty years of brain tissue mechanical testing: From in vitro to in vivo investigations," *Biorheology*, vol. 47, no. 5–6, pp. 255–276, 2010, doi: 10.3233/BIR-2010-0576.

[10] T. Hines, "Brain Anatomy, Anatomy of the Human Brain," *Mayfield Clinic*, 2018. http://www.mayfieldclinic.com/pe-anatbrain.htm (accessed Jan. 25, 2021).

[11] J. Guo *et al.*, "Towards an Elastographic Atlas of Brain Anatomy," *PLOS ONE*, vol. 8, no. 8, p. e71807, Aug. 2013, doi: 10.1371/journal.pone.0071807.

[12] K.-J. Streitberger *et al.*, "High-Resolution Mechanical Imaging of Glioblastoma by Multifrequency Magnetic Resonance Elastography," *PLoS ONE*, vol. 9, no. 10, p. e110588, Oct. 2014, doi: 10.1371/journal.pone.0110588.

[13] I. Sack, B. Beierbach, U. Hamhaber, D. Klatt, and J. Braun, "Non-invasive measurement of brain viscoelasticity using magnetic resonance elastography," *NMR in Biomedicine*, vol. 21, no. 3, pp. 265–271, Apr. 2008, doi: 10.1002/nbm.1189.

[14] M. C. Murphy *et al.*, "Preoperative assessment of meningioma stiffness using magnetic resonance elastography: Clinical article," *Journal of Neurosurgery*, vol. 118, no. 3, pp. 643–648, Mar. 2013, doi: 10.3171/2012.9.JNS12519.

[15] U. Hamhaber *et al.*, "In vivo magnetic resonance elastography of human brain at 7 T and 1.5 T," *Journal of Magnetic Resonance Imaging*, vol. 32, no. 3, pp. 577–583, Aug. 2010, doi: 10.1002/jmri.22294.

[16] E. H. Clayton, G. M. Genin, and P. V. Bayly, "Transmission, attenuation and reflection of shear waves in the human brain," *Journal of The Royal Society Interface*, vol. 9, no. 76, pp. 2899–2910, Nov. 2012, doi: 10.1098/rsif.2012.0325.

[17] C. L. Johnson *et al.*, "Magnetic resonance elastography of the brain using multishot spiral readouts with self-navigated motion correction: Multishot Spiral Brain MRE," *Magnetic Resonance in Medicine*, vol. 70, no. 2, pp. 404–412, Aug. 2013, doi: 10.1002/mrm.24473.

[18] J. Zhang, M. A. Green, R. Sinkus, and L. E. Bilston, "Viscoelastic properties of human cerebellum using magnetic resonance elastography," *Journal of Biomechanics*, vol. 44, no. 10, pp. 1909–1913, Jul. 2011, doi: 10.1016/j.jbiomech.2011.04.034.

[19] K. M. Pepin *et al.*, "MR Elastography Analysis of Glioma Stiffness and *IDH1* -Mutation Status," *American Journal of Neuroradiology*, vol. 39, no. 1, pp. 31–36, Jan. 2018, doi: 10.3174/ajnr.A5415.

[20] K. Uffmann *et al.*, "In vivo elasticity measurements of extremity skeletal muscle with MR elastography," *NMR in Biomedicine*, vol. 17, no. 4, pp. 181–190, Jun. 2004, doi: 10.1002/nbm.887.

[21] P. J. McCracken, A. Manduca, and R. L. Ehman, "MR Elastography for Studying the Biomechanics of Traumatic Brain Injury," p. 1.

[22] J. Braun *et al.*, "High-resolution mechanical imaging of the human brain by three-dimensional multifrequency magnetic resonance elastography at 7T," *NeuroImage*, vol. 90, pp. 308–314, Apr. 2014, doi: 10.1016/j.neuroimage.2013.12.032.

[23] M. ElSheikh *et al.*, "MR Elastography Demonstrates Unique Regional Brain Stiffness Patterns in Dementias," *American Journal of Roentgenology*, vol. 209, no. 2, pp. 403–408, Aug. 2017, doi: 10.2214/AJR.16.17455.

[24] A. Arani *et al.*, "Measuring the effects of aging and sex on regional brain stiffness with MR elastography in healthy older adults," *NeuroImage*, vol. 111, pp. 59–64, May 2015, doi: 10.1016/j.neuroimage.2015.02.016.

[25] J. Huston *et al.*, "Magnetic resonance elastography of frontotemporal dementia: MRE of Frontotemporal Dementia," *Journal of Magnetic Resonance Imaging*, vol. 43, no. 2, pp. 474–478, Feb. 2016, doi: 10.1002/jmri.24977.

[26] M. C. Murphy *et al.*, "Regional brain stiffness changes across the Alzheimer's disease spectrum," *NeuroImage: Clinical*, vol. 10, pp. 283–290, 2016, doi: 10.1016/j.nicl.2015.12.007.

[27] Z. Yin, A. J. Romano, A. Manduca, R. L. Ehman, and J. Huston, "Stiffness and Beyond: What MR Elastography Can Tell Us About Brain Structure and Function Under Physiologic and Pathologic Conditions," *Top Magn Reson Imaging*, vol. 27, no. 5, pp. 305–318, Oct. 2018, doi: 10.1097/RMR.0000000000000178.

[28] N. Fattahi *et al.*, "MR Elastography Demonstrates Increased Brain Stiffness in Normal Pressure Hydrocephalus," *American Journal of Neuroradiology*, vol. 37, no. 3, pp. 462–467, Mar. 2016, doi: 10.3174/ajnr.A4560.

[29] N. Sakai *et al.*, "Shear Stiffness of 4 Common Intracranial Tumors Measured Using MR Elastography: Comparison with Intraoperative Consistency Grading," *American Journal of Neuroradiology*, vol. 37, no. 10, pp. 1851–1859, Oct. 2016, doi: 10.3174/ajnr.A4832.

[30] P. Morar, N. M. Bagnall, and O. Faiz, "Preoperative Magnetic Resonance Enterography in Predicting Findings and Optimizing Surgical Approach in Crohn's Disease," *J Gastrointest Surg*, vol. 18, no. 9, pp. 1721–1721, Sep. 2014, doi: 10.1007/s11605-014-2535-z.

[31] E. C. Ehman, P. J. Rossman, S. A. Kruse, A. V. Sahakian, and K. J. Glaser, "Vibration safety limits for magnetic resonance elastography," *Phys Med Biol*, vol. 53, no. 4, pp. 925–935, Feb. 2008, doi: 10.1088/0031-9155/53/4/007.

[32] K.-J. Streitberger *et al.*, "In vivo viscoelastic properties of the brain in normal pressure hydrocephalus," *NMR in Biomedicine*, p. n/a-n/a, 2010, doi: 10.1002/nbm.1602.

[33] M. Simon *et al.*, "Non-invasive characterization of intracranial tumors by magnetic resonance elastography," *New Journal of Physics*, vol. 15, no. 8, p. 085024, Aug. 2013, doi: 10.1088/1367-2630/15/8/085024.

[34] J. D. Hughes, N. Fattahi, J. Van Gompel, A. Arani, R. Ehman, and J. Huston, "Magnetic resonance elastography detects tumoral consistency in pituitary macroadenomas," *Pituitary*, vol. 19, no. 3, pp. 286–292, Jun. 2016, doi: 10.1007/s11102-016-0706-5.

[35] R. Sinkus, M. Tanter, T. Xydeas, S. Catheline, J. Bercoff, and M. Fink, "Viscoelastic shear properties of in vivo breast lesions measured by MR elastography," *Magnetic Resonance Imaging*, vol. 23, no. 2, pp. 159–165, Feb. 2005, doi: 10.1016/j.mri.2004.11.060.

[36] T. Deffieux *et al.*, "Investigating liver stiffness and viscosity for fibrosis, steatosis and activity staging using shear wave elastography," *Journal of Hepatology*, vol. 62, no. 2, pp. 317–324, Feb. 2015, doi: 10.1016/j.jhep.2014.09.020.

[37] L. Landau & E. Lifchitz., *Physique théorique tome 7: Théorie de l'élasticité. MIR, 1967.* .

[38] D.Royer & E.Dileulesaint, *Elastic Waves in Solids I - Free and Guided Propagation | Daniel Royer | Springer.* .

[39] P. H. Mott and C. M. Roland, "Limits to Poisson's ratio in isotropic materials," *Phys. Rev. B*, vol. 80, no. 13, p. 132104, Oct. 2009, doi: 10.1103/PhysRevB.80.132104.

[40] N. F. Osman, "Detecting stiff masses using strain-encoded (SENC) imaging," *Magnetic Resonance in Medicine*, vol. 49, no. 3, pp. 605–608, 2003, doi: https://doi.org/10.1002/mrm.10376.

[41] J. B. Fowlkes *et al.*, "Magnetic-resonance imaging techniques for detection of elasticity variation," *Med Phys*, vol. 22, no. 11 Pt 1, pp. 1771–1778, Nov. 1995, doi: 10.1118/1.597633.

[42] J. Bishop, A. Samani, J. Sciarretta, and D. B. Plewes, "Two-dimensional MR elastography with linear inversion reconstruction: methodology and noise analysis," *Phys. Med. Biol.*, vol. 45, no. 8, pp. 2081–2091, Jul. 2000, doi: 10.1088/0031-9155/45/8/302.

[43] R. Muthupillai, P. J. Rossman, D. J. Lomas, J. F. Greenleaf, S. J. Riederer, and R. L. Ehman, "Magnetic resonance imaging of transverse acoustic strain waves," *Magnetic Resonance in Medicine*, vol. 36, no. 2, pp. 266–274, 1996, doi: https://doi.org/10.1002/mrm.1910360214.

[44] J. Braun, G. Buntkowsky, J. Bernarding, T. Tolxdorff, and I. Sack, "Simulation and analysis of magnetic resonance elastography wave images using coupled harmonic oscillators and Gaussian local frequency estimation," *Magnetic Resonance Imaging*, vol. 5, no. 19, pp. 703–713, 2001.

[45] R. Muthupillai, P. J. Rossman, D. J. Lomas, J. F. Greenleaf, S. J. Riederer, and R. L. Ehman, "Magnetic resonance imaging of transverse acoustic strain waves," *Magnetic Resonance in Medicine*, vol. 36, no. 2, pp. 266–274, 1996, doi: https://doi.org/10.1002/mrm.1910360214.

[46] J. Braun, G. Buntkowsky, J. Bernarding, T. Tolxdorff, and I. Sack, "Simulation and analysis of magnetic resonance elastography wave images using coupled harmonic oscillators and Gaussian local frequency estimation," *Magn Reson Imaging*, vol. 19, no. 5, pp. 703–713, Jun. 2001, doi: 10.1016/s0730-725x(01)00387-3.

[47] J. Braun, K. Braun, and I. Sack, "Electromagnetic actuator for generating variably oriented shear waves in MR elastography," *Magnetic Resonance in Medicine*, vol. 50, no. 1, pp. 220–222, 2003, doi: https://doi.org/10.1002/mrm.10479.

[48] Y. K. Mariappan, K. J. Glaser, and R. L. Ehman, "Magnetic resonance elastography: A review," *Clinical Anatomy*, vol. 23, no. 5, pp. 497–511, 2010, doi: https://doi.org/10.1002/ca.21006.

[49] P. Asbach *et al.*, "Assessment of liver viscoelasticity using multifrequency MR elastography," *Magnetic Resonance in Medicine*, vol. 60, no. 2, pp. 373–379, 2008, doi: https://doi.org/10.1002/mrm.21636.

[50] D. Klatt *et al.*, "In Vivo Determination of Hepatic Stiffness Using Steady-State Free Precession Magnetic Resonance Elastography:," *Investigative Radiology*, vol. 41, no. 12, pp. 841–848, Dec. 2006, doi: 10.1097/01.rli.0000244341.16372.08.

[51] M. Yin, O. Rouvière, and R. L. Ehman, "Shear Wave Diffraction Fields Generated by Longitudinal MRE Drivers," p. 1.

[52] Z. T. H. Tse, Y. J. Chan, H. Janssen, A. Hamed, I. Young, and M. Lamperth, "Piezoelectric actuator design for MR elastography: implementation and vibration issues," *The International Journal of Medical Robotics and Computer Assisted Surgery*, vol. 7, no. 3, pp. 353–360, 2011, doi: https://doi.org/10.1002/rcs.405.

[53] P. J. Rossman and R. Muthupillai, "DRIVER DEVICE FOR MR ELASTOGRAPHY," p. 12.

[54] S. A. Kruse *et al.*, "Magnetic Resonance Elastography of the Brain," *Neuroimage*, vol. 39, no. 1, pp. 231–237, Jan. 2008, doi: 10.1016/j.neuroimage.2007.08.030.

[55] S. A. Kruse, M. A. Dresner, P. J. Rossman, J. P. Felmlee, C. R. Jack, and R. L. Ehman, "'Palpation of the Brain' Using Magnetic Resonance Elastography," p. 1.

[56] M. A. Green, L. E. Bilston, and R. Sinkus, "In vivo brain viscoelastic properties measured by magnetic resonance elastography," *NMR Biomed*, vol. 21, no. 7, pp. 755–764, Aug. 2008, doi: 10.1002/nbm.1254.

[57] Uffmann, "Determination of Gray and White Matter Elasticity with MR Elastography.," presented at the In Proceedings of the 12th Meeting of the International Society for Magnetic Resonance in Medicine (Kyoto) ; 1768, 2004, Accessed: Nov. 26, 2020. [Online]. Available: https://cds.ismrm.org/ismrm-2004/Files/001768.pdf.

[58] P. J. McCracken, A. Manduca, J. Felmlee, and R. L. Ehman, "Mechanical transient-based magnetic resonance elastography," *Magn Reson Med*, vol. 53, no. 3, pp. 628–639, Mar. 2005, doi: 10.1002/mrm.20388.

[59] L. Xu, Y. Lin, Z. N. Xi, H. Shen, and P. Y. Gao, "Magnetic Resonance Elastography of the Human Brain: A Preliminary Study," *Acta Radiologica*, vol. 48, no. 1, pp. 112–115, Jan. 2007, doi: 10.1080/02841850601026401.

[60] U. Hamhaber, I. Sack, S. Papazoglou, J. Rump, D. Klatt, and J. Braun, "Three-dimensional analysis of shear wave propagation observed by in vivo magnetic resonance elastography of the brain," *Acta Biomater*, vol. 3, no. 1, pp. 127–137, Jan. 2007, doi: 10.1016/j.actbio.2006.08.007.

[61] U. Hamhaber *et al.*, "In vivo magnetic resonance elastography of human brain at 7 T and 1.5 T," *J Magn Reson Imaging*, vol. 32, no. 3, pp. 577–583, Sep. 2010, doi: 10.1002/jmri.22294.

[62] I. Sack, B. Beierbach, U. Hamhaber, D. Klatt, and J. Braun, "Non-invasive measurement of brain viscoelasticity using magnetic resonance elastography," *NMR Biomed*, vol. 21, no. 3, pp. 265–271, Mar. 2008, doi: 10.1002/nbm.1189.

[63] D. Klatt, U. Hamhaber, P. Asbach, J. Braun, and I. Sack, "Noninvasive assessment of the rheological behavior of human organs using multifrequency MR elastography: a study of brain and liver viscoelasticity," *Phys. Med. Biol.*, vol. 52, no. 24, p. 7281, Nov. 2007, doi: 10.1088/0031-9155/52/24/006.

[64] J. Wuerfel *et al.*, "MR-elastography reveals degradation of tissue integrity in multiple sclerosis," *Neuroimage*, vol. 49, no. 3, pp. 2520–2525, Feb. 2010, doi: 10.1016/j.neuroimage.2009.06.018.

[65] K.-J. Streitberger *et al.*, "In vivo viscoelastic properties of the brain in normal pressure hydrocephalus," *NMR in Biomedicine*, vol. 24, no. 4, pp. 385–392, 2011, doi: https://doi.org/10.1002/nbm.1602.

[66] P. Latta, M. L. H. Gruwel, P. Debergue, B. Matwiy, U. N. Sboto-Frankenstein, and B. Tomanek, "Convertible pneumatic actuator for magnetic resonance elastography of the brain," *Magnetic Resonance Imaging*, vol. 29, no. 1, pp. 147–152, Jan. 2011, doi: 10.1016/j.mri.2010.07.014.

[67] D. Gallichan, M. D. Robson, A. Bartsch, and K. L. Miller, "TREMR: Table-resonance elastography with MR," *Magn Reson Med*, vol. 62, no. 3, pp. 815–821, Sep. 2009, doi: 10.1002/mrm.22046.

[68] S. Zhao, A. Jackson, and G. J. Parker, "Auto-elastography of the brain," p. 1.

[69] J. B. Weaver *et al.*, "Brain mechanical property measurement using MRE with intrinsic activation," *Phys Med Biol*, vol. 57, no. 22, pp. 7275–7287, Nov. 2012, doi: 10.1088/0031-9155/57/22/7275.

[70] S. Catheline, "Passive elastography: A shear wave tomography of the human body," *The Journal of the Acoustical Society of America*, vol. 141, no. 5, pp. 3527–3527, May 2017, doi: 10.1121/1.4987440.

[71] T. Gallot, S. Catheline, P. Roux, J. Brum, N. Benech, and C. Negreira, "Passive elastography: shear-wave tomography from physiological-noise correlation in soft tissues," *IEEE Transactions on Ultrasonics, Ferroelectrics, and Frequency Control*, vol. 58, no. 6, pp. 1122–1126, Jun. 2011, doi: 10.1109/TUFFC.2011.1920.

[72] B. Giammarinaro and S. Catheline, "Passive elastography in soft-tissues: Phase velocity measurement," *The Journal of the Acoustical Society of America*, vol. 141, no. 5, pp. 3955–3955, May 2017, doi: 10.1121/1.4988987.

[73] Samuel Patz et al., "Observation of Functional Magnetic Resonance Elastography (fMRE) in Mouse Brain," *ISMRM 2015*.

[74] M. Tardieu, "Élastographie par résonance magnétique et onde de pression guidée," Thesis, Université Paris-Saclay, Orsay, France, 2014.

[75] P. Garteiser *et al.*, "Rapid acquisition of multifrequency, multislice and multidirectional MR elastography data with a fractionally encoded gradient echo sequence," *NMR Biomed*, vol. 26, no. 10, pp. 1326–1335, Oct. 2013, doi: 10.1002/nbm.2958.

[76] J. Rump, D. Klatt, J. Braun, C. Warmuth, and I. Sack, "Fractional encoding of harmonic motions in MR elastography," *Magn Reson Med*, vol. 57, no. 2, pp. 388–395, Feb. 2007, doi: 10.1002/mrm.21152.

[77] R. Sinkus, J. Lorenzen, D. Schrader, M. Lorenzen, M. Dargatz, and D. Holz, "High-resolution tensor MR elastography for breast tumour detection," *Phys. Med. Biol.*, vol. 45, no. 6, pp. 1649–1664, May 2000, doi: 10.1088/0031-9155/45/6/317.

[78] F. Julea, "Conditions de validité de l'Élastographie par Résonance Magnétique," p. 195.

[79] A. A. Oberai, N. H. Gokhale, and G. R. F. o, "Solution of inverse problems in elasticity imaging using the adjoint method," *Inverse Problems*, vol. 19, no. 2, pp. 297–313, Feb. 2003, doi: 10.1088/0266-5611/19/2/304.

[80] E. E. Van Houten, K. D. Paulsen, M. I. Miga, F. E. Kennedy, and J. B. Weaver, "An overlapping subzone technique for MR-based elastic property reconstruction," *Magn Reson Med*, vol. 42, no. 4, pp. 779–786, Oct. 1999, doi: 10.1002/(sici)1522-2594(199910)42:4<779::aid-mrm21>3.0.co;2-z.

[81] F. Kallel and M. Bertrand, "Tissue elasticity reconstruction using linear perturbation method," *IEEE Trans Med Imaging*, vol. 15, no. 3, pp. 299–313, 1996, doi: 10.1109/42.500139.

[82] H. Eskandari, S. E. Salcudean, R. Rohling, and I. Bell, "Real-time solution of the finite element inverse problem of viscoelasticity," *Inverse Problems*, vol. 27, no. 8, p. 085002, Jul. 2011, doi: 10.1088/0266-5611/27/8/085002.

[83] M. Honarvar, R. Rohling, and S. E. Salcudean, "A comparison of direct and iterative finite element inversion techniques in dynamic elastography," *Phys Med Biol*, vol. 61, no. 8, pp. 3026–3048, Apr. 2016, doi: 10.1088/0031-9155/61/8/3026.

[84] J. Zhang *et al.*, "Short-Term Repeatability of Magnetic Resonance Elastography at 3.0T: Effects of Motion-Encoding Gradient Direction, Slice Position, and Meal Ingestion," *Journal of magnetic resonance imaging : JMRI*, vol. 43, Sep. 2015, doi: 10.1002/jmri.25035.

[85] E. Park and A. M. Maniatty, "Shear modulus reconstruction in dynamic elastography: time harmonic case," *Phys Med Biol*, vol. 51, no. 15, pp. 3697–3721, Aug. 2006, doi: 10.1088/0031-9155/51/15/007.

[86] A. Manduca, R. Muthupillai, P. Rossman, J. Greenleaf, and R. Ehman, "Local wavelength estimation for magnetic resonance elastography," *Proceedings of 3rd IEEE International Conference on Image Processing*, 1996, doi: 10.1109/ICIP.1996.560548.

[87] H. Knutsson, C. Westin, and G. Granlund, "Local multiscale frequency and bandwidth estimation," *Proceedings of 1st International Conference on Image Processing*, 1994, doi: 10.1109/ICIP.1994.413270.

[88] K. P. McGee *et al.*, "Calculation of Shear Stiffness in Noise Dominated Magnetic Resonance Elastography (MRE) Data Based on Principal Frequency Estimation," *Phys Med Biol*, vol. 56, no. 14, pp. 4291–4309, Jul. 2011, doi: 10.1088/0031-9155/56/14/006.

[89] A. J. Romano, J. J. Shirron, and J. A. Bucaro, "On the noninvasive determination of material parameters from a knowledge of elastic displacements theory and numerical simulation," *IEEE Trans Ultrason Ferroelectr Freq Control*, vol. 45, no. 3, pp. 751–759, 1998, doi: 10.1109/58.677725.

[90] T. E. Oliphant, A. Manduca, R. L. Ehman, and J. F. Greenleaf, "Complex-valued stiffness reconstruction for magnetic resonance elastography by algebraic inversion of the differential equation," *Magn Reson Med*, vol. 45, no. 2, pp. 299–310, Feb. 2001, doi: 10.1002/1522-2594(200102)45:2<299::aid-mrm1039>3.0.co;2-o.

[91] A. Manduca *et al.*, "Magnetic resonance elastography: non-invasive mapping of tissue elasticity," *Med Image Anal*, vol. 5, no. 4, pp. 237–254, Dec. 2001, doi: 10.1016/s1361-8415(00)00039-6.

[92] Y. K. Mariappan, K. J. Glaser, R. D. Hubmayr, A. Manduca, R. L. Ehman, and K. P. McGee, "Magnetic Resonance Elastography of human lung parenchyma: technical development, theorotical modeling and in vivo validation.," *J Magn Reson Imaging*, vol. 33, no. 6, pp. 1351–1361, Jun. 2011, doi: 10.1002/jmri.22550.

[93] N. Connesson, E. H. Clayton, P. V. Bayly, and F. Pierron, "Extension of the Optimized Virtual Fields Method to estimate viscoelastic material parameters from 3D dynamic displacement fields," *Strain*, vol. 51, no. 2, pp. 110–134, Apr. 2015, doi: 10.1111/str.12126.

[94] D. Fovargue, S. Kozerke, R. Sinkus, and D. Nordsletten, "Robust MR elastography stiffness quantification using a localized divergence free finite element reconstruction," *Med Image Anal*, vol. 44, pp. 126–142, 2018, doi: 10.1016/j.media.2017.12.005.

[95] J. Mclaughlin, D. Renzi, J. R. Yoon, R. L. Ehman, and A. Manduca, "Variance controlled shear stiffness images for MRE data," in *3rd IEEE International Symposium on Biomedical Imaging: Nano to Macro, 2006.*, Apr. 2006, pp. 960–963, doi: 10.1109/ISBI.2006.1625079.

[96] K. Riek *et al.*, "Wide-range dynamic magnetic resonance elastography," *J Biomech*, vol. 44, no. 7, pp. 1380–1386, Apr. 2011, doi: 10.1016/j.jbiomech.2010.12.031.

[97] S. Papazoglou, U. Hamhaber, J. Braun, and I. Sack, "Algebraic Helmholtz inversion in planar magnetic resonance elastography," *Phys Med Biol*, vol. 53, no. 12, pp. 3147–3158, Jun. 2008, doi: 10.1088/0031-9155/53/12/005.

[98] R. Okamoto, E. Clayton, and P. Bayly, "Viscoelastic properties of soft gels: a comparison of magnetic resonance elastography and dynamic shear testing in the shear wave regime," *Phys Med Biol*, vol. 56, no. 19, pp. 6379–6400, Oct. 2011, doi: 10.1088/0031-9155/56/19/014.

[99] A. Manduca, R. Muthupillai, P. J. Rossman, J. F. Greenleaf, and R. L. Ehman, "Image processing for magnetic resonance elastography," in *Proceedings of SPIE - The International Society for Optical Engineering*, Dec. 1996, vol. 2710, pp. 616–623, doi: 10.1117/12.237965.

[100] X. Maitre, E. Lamain, R. Sinkus, B. Louis, and L. Darrasse, "Whole brain MRE with guided pressure waves," p. 1.

[101] Hagot et al., "Magnetic Resonance Elastography of the Upper Airways with Guided Pressure Waves," presented at the ISMRM, Salt Lake City, 2013, Accessed: Nov. 26, 2020. [Online]. Available: http://archive.ismrm.org/2013/2426.html.

[102] H. Souris L., "Suivi en imagerie par résonance magnétique de la température et des propriétés viscoélastiques des tissus cérébraux dans le cadre des thermothérapies," p. 187.

[103] J. L. Yue *et al.*, "Acquisition and reconstruction conditions *in silico* for accurate and precise magnetic resonance elastography," *Physics in Medicine & Biology*, vol. 62, no. 22, pp. 8655–8670, Nov. 2017, doi: 10.1088/1361-6560/aa9164.

[104] Yue, "L'élastographie par résonance magnétique et l'élastographie ultrasonore par ondes de cisaillement supersonic: simulation, comparaison expérimentale et l'application pour la caractérisation du foie," Thesis, Université Paris-Saclay, Orsay, France, 2018.

[105] J. M. Horowitz *et al.*, "ACR Appropriateness Criteria® Chronic Liver Disease," *Journal of the American College of Radiology*, vol. 14, no. 5, pp. S103–S117, May 2017, doi: 10.1016/j.jacr.2017.02.011.

[106] N. G. Ramião, P. S. Martins, R. Rynkevic, A. A. Fernandes, M. Barroso, and D. C. Santos, "Biomechanical properties of breast tissue, a state-of-the-art review," *Biomech Model Mechanobiol*, vol. 15, no. 5, pp. 1307–1323, Oct. 2016, doi: 10.1007/s10237-016-0763-8.

[107] H. S. Leitão *et al.*, "Hepatic Fibrosis, Inflammation, and Steatosis: Influence on the MR Viscoelastic and Diffusion Parameters in Patients with Chronic Liver Disease," *Radiology*, vol. 283, no. 1, pp. 98–107, Apr. 2017, doi: 10.1148/radiol.2016151570.

[108] A. Manduca *et al.*, "Magnetic resonance elastography: Non-invasive mapping of tissue elasticity," *Medical Image Analysis*, vol. 5, no. 4, Art. no. 4, Dec. 2001, doi: 10.1016/S1361-8415(00)00039-6.

[109] A. Baghani, S. Salcudean, and R. Rohling, "Theoretical limitations of the elastic wave equation inversion for tissue elastography," *The Journal of the Acoustical Society of America*, vol. 126, no. 3, pp. 1541–1551, Sep. 2009, doi: 10.1121/1.3180495.

[110] S. Papazoglou, U. Hamhaber, J. Braun, and I. Sack, "Algebraic Helmholtz inversion in planar magnetic resonance elastography," *Phys. Med. Biol.*, vol. 53, no. 12, pp. 3147–3158, May 2008, doi: 10.1088/0031-9155/53/12/005.

[111] F. Julea, "Conditions de validité de l'Élastographie par Résonance Magnétique," thesis, Université Paris-Saclay (ComUE), 2018.

[112] F. Dittmann, S. Hirsch, H. Tzschätzsch, J. Guo, J. Braun, and I. Sack, "In vivo wideband multifrequency MR elastography of the human brain and liver," *Magnetic Resonance in Medicine*, vol. 76, no. 4, Art. no. 4, Oct. 2016, doi: 10.1002/mrm.26006.

[113] F. Julea, H. Wang, J. L. Yue, T. Boucneau, C. Pellot-Barakat, and X. Maître, "Magnetic resonance elastography accuracy and precision in rat lung and liver at 1.5 T," presented at the ISMRM-ESMRMB, Paris, France, 2018.

[114] Y. S. Kim, Y. N. Jang, and J. S. Song, "Comparison of gradient-recalled echo and spin-echo echo-planar imaging MR elastography in staging liver fibrosis: a meta-analysis," *Eur Radiol*, vol. 28, no. 4, pp. 1709–1718, Apr. 2018, doi: 10.1007/s00330-017-5149-5.

[115] T. Lefebvre *et al.*, "Prospective comparison of transient, point shear wave, and magnetic resonance elastography for staging liver fibrosis," *Eur Radiol*, vol. 29, no. 12, pp. 6477–6488, Dec. 2019, doi: 10.1007/s00330-019-06331-4.

[116] L. Z. Shuck and S. H. Advani, "Rheological Response of Human Brain Tissue in Shear," *J. Basic Eng*, vol. 94, no. 4, pp. 905–911, Dec. 1972, doi: 10.1115/1.3425588.

[117] M. Bigot, F. Chauveau, C. Amaz, R. Sinkus, O. Beuf, and S. A. Lambert, "The apparent mechanical effect of isolated amyloid-β and α-synuclein aggregates revealed by multi-frequency MRE," *NMR in Biomedicine*, vol. 33, no. 1, p. e4174, 2020, doi: 10.1002/nbm.4174.

[118] J. Oudry, J. Vappou, P. Choquet, R. Willinger, L. Sandrin, and A. Constantinesco, "Ultrasound-based transient elastography compared to magnetic resonance elastography in soft tissue-mimicking gels," *Phys. Med. Biol.*, vol. 54, no. 22, pp. 6979–6990, Nov. 2009, doi: 10.1088/0031-9155/54/22/015.

[119] R Core team, *R: A Language and Environment for Statistical Computing*. Vienna, Austria: R Foundation for Statistical Computing.

[120] J. Oudry, T. Lynch, J. Vappou, L. Sandrin, and V. Miette, "Comparison of four different techniques to evaluate the elastic properties of phantom in elastography: is there a gold standard?," *Phys Med Biol*, vol. 59, no. 19, pp. 5775–5793, Oct. 2014, doi: 10.1088/0031-9155/59/19/5775.

[121] R. J. Okamoto, E. H. Clayton, and P. V. Bayly, "Viscoelastic properties of soft gels: comparison of magnetic resonance elastography and dynamic shear testing in the shear wave regime," *Phys. Med. Biol.*, vol. 56, no. 19, pp. 6379–6400, Sep. 2011, doi: 10.1088/0031-9155/56/19/014.

[122] S. Papazoglou, U. Hamhaber, J. Braun, and I. Sack, "Algebraic Helmholtz inversion in planar magnetic resonance elastography," *Phys. Med. Biol.*, vol. 53, no. 12, pp. 3147–3158, May 2008, doi: 10.1088/0031-9155/53/12/005.

[123] J. Oudry, J. Vappou, P. Choquet, R. Willinger, L. Sandrin, and A. Constantinesco, "Ultrasound-based transient elastography compared to magnetic resonance elastography in soft tissue-mimicking gels," *Phys. Med. Biol.*, vol. 54, no. 22, pp. 6979–6990, Nov. 2009, doi: 10.1088/0031-9155/54/22/015.

[124] M. W. Urban, J. Chen, and R. L. Ehman, "Comparison of shear velocity dispersion in viscoelastic phantoms measured by ultrasound-based shear wave elastography and magnetic resonance elastography," in *2017 IEEE International Ultrasonics Symposium (IUS)*, Sep. 2017, pp. 1–4, doi: 10.1109/ULTSYM.2017.8092418.

[125] J. M. Horowitz *et al.*, "ACR Appropriateness Criteria® Chronic Liver Disease," *Journal of the American College of Radiology*, vol. 14, no. 5, pp. S103–S117, May 2017, doi: 10.1016/j.jacr.2017.02.011.

[126] M. Yin, K. J. Glaser, J. A. Talwalkar, J. Chen, A. Manduca, and R. L. Ehman, "Hepatic MR Elastography: Clinical Performance in a Series of 1377 Consecutive Examinations," *Radiology*, vol. 278, no. 1, pp. 114–124, Jul. 2015, doi: 10.1148/radiol.2015142141.

[127] P. Garteiser, S. Doblas, and B. E. V. Beers, "Magnetic resonance elastography of liver and spleen: Methods and applications," *NMR in Biomedicine*, vol. 31, no. 10, p. e3891, 2018, doi: 10.1002/nbm.3891.

[128] R. Muthupillai and R. L. Ehman, "Spectrally-Selective Gradient Waveforms: Applications in MR Elastography," in *Proceedings of the International Society for Magnetic Resonance in Medicine, Scientific Meeting and Exhibition*, 1998, p. 1.

[129] D. Klatt, U. Hamhaber, P. Asbach, J. Braun, and I. Sack, "Noninvasive assessment of the rheological behavior of human organs using multifrequency MR elastography: a

study of brain and liver viscoelasticity," *Phys. Med. Biol.*, vol. 52, no. 24, Art. no. 24, 2007, doi: 10.1088/0031-9155/52/24/006.

[130] P. Asbach *et al.*, "Assessment of liver viscoelasticity using multifrequency MR elastography," *Magnetic Resonance in Medicine*, vol. 60, no. 2, Art. no. 2, 2008, doi: 10.1002/mrm.21636.

[131] K.-J. Streitberger *et al.*, "Multifrequency magnetic resonance elastography of the brain reveals tissue degeneration in neuromyelitis optica spectrum disorder," *Eur Radiol*, vol. 27, no. 5, pp. 2206–2215, May 2017, doi: 10.1007/s00330-016-4561-6.

[132] F. Schrank *et al.*, "Cardiac-gated steady-state multifrequency magnetic resonance elastography of the brain: Effect of cerebral arterial pulsation on brain viscoelasticity," *J Cereb Blood Flow Metab*, p. 0271678X19850936, May 2019, doi: 10.1177/0271678X19850936.

[133] C. Balleyguier, A. B. Lakhdar, A. Dunant, M.-C. Mathieu, S. Delaloge, and R. Sinkus, "Value of whole breast magnetic resonance elastography added to MRI for lesion characterization," *NMR in Biomedicine*, vol. 31, no. 1, p. e3795, 2018, doi: 10.1002/nbm.3795.

[134] A. L. McKnight, J. L. Kugel, P. J. Rossman, A. Manduca, L. C. Hartmann, and R. L. Ehman, "MR Elastography of Breast Cancer: Preliminary Results," *American Journal of Roentgenology*, vol. 178, no. 6, pp. 1411–1417, Jun. 2002, doi: 10.2214/ajr.178.6.1781411.

[135] J. Bishop, G. Poole, M. Leitch, and D. B. Plewes, "Magnetic resonance imaging of shear wave propagation in excised tissue," *Journal of Magnetic Resonance Imaging*, vol. 8, no. 6, pp. 1257–1265, 1998, doi: 10.1002/jmri.1880080613.

[136] M. Reiss-Zimmermann *et al.*, "High Resolution Imaging of Viscoelastic Properties of Intracranial Tumours by Multi-Frequency Magnetic Resonance Elastography," *Clin Neuroradiol*, vol. 25, no. 4, pp. 371–378, Dec. 2015, doi: 10.1007/s00062-014-0311-9.

[137] L. Xu, Y. Lin, J. C. Han, Z. N. Xi, H. Shen, and P. Y. Gao, "Magnetic resonance elastography of brain tumors: preliminary results," *Acta Radiol*, vol. 48, no. 3, pp. 327–330, Apr. 2007, doi: 10.1080/02841850701199967.

[138] J. D. Hughes *et al.*, "Higher-Resolution Magnetic Resonance Elastography in Meningiomas to Determine Intratumoral Consistency," *Neurosurgery*, vol. 77, no. 4, pp. 653–659, Oct. 2015, doi: 10.1227/NEU.0000000000000892.

[139] J. Weickenmeier *et al.*, "Brain stiffens post mortem," *Journal of the Mechanical Behavior of Biomedical Materials*, vol. 84, pp. 88–98, Aug. 2018, doi: 10.1016/j.jmbbm.2018.04.009.

[140] Y. Feng, E. H. Clayton, Y. Chang, R. J. Okamoto, and P. V. Bayly, "Viscoelastic properties of the ferret brain measured in vivo at multiple frequencies by magnetic resonance elastography," *Journal of Biomechanics*, vol. 46, no. 5, pp. 863–870, Mar. 2013, doi: 10.1016/j.jbiomech.2012.12.024.

[141] Tardieu et al., "Magnetic resonance elastography with guided pressure waves," Submission in progress.

[142] P. D. Hodkinson, R. A. Anderton, B. N. Posselt, and K. J. Fong, "An overview of space medicine," *British Journal of Anaesthesia*, vol. 119, pp. i143–i153, Dec. 2017, doi: 10.1093/bja/aex336.

[143] M. Kermorgant *et al.*, "Impacts of Microgravity Analogs to Spaceflight on Cerebral Autoregulation," *Frontiers in Physiology*, vol. 11, Jul. 2020, doi: 10.3389/fphys.2020.00778.

[144] R. Zhang, J. H. Zuckerman, J. A. Pawelczyk, and B. D. Levine, "Effects of head-down-tilt bed rest on cerebral hemodynamics during orthostatic stress," *Journal of Applied Physiology*, vol. 83, no. 6, pp. 2139–2145, Dec. 1997, doi: 10.1152/jappl.1997.83.6.2139.

[145] V. Novak, P. Novak, J. M. Spies, and P. A. Low, "Autoregulation of cerebral blood flow in orthostatic hypotension," *Stroke*, vol. 29, no. 1, pp. 104–111, Jan. 1998, doi: 10.1161/01.str.29.1.104.

[146] K. I. Iwasaki, R. Zhang, J. H. Zuckerman, J. A. Pawelczyk, and B. D. Levine, "Effect of head-down-tilt bed rest and hypovolemia on dynamic regulation of heart rate and blood pressure," *Am J Physiol Regul Integr Comp Physiol*, vol. 279, no. 6, pp. R2189-2199, Dec. 2000, doi: 10.1152/ajpregu.2000.279.6.R2189.

[147] K. Marshall-Goebel *et al.*, "Effects of short-term exposure to head-down tilt on cerebral hemodynamics: a prospective evaluation of a spaceflight analog using phase-contrast MRI," *Journal of Applied Physiology*, vol. 120, no. 12, pp. 1466–1473, Jun. 2016, doi: 10.1152/japplphysiol.00841.2015.

[148] S. E. Parazynski, A. R. Hargens, B. Tucker, M. Aratow, J. Styf, and A. Crenshaw, "Transcapillary fluid shifts in tissues of the head and neck during and after simulated microgravity," *Journal of Applied Physiology*, vol. 71, no. 6, pp. 2469–2475, Dec. 1991, doi: 10.1152/jappl.1991.71.6.2469.

[149] T. P. Moore and W. E. Thornton, "Space shuttle inflight and postflight fluid shifts measured by leg volume changes," *Aviat Space Environ Med*, vol. 58, no. 9 Pt 2, pp. A91-96, Sep. 1987.

[150] K. Marshall-Bowman, M. R. Barratt, and C. R. Gibson, "Ophthalmic changes and increased intracranial pressure associated with long duration spaceflight: An emerging understanding," *Acta Astronautica*, vol. 87, pp. 77–87, Jun. 2013, doi: 10.1016/j.actaastro.2013.01.014.

[151] V. Koppelmans, J. J. Bloomberg, A. P. Mulavara, and R. D. Seidler, "Brain structural plasticity with spaceflight," *npj Microgravity*, vol. 2, no. 1, Art. no. 1, Dec. 2016, doi: 10.1038/s41526-016-0001-9.

[152] D. R. Roberts, X. Zhu, A. Tabesh, E. W. Duffy, D. A. Ramsey, and T. R. Brown, "Structural Brain Changes following Long-Term 6° Head-Down Tilt Bed Rest as an Analog for Spaceflight," *American Journal of Neuroradiology*, vol. 36, no. 11, pp. 2048–2054, Nov. 2015, doi: 10.3174/ajnr.A4406.

[153] D. R. Roberts *et al.*, "Effects of Spaceflight on Astronaut Brain Structure as Indicated on MRI," *New England Journal of Medicine*, vol. 377, no. 18, pp. 1746–1753, Nov. 2017, doi: 10.1056/NEJMoa1705129.

[154] L. A. Kramer *et al.*, "Intracranial Effects of Microgravity: A Prospective Longitudinal MRI Study," *Radiology*, vol. 295, no. 3, pp. 640–648, Jun. 2020, doi: 10.1148/radiol.2020191413.

[155] A. Caprihan, J. A. Sanders, H. A. Cheng, and J. A. Loeppky, "Effect of head-down tilt on brain water distribution," *European Journal of Applied Physiology*, vol. 79, no. 4, pp. 367–373, Apr. 1999, doi: 10.1007/s004210050522.

[156] V. A. Convertino, R. Bisson, R. Bates, D. Goldwater, and H. Sandler, "Effects of antiorthostatic bedrest on the cardiorespiratory responses to exercise," *Aviat Space Environ Med*, vol. 52, no. 4, pp. 251–255, Apr. 1981.

[157] J. E. Greenleaf, L. Silverstein, J. Bliss, V. Langenhcim, H. Rossow, and C. Chao, "Physiological Responses to Prolonged Bed Rest and Fluid Immersion in Man: A Compendium of Research (1974-1980)," p. 111.

[158] L. I. Kakurin, V. I. Lobachik, V. M. Mikhailov, and Y. A. Senkevich, "Antiorthostatic hypokinesia as a method of weightlessness simulation," *Aviat Space Environ Med*, vol. 47, no. 10, pp. 1083–1086, Oct. 1976.

[159] A. R. Hargens, C. M. Tipton, P. D. Gollnick, S. J. Mubarak, B. J. Tucker, and W. H. Akeson, "Fluid shifts and muscle function in humans during acute simulated weightlessness," *J Appl Physiol Respir Environ Exerc Physiol*, vol. 54, no. 4, pp. 1003–1009, Apr. 1983, doi: 10.1152/jappl.1983.54.4.1003.

[160] N. Maurice, B. Roussel, H. Mehier, G. Gauquelin, and C. Gharib, "Relationship between hormones and brain water content measured by 1H magnetic resonance

spectroscopy during simulated weightlessness in man," *Physiologist*, vol. 33, no. 1 Suppl, pp. S104-105, Feb. 1990.

[161] D. R. Roberts *et al.*, "Prolonged Microgravity Affects Human Brain Structure and Function," *American Journal of Neuroradiology*, Oct. 2019, doi: 10.3174/ajnr.A6249.

[162] F. Yamashita *et al.*, "Voxel-Based Morphometry of Disproportionate Cerebrospinal Fluid Space Distribution for the Differential Diagnosis of Idiopathic Normal Pressure Hydrocephalus," *Journal of Neuroimaging*, vol. 24, no. 4, pp. 359–365, 2014, doi: 10.1111/jon.12049.

[163] K. Ishii *et al.*, "Voxel-based analysis of gray matter and CSF space in idiopathic normal pressure hydrocephalus," *Dement Geriatr Cogn Disord*, vol. 25, no. 4, pp. 329–335, 2008, doi: 10.1159/000119521.

[164] T. Kubíková, P. Kochová, P. Tomášek, K. Witter, and Z. Tonar, "Numerical and length densities of microvessels in the human brain: Correlation with preferential orientation of microvessels in the cerebral cortex, subcortical grey matter and white matter, pons and cerebellum," *Journal of Chemical Neuroanatomy*, vol. 88, pp. 22–32, Mar. 2018, doi: 10.1016/j.jchemneu.2017.11.005.

[165] Y. Asai, S. Inoue, K. Tatebayashi, Y. Shiraishi, and Y. Kawai, "Effects of head-down tilt on cerebral blood flow in humans and rabbits," *Journal of gravitational physiology : a journal of the International Society for Gravitational Physiology*, vol. 9, pp. P89-90, Aug. 2002.

[166] J. Ashburner and K. J. Friston, "Unified segmentation," *NeuroImage*, vol. 26, no. 3, pp. 839–851, Jul. 2005, doi: 10.1016/j.neuroimage.2005.02.018.

[167] I. Despotović, B. Goossens, and W. Philips, "MRI Segmentation of the Human Brain: Challenges, Methods, and Applications," *Computational and Mathematical Methods in Medicine*, Mar. 01, 2015. https://www.hindawi.com/journals/cmmm/2015/450341/ (accessed Oct. 28, 2020).

[168] G. Pagé *et al.*, "Assessing Tumor Mechanics by MR Elastography at Different Strain Levels," *Journal of Magnetic Resonance Imaging*, vol. 50, no. 6, pp. 1982–1989, Dec. 2019, doi: 10.1002/jmri.26787.

Titre : Conditions optimales et sensibilité de l'ERM cérébrale : milieux homogènes à hétérogènes

Mots clés : Élastographie, IRM, biomécanique, cerveau, conditions optimales, sensibilité

Résumé : L'élastographie par résonance magnétique (ERM) est une technique d'imagerie permettant la caractérisation mécanique des tissus biologiques. Cette technique consiste à enregistrer par IRM les champs de déplacement induits par la propagation d'une onde de cisaillement générée dans un tissu cible. Des paramètres mécaniques tels que la vitesse de l'onde de cisaillement, le module d'élasticité ou de viscosité de cisaillement peuvent ensuite être déduits en inversant les équations différentielles des champs de déplacement acquis.

Des travaux récents ont montré la difficulté d'une quantification absolue des paramètres mécaniques et ont permis de souligner les facteurs déterminant l'exactitude et la précision de la mesure par ERM qui peuvent finalement être ramenés à deux paramètres caractérisant essentiellement la qualité de l'échantillonnage de l'onde de cisaillement qui se propage dans le milieu étudié : le facteur d'échantillonnage spatial, $s = \lambda/a$, et le facteur d'échantillonnage d'amplitude, $Q = q \,/\, \Delta q$, où λ est la longueur d'onde de cisaillement, a, la taille du voxel, q, l'amplitude du rotationnel du champ de déplacement, et Δq , l'incertitude de mesure associée. Ainsi, dans des milieux mécaniquement homogènes, les conditions optimales sur s et Q doivent être remplies pour que les résultats de l'ERM soient valides.

Dans ce travail de thèse, les conditions optimales ont été étudiées dans des milieux hétérogènes et structurés pour pouvoir les appliquer in vivo dans le cerveau. Premièrement, l'incertitude de mesure en ERM a été évaluée pour des stratégies d'échantillonnage optimales en réalisant des expériences multifréquences sur un ensemble de quatre fantômes homogènes calibrés mécaniquement qui reprennent les stades de la fibrose hépatique. Une quantification mécanique absolue et une gradation significative n'ont pu être obtenues que lorsque les conditions optimales étaient remplies pour l'ensemble des fantômes soit prospectivement par une excitation multifréquence adéquate, soit rétrospectivement par un multi-rééchantillonnage des données. Deuxièmement, les conditions optimales de l'ERM ont été établies sur un fantôme mammaire hétérogène contenant des inclusions modélisant des lésions tumorales plus rigides que le parenchyme homogène autour. Cette étude a mis en évidence la nécessité d'un échantillonnage multiple des champs de déplacement à travers des acquisitions à différentes fréquences d'excitation afin, d'une part, de déterminer les paramètres mécaniques régionaux avec les meilleures précision et exactitude possibles et, d'autre part, de discriminer significativement mieux différentes régions mécaniques du fantôme. Troisièmement, des acquisitions d'ERM cérébrale à différentes fréquences d'excitation ont été réalisées afin d'étudier les meilleures conditions pour discriminer avec précision et exactitude la matière blanche, la matière grise et le cervelet chez un sujet sain. Le cervelet s'est avéré moins viscoélastique que les matières blanches et grises cérébrales, qui présentaient des modules viscoélastiques de cisaillement similaires en dépit de leurs structures anatomiques différentes. Enfin, des conditions physiologiques analogues à la microgravité ont été mises en place pour modifier les propriétés mécaniques du cerveau et éprouver la sensibilité de l'ERM aux changements induits. En position inclinée tête en bas, l'ERM a révélé une augmentation significative de la vitesse et des modules viscoélastiques dans tout le cerveau, en particulier dans les régions périphériques supérieures. Cette étude a permis de montrer que l'ERM cérébrale, réalisée dans des conditions optimales, pourrait être avantageusement utilisée pour détecter des altérations mécaniques dues à des changements de pression similaires ou inverses dans des processus pathologiques tels que l'hémorragie, l'hydrocéphalie ou le cancer qui s'accompagnent d'une redistribution du flux sanguin et une accumulation ou une perte de liquide cérébrospinal.

Title: Optimal conditions and sensitivity of brain MRE: from homogeneous to heterogeneous media

Keywords: Elastography, MRI, biomechanics; brain, optimal conditions, sensitivity

Abstract: Magnetic Resonance Elastography (MRE) is an imaging technique for the mechanical characterization of biological tissues. This technique consists in recording by MRI the displacement fields induced by the propagation of an induced shear wave in a target tissue. Mechanical parameters such as the shear wave velocity, shear elasticity or shear viscosity moduli can then be deduced by inverting the differential equations of the acquired displacement fields. Thus, MRE allow to map the mechanical parameters of the medium which are recognized as relevant biomarkers to characterize the pathophysiological state of biological tissues.

However, the promise of absolute quantification of shear viscoelastic moduli by MRE is undermined by the multiple dependence of the results on acquisition parameters and reconstruction methods. Recent works have shown that the factors determining the accuracy and precision of MRE measurement can ultimately be subsumed with two parameters that essentially characterize how well the propagating shear wave is sampled: the spatial sampling factor, $s = \lambda/a$, and the amplitude sampling factor, $Q = q/\Delta q$, where λ is the shear wavelength, a, the voxel size, q, the amplitude of the curl of the displacement field, and Δq, the associated measurement uncertainty. Optimal conditions on s and Q must be fulfilled to validate MRE outcomes as proven in mechanically homogeneous media.

In this work, optimal conditions were studied in heterogeneous and structured media so that they could be applied to the brain.

First, MRE accuracy and precision were investigated with optimal sampling strategies by carrying out multi-frequency experiments on a set of four mechanically-calibrated phantoms that mimic the stages of liver fibrosis. Absolute quantification and significant grading could be achieved only when optimal conditions were fulfilled either prospectively by adequate multi-frequency excitation or retrospectively by data multi-resampling. Second, MRE optimal conditions were investigated on a heterogeneous breast phantom containing inclusions mimicking tumor lesions stiffer than the surrounding homogeneous parenchyma. This second study allowed to show the need to set different optimal sampling factors by acquiring with multiple excitation frequencies in order to regionally determine the mechanical parameters with the best accuracy and precision and more significantly discriminate the mechanically different regions.

Third, multi-frequency brain MRE was performed in order to investigate the best conditions to accurately and precisely discriminate cerebral white matter, grey matter, and the cerebellum in a healthy subject. The cerebellum was found to be less elastic and viscous than cerebral white and grey matters, which exhibited similar shear viscoelastic moduli despite their different anatomical structures. These findings corroborated results recently found in the literature and questioned the general sensitivity of the technique for mechanically characterizing brain diseases. Fourth, physical conditions analogous to microgravity were implemented in the bore of the MRI system to tune brain mechanical properties and challenge MRE sensitivity to inferred changes. During head-down tilt at rest, the expected cephalad fluid shift may increase intracranial pressure in healthy subjects like in a zero gravity spaceflight. Associated tissue stiffening was revealed with optimal MRE by a significant increase of the shear velocity and shear dynamic modulus throughout the brain, especially in the superior peripheral regions. Thereafter, brain MRE, performed in optimal conditions, could be advantageously used to detect mechanical alterations due to similar or inverse pressure changes in pathological processes like hemorrhage, hydrocephalus, or cancer with blood flow redistribution and cerebrospinal fluid accumulation or depletion.